Università degli Studi di Torino
Scuola di Dottorato

UNIVERSITÀ
DI TORINO

Inclusive semileptonic decays of heavy mesons and other challenging problems in lattice QCD

Antonio Smecca

Università degli Studi di Torino
Scuola di Dottorato

Dottorato in Fisica
XXXVI ciclo

Inclusive semileptonic decays of heavy mesons and other challenging problems in lattice QCD

Antonio Smecca

Tutor: Prof. Marco Panero

Se non ci divertiamo
a risolvere questo problema,
perché dovremmo studiarlo?

Nicola Cabibbo

Abstract

This doctoral thesis addresses some open problems, of a non-perturbative nature, in the context of quantum chromodynamics (QCD), the theory that describes the strong nuclear interaction in the Standard Model of elementary particle physics, and in statistical models of spin systems, by means of lattice field theory. The main topic addressed in this work is the investigation of inclusive semileptonic decays of heavy mesons through numerical simulations of lattice QCD and through the reconstruction of spectral functions by means of a variant of the Backus-Gilbert method. After presenting the original results obtained, the future prospects and possible generalizations in this research line are discussed.

Riassunto in italiano

Questa tesi di dottorato affronta alcuni problemi aperti, di natura non perturbativa, nell'ambito della cromodinamica quantistica (QCD), la teoria che descrive l'interazione nucleare forte nel Modello Standard della fisica delle particelle elementari, e nei modelli statistici dei sistemi di spin, mediante la teoria dei campi su reticolo. L'argomento principale affrontato in questo lavoro è lo studio di decadimenti semileptonici inclusivi di mesoni pesanti attraverso simulazioni numeriche di QCD su reticolo e attraverso la ricostruzione di funzioni spettrali per mezzo di una variante del metodo di Backus-Gilbert. Dopo aver presentato i risultati originali ottenuti, vengono discusse le prospettive future e le possibili generalizzazioni in questa linea di ricerca.

Aknowledgements

This manuscript is the result of three years of hard work, which have been possible thanks to the help and support of the many people I was lucky enough to interact with. All these people contributed to my academic and personal growth and made my time in Torino truly memorable.

First and foremost, I thank my supervisor Marco, for the trust given to me from day one, for his constant support and advice during these years and for his essential assistance in writing this thesis. I am forever grateful to him for teaching me a profound new way of looking at lattice field theories and lattice QCD.

Thanks to his involvement in the inclusive semileptonic decays project, I had the privilege and luck to work side by side with Nazario Tantalo, who has been *de facto* my second supervisor. I am indebted to Nazario for his patience and support during the project, but perhaps most importantly, for the all the things he taught me during our countless meetings both remotely and during my visit to Rome. The way I approach physics problems and pursue research objectives has been shaped by our discussions.

I am deeply grateful to Prof. Paolo Gambino, Dr. Francesco Sanfilippo and Dr. Silvano Simula for their excellent advice during the inclusive project. I am also grateful to Sandro Mächler, a fellow Ph.D. student with whom I shared the workload of this very intense project.

I wish to thank the thesis referees Dr. Alberto Ramos and Prof. Alexander Lenz for sharing with me very useful comments and corrections to the thesis. I hope to have addressed them appropriately in the final version of this manuscript.

I would also like to thank the lattice group at the University of Turin, in particular Prof. Michele Caselle, Dr. Alessandro Nada, Elia Cellini and Andrea Bulgarelli, for their help and the useful discussions. I am looking forward to seeing you at future conferences and hopefully find a way to continue our physics collaboration.

During my time at the University of Turin I shared an "open space" office in the underground floor together with almost all the other theory Ph.D. students. This set up allowed me to meet some really good researchers and even better people, some of

them I was lucky enough to call friends. I warmly thank Luca, Gloria, Andrea, Giorgio, Francesco and Alberto for the fun and stimulating discussions inside and outside the physics department.

I would like to express my sincere gratitude to my physics teacher Concetto Gianino, who has played a main role in my decision to pursue an academic career in physics and without whom this thesis would not exist.

I would also like to thank all my friends in Italy and abroad. In particular I thank Noel, Federico, Giuseppe, Adam, Sid, Ody, Tom, Nik, Vito, Francesco, Leonardo, Stefano, Giulia, Alberto, Jack, Tambu, Anna, Umberto, Anna, Salvo and Giuliana for their sincere friendship over the years.

A warm thank you also to the San Salvario A.S.D. Basketball team.

I dedicate this thesis to my parents and my brother Lorenzo, to whom I owe everything I am and all of my achievements.

Finally, a special thank you to Fede, who is so very important to me. I am excited for the years to come.

Contents

Chapter 1

Introduction

Exactly solvable models are relatively rare in quantum field theory, and most often they are not of direct phenomenological relevance. While many interesting phenomena occurring in nature can be described by theories that can be studied by means of perturbative techniques (whereby one typically starts from an idealised limit of the theory, in which interactions between the fundamental degrees of freedom are neglected, and then introduces the effects of the interaction, parameterised in terms of a "small" numerical coefficient, by computing subsequent corrections to the non-interacting limit), many others are of intrinsically non-perturbative nature, and consequently evade any attempt to capture them through weak-coupling-expansion methods.

Hadrons, which are composite states bound by the strong nuclear interaction, provide a prime example: while the theory of the Standard Model describing the strong nuclear interaction is quantum chromodynamics (QCD), which reduces to a theory of non-interacting quarks and gluons at an infinitely high energy scale, and can be approximated analytically by perturbation theory at very large, but finite, energy scales, the perturbative approach misses the most relevant physical phenomena determining the low-energy spectrum of the theory, namely confinement of colour charges in colour singlets, and the dynamical breaking of chiral symmetry.

Even though over the years many analytic and numerical methods have been developed to obtain a quantitative understanding of the physics underlying these phenomena, the most fundamental and most reliable one consists in regularising the theory on a spacetime lattice. This method, which was proposed by Kenneth G. Wilson in ref. [1], provides a mathematically well-defined, gauge-invariant, non-perturbative definition of the path integrals to quantise the theory, and allows one to estimate these integrals numerically, by means of Monte Carlo calculations. With present (super-)computing resources, this approach (which is systematically improvable and directly based on the

underlying microscopic theory) leads to very precise theoretical predictions. While people who are not lattice-QCD practitioners occasionally regard the lattice regularisation simply as a crude approximation of the theory defined in the continuum, it is worth remarking that this is a misconception. In the limit of vanishing lattice spacing, lattice QCD *is* QCD; more precisely, one can state that continuum QCD is a good low-energy effective description of the lattice theory, where, in this case "low energies" means "energies much smaller than the lattice cutoff scale", which is inversely proportional to the lattice spacing a and, thus, goes to infinity in the $a \to 0$ limit. This crucial property, which holds not only at the classical but also at the quantum level, is a consequence of the way in which the symmetries of the continuum theory are explicitly partially broken (like the Lorentz-Poincaré symmetries, which are reduced to discrete subgroups) or are explicitly preserved (like the gauge symmetry) by the lattice regularisation at every value of the lattice spacing.

The regularisation of QCD on a lattice was motivated by the close analogy between Euclidean quantum field theory and statistical field theory, and, following this analogy, one of the problems addressed in this doctoral thesis deals with the properties of a particular type of excitations in the Heisenberg spin model.

Another problem that is studied in this thesis has to do, instead, with the mechanism by which, in confining non-Abelian gauge theories, the flux lines generated by colour sources form thin tubes, whose energy grows with their length (implying linear confinement of colour charges) and whose dynamics can be modelled in terms of a bosonic string theory. It is particularly interesting to study the behaviour of such confining flux tubes at finite temperature, in particular in the proximity of a transition point, in which one expects the long-distance properties of the theory to be captured by a spin model.

Finally, it is worth remarking that, in addition to serving as a tool to study important properties of QCD, lattice QCD also play a very important role in flavour physics, due to the fact that quarks undergoing processes mediated by the weak interaction are not isolated particles: instead, these processes occur for quarks that are bound by the non-perturbative effects of the strong interaction into colour-singlet states. Among these processes, semileptonic decays play a pivotal role in our understanding of flavor physics and the determination of important parameters, such as the Cabibbo-Kobayashi-Maskawa (CKM) matrix element $|V_{cb}|$. These processes are of particular interest due to their sensitivity to possible new physics effects, as they may be indirectly affected by the dynamics of particles with masses even higher than those potentially accessible at the Large Hadron Collider at CERN.

For many years, lattice QCD provided precise theoretical predictions for quanti-

ties related to exclusive semileptonic decays, in which a single hadron state decays into another single state with a different valence quark content. The computation of inclusive semileptonic decays, on the other hand, requires the simultaneous computation of several different hadronic states which has been considered for many years as prohibitively complicated for lattice QCD simulations. The situation, however, has dramatically changed in recent years, with the advent of new formal methods to capture inclusive decays on the lattice, and with the parallel development of sophisticated spectral-reconstruction techniques that allow one to access precise information on the physical states contributing to lattice QCD correlation functions. The combination of these two novel methods into a lattice QCD study of inclusive semileptonic decays of heavy mesons is the third and main problem addressed in this thesis.

Overall, this thesis aims therefore to contribute to the growing body of knowledge in the field of lattice QCD, with a specific focus on inclusive semileptonic decays of heavy mesons and tackling various challenging problems in non-perturbative QCD, such as the extraction of spectral functions from lattice correlators, the study of confinement in Yang-Mills theory and the behaviour of non-trivial topological excitations in spin models. By shedding light on these physical phenomena, we hope to deepen our understanding of strongly coupled theories.

The structure of this doctoral thesis is the following: In chapter 2 we introduce the theoretical background of lattice gauge theories and discuss its connection to statistical mechanics. In chapter 3 we will describe how the full theory of QCD can be regularised on the lattice and we will introduce the formalism used in order to simulate quarks on the lattice, while in chapter 4 we will review the numerical techniques employed in modern day lattice field theory simulations. In chapter 5, we discuss our results in the study of monopole-like configurations in the classical Heisenberg spin-model and in chapter 6 we investigate the description of confinement due to vibrating strings at finite temperatures. In chapter 7 we discuss the HLT method used in the extraction of spectral functions from lattice correlation functions and we also show how they can be used in order to extract glueball masses in $SU(3)$ Yang-Mills theory, before describing the details of our new method to compute inclusive semileptonic decays on the lattice in chapter 8. Finally, in chapter 9 the main findings of this work are summarised. Some notations and technical details are collected in the Appendices.

The original research work discussed in this doctoral thesis has resulted in the publication of three peer-reviewed scientific articles [2, 3, 4] and was presented at various international conferences [5, 6, 7, 8].

Chapter 2

Lattice gauge theory

Quantum field theories are the cornerstone of the modern theoretical description of elementary particle physics. They combine the two main advances that shook fundamental physics during the first half of the XX century, namely, quantum mechanics and the theory of (special) relativity, into a tight theoretical framework, from which one can derive far-reaching implications.

The predictions of quantum field theories (including those that can be formulated in terms of invariance under local internal symmetries, i.e., gauge theories) are often derived in a perturbative approach, in the path-integral framework due to Richard P. Feynman [9]. Yet, the existence of various types of divergences makes a mathematically well-defined, gauge-invariant formulation of these theories beyond perturbation theory non trivial. This may be surprising, given that effects not captured by perturbation theory are predominant in at least one of the gauge theories in the Standard Model of elementary particle physics – namely quantum chromodynamics (QCD), the theory of the strong nuclear interaction, which is based on the unbroken gauge invariance under the $SU(3)$ group acting on "colour" degrees of freedom. In particular, the nature and the structure of the lightest physical states in the spectrum of the theory is determined by phenomena of non-perturbative nature, namely confinement of colour charges into color-singlet states and the dynamical breaking of the (approximate) chiral symmetry for the lightest quark species ("flavours").

The formulation on a discrete lattice (rather than in a continuous space-time) is a way to provide a mathematically rigorous, gauge-invariant, non-perturbative definition of a gauge theory. The first formulation of a lattice gauge theory was presented in a seminal article by Kenneth G. Wilson in 1974 [1]. In the article, Wilson set up an Abelian gauge theory (the generalisation to non-Abelian gauge theories being straightforward) on a four-dimensional Euclidean lattice with a lattice spacing a, which provide

a natural ultraviolet cutoff – the modulus of each component of the momentum that can be probed on a lattice of spacing a cannot exceed π/a.

The most common method for regularising a quantum field theory on the lattice is based on a Wick-rotated version of the original space-time (replacing the Minkowski time t with Euclidean time τ, namely: $t \to -i\tau$), whereby the Minkowski metric $g_{\mu\nu} = \text{diag}(-1, 1, 1, 1)$ traded for the Euclidean one $\eta_{\mu\nu} = \text{diag}(1, 1, 1, 1)$: this explicitly reveals the connection between a quantum field theory and a statistical-mechanics model, allowing one to make use of techniques such as Monte Carlo simulations to evaluate expectation values of operators as well as correlation functions.

Thus, trough the lattice regularisation one is able to study intrinsically non-perturbative phenomena, such as colour confinement in Yang-Mills theories, with the aid of numerical simulations.

2.1 Path integral formalism

In order to evolve a quantum state from time t_i to t_f one can define the time-evolution operator in Euclidean space-time as

$$\hat{U}(t_f, t_i) = e^{-\hat{H}(t_f - t_i)}, \tag{2.1}$$

where $\hat{H}$ is the quantum Hamiltonian operator. One can note the difference with the time-evolution operator in Minkowski space-time $U_M(t) = e^{-i\hat{H}t}$, where the extra imaginary unit comes from the Wick rotation. The discrete energy states of the system and the Hamiltonian operator are related by the familiar eigenvalue equation

$$\hat{H}|\phi_n\rangle = E_n|\phi_n\rangle, \tag{2.2}$$

where $|\phi_n\rangle$ are eigenvectors; one can choose an orthonormal basis of states fulfilling the condition

$$\int d^3\phi_n |\phi_n\rangle\langle\phi_n| = \mathbb{1}. \tag{2.3}$$

In the path integral formalism, one can evaluate the matrix element associated with the evolution of a state from an initial to a final time as

$$\langle\phi_f|\hat{U}(t_f, t_i)|\phi_i\rangle = \lim_{N\to\infty} \int \prod_{n=0}^{N} d\phi_n e^{-\tau \sum_{n=0} \mathcal{L}(\phi_n)} \tag{2.4}$$

$$= \int \mathcal{D}\phi \; e^{-\int d^4x \mathcal{L}(\phi)}, \tag{2.5}$$

which makes it explicit that the matrix element of the time-evolution operator is equal to the integral over all possible classical paths. Thus, borrowing the terminology from statistical mechanics, one can define the partition function as

$$Z = \int \mathcal{D}\phi \; e^{-\int d^4x \mathcal{L}(\phi)} = \int \mathcal{D}\phi \; e^{-S(\phi)}, \tag{2.6}$$

where $S(\phi)$ is the Euclidean action of the quantum field theory.

In order to clarify the parallelism between a quantum field theory on the lattice and a statistical field theory, it is convenient to think of a lattice field theory as a spin model. Indeed, a statistical field theory in D dimensions is related to a quantum field theory in $D-1$ dimensions. This connection is very important in order to understand the role of the transfer matrix in lattice field theory. The Euclidean action is real and bounded from below, so the above equation can be understood as the partition function of a statistical mechanics system in which the exponential of the Euclidean action e^{-S_E} plays the role of the weight of a given configuration of the fields, replacing the familiar Boltzmann factor $e^{-\beta H}$ [10].

Once a lattice field theory has been formulated, the original field theory problem becomes one of statistical mechanics [11].

2.2 Transfer matrix

The analogy between QFT and classical statistical field theory suggests that there exists an analog of the quantum time-evolution operator in the context of classical statistical mechanics. This operator is the transfer matrix $\hat{T}$. Imposing periodic boundary conditions in time we have for a generic scalar field

$$\phi(0, \boldsymbol{x}) = \phi_i(\boldsymbol{x}), \qquad \phi(T, \boldsymbol{x}) = \phi_f(\boldsymbol{x}). \tag{2.7}$$

The Hamiltonian operator induces infinitesimal translations in time. In classical statistical mechanics what we have is a D-dimensional spatial lattice. Therefore, the transfer matrix induces translation by one lattice spacing a, which is the smallest possible distance on an Euclidean lattice.

$$\hat{T} = \exp(-a\hat{H}). \tag{2.8}$$

Given that the partition function for a classical statistical mechanics system is $Z = \prod_x \sum_s e^{\beta H}$ and assuming periodic boundary conditions, the transfer matrix obeys

$$Z = \mathrm{Tr}[\hat{T}^N], \tag{2.9}$$

where N is the number of lattice sites in the direction of the evolution.

Another quantity which is often used in statistical mechanics and in finite temperature QFT is the equilibrium density matrix $\hat{\rho}$, which describes an ensemble of states. One can define the density matrix in terms of the transition matrix

$$\hat{\rho} = \frac{1}{Z} e^{-aN\hat{H}} = \frac{1}{Z}\hat{T}^N; \tag{2.10}$$

it is then possible to estimate the expectation value of a generic operator as an average over an ensemble of states described by the density matrix

$$\langle \hat{O} \rangle = \frac{1}{Z}\,\mathrm{Tr}[\hat{T}^N \hat{O}] = \mathrm{Tr}[\hat{\rho}\ \hat{O}]. \tag{2.11}$$

At this point, it is convenient to discretise the Euclidean quantum field theory defined on a hyper-cubic lattice Λ_4 of lattice spacing a

$$\Lambda_4 = \left\{ x : x = \sum_{\mu=1}^{4} a n_\mu, n_\mu \in Z_4 \right\} \tag{2.12}$$

where n_μ label the lattice sites and a is the lattice spacing [10, 12]. The lattice spatial volume is defined as L^3 (where, for simplicity, we take the lattice size in all spatial dimensions to be L) while T denotes the extent of the lattice along the Euclidean-time direction.

Then, the integration measure appearing in equation 2.6 can be rewritten as a multiple and high-dimensional, but ordinary, integration measure

$$\mathcal{D}[\phi] = \prod_{n \in \Lambda} d\phi(n) \tag{2.13}$$

and we can write the partition function of the system described by the QFT as

$$Z = \int \prod_{n \in \Lambda} d\phi(\boldsymbol{n}) e^{-S[\phi]} = \langle \phi_f | \hat{T}^{N_T} | \phi_i \rangle = \mathrm{Tr}[\hat{T}^{N_T}], \tag{2.14}$$

where $N_T = T/a$ is the number of lattice sites along the Euclidean-time direction.

On the lattice, the operator responsible for translations is the transfer matrix, hence

the Hamiltonian becomes a derived quantity

$$\hat{H} \equiv \lim_{a\to 0} -\frac{1}{a}\ln \hat{T}. \tag{2.15}$$

In order for $\hat{H}$ to be a self-adjoint Hamiltonian, one needs $\hat{T}$ to be a symmetric, bounded, and positive operator acting on a Hilbert space of states with a positive norm. The necessary condition for this is the Osterwalder-Schrader reflection positivity [13] which was demonstrated to hold for lattice gauge theories by Martin Lüscher in [14]. The consequence of this is that the correlation functions in the desired physical Minkowski space-time can be obtained by analytic continuation of their Euclidean counterpart. In other words, it means that the operator $\hat{T}$ will give us the same physics one would normally obtain with $\hat{H}$.

When we evaluate the partition function, as in equation 2.14, we sandwich the operator between vectors of an orthonormal basis and sum over all basis vectors. Using $|\alpha(\boldsymbol{p})\rangle$ as the basis of the eigenstates of $\hat{H}$, where $\boldsymbol{p}$ is the state momentum. These states are the eigenstates of the Hamiltonian, which is invariant under translation and therefore commutes with the momentum operator $[\hat{H}, \hat{P}]$. Therefore, the eigenstates of the Hamiltonian are also momentum eigenstates

$$\hat{P}|\alpha(\boldsymbol{p})\rangle = \boldsymbol{p}|\alpha(\boldsymbol{p})\rangle, \tag{2.16}$$

$$\hat{H}|\alpha(\boldsymbol{p})\rangle = E_{\boldsymbol{p}}(\alpha)|\alpha(\boldsymbol{p})\rangle, \tag{2.17}$$

with $E^2_{\boldsymbol{p}}(\alpha) = m(\alpha)^2 + |\boldsymbol{p}|^2$. Here $m(\alpha)$ is not necessarily a one-particle mass, since $|\alpha(\boldsymbol{p})\rangle$ could represent a multi-particle state with total momentum $\boldsymbol{p}$ belonging to the energy level α. Using the completeness relation for the full Hilbert space:

$$\mathbb{1} = |0\rangle\langle 0| + \sum_{\alpha}\int \frac{d^3p}{(2\pi)^3 2E_\alpha(\boldsymbol{p})}|\alpha(\boldsymbol{p})\rangle\langle\alpha(\boldsymbol{p})|, \tag{2.18}$$

one can write the partition function as

$$Z = \frac{1}{L^3}\sum_{\alpha}\frac{1}{2E_\alpha(\boldsymbol{p})}\langle\phi_i|e^{-N_T\hat{H}}|\alpha(\boldsymbol{p})\rangle\langle\alpha(\boldsymbol{p})|\phi_f\rangle \tag{2.19}$$

$$= \frac{1}{L^3}\sum_{\alpha}\frac{1}{2E_\alpha(\boldsymbol{p})}\langle\phi_i|\alpha(\boldsymbol{p})\rangle e^{-N_T E_\alpha}\langle\alpha(\boldsymbol{p})|\phi_f\rangle. \tag{2.20}$$

Finally, taking the limit in which the time extent becomes infinitely large, one gets

$$\lim_{N_T\to\infty} Z = \langle\phi_i|0\rangle e^{-N_T E_0}\langle 0|\phi_f\rangle. \tag{2.21}$$

The ground state of the Hamiltonian $|0\rangle$ defines the vacuum with energy $E_0 = E_0(\mathbf{0})$ and it is normalised to one. In the $N_T \to \infty$ only the states with E_0 survive and $|\phi_{i,f}\rangle$ become a linear combination of all the states with vacuum quantum numbers.

Exactly like in statistical field theory, one can define Euclidean correlation functions of two generic operators $\hat{O}_{1,2}$

$$\langle\hat{O}_1(x)\hat{O}_2(y)\rangle_{N_T} = \frac{1}{Z}\langle\phi_f|e^{-(N_T-n_x^0)\hat{H}}\hat{O}_1(\boldsymbol{n}_x)e^{(n_x^0-n_y^0)\hat{H}}\hat{O}_2(\boldsymbol{n}_y)e^{-n_y^0\hat{H}}|\phi_f\rangle, \tag{2.22}$$

where n_x^0 and n_y^0 are the time components of the position 4-vectors n_x, n_y. Again, inserting a complete set of states

$$\langle\hat{O}_1(x)\hat{O}_2(y)\rangle_{N_T} = \frac{1}{Z}\frac{1}{L^9}\sum_{\alpha,\beta,\gamma}\frac{1}{(2\pi)^3 E_\alpha(\boldsymbol{q})E_\beta(\boldsymbol{p})E_\gamma(\boldsymbol{s})}\langle\phi_f|\alpha(\boldsymbol{q})\rangle e^{-(N_T-n_x^0)E_\alpha(\boldsymbol{q})} \tag{2.23}$$

$$\times\,\langle\alpha(\boldsymbol{q})|\hat{O}_1(\boldsymbol{n}_x)|\beta(\boldsymbol{p})\rangle e^{-(n_x^0-n_y^0)E_\beta(\boldsymbol{p})}\langle\beta(\boldsymbol{p})|\hat{O}_2(\boldsymbol{n}_y)|\gamma(\boldsymbol{s})\rangle e^{-n_y^0 E_\gamma(\boldsymbol{s})}\langle\gamma(\boldsymbol{s})|\phi_i\rangle. \tag{2.24}$$

The two exponentials with temporal arguments $(N_T - n_x^0)$ and n_y^0 produce contributions from the boundary states $\phi_{i,f}$. Then, upon very large time separations $(N_T - x_0), y_0 \to \infty$ the only surviving contributions come from $E_\alpha(\boldsymbol{q})$ and $E_\beta(\boldsymbol{s})$, which in this limit are equivalent to E_0 and therefore will cancel with the argument coming from the partition function. Thus, all the energy states propagating between the two operators will be correctly normalised with the ground state energy $\tilde{E}_\alpha(\boldsymbol{q}) = E_\alpha(\boldsymbol{p}) - E_0(\mathbf{0})$. In this limit, the matrix elements $\langle\phi_f|0\rangle$ and $\langle 0|\phi_i\rangle$ drop out in the ratio with the partition function, giving the familiar vacuum expectation value of two-point correlator

$$\lim_{N_T\to\infty}\langle\hat{O}_1(x)\hat{O}_2(y)\rangle_{N_T} = \frac{1}{L^3}\sum_{\alpha}\frac{1}{(2\pi)E_\alpha(\boldsymbol{p})}\langle 0|\hat{O}_1(\boldsymbol{n}_x)|\alpha(\boldsymbol{p})\rangle e^{-(n_x^0-n_y^0)\tilde{E}_\alpha(\boldsymbol{p})}\langle\alpha(\boldsymbol{p})|\hat{O}_2(\boldsymbol{n}_y)|0\rangle. \tag{2.25}$$

The formula above should be familiar. For large time separations $n_x^0 - n_y^0$, the Euclidean correlation function of two operators decays exponentially in terms of the energy gap of the system $E_\alpha - E_0$. This is the same behaviour of Euclidean correlation functions in spin systems for large spatial separations $|\boldsymbol{n}_x - \boldsymbol{n}_y|$ where the decay is exponential in terms of the inverse of the correlation length ξ. From this simple argument it is natural to establish a connection between the correlation length of two

operators and the energy gap of the theory, giving the relation

$$\frac{1}{\xi} = E_\alpha - E_0 = m. \tag{2.26}$$

Assuming the invariance of the vacuum state under the transfer matrix $\hat{T}$ and exploiting the fact that $\hat{H}$ and $\hat{P}$ commute, one can write the matrix elements as

$$\langle 0|\hat{O}(x)|\alpha(\boldsymbol{p})\rangle = \langle 0|e^{i\hat{P}\cdot n_x}\hat{O}(0)e^{-i\hat{P}\cdot n_x}|\alpha(\boldsymbol{p})\rangle \tag{2.27}$$

$$= \langle 0|\hat{O}(0)|\alpha(\boldsymbol{p})\rangle e^{-ip\cdot n_x}|_{p^0=E_\alpha(\boldsymbol{p})}, \tag{2.28}$$

which allows to write the Euclidean two-point correlation function in the Källén-Lehmann representation

$$\langle \hat{O}_1(x)\hat{O}_2(y)\rangle = \frac{1}{L^3}\sum_\alpha \frac{e^{ip\cdot(\boldsymbol{n}_x-\boldsymbol{n}_y)}}{2\pi E_\alpha(\boldsymbol{p})}|\langle\alpha(\boldsymbol{p})|\hat{O}(0)|0\rangle|^2 e^{(n_x^0-n_y^0)(E_\alpha(\boldsymbol{p})-E_0)} \tag{2.29}$$

$$= \frac{1}{L^3}\sum_\omega \rho(\omega,\boldsymbol{p})e^{-\omega(n_x^0-n_y^0)}e^{ip\cdot(\boldsymbol{n}_x-\boldsymbol{n}_y)} \tag{2.30}$$

where $\rho(\omega,\boldsymbol{p})$ is the finite volume spectral density function. In a finite volume, the energy spectrum is naturally discretised, thus, $\rho(\omega_\alpha)$ is not a continuous function of ω but rather a distribution of isolated δ-functions spanning the discretised energy spectrum. A formal treatment of spectral functions will be introduced in sec. 7.1. As one approach the continuum limit, sending $a \to 0$, the summation in equation 2.30 becomes an integral and the spectral density $\rho(\omega)$ will become a function of a continuous spectrum of states.

On the lattice, one can build quantum operators from field operators and their conjugate momenta, defined at each lattice site ϕ

$$\hat{O}_A = \hat{\phi}(n_0)^\dagger, \qquad \hat{O}_B = \sum_{\boldsymbol{n}\in\Lambda_3}\hat{\phi}(\boldsymbol{n})e^{-a\boldsymbol{n}\cdot\boldsymbol{p}}, \tag{2.31}$$

where in this example the operator $\hat{O}_A$ creates a field from the vacuum at some position n_0, and the operator $\hat{O}_B$ annihilates a field with projected momentum $\boldsymbol{p}$.

Using the eigenvalue equation and considering a complete set of orthogonal state

$$\hat{\phi}(\boldsymbol{n})|\phi\rangle = \phi(\boldsymbol{n})|\phi\rangle, \tag{2.32}$$

$$\langle\phi'|\phi\rangle = \delta(\phi'-\phi) \equiv \prod_{\boldsymbol{n}\in\Lambda_3}\delta(\phi'(\boldsymbol{n})-\phi(\boldsymbol{n})), \tag{2.33}$$

one can write the matrix elements as

$$\langle\tilde{\phi}|\hat{O}|\phi\rangle = O[\phi]\delta\big(\tilde{\phi}-\phi\big). \tag{2.34}$$

The object $O[\phi]$ is no longer an operator, but a functional of the classical field variables ϕ. The functional maps a field configuration ϕ, specified by the set of all field values $\phi(\boldsymbol{n})$, $\boldsymbol{n} \in \Lambda_3$, into the complex numbers $\mathbb{C}$. One can then rewrite the operators in equation 2.33 as functionals

$$O_A[\phi] = \phi(n_0)^*, \qquad O_B[\phi] = \sum_{\boldsymbol{n}\in\Lambda_3} \phi(\boldsymbol{n}) e^{a\boldsymbol{n}\cdot\boldsymbol{p}}, \tag{2.35}$$

and write the Euclidean two-point correlation function as the path integral of functionals

$$\langle O_2(t)O_1(0)\rangle = \frac{1}{Z}\int \mathcal{D}[\phi] e^{-S_e[\phi]} O_2[\phi(\boldsymbol{n},n_t)] O_q[\phi(\boldsymbol{n},0)]. \tag{2.36}$$

2.3 Purely gluonic theory in the continuum

In pure gauge theory, the action is a function of gauge fields only. Theories based on non-Abelian gauge group are known as Yang-Mills theories and their action can be written in Euclidean space as

$$S_{YM}[A] = \frac{1}{2g^2}\int d^4x \,\mathrm{Tr}[F_{\mu\nu}(x)F_{\mu\nu}(x)]. \tag{2.37}$$

$F_{\mu\nu}$ is the field strength tensor and is defined as the commutator

$$F_{\mu\nu}(x) = -i[D_\mu(x), D_\nu(x)] = \partial_\mu A_\nu(x) - \partial_\nu A_\mu(x) + i[A_\mu(x), A_\nu(x)], \tag{2.38}$$

and D_μ is the covariant derivative which ensure the gauge invariance of the action

$$D_\mu(x) = \partial_\mu + iA_\mu(x). \tag{2.39}$$

The gauge fields $A_\mu(x)$ are Hermitian, traceless matrices. When we work in $SU(3)$ Yang-Mills theory, the gauge fields are elements of the $\mathfrak{su}(3)$ Lie algebra

$$A_\mu^{(a)}(x) = \sum_{a=1}^{8} a_\mu^{(a)}(x) T_a. \tag{2.40}$$

The components $A_\mu^{(a)}$, $a = 1, 2, \ldots 8$, are real-valued fields, the so-called colour com-

ponents, and the T_a are a basis for traceless Hermitian 3×3 matrices, also known as Gell-Mann matrices. The internal index a denotes the different "colour" of the gauge boson of the theory which in $SU(3)$ are 8 and are known as *gluons*.

Making explicit the dependence on the colour indices, one can redefine the field strength tensor as

$$F_{\mu\nu}(x) = \sum_{a=1}^{8} F_{\mu\nu}^{(a)} T_a, \tag{2.41}$$

$$F_{\mu\nu}^{(a)}(x) = \partial_\mu A_\nu^{(a)}(x) - f_{abc} A_\mu^{(b)}(x) A_\nu^{(c)}(x). \tag{2.42}$$

Evaluating the trace, the Euclidean Yang-Mills action becomes

$$S_{YM} = \frac{1}{4g^2} \sum_{a=1}^{8} \int d^4x \; F_{\mu\nu}^{(a)}(x) F_{\mu\nu}^{(a)}(x). \tag{2.43}$$

From the right-hand side of equation 2.42 one can see that cubic and quartic terms are present in the definition of the field strength tensor. This is something which does not appear in Abelian gauge theories. These extra terms are responsible for the self interaction of gluons which make pure non-Abelian gauge theories highly non-trivial.

2.4 The Wilson gauge action

Following Wilson's seminal work (ref. [1]), the first step to build a lattice gauge theory is to discretise the action on a hyper-cubic lattice with the gauge fields defined on the links connecting the lattice sites. In contrast to continuum gauge theories, on the lattice one does not need to introduce a gauge fixing because the lattice formulation preserves gauge invariance [1].

Following the discussion introduced in section 2.2, one needs to replace continuous space-time by a $4D$ finite lattice Λ_4: The first thing to notice when going from continuum to discrete space-time is to replace derivatives with finite difference approximations and space-time integrals with a sum over all lattice points:

$$\partial_\mu \phi \to \frac{1}{2a}(\phi(n + a\hat{\mu}) - \phi(n - a\hat{\mu})), \tag{2.44}$$

$$\int d^4x \to \sum_{n \in \Lambda_4} a^4. \tag{2.45}$$

The next step is to discretise the action on the lattice. The local gauge transforma-

tion is implemented by introducing an element $\Omega(x)$ of the gauge group defining the theory discretised on the lattice

$$\psi(n) \to \psi' = \Omega(n)\psi(n), \quad \overline{\psi}(n) \to \overline{\psi}'(n) = \overline{\psi}(n)\Omega(n)^\dagger. \tag{2.46}$$

However, this result in an action which is not gauge-invariant for non-zero values of a [1, 10]. For this reason, one can instead build a gauge-invariant action starting by defining a gauge-invariant field:

$$U_\mu(n) = \mathcal{P}\left[e^{(iag\int_n^{n+a\hat{\mu}} A_\mu)}\right] \tag{2.47}$$

where $\mathcal{P}$ is the path-ordering operator, A_μ is the continuum gauge field operator and g is the bare coupling. U_μ is called a *link variable* as it acts as a parallel transporter connecting two lattice sites n and $n + \hat{\mu}$. The link variables $U(n)$ are elements of the gauge group of the gauge theory defined in the continuum.

The link variables transform under gauge transformation as

$$U_\mu(n) \to U'_\mu(n) = \Omega(n)U_\mu(n)\Omega^\dagger(n + a\hat{\mu}), \tag{2.48}$$

so we can form a gauge invariant quantity by attaching fermion fields to the link variables: $\overline{\psi}(n)U_\mu(n)\psi(n + a\hat{\mu})$. This is true for any product of link variables along an ordered path $\mathcal{P}$. Alternatively, one can form a gauge invariant object by taking the trace of any path ordered closed loop of link variables: The Wilson Loop [1]

$$\mathcal{W} = \mathrm{Tr}\left[\prod_{n,\mu\in\mathcal{P}} U_\mu(n)\right]. \tag{2.49}$$

The simplest way of forming a Wilson loop is by attaching link variables to form the shortest possible, non-trivial closed loop on the lattice which takes the name of the *plaquette*

$$P_{\mu\nu} = U_\mu(n)U_\nu(n + a\hat{\mu})U_\mu(n + a\hat{\nu})^\dagger U_\nu(n)^\dagger. \tag{2.50}$$

The Wilson action is defined in terms of plaquettes and it is a gauge invariant action for the gauge fields from which one can recover the standard continuum action after the naive continuum limit $a \to 0$ is taken

$$S_G = \frac{\beta}{N}\sum_{n\in\Lambda}\sum_{\mu<\nu} \mathrm{Re}\,\mathrm{Tr}[\mathbb{1} - P_{\mu\nu}] \tag{2.51}$$

where β is the inverse coupling $\frac{2N}{g^2}$, N being the degree of the gauge group [1].

Having discretised the gauge action on the lattice, one can then see how to discretise a quantum gauge theory on the lattice starting with the path integral formulation. In particular, one can obtain the expectation value of a certain observable $\mathcal{O}$ by evaluating the Euclidean path integral

$$\langle \mathcal{O} \rangle = \frac{1}{Z} \int \mathcal{D}[U] \; e^{-S_G[U]} \mathcal{O}[U] \tag{2.52}$$

where the partition function Z is defined as

$$Z = \int \mathcal{D}[U] \; e^{-S_G[U]} \tag{2.53}$$

and S_G is the Wilson gauge action [10].

The integration measure $\mathcal{D}$ on the lattice can be written as the product measure of link variables

$$\int \mathcal{D}[U] = \prod_{n \in \Lambda} \prod_{\mu=1}^{4} \int dU_\mu(n). \tag{2.54}$$

Now, since the link variables are elements of the gauge group, one needs to introduce the concept of Haar measure in order to define the integration over a continuous group. In particular, this is needed in order to make sure that the integration measure will also be invariant under gauge transformation. Indeed, upon gauge transformation, we have

$$dU_\mu \to dU'_\mu = d(\Omega(n) U_\mu(n) \Omega^\dagger(n)). \tag{2.55}$$

One of the defining properties of the Haar measure is that for any element V of the group, the following is true [10]

$$dU = d(UV) = d(VU). \tag{2.56}$$

This avoids the introduction of gauge fixing term in the path integral when working with lattice gauge theories. Hence, there are no divergences and one can normalise the measure by defining

$$\int dU = 1. \tag{2.57}$$

2.5 Static quark-antiquark potential and confinement

One of the main purposes behind the formulation of lattice gauge theories has always been the study of colour confinement in Yang-Mills theories. Yang-Mills theories are gauge theories based on the special unitary group $SU(N)$, which is the Lie group of $N \times N$ unitary matrices with determinant equal to one. When studying Yang-Mills theories one usually refers to the number N as the number of colour charges of the Yang-Mills theory in analogy to the additional quantum numbers introduced with the quark-model. Confinement is a mechanism which arises from the self-interaction of the gauge bosons of the theory, such as gluons in $SU(3)$, which results in a linear term appearing in the definition of the potential between two colour charged quarks, and implies that the energy increases together with the space separation. Thus, two particles with different colour charges will be "confined" in a strongly bound colour neutral state that can be observed, while the same is not true for colour charged particles [10].

The two main observables used to study the static quark-antiquark potential are the Wilson and Polyakov loops. As shown in equation 2.49, Wilson loops are defined as the trace of the product of link variables along a closed path $\mathcal{P}$. In fact, Wilson loops are formed by two objects: Wilson lines, which propagate a point on a spatial site in the temporal direction and temporal transporters which connects two spatial points on the same time-slice. Now, temporal transporters in the temporal gauge ($A_4(x) = 0$) become trivial. Therefore, one can rewrite the Wilson loop simply as the correlation function between two spatially separated Wilson lines $S(\boldsymbol{m}, \boldsymbol{n}; n_t)$ and $S(\boldsymbol{m}, \boldsymbol{n}; 0)$

$$\langle \mathcal{W} \rangle = \langle \mathrm{Tr}[S(\boldsymbol{m}, \boldsymbol{n}; n_t) S^\dagger(\boldsymbol{m}, \boldsymbol{n}; 0)] \rangle \tag{2.58}$$

where the distance between the Wilson lines is defined as $r = a|\boldsymbol{m} - \boldsymbol{n}|$. Using equation 2.25 and inserting a complete set of states $|k\rangle$ one can write the correlator as

$$\lim_{N_T \to \infty} \langle \mathrm{Tr}[S(\boldsymbol{m}, \boldsymbol{n}; n_t) S^\dagger(\boldsymbol{m}, \boldsymbol{n}; 0)] \rangle_{N_T} = \sum_k \langle 0|S(\boldsymbol{m}, \boldsymbol{n}; n_t)|k\rangle \langle k|S^\dagger(\boldsymbol{m}, \boldsymbol{n}, 0)|0\rangle e^{-tE_k}, \tag{2.59}$$

where the Euclidean time t is related to n_t via $t = an_t$. The states $S^\dagger(\boldsymbol{m}, \boldsymbol{n}; n_t)_{ab}|0\rangle$ have a non-zero overlap with a quark-antiquark pair, hence, they transform in exactly the same way under gauge transformations. The accurate definition of fermion fields on the lattice will be given in chapter 3. In the discussion that follows, one can consider the Wilson lines equivalent to an infinitely quark-antiquark pair located at

different spatial sites $\boldsymbol{m}$ and $\boldsymbol{n}$. Thus, the lowest energy state E_0 will be the energy associated with the static quark-antiquark pair, with the excited states describing additional particle-antiparticle combinations with the same quantum numbers of the vacuum. Therefore, the energy E_0 can be identified as being the quark-antiquark potential at spatial separation r

$$E_0 = V(r), \quad r = a|\boldsymbol{m} - \boldsymbol{n}|. \tag{2.60}$$

This means that we can calculate the static quark-antiquark potential from the large time behaviour of the Wilson loop. Furthermore, Wilson loops may also be used as operators for purely gluonic bound states known as *glueballs*. The detailed discussion on how one can study these objects on the lattice will be presented in section 2.7.

One can exploit the periodic boundary conditions in the time direction to modify the Wilson loop. In particular, one can increase the temporal extent of the Wilson loop to be equivalent to the total number of lattice points in the time direction $n_t = N_T$. This means that we create two disconnected paths, oriented in opposite directions located in space at the two positions $\boldsymbol{m}$ and $\boldsymbol{n}$: $T(\boldsymbol{m}; N_T), T^\dagger(\boldsymbol{n}; N_T)$. Both paths wind around the temporal dimension of the lattice but with opposite orientations. This new observable, known as Polyakov loop, can be made gauge invariant if we take the trace of each of the two paths individually

$$P(\boldsymbol{m}) = \mathrm{Tr}\left[\prod_{j=0}^{N_T-1} U_4(\boldsymbol{m}, j)\right], \tag{2.61}$$

which, as any trace over a closed loop is gauge invariant. The static quark-antiquark potential can also be obtained by the correlation function of oppositely oriented Polyakov loops

$$\langle P(\boldsymbol{m})P^\dagger(\boldsymbol{n})\rangle \propto e^{-N_T a V(r)}\Big(1 + \mathcal{O}(e^{-N_T a V(r)})\Big). \tag{2.62}$$

with $r = |\boldsymbol{m} - \boldsymbol{n}|$.

The general form of the static quark-antiquark potential can be parametrised as

$$V(r) = A + \frac{B}{r} + \sigma r. \tag{2.63}$$

The linear rising term depends on σ which is known as the string tension. This name comes from the fact that the mechanism which leads to the linearly rising term is the formation formation of a flux tube between the two colour sources which can be thought of as a string connecting the quark-antiquark pair. The linearly rising term in

the potential implies that the energy keeps rising as one tries to pull the two constituents apart. Thus, the quark and antiquark will be confined in a strongly bound meson state. Due to the fact that in Yang-Mills theories the gauge field are self-interacting, we can have quarkless colour neutral bound states *i.e.* the glueballs. In general, one can state that confinement is the phenomenon for which only colour neutral combinations can be observed.

2.6 Lattice Yang-Mills theory at finite temperature

In the previous sections the relation between lattice gauge theory and statistical mechanics has been discussed in details. However, when discussing how to extract the energy levels from correlation functions we stressed that one would need to take the $N_T \to \infty$ limit, with N_T being the maximum time extent of the lattice. In other words, space and time extent were considered much larger than the largest correlation length of the system [10]. Keeping the time extent finite, while still sending the spatial extent to infinity, one can study the system at a finite temperature exploiting the relation

$$aN_T = \frac{1}{T}, \tag{2.64}$$

where T is the temperature of the system.

The fact that the temperature is kept finite has important physical consequences. If one performs a Fourier transformation on the finite time lattice points, one finds that only discrete energy levels are allowed $\omega_n = 2\pi T n$, known as Matsubara frequencies. Due to the lattice structure, the Matsubara frequencies are limited to the Brillouin zone $(-\pi/a, \pi/a]$.

Now, exploiting the relation between time and temperature, we can rewrite equation 2.62 as

$$\langle P(\boldsymbol{m}) P^\dagger(\boldsymbol{n}) \rangle \propto e^{-\frac{V(r)}{T}}. \tag{2.65}$$

Identifying $V(r)$ as the free energy of the system, we need to normalise it by studying its long distance behaviour which gives us the following factorisation

$$\lim_{a|\boldsymbol{m}-\boldsymbol{n}|\to\infty} \langle P(\boldsymbol{m}) P^\dagger(\boldsymbol{n}) \rangle = \langle P(\boldsymbol{m}) \rangle \langle P^\dagger(\boldsymbol{n}) \rangle = |\langle P \rangle|^2, \tag{2.66}$$

where in the last step P is averaged over all spatial sites, and therefore is independent of position. For static potentials that grow with separation, which is the case of the static quark-antiquark potential, one can see that for $\sigma > 0$, $|\langle P \rangle|$ has to vanish. Therefore

one can study of confinement is related to $|\langle P \rangle|$:

$$\begin{aligned} \langle P \rangle = 0 &\iff \text{confinement}, \\ \langle P \rangle \neq 0 &\iff \text{no confinement}. \end{aligned} \tag{2.67}$$

At low temperature, Yang-Mills theories are confining. As temperature is increased pure gauge theory undergoes a phase transition at a certain critical temperature T_c [15, 16], and $\langle P \rangle$ acquires a non-vanishing value. The Polyakov loop is then an order parameter distinguishing between a confining phase, where free (colour) charges cannot be found in isolation, and a deconfined phase, where isolated colour charges are screened and can be observed.

The deconfinement transition in pure gauge theory has an interesting interpretation in terms of the *centre symmetry* (Z_N *symmetry* in $SU(3)$ Yang-Mills theory). Acting with a centre transformation on the temporal links will result in

$$U_4(\boldsymbol{n}, t_0) \to z U_4(\boldsymbol{n}, t_0) \quad z \in Z_3. \tag{2.68}$$

The symmetry arises from the fact that the gauge action is built from products of variables in trivially closed loops, so that the action is invariant under centre transformations. The Polyakov loop, on the other hand, does not close trivially and therefore is not invariant under the transformation. For temperatures below T_c, the sum over the centre elements is zero and the symmetry is left intact, while above the critical temperature the symmetry is spontaneously broken. The centre symmetry property resembles that of three-state spin-model with spin variables $\in Z_3$, living on the sites of a $3D$ spatial lattice [17, 18].

2.7 Glueballs

Glueballs are colour singlet quarkless bound states which have been predicted in the early days of Quantum Chromodynamics (QCD) and the quark-gluon model [19]. Exactly like for the other hadrons, each glueball state can be characterised by spin J, parity P and charge C quantum numbers: J^{PC}.

One can interpret glueballs as the eigenstates of the Hamiltonian of the pure Yang-Mills theory with Lagrangian density

$$\mathcal{L}_{YM} = \frac{1}{4} G^a_{\mu\nu} G^{a\mu\nu}, \tag{2.69}$$

J	A_1	A_2	E	T_1	T_2
0	1	0	0	0	0
1	0	0	0	1	0
2	0	0	1	0	1
3	0	1	0	1	1
4	1	0	1	1	1

Table 2.1: Subduced representations $J \downarrow \mathcal{G}_O$ of the octahedral group up to $J = 4$. The elements 1 of the matrix correspond to representation R^{PC} that become part of the representation J in the continuum limit

with $G^a_{\mu\nu} = A^a_{\nu,\mu} - A^a_{\mu,\nu} + igf_{abc}A^b_\mu A^c_\nu$, f_{abc} being the gauge group structure constants and g the gauge coupling.

As discussed in the previous sections, when we discretise the theory on the lattice we lose the Lorentz symmetry of the continuum. The complete rotational symmetry, which exists throughout the entire continuum theory, is only restored when the lattice spacing is sent to zero $a \to 0$. In the lattice framework, the eigenstates of the Hamiltonian must belong to the irreducible representations of the octahedral point group $\mathcal{G}_O$, which represents the symmetry of a cube. The octahedral point group consists of five irreducible representations, namely A_1, A_2, E, T_1 and T_2 with dimensions 1, 1, 2, 3, 3 respectively. Since our focus is on the glueball spectrum of the gauge theory in the continuum, one can consider $\mathcal{G}_O$ as a subgroup of the complete rotation group $SO(3)$. The irreducible representations of integer spin J in $SO(3)$, now restricted to $\mathcal{G}_O$, are referred to as subduced representations $J \downarrow \mathcal{G}_O$. Thus, the degeneracy of a continuum spin state J is divided among the different irreducible representations of $\mathcal{G}_O$. As one approaches the continuum limit, one can determine the masses of spin J glueballs by comparing the patterns of degeneracies of the subduced representations $J \downarrow \mathcal{G}_O$, with the degeneracy coefficients provided in table 2.1 taken from ref. [20].

On order to construct the correct form of lattice operator $\overline{O}$, one need to introduce a rotation transformation denoted as $\mathcal{R}_i(\overline{O})$, where the index i denotes the elements of the group $\mathcal{G}_O$. Since a generic representation of the group is not necessarily irreducible, in order to construct states that transform exclusively within a specific symmetry channel, one must combine the rotations of the original operator in a suitable linear combination. This is done by defining an operator in the irreducible representation R as

$$\Phi^R(t) = \sum_i c_i^{(R)} \mathcal{R}_i(\overline{O}(t)), \tag{2.70}$$

where the coefficients $c_i^{(R)}$ involved in the summation are derived from a unitary operator that facilitates the basis transformation from our chosen 24 dimensional representa-

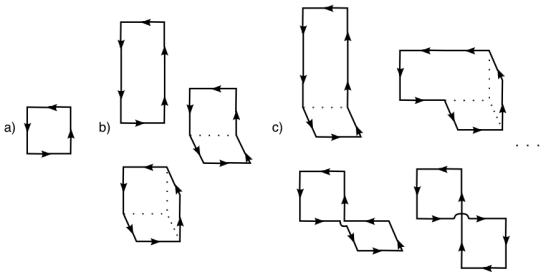

Figure 2.1: A sample of the lattice paths on which the glueball operators are defined. Taken from ref. [20]

tion into an orthonormal basis for for each of the 5 invariant subspaces [21]. By adding parity and charge conjugation to the group of pure rotations, one get the full symmetry group of glueball states on the lattice, which is referred to as $\mathcal{G}_O^{PC}$. The group $\mathcal{G}_O^{PC}$ has a total of 20 irreducible representations labeled by R^{PC}, where R indicates one of the 5 irreducible representations of $\mathcal{G}_O$, P is the parity eigenvalue and C is the charge conjugation eigenvalue.

When performing lattice simulations one is constrained by the volume of the lattice being finite. In this case, the single-particle glueball spectrum can get significant corrections from multi-glueball states. Moreover, if one consider periodic boundary conditions in time, as it is often the case, one can get contributions from topological excitations which wrap around the compact time direction, also known as *torelons*. Torelons have the same quantum numbers of the glueball operators, thus if not correctly accounted for could affect significantly the glueball spectrum. In order to control and possibly remove these contributions one need to use techniques like the variational method including also a set of operators that best overlap with two-glueballs and torelon states.

The operators used in order to create and annihilate glueball states are gauge-invariant and vacuum-subtracted

$$\overline{O}(t) = O(t) - \langle 0|O(t)|0\rangle. \tag{2.71}$$

The single-trace operator that is used to project onto glueball states is defined simply as

$$O(t) = \phi(t), \tag{2.72}$$

where ϕ is a zero-momentum operator given by the wall average over the temporal slice

$$\phi(t) = \frac{1}{N_L^3} \sum_{x \in \Lambda_3} \phi(x,t) \qquad\qquad \phi(x,t) = \mathrm{Tr} \prod_{(i,\hat{\mu}) \in \mathcal{C}} U_\mu(i). \tag{2.73}$$

$\mathcal{C}$ is a closed Wilson loop with lengths usually between 4 and 8 lattice spacings. Figure 2.1 shows some of the basic shapes of the Wilson loop.

In a given symmetry channel, the operators are built in the following form

$$\Phi^{(R)}(t) = \sum_i c_i^{(R)} \mathcal{R}_i(\phi(t)) - \sum_i c_i^{(R)} \mathcal{R}_i(\langle \phi(t) \rangle) \tag{2.74}$$

$$= \sum_i^{(R)} \mathcal{R}_i(\phi(t)) - \langle \phi(t) \rangle \sum_i c_i^{(R)}, \tag{2.75}$$

where the last term in the second line is different from zero only when $R = A_1^{++}$.

The variational method has been used in the lattice calculation of the glueball spectrum since the very early days of the formulation of lattice gauge theories [22, 23]. The method requires the computation of a matrix of correlators for a given set of interpolating operators Φ_i, $i = 1, \ldots, N$

$$C_{ij}(t) = \sum_\tau \langle 0 | \Phi_i^\dagger(t+\tau) \Phi_j(\tau) | 0 \rangle \tag{2.76}$$

All the operators need to have the same quantum number as the state that one is interested in, so in the case of glueball states one need to include also multi-glueball and torelon operators to the set. The goal of the variational procedure is to find an appropriate linear combination of the basis operator by finding the optimal v_i

$$\tilde{\Phi}(t) = \sum_i v_i \Phi_i(t). \tag{2.77}$$

This is done by solving the generalised eigenvalue problem (GEVP), which may be written as

$$\sum_j \overline{C}_{ij}(t_0) v_j = \sum_j \lambda_j(t_0) \overline{C}_{ij}(0) v_j, \tag{2.78}$$

where the eigenvalues $\lambda_j(t_0)$ of the correlation matrix can be shown to behave as $\lambda_j(t_0) = e^{-E_j(t_0)t_0}$. Each eigenvalue corresponds to an energy state E_j, with the biggest eigenvalue corresponding the the ground state E_0. By diagonalising the correlator matrix $\overline{C}(t_0) = C^{-1}(0)C(t_0)$ one can solve the eigenvalue problem, which allow to disentangle the physical states contained in the correlation functions. For a given

eigenvalue, the corresponding eigenvector v_j is used to construct the operator which best overlap with the corresponding energy state E_j, as shown in equation 2.77.

Once the optimal operators are found, one get the corresponding optimal correlator from the matrix of correlation functions. The ground state mass of the glueball can then be found in the usual way by studying the long time behaviour of the correlator.

Chapter 3

Lattice QCD

There is firm experimental evidence that the laws of particle physics are accurately described by quantum field theory (QFT), and there is little doubt that quantum chromodynamics (QCD) is the quantum field theory that correctly describes the strong nuclear interaction in elementary particle physics. The fundamental degrees of freedom of QCD are quarks and gluons, respectively the fermion fields and gauge fields of the theory.

Discretising QCD on the lattice is not a trivial task and a lot of effort has been done over the years to bring the field to its modern state. One of the most delicate aspects in discretising QCD on the lattice is the treatment of chiral symmetry, which is severely limited by a no-go theorem due to Nielsen and Ninomiya [24]. This fact led to the development of different fermion actions, each of which bypassing some of the assumptions of the Nielsen-Ninomiya no-go theorem.

3.1 QCD in the continuum

For each flavour, quark fields have a total of twelve independent components, resulting from the four Dirac components for each of the three colour indices. In addition, quarks can come in six different flavours: up (u), down (d), strange (s), charm (c), bottom (b) and top (t). The up and down (and sometimes also the strange) quarks are referred to as light quarks while the charm and bottom quarks are referred to as heavy quarks; finally, the top quark is the heaviest elementary particle in the Standard Model (SM) and since its lifetime is one order of magnitude smaller than the timescale characteristic of the strong interaction, unlike the other flavours it does not form observable bound states. For this reason, the top quark does not enter lattice QCD calculations. In Minkowski space-time, the spinor field $\psi(x)$ is related to $\overline{\psi}(x)$ by the Dirac gamma matrix γ_0,

namely: $\overline{\psi}(x) = \psi^\dagger(x)\gamma_0$. This is not true in Euclidean space-time where $\psi(x)$ and $\overline{\psi}(x)$ are treated as independent integration variables in the path integral. The Dirac gamma matrices are also different in Euclidean space-time, as they respect the anti-commutation relation $\{\gamma_\mu, \gamma_\nu\} = 2\delta_{\mu\nu}\mathbb{1}$, where $\delta_{\mu\nu}$ is the Kronecker delta. An explicit representation of the Euclidean gamma matrices can be found in the appendix A.

The continuum QCD action in Euclidean space-time can be written (suppressing the colour indices for clarity) as

$$S_{QCD} = \int d^4x \sum_f \overline{\psi}_f(\gamma_\mu D_\mu + m_f)\psi_f + S_{YM}, \tag{3.1}$$

where S_{YM} is the gauge action defined in eq. 2.37, D_μ is the covariant derivative of eq. 2.39, $\overline{\psi}_f$ and ψ_s are the spinor fields describing the quark flavour labeled by f, with an associated bare mass m_f.

At the classical level, the QCD action is invariant under Lorentz-Poincaré symmetry and under the discrete symmetries $\mathcal{C}$ (charge conjugation), $\mathcal{P}$ (parity[1]), and $\mathcal{T}$ (time reversal). In addition, it is also invariant under $SU(3)$ gauge symmetry acting on the internal colour degrees of freedom. Finally, for massless quarks, QCD is also invariant under chiral symmetry: the latter (and its fate at the quantum level), together with confinement of colour degrees of freedom within colour-neutral bound states, plays a major role in determining the properties of the physical spectrum of the theory, as we shall now discuss shortly.

In the case in which the fermion masses are zero, the classical QCD action is invariant under a global chiral symmetry $U(N_f)_L \times U(N_f)_R$, which encodes the fact that QCD "treats equally" all quark flavours with the same mass, and when $m_f = 0$ the left- and right-handed components of the spinor fields are decoupled from each other. (With a slight abuse of mathematical notation,) it is convenient to rewrite the chiral symmetry in terms of "vector" and "axial" (rather than left and right) symmetry groups, and to single out the $U(1)$ subgroup associated with the complex phase of the determinant for each of the two unitary groups, yielding $SU(N_f)_V \times SU(N_f)_A \times U(1)_V \times U(1)_A$. Once the theory is quantised, the axial symmetry $U(1)_A$ is broken explicitly, leading to the axial anomaly, which leaves $SU(N_f)_V \times SU(N_f)_A \times U(1)_V$. Moreover, the $SU(N_f)_A$ part of this symmetry is dynamically broken by the existence of a non-vanishing quark condensate $\langle\overline{\psi}\psi\rangle$ in the QCD vacuum; the associated (pseudo-)Nambu-Goldstone bosons are the pions (if only the up and down quarks are considered as

[1]Note that here we follow the most commonly used notation for the parity symmetry operator, with the same symbol that we previously used for the path-ordering prescription. The distinction between the two meanings of this symbol should be clear from the context.

approximately massless) or the pions, the kaons and the η meson (if, in addition to the up and down, also the strange quark is approximated as a massless particle). In contrast, both the $SU(N_f)_V$ and the $U(1)_V$ symmetries hold also at the quantum level: the former is responsible, for instance, for the near-degeneracy in mass between the proton and the neutron, while the latter simply encodes the fact that QCD is a theory in which baryon number is conserved. Note that introducing non-vanishing degenerate masses breaks the left-right symmetry explicitly, reducing the classical symmetry of QCD to $SU(N_f)_V \times U(1)_V$.

It should be noted that in the real world, the masses of all quark flavours are non-zero (even though those of the up and down quarks are small, of the order of some MeV, namely two orders of magnitude smaller than the typical masses of hadrons) and all different from each other; thus, for example, the pions are lighter than other hadrons, but not massless. Additionally, the masses of light hadrons also receive corrections due to the electroweak interactions, which contribute to break, for instance, the mass degeneracy between the proton and the neutron. Nevertheless, the approximate chiral symmetry and its breaking pattern that we described above remains a useful tool to interpret the physical hadron spectrum, at least at a qualitative or semi-quantitative level.

3.2 Discretising QCD

The naive approach to the discretisation of the QCD action on the lattice involves the definition of the quark spinors on the lattice sites $\psi(n)$; these lattice fields will then be coupled with the link variables $U_\mu(n)$

$$S[\psi, \overline{\psi}] = a^4 \sum_{n \in \Lambda} \sum_f \overline{\psi}^{(f)}(n) \frac{1}{2} [\gamma_\mu (\nabla_\mu + \nabla^*_\mu) + m^{(f)}] \psi^{(f)}(n), \tag{3.2}$$

where we substituted the integral over d^4x with $\sum_{n \in \Lambda}$ and used the gauge covariant derivatives

$$\nabla_\mu \psi(n) = \frac{1}{a}[U(n,\mu)\psi(n+\hat{\mu}) - \psi(n)],$$

$$\nabla^*_\mu \psi(n) = \frac{1}{a}[\psi(n) - U^{-1}(n-\hat{\mu},\mu)\psi(n-\hat{\mu})]. \tag{3.3}$$

In order to write the correct integration measure over the fermion fields in the path integral, one has to regard ψ and $\overline{\psi}$ in as the generators of a $2N$ Graßmann algebra $\eta, \overline{\eta}$. As such, the generators will anti-commute with each other, enforcing the correct

Fermi-Dirac statistics in the path integral formulation of the quantum theory.

In particular, the mapping between the generator of the Graßmann algebra and the fermion spinors is

$$\{\eta_1, \ldots, \eta_N; \overline{\eta}_1, \ldots, \overline{\eta}_N\} \to \{\psi_\alpha; \overline{\psi}_\alpha\}_a^{\alpha=1,\ldots,4}, \tag{3.4}$$

where α is the Dirac index and a the colour index.

One can use the Matthews-Salam formula [25, 26] to write the partition function for a pair of Graßmann generators $\eta, \overline{\eta}$

$$Z = \int d\eta_N \overline{\eta}_N \ldots d\phi_1 d\overline{\eta} \ \exp\Big(\sum_{i,j=1}^{N} \overline{\eta}_i M_{ij} \eta_j\Big) = \det[M_{ij}]. \tag{3.5}$$

This can be further generalised by Wick's theorem for fermions, whereby an n-point fermionic correlation function can be written as

$$\langle \eta_{i_1} \overline{\eta}_{j_1} \ldots \eta_{i_n} \overline{\eta}_{j_n} \rangle = \frac{1}{Z} \int \prod_{k=1}^{N} d\eta_k d\overline{\eta}_k \ \eta_{i_1} \overline{\eta}_{j_1} \ldots \eta_{i_n} \overline{\eta}_{j_n} \exp\left(\sum_{l,m=1}^{N} \overline{\eta}_l M_{lm} \eta_m\right) \tag{3.6}$$

$$= (-1)^n \sum_{P(1,2,\ldots,n)} \mathrm{sign}(P) (M^{-1})_{i_1 j_{P1}} (M^{-1})_{i_2 j_{P2}} \ldots (M^{-1})_{i_n j_{Pn}}, \tag{3.7}$$

where the sum is over all the permutations $P(1, 2, \ldots, n)$ and $\mathrm{sign}(P)$ is the sign of the permutation.

The above formula can be readily applied to the fermion fields, so that one can write the fermion propagator as

$$\langle \psi^{(f)}(n)_a^\alpha \overline{\psi}^{(f)}(n)_b^\beta \rangle = \int \mathcal{D}[\psi, \overline{\psi}] e^{-S[\psi, \overline{\psi}, U]} = \frac{1}{a^4} D_{a,b}^{-1\ (f)\alpha,\beta}, \tag{3.8}$$

where in the above equation, the action has all the indices written explicitly.

Writing the Dirac operator in momentum space will give us

$$\tilde{D}(p) = m\mathbb{1} + \frac{i}{a} \sum_{\mu=1}^{4} \gamma_\mu \sin(p_\mu a), \qquad p_\mu \in (-\pi/a, \pi/a]. \tag{3.9}$$

The above equations can be used to write the massless propagator in momentum space

$$\tilde{D}^{-1}(p) = \frac{-ia^{-1} \sum_\mu \gamma_\mu \sin(p_\mu a)}{a^{-2} \sum_\mu \sin(p_\mu a)^2} \xrightarrow{a \to 0} \frac{-i \sum_\mu \gamma_\mu p_\mu}{p^2}, \tag{3.10}$$

which leads to the correct pole for the massless propagator in the continuum, that

is $p_\mu = 0$. However, one immediately notes that the propagator has additional poles coming from the zeros of the $\sin(p_\mu a)$ functions at $p_\mu = \pi/a$. Therefore, the naive discretisation of the fermion action produces fifteen additional poles, which are known as *doublers*.

3.2.1 Wilson fermions

The first solution to the fermion doubling problem was proposed by K. G. Wilson, who suggested the addition of a term to the momentum space Dirac operator, which can then be written as

$$\tilde{D}(p) = m\mathbb{1} + \frac{1}{a}\sum_{\mu=1}^{4}\gamma_\mu \sin(p_\mu a) + \mathbb{1}\frac{1}{a}\sum_{\mu=1}^{4}(1 - \cos(p_\mu a)). \tag{3.11}$$

The extra term does not modify the $p_\mu = 0$ pole, while it acts as an extra mass term for all the momentum components $p_\mu = \pi/a$: $m + \frac{1}{a}$. In the limit of $a \to 0$ the doublers' mass becomes extremely heavy so that they naturally decouple from the theory, leaving only the true $p_\mu = 0$ pole. The extra term is known as the Wilson term, it is the discretisation of the negative Laplace operator

$$-a\frac{r}{2}\sum_{\mu=1}^{4}\nabla_\mu^*\nabla_\mu, \tag{3.12}$$

where r is known as the Wilson parameter. Simple dimensional analysis shows that the Wilson term is (in the language of the renormalisation group) an irrelevant one. Including the Wilson term in the coordinate space Dirac operator gives

$$D_m = D_W^{(f)} + m^{(f)} = \frac{1}{2}[\gamma_\mu(\nabla_\mu^* + \nabla_\mu) - ar\nabla_\mu^*\nabla_\mu] + m^{(f)}, \tag{3.13}$$

where D_W is referred to as the Wilson's Dirac operator and D_m is the massive Dirac operator.

In lattice calculations, the Wilson's Dirac operator is sometimes expanded in terms of the quark mass in what is known in literature as *hopping expansion*

$$D_m = \mathbb{1} - \kappa H, \qquad \kappa = \frac{1}{2(am+4)}, \tag{3.14}$$

where κ is the hopping parameter and H is the hopping matrix.

3.2.2 Nielsen-Ninomiya theorem

While solving the doubling problem, the Wilson term introduces a new one: the explicit breaking of chiral symmetry also in the massless case. In fact, this undesired feature is one of the consequences of the Nielsen-Ninomiya theorem [27], a no-go theorem for lattice fermions which states that on the lattice, regardless of the discretisation strategy used, one cannot respect simultaneously all the following conditions:

1. $\tilde{D}(p)$ is a periodic analytic function of p_μ, *i.e.* $D(n)$ is a local operator;
2. $\tilde{D}(p) = i\gamma_\mu p_\mu + \mathcal{O}(a)$, hence the Dirac operator reproduces the correct physics in the limit $a \to 0$;
3. $\tilde{D}(p)$ is invertible everywhere except $p_\mu = 0$, where the zero correspond to a single particle;
4. $\{\gamma_5, D\} = 0$, Dirac operator respects chiral symmetry.

From the discussion above, it is clear that the naive discretisation of eq. 3.2 violates the third of these, while the Wilson's Dirac operator violates the fourth condition (and, ultimately, leads to additive mass renormalisation for Wilson fermions, implying that to represent massless fermions using the Wilson's Dirac operator one has to fine-tune the bare mass).

The Nielsen-Ninomiya theorem suggests that the treatment of chiral symmetry on the lattice is a delicate topic. In a seminal work (ref. [28]) Ginsparg and Wilson proposed an equation for chiral symmetry on the lattice

$$\gamma_5 D + D\gamma_5 = aD\gamma_5 D. \tag{3.15}$$

One solution of the Ginsparg-Wilson equation is the overlap Dirac operator [29]

$$D_{ov} = \frac{1}{a}(\mathbb{1} + \gamma_5 \,\mathrm{sign}[H]), \qquad H = \gamma_5 A, \tag{3.16}$$

where A is a γ_5-Hermitian kernel Dirac operator and H is Hermitian with real eigenvalues. The simplest available choice for A is the Wilson's Dirac operator (eq. 3.13. Note, however, that, because of the sign function appearing in its definition, the overlap operator is not ultra-local (namely, it does not involve interactions that are non-vanishing only up to a finite distance), which allows it to evade the first hypothesis of the Nielsen-Ninomiya theorem. While the overlap operator provides a mathematically elegant way to formulate fermions on the lattice, its numerical simulation is particularly costly, hence it is used less frequently than Wilson's Dirac operator.

The Wilson formulation of lattice QCD is invariant under the action of charge $\mathcal{C}$ and parity $\mathcal{P}$ transformations, as well as their product operation $\mathcal{CP}$. This is an important statement as these quantum numbers are used in the construction of meson operators on the lattice. The third important discrete symmetry of the continuum is time reflection $\mathcal{T}$. This symmetry is well defined in Minkowski space-time where the time direction is explicitly different from the spatial directions by having the opposite sign in the metric. In Euclidean space-time there is no such distinction as the time direction is Wick rotated, hence the Wilson action is actually invariant under the more general transformations: $\mathcal{P}_\mu$ with $\mu = 1, 2, 3, 4$, where the transformation flips the sign of all the components of n except for n_μ. In this context, the product operation $\mathcal{P}_1\mathcal{P}_2\mathcal{P}_3$ is the Euclidean equivalent to the Minkowskian time reflection. This is an essential operation when it comes to simulations with fermions, and indeed anti-periodic temporal boundary conditions are used to implement the correct physical transformations.

3.2.3 Correlation functions

Let us use for now the Wilson fermion action for lattice QCD (eq. 3.13) in order to discuss how to calculate fermion propagators. From the discussion in the previous sections, one can exploit the properties of Graßmann variables in order to write the expectation value of an operator O in full lattice QCD as

$$\langle O \rangle = \langle \langle O \rangle_F \rangle_G = \frac{1}{Z} \int \mathcal{D}[U] e^{-S_G[U]} \mathcal{D}[\psi, \overline{\psi}] e^{-S_F[\psi, \overline{\psi}, U]} O[\psi, \overline{\psi}, U]. \tag{3.17}$$

The physical content of a quantum field theory can be extracted from the set of its n-point correlation functions. A particularly simple correlation function of this type is the two-point correlation function of meson operators. Meson operators in lattice QCD are functionals of lattice fermion fields with the quantum numbers of the physical state one is interested in studying. The particle states are generated on the lattice by the action of meson interpolators that create and annihilate the state at different lattice sites

$$O_M(n) = \overline{\psi}^{(f_1)}(n) \Gamma \psi^{(f_2)}(n), \tag{3.18}$$

where O_M is the meson interpolator, $\psi^{(f_1)}(n)$ is a specific flavour fermion field and Γ is a combination of Euclidean Dirac gamma matrices. One can also construct baryonic interpolators in a similar manner.

To compute correlation functions of mesonic interpolators, one starts by writing

explicitly the fermionic part of the expectation value

$$\langle O(n)\overline{O}(m)\rangle_F = \langle \overline{\psi}^{(f_1)}(n)\Gamma\psi^{(f_2)}\overline{\psi}^{(f_2)}(m)\Gamma\psi^{(f_1)}(m)\rangle, \tag{3.19}$$

then, applying Wick's theorem it is possible to contract the fermion fields and one can rewrite the above equation as

$$\langle O(n)\overline{O}(m)\rangle_F = -\operatorname{Tr}[\Gamma D_{f_1}^{-1}(n|m)\Gamma D_{f_2}^{-1}(m|n)_{f_2}], \tag{3.20}$$

where it is made explicit how the propagator D^{-1} propagates fermion fields from one lattice site to another. In particular, one often refers to the $O(n)$ and $\overline{O}(m)$ operators as source and sink respectively. The above equation is true for any combination of flavours and represents a connected correlator. In the case in which one requires an isospin-singlet meson interpolator containing a linear combination of quark flavour fields, one needs to add additional terms coming from the fermion contractions of the quark fields being transported back to the same lattice point. These additional terms are known as disconnected propagators and their numerical computation is challenging. The final step is to perform the Graßmann integration and then compute the gluonic expectation value, which allows one to write the two-point correlation function as

$$\langle O(n)\overline{O}(m)\rangle = -\frac{1}{Z}\int \mathcal{D}[U]e^{-S_G[U]}\det[D_{f_1}]\det[D_{f_2}]\operatorname{Tr}[\Gamma D_{f_1}^{-1}(n|m)\Gamma D_{f_2}^{-1}(m|n)_{f_2}], \tag{3.21}$$

where (assuming that the only quark flavours contributing to the dynamics of the theory are f_1 and f_2, e.g., the up and down quark flavours)

$$Z = \int \mathcal{D}[U]e^{-S_G[U]}\det[D_{f_1}]\det[D_{f_2}] \tag{3.22}$$

denotes the partition function of the theory. The formula in eq. 3.21 can then be used in Monte Carlo simulations in order to numerically estimate the two-point correlation function. The quark flavours contained in the determinant of the Dirac operators in eq. 3.21 are called *sea* quarks and their dynamics has to be included in the gauge configurations generation in order to produce accurate results. However, as it will be discussed in chapter 4, their inclusion in numerical simulations implies a significant increase in computational costs, which was prohibitive in the early days of lattice QCD (so that, until the end of the 1990's, most numerical calculations in lattice QCD ignored the effect of sea quarks: this rather crude approximation, which leads to a number of unphysical effects, was called the *quenched approximation* of lattice QCD and has now

become obsolete). The quark flavours contained in the operator definition, on the other hand, are referred to as *valence* quarks.

Temporal correlation functions of the form of eq. 3.21 are often constructed in terms of spatially-averaged operators defined at a fixed Euclidean time (this average amounts to project each operator onto its zero-momentum Fourier component, in which case the relativistic energy reduces to the mass) and can also be written in terms of a spectral decomposition as was done in eq. 2.30

$$C(n_t) = \langle O(n_t)\overline{O}(0)\rangle = \sum_k \langle 0|\hat{O}|k\rangle\langle k|\hat{O}|0\rangle e^{-an_tE_k}. \tag{3.23}$$

Studying the long time behaviour of eq. 3.23 on a periodic lattice, one can compute the effective mass of the correlator

$$m_{eff}(n_t) = \cosh^{-1}\Big[\frac{C(n_t+1)+C(n_t-1)}{2C(n_t)}\Big] \tag{3.24}$$

and extract the ground state energy from fits of the data in the plateau of the effective mass plot. Note that the presence of (the inverse of) the hyperbolic cosine function, rather than the exponential function, is due to the periodicity of the lattice.

The interpolating operators from which the lattice correlation functions are built are defined at a source and sink point (eq. 3.18), connected by the appropriate quark propagator. The simplest type of source that one can choose is a point source placed at the lattice site where the meson interpolator is defined. All possible operators with the same quantum number as the meson interpolator will contribute to the two-point correlation functions, although with a different overlap to the matrix elements shown in eq. 3.23. This plethora of possible contributions could potentially spoil the possibility to extract, e.g, the mass of a state from the lattice correlation function; for this reason, one often chooses to apply a smearing procedure to the point source: this has the effect of improving the overlap of the ground-to-ground matrix element, suppressing the contamination of the signal coming from excited states. A typical choice of smearing is the Gaußian shaped one, defined in ref. [30], which can be obtained by applying the following operator to the source site

$$M = \sum_{n=0}^{N} \kappa H^n, \tag{3.25}$$

where H is the hopping matrix defined in eq. 3.14 and N is the total number of smearing steps. In typical simulations, one computes the lattice propagator G, which propagates

fermions from the smeared source to a point-like sink, solving the set of linear equations

$$DG = \eta^H, \tag{3.26}$$

where η^H is the smeared source and D is the lattice Dirac operator. The above equation is solved iteratively for every quark flavour considered in the correlation function. An example of a propagator solver can be found in refs. [31, 32], which allows to invert the Dirac operator for several quark masses at a relatively low computational cost.

The application of smearing is not the only method which improves the signal of correlation functions that are computed in numerical lattice QCD calculations. In refs. [33, 34], a stochastic method was proposed to improve the way quark sources are dealt with; this method is known as the "one-end-trick". The method reduces the statistical uncertainties affecting the numerical estimates of lattice propagators by diluting the set of stochastic sources used in the propagator inversion.

In order to evaluate the effects of the application of the smearing operators, one can construct lattice correlation functions with different combinations of smearing sources and compare the results. In figure 3.1 we studied the effective mass plots of two-point correlation functions computed using the stochastic method with 10 spatial stochastic sources and Gaußian smearing with $N = 30$ and $\kappa = 4$. These correlators were obtained using meson interpolators with the same quantum numbers as the B_s meson, computing quark propagators for the s and b quarks [2]. The difference between the two lattice correlation functions used to produce the plot in figure 3.1 is that the correlator corresponding to the orange data points was constructed applying the smearing operator only at the source, keeping the sink local, while the correlator corresponding to the data in blue was constructed applying the smearing operator at both the source and sink lattice points. Figure 3.1 shows clearly that in the case in which the correlator was smeared also at the sink, the data approach the plateau more rapidly compared to the case in which only the source was smeared. This behaviour in the effective mass plot reflects the stronger suppression of the excited state contamination to the correlator when smearing is applied. Finally, fitting the correlation function in the plateau region it is possible to extract the ground state mass of the B_s meson (in units of the inverse of the lattice spacing used for this simulation) using eq. 3.24, giving

$$am_{B_s} = 1.2712(12), \tag{3.27}$$

which corresponds to a value of the B_s-meson mass of $m_{B_s} = 3.08(11)$ GeV. The

[2] In fact, as it will be explained in section 4.3, we could only simulate a heavier version of the c quark as the bottom quark is too heavy to be simulated relativistically on the lattice

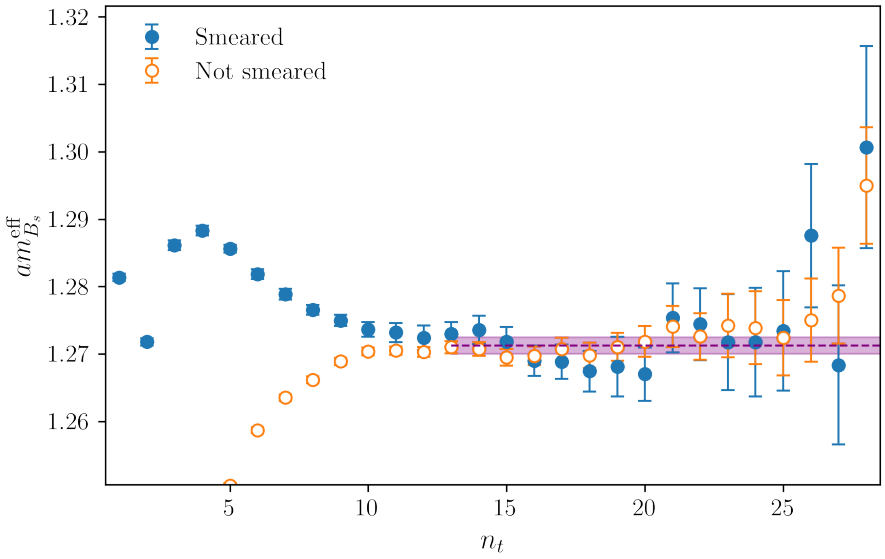

Figure 3.1: Effective mass plots of the two-point correlation functions with B_s interpolators. The blue points are obtained applying smearing at the sink and source points, while the orange points are obtained applying smearing only at the sink. The purple band corresponds to the plateau which was used to extract the ground state of the B_s meson. Plot generated using `pyerrors` [35].

correlation function discussed above was also used in the calculation of inclusive heavy-meson decays discussed in chapter 8.

In order to be able to calculate all the physical states in lattice QCD, one needs to be able to simulate hadrons also at non-vanishing spatial momentum. One can define a meson interpolator on a single time-slice n_t projected to definite spatial momentum

$$\tilde{O}(\boldsymbol{p}, n_t) = \frac{1}{\sqrt{\Lambda_3}} \sum_{\boldsymbol{n} \in \Lambda_3} O(\boldsymbol{n}, n_t) e^{-ia\boldsymbol{n}\cdot\boldsymbol{p}}, \tag{3.28}$$

where the momentum can only take the discrete values allowed by the Fourier transform

$$p_i = \frac{2\pi n_i}{L}, \tag{3.29}$$

where L is the spatial extent of the lattice. When building the correlation function, it is sufficient to project the momentum for only one operator, typically the sink operator. The limitation imposed by the Fourier transform can be lifted employing twisted boundary condition in the spatial directions [36, 37, 38]. The use of this type of boundary condition for one of the flavour implies a shift of the quark field of the type: $\psi(n + \boldsymbol{e}_i L) = e^{i\theta_i}\psi(n)$. This is automatically translated in Fourier space giving the

allowed values of the spatial momentum

$$p_i = \frac{\theta_i}{L} + \frac{2\pi n_i}{L}, \tag{3.30}$$

where the momentum is still quantised as in the case of periodic boundary conditions (eq. 3.29) with an additional shift equal to θ_i/L. The shift is not restricted by the lattice formulation and can be any continuous value, which gives the possibility to simulate mesons having different valence quark flavours at any value of the spatial momentum. The effect of adding the term θ naturally affects also the covariant lattice derivatives shown in eq. 3.3

$$\nabla_\mu \psi(n) = \frac{1}{a}[\lambda_\mu U(n,\mu)\psi(n+\hat{\mu}) - \psi(n)],$$

$$\nabla^*_\mu \psi(n) = \frac{1}{a}[\psi(n) - U^{-1}(n-\hat{\mu},\mu)\psi(n-\hat{\mu})], \tag{3.31}$$

where $\lambda_\mu = e^{\frac{ia\theta_\mu}{L}}$. Finally, one can write the dispersion relation for the simulated particle as

$$E^2_{ij} = M^2_{ij} + \left(\frac{\theta}{L}\right)^2. \tag{3.32}$$

3.2.4 Exceptional configurations

In eq. 3.21 it is manifest the dependence of the Dirac operator with respect to the link variable U, and any fluctuation of the latter will directly affect the form of $D[U]$. In order to see this one can consider the eigenvalues of the Dirac operators, obtained by the standard eigenvalue equation

$$D_W v_\lambda = \lambda v_\lambda. \tag{3.33}$$

Considering that the massless Wilson's Dirac operator is γ_5 Hermitian $\gamma_5 D_W \gamma_5^\dagger = D_W^\dagger$, one can show that the characteristic polynomial satisfies $P(\lambda) = P(\lambda^*)^*$. As a consequence, the possible eigenvalues of the Dirac operator are either real or will come in complex conjugate pairs. Now, since the Dirac operator depends on U, so will the eigenvalues $\lambda[U]$. When we add the mass term, the eigenvalues of the Wilson's Dirac operator will be of the form

$$m + \lambda_i[U]. \tag{3.34}$$

As long as $\lambda_i[U]$ is positive there is no issues regarding the inversion of the Dirac operator. However, due to fluctuations in U, $\lambda_i[U]$ can be real and negative, which can drive the eigenvalue very close to zero. When this *exceptional configurations* occur, the

inversion of the Dirac operator breaks down.

One solution to the problem of exceptional configuration is the introduction of a twisted mass term in the expression of the Wilson's Dirac operator of eq. 3.13. This modification leads to what is known in literature as twisted mass action which is one of the actions currently used for modern lattice QCD simulations.

3.3 Twisted mass action

In order to best describe the twisted mass formalism, we will first consider only the two lightest mass-degenerate quark flavours, u and d, and we will add the heavier flavours later on in the section. According to the review of Ref. [39], the first work to introduce the twisted mass term in a lattice QCD action was ref. [40]. However, there is little doubt that the discussion of the twisted mass term as an infrared regulator and then as a $\mathcal{O}(a)$ improved regulator of lattice QCD appear for the first time in the works published in [41, 42, 43].

We begin writing the discretised twisted mass QCD action in the twisted basis $\chi, \overline{\chi}$

$$S_F^{tm}[\chi, \overline{\chi}, U] = a^4 \sum_{n \in \Lambda} \overline{\chi}(n) \Big(D_W + m_0 + i\mu_q \gamma_5 \tau^3 \Big) \chi(n) \tag{3.35}$$

where D_W is Wilson's Dirac operator (eq. 3.13), m_0 is the bare untwisted quark mass and $i\mu_q\gamma_5\tau^3$ is the twisted mass term. The twisted mass term is trivial in colour space, it contains the γ_5 gamma matrix acting in Dirac space and τ^3, the third Pauli matrix (for an explicit definition see app. A), acting in flavour space. A non-vanishing values of the twisted mass μ_q ensures that the determinant of the twisted mass Dirac operator is strictly positive, and consequently zero eigenvalues which otherwise would give rise to exceptional configurations, are excluded [39, 41]. The mass term of the action can be written as

$$m_q + i\gamma_5\mu_q\tau^3 = Me^{i\omega} \tag{3.36}$$

where M is known as the polar mass and defined as $M = \sqrt{m_q^2 + \mu_q^2}$ and ω is the twist angle $\tan(\omega) = \mu_q/m_q$. The untwisted mass parameter m_q is defined as $m_q = m_0 - m_{cr}$, where m_{cr} is the critical mass counter-term which arise from the fact that due to the loss of chiral symmetry the mass term renormalises also additively. To close the description of the twisted mass action it is useful to write equation 3.35 in the physical basis

$$S_F^{tm}[\psi, \overline{\psi}, U] = a^4 \sum_n \overline{\psi}(n) \Big(\frac{1}{2}\gamma_\mu(\nabla_\mu + \nabla_\mu^*) - i\gamma_5\tau^3[m_0 - \frac{a}{2}\nabla_\mu\nabla_\mu^*] + \mu \Big) \psi(n). \tag{3.37}$$

If one re-writes eq. 3.35 in the continuum, it can be revealed that the continuum twisted mass formulation is equivalent to the standard formulation of QCD upon a basis axial rotation

$$\psi = \exp\Big(\frac{i\omega\gamma_5\tau^3}{2}\Big)\chi\ , \qquad \overline{\psi} = \overline{\chi}\exp\Big(\frac{i\omega\gamma_5\tau^3}{2}\Big). \tag{3.38}$$

In the twisted basis, one can then define axial and vector currents as

$$A^a_\mu = \overline{\chi}\gamma_\mu\gamma_5\frac{\tau^a}{2}\chi, \qquad V^a_\mu = \overline{\chi}\gamma_\mu\frac{\tau^a}{2}\chi, \tag{3.39}$$

and the pseudo-scalar and scalar densities

$$P^a = \overline{\chi}\gamma_5\frac{\tau^a}{2}\chi, \qquad S^a = \overline{\chi}\chi. \tag{3.40}$$

At the continuum level, all the symmetries of the standard QCD action (eq. 3.1) will be transcribed into the twisted mass basis by the action of the axial transformation. One important example are chiral $SU(2)_V \times SU(2)_A$ symmetry transformations

$$\delta\chi(x) = i[\alpha^a_V(x)\frac{\tau^a}{2} + \alpha^a_A(x)\frac{\tau^a}{2}\gamma_5]\chi(x), \tag{3.41}$$

$$\delta\overline{\chi} = i\overline{\chi}(x)[-\alpha^a_V(x)\frac{\tau^a}{2} + \alpha^a_A(x)\frac{\tau^a}{2}\gamma_5], \tag{3.42}$$

which through Ward-Takahashi identities [44, 45] give the partially conserved axial current (PCAC) and partially conserved vector current (PCVC)

$$\partial_\mu A^a_\mu(x) = 2m_q P^a + i\mu_q\delta^{3a}S^0, \tag{3.43}$$

$$\partial_\mu V^a_\mu = -2\mu_q\epsilon^{3ab}P^b. \tag{3.44}$$

The equivalence between the standard and the twisted formalism is not trivial once we study the regularised theory on the lattice as the Wilson term breaks chiral symmetry explicitly. However, it is possible to prove rigorously the twisted mass QCD (tmQCD) and QCD are equivalent also at finite lattice spacing if one uses the overlap Dirac operator (eq. 3.16), as it is the only discretisation obeying the Ginsparg-Wilson equation which guarantees the correct chiral transformation on the lattice. If tmQCD and QCD are the same also in the lattice regularisation then they must share the same continuum limit. Based on universality, one can then expect that this equivalence still

holds even when one employs a regularisation not necessarily chirally invariant and that renormalised correlation functions computed in tmQCD are equivalent to those in standard QCD up to cutoff effects [42].

In fact, the twist angle ω parametrises a family of twisted mass regularisations all sharing the same continuum limit. Among the possible values of the twist angle, the most important one is the case in which $\omega = \pi/2$ referred to as maximal twist. At maximal twist one has an automatic $\mathcal{O}(a)$ improvement of the discretisation effects, with the leading correction appearing only at $\mathcal{O}(a^2)$. In order to understand where does this automatic improvement come from, it is useful to consider the twisted mass propagator in momentum space

$$\tilde{G}(p) = \frac{-i\gamma_\mu \hat{p}_\mu + \mathcal{M}(p) - i\mu_q \gamma_5 \tau^3}{\hat{p}_\mu^2 + \mathcal{M}(p)^2 + \mu_q^2}, \tag{3.45}$$

where we defined $\hat{p}_\mu$ and $\mathcal{M}(p)$ as

$$\hat{p}_\mu = \frac{1}{a}\sin(ap_\mu)\ , \qquad \mathcal{M}(p) = m_0 + \frac{2r}{a}\sin^2\left(\frac{ap_\mu}{2}\right). \tag{3.46}$$

The poles of the propagator gives us the spectrum of the theory. Expanding with respect to a and neglecting any $\mathcal{O}(a^2)$ contribution, one gets

$$p^2 + m_0^2 + arp^2 m_0 + \mu_q^2. \tag{3.47}$$

At maximal twist, the bare mass term m_0 vanishes and so does the only $\mathcal{O}(a)$ term in the expansion. This can be understood by saying that the Wilson term and the mass term m_0 in the twisted mass formalism point point in different directions in the chiral-flavour space.

In order to understand the chiral orthogonality of the Wilson term and the mass parameter, one needs to first describe how tmQCD on the lattice behaves under vector and axial transformations. As mentioned before, while in the continuum vector and axial transformations in tmQCD are related to the axial and vector transformations in standard QCD, on the lattice different terms in the action break different sectors of the axial and vector transformations. To begin with, the ordinary iso-vector $SU(2)_V$ symmetry is broken explicitly by the μ_q term down to $U_V(1)_3$ subgroup. At maximal twist, the Wilson term breaks the "charged" twisted vector symmetry and is invariant

under "charged" twisted axial symmetry which are defined respectively as

$$\Big[U_A(1)_{\frac{\pi}{2}}\Big]_{1,2} : \chi(n) \to \exp\Big(\pm i\frac{\alpha_A^{1,2}}{2}\tau^{2,1}\Big)\chi(n), \quad \overline{\chi}(n) \to \overline{\chi}(n)\exp\Big(\mp i\frac{\alpha_A^{1,2}}{2}\tau^{2,1}\Big), \tag{3.48}$$

$$\Big[U_V(1)_{\frac{\pi}{2}}\Big]_{1,2} : \chi(n) \to \exp\Big(\pm i\frac{\alpha_V^{1,2}}{2}\gamma_5\tau^{2,1}\Big)\chi(n), \quad \overline{\chi}(n) \to \overline{\chi}(n)\exp\Big(\pm i\frac{\alpha_V^{1,2}}{2}\gamma_5\tau^{2,1}\Big). \tag{3.49}$$

The mass term has an orthogonal behavior and breaks "charged" twisted axial symmetry while being invariant under "charged" twisted vector symmetry.

In fact, the "charged" axial transformation is only softly broken by the mass term and is an exact symmetry of tmQCD in the massless limit. This statement as important consequences, since the pion is then protected from chiral symmetry breaking cutoff effects and the vector current is protected from renormalisation. One then does not require renormalisation for the pseudo-scalar decay constant of the charged pion as the current does not need to be renormalised. Another important characteristic of the tmQCD formalism is that since the twist transformations of eq. 3.38 are non-anomalous, they do not change the integration measure in the path integral formalism giving the same result for the expectation value of a certain observable [10]. In more general terms, it is possible to write correlation functions in standard QCD as a linear combination of correlation functions computed in tmQCD [39].

In order to be certain that the physical content of QCD in Minkowski space can be reconstructed from Euclidean Green's functions, the regularised theory, in this case tmQCD is required to satisfy some necessary and sufficient conditions formulated by Osterwalder and Schrader [13]. One of these conditions is the requirement that the transfer matrix of the Euclidean theory (see sec. 2.2) is strictly positive. This condition was demonstrated by Lüscher for Wilson fermions and the argument can be extended to twisted mass fermions [14, 43].

Exploiting the relation between the twist angle ω and the two mass parameters m_q,μ_q it is possible to find a prescription to tune ω to maximal twist. This is often done by computing the PCAC mass (eq 3.50) from lattice correlation function and studying its long Euclidean time behaviour

$$m_{PCAC} = \frac{\sum_n \langle \partial_0 A_0^a(n) P^a(0)\rangle}{2\sum_n \langle P^a(n) P^a(0)\rangle}. \tag{3.50}$$

Using the definition for the renormalised mass in terms of the PCAC mass m_R =

$(Z_A/Z_P)m_{PCAC}$ and the definition of the renormalised mass in terms of the critical mass $m_R = Z_m m_q = Z_m(m_0 - m_{cr})$, one gets an expression of the twist angle in terms of m_{PCAC}

$$\tan\omega = \frac{\mu_q}{Z_A m_{PCAC}}. \tag{3.51}$$

The renormalisation constants Z_A, Z_m, Z_P, Z_μ depend on the bare gauge coupling squared g_0^2 and the lattice twisted mass $a\mu$ and can be determined non-perturbatively in a mass independent scheme. The most commonly used scheme is the regularisation independent (RI'/MOM) scheme, sometime referred to as Rome-Southampton method [10, 46].

As the PCAC mass vanishes in the long time regime of the numerical study of eq. 3.50, the critical mass gets tuned to the same value of m_0, the twist angle acquires the value for maximal twist $\pi/2$ and we get automatic $\mathcal{O}(a)$ improvement. Together with the PCAC mass method, there are currently many other methods which can be used to tune the twist parameter, most of which can be found in ref. [39].

Until now, the discussion involved only light degenerate flavour of quarks, namely u, d. Following ref. [47] it is possible to write the twisted mass action for non-degenerate heavy flavour quarks in the physical basis

$$S_F^{tm}[\psi,\overline{\psi},U] = a^4\sum_n \overline{\psi}(n)\Big(\frac{1}{2}\gamma_\mu(\nabla_\mu+\nabla_\mu^*) - i\gamma_5\tau^1[m_0 - \frac{a}{2}\nabla_\mu\nabla_\mu^*] + \mu_\sigma + \mu_\delta\tau^3\Big)\psi(n), \tag{3.52}$$

where μ_σ and μ_δ are the twisted masses which can be related to the renormalised strange and charm masses using the relation [48]

$$m_{c,s} = \frac{1}{Z_P}\left(\mu_\sigma \pm \frac{Z_P}{Z_S}\mu_\delta\right). \tag{3.53}$$

3.3.1 Osterwalder-Seiler fermions

In principle, it is possible to simulate both sea quarks and valence quarks using the same fermion action. However, since the twisted mass formalism does not preserve chiral symmetry, positive parity operators are allowed to mix [49, 50]. Moreover, at finite lattice spacing, the misalignment in chiral space between the mass term and the Wilson term leads to the disruption of both iso-spin and parity symmetry. These symmetries appear as $\mathcal{O}(a^2)$ cutoff effects, in particular the iso-spin breaking which can induce splitting among flavour multiplets.

In order to mitigate these effects and avoid operator mixing, it is convenient to employ a non-unitary set-up and use different actions to simulate different quark flavours

which possibly do not break flavour symmetry. This mixed action technique was used in order to compute the correlation functions used in chapter 8. In particular, all the sea quark flavours were simulated using the twisted mass fermion action, eq. 3.35 for the light degenerate and eq. 3.52 for the strange and charm quarks. The valence quarks, which in chapter 8 are the strange and the charm, were simulated using the Osterwalder-Seiler action [51]

$$S_F^{OS}[\psi,\overline{\psi},U] = a^4 \sum_n \overline{\psi}^{(f)}(n)\left(\frac{1}{2}\gamma_\mu(\nabla_\mu + \nabla_\mu^*) - i\gamma_5 r^{(f)}[m_0 - \frac{a}{2}\nabla_\mu\nabla_\mu^*] + \mu^{(f)}\right)\psi(n), \tag{3.54}$$

where the Wilson parameters $r^{(f)}$ are set to unity and opposite in sign, which guarantees that the squared pseudo-scalar meson mass differs from its continuum counterpart only by terms of $O(a^2\mu)$ [52, 53].

3.4 Improvements to the gluon action

As we it was discussed in the previous section, it is possible to improve the lattice fermion action, one example being the twisted mass action. In modern lattice QCD simulations it is now widely common to use improved versions of the naive lattice gauge action of eq. 2.51 in order to reduce discretisation effects. The results discussed in chapter 8 were obtained using the improved Iwasaki action [54, 55].

In fact, the Wilson gauge action of eq. 2.51 belongs to a set of several possible lattice actions that can be used to simulate a pure gauge theory. The actions differ from each other by the number of different shapes of Wilson loops included in their definition together with the plaquette operator, each of this contributions being weighted by a coefficient. However, universality guarantees that all these lattice gauge actions all share the same fixed point and therefore will give the same result in the continuum limit. In other words, all these lattice actions will approach asymptotically the same renormalised trajectory. However, the rapidity of the asymptotic approach is determined by the form of the action.

The strategy used to select the improved lattice action is to first assume a general form for the lattice action that describe the system at the renormalised trajectory in terms of some coefficients K. Then, starting from the simplest lattice gauge action, one can perform block link transformations which modify the lattice spacing a and therefore produce different actions along a trajectory towards the fixed point. The correlation functions for each of the lattice actions produced following this method can be computed in perturbation theory. The next step is to expand the action on the

renormalised trajectory and compute the correlation functions in perturbation theory. The correlation functions obtained following the block link transformations in the limit of an infinite number of such operations will all approach that on the renormalised trajectory, and so will the corresponding lattice actions. By defining a distance between the set of improved lattice action and the one on the renormalised trajectory it is possible to determine the coefficients which minimise such distance. These coefficients will then select the improved Iwasaki lattice gauge action.

Finally, another improvement that has been implemented in the lattice simulations discussed in chapter 8 is the use of APE smearing of the gauge links [56]. The smearing consists in averaging each link variable its six perpendicular staples together with a parameter α which is tuned with respect to the gauge coupling. In particular, the results shown in this documents were obtained using $\alpha = 0.5$.

Chapter 4

Numerical methods for lattice field theory

One of the advantages of the Euclidean lattice regularisation of gauge theories is the possibility to use numerical methods to compute physical observables.

In particular, the numerical evaluation of expectation values in a lattice theory requires Monte Carlo integration: the need to resort to Monte Carlo calculations to evaluate the path integrals of a lattice theory can be understood by considering one of the simplest models defined on a lattice, namely the classical Ising spin model in 3 dimensions, in which the spins are defined at every lattice site and can take either the value $+1$ or -1. Counting all possible combinations of values, this gives a number of possible configurations equal to 2^{N^3}. Thus, calculating the expectation value of an operator exactly would require summing over all of the 2^{N^3} configurations. This task is clearly impossible for every value of N (except for the smallest ones) so one has to use Monte Carlo methods to find an approximate estimate for the expectation values of the model; these approximate values will be affected by finite uncertainties. By choosing a random x_n from a uniform distribution $\rho_u(x_n) = 1/(b-a)$, in the interval $[a, b]$, one can evaluate an integral of the function $f(x)$ writing

$$\frac{1}{b-a}\int_b^a dx f(x) = \langle f \rangle_{\rho_u} = \lim_{N\to\infty} \frac{1}{N}\sum_{n=1}^{N} f(x_n). \tag{4.1}$$

In eq. 4.1, N denotes the order of a finite sample of the possible configurations; it can be proven that the statistical error associated to the estimator for the expectation value of f behaves like $\frac{1}{\sqrt{N}}$ [57]. When evaluating the Euclidean path integrals, the probability distribution of the various configurations of lattice fields is proportional to e^{-S}, which acts as a Boltzmann weight factor, giving different importance to different

configurations when evaluating the Monte Carlo integration. This *importance sampling* of the possible configurations is at the heart of lattice simulations.

The generalisation of the Monte Carlo simulation to lattice gauge theory and lattice QCD is quite straightforward: basically, one simply needs to replace the integration over the random variable x_n with the integration over $U_\mu(n)$. Considering that (focusing on QCD with two dynamical quark flavours for simplicity) one can write the expectation value of a generic operator as

$$\langle O \rangle = \frac{1}{Z} \int \mathcal{D}[U] \{\det D[U]\}^2 e^{-S_G[U]} O[U], \tag{4.2}$$

it is possible to identify the measure of the probability distribution for the various configurations as

$$dP[U] = \frac{1}{Z} \mathcal{D}[U] \{\det D[U]\}^2 e^{-S_G[U]}. \tag{4.3}$$

Thus, it follows that one can use a similar version of equation 4.1 to evaluate an approximation of the expectation value of O as

$$\langle O \rangle = \lim_{N \to \infty} \sum_{n=1}^{N} O[U_n], \tag{4.4}$$

where the variables U_n are sampled according to the $dP[U]$ measure, also known as Gibbs measure.

4.1 Markov chain Monte Carlo

Given an initial gauge configuration taken from a certain type of distribution, one can build a stochastic sequence of configurations along what is known as Markov chain

$$U_1 \to U_2 \to \ldots \to U_n, \tag{4.5}$$

where the subscripts running from 1 to n denote the Monte Carlo time. Markov chains are constructed in such a way that configurations with a larger Boltzmann factor will be visited more frequently in configuration space. The updates from one configuration to the next one along the Markov chain are regulated by a certain transition probability $T(U' \leftarrow U)$. The transition probability is independent of the Monte Carlo time and must obey the conditions

$$0 \leq T(U' \leftarrow U) \leq 1, \qquad \sum_{U'} T(U' \leftarrow U) = 1. \tag{4.6}$$

As the Markov chain evolves in Monte Carlo time, it will eventually reach an "equilibrium" state in which the transition probability of moving into a certain configuration will be the same to the probability of moving out from that configuration. The time it takes for the Markov process to reach equilibrium is called *thermalisation* time; as will be discussed below, its estimate in numerical simulations may be non-trivial. As well as being stable, Markov processes must satisfy ergodicity, meaning that they must be able to access all possible configurations in configuration space. The simplest update algorithm that satisfies all the above conditions on the transition probability was initially proposed by Metropolis *et al.* in ref. [58] for symmetric probability distributions and later generalised by Hastings in ref. [59]. The algorithm consists in starting from an arbitrary configuration U followed by an accept/reject updating step based on the transition probability and the Boltzmann factor

$$T_A(U' \leftarrow U) = \min\left(1, \frac{T_0(U \leftarrow U')e^{-S[U']}}{T_0(U' \leftarrow U)e^{-S[U]}}\right), \tag{4.7}$$

where T_A is the transition probability and T_0 is the selection probability. The process is then iterated over all the available configurations. In the case of symmetric selection probability, the accept/reject step is based on the change in the action appearing in the Boltzmann factor $\Delta S = S[U'] - S[U]$. In particular, the proposed new configuration is accepted when it reduces the action, but it can also be accepted, with probability $\exp(-\Delta S[U])$, if the action increases. This allows for the existence of fluctuations, which are natural in a statistical or in a quantum system.

Over time, newer and more efficient algorithms have been developed for the simulation of lattice gauge theory and lattice QCD, for instance the pseudo heath-bath algorithm of ref. [60]. Nowadays, a very popular choice when simulating Yang-Mills theory or spin systems is the heat-bath algorithm, first proposed in ref. [61]. The heat-bath algorithm is essentially an iterated Metropolis-Hastings algorithm with an improved local acceptance rate. Often, the heat-bath algorithm is alternated with some overrelaxation steps [62] which consist in taking as the new configuration U' a variable with the same probability weight as U but as far away in configuration space as possible. Overrelaxation updates improve the efficiency of the in sampling the configuration space, however they are not ergodic, hence they have to be combined with some ergodic updates.

4.2 Simulating dynamical quarks

For many years since the advent of lattice gauge theory, calculation of lattice QCD could only be performed in quenched approximation, which consisted in simulating gauge configurations without including the determinant of the Dirac operator describing sea quarks. The reason it took some time before the appearance of simulations including the full dynamics of quarks is that the computation of the light quark Dirac operator determinant is particularly challenging from the numerical point of view. The way to include the dynamical contribution of (one flavour of) dynamical quarks in lattice simulations is to include the Dirac operator determinant as a probability weight factor when generating the Markov chain of gauge configurations

$$\rho(U) = \frac{1}{Z} e^{-S_G[U]} \det[D_q], \tag{4.8}$$

where D_q is the Dirac operator. Often, in order to guarantee the positivity of the determinant, the light quark flavours up and down are taken to be degenerate allowing to raise the Dirac operator to an even power. The Dirac operator determinant is conveniently expressed in terms of pseudo-fermions [63], which allow one to express the determinant in terms of bosonic fields

$$\int \mathcal{D}[\psi]\mathcal{D}[\overline{\psi}] e^{-\overline{\psi}_u D \psi_u - \overline{\psi}_d D \psi_d} = \pi^{-N} \int \mathcal{D}[\phi_R]\mathcal{D}[\phi_I] e^{-\phi^\dagger (DD^\dagger)^{-1}\phi} = \det[DD^\dagger], \tag{4.9}$$

where the contribution are divided into real and imaginary parts and π^{-N} is an irrelevant factor, which will cancel out in expectation values. The above equation suggests to treat the pseudo-fermion action as an effective action to be added to the gauge action in order to have a correct Boltzmann weight factor when generating gauge configurations for the Markov chain process. However, computing the pseudo-fermion weight factor requires new numerical algorithms.

4.2.1 Hybrid Monte Carlo

In a nutshell, the central idea behind the hybrid Monte Carlo (HMC) algorithm [64] is that, starting from the gluonic action and the part of the action involving the pseudo-fermions, one can introduce conjugate momenta to these bosonic variables (which are interpreted as "coordinates" in a generalised phase space), and construct an Hamiltonian defined as the sum the original action plus the kinetic terms constructed from these conjugate momenta. Then, one lets the coordinates and momenta appearing in the new Hamiltonian evolve according to (a discretised version of) their classical

equations of motion, which allows the original system to efficiently explore the configuration space, without incurring into large, positive variations of the action; typically, a leap-frog strategy is used for the alternating updating of coordinates and momenta, and an accept/reject step is included to ensure that the discretisation of the equations of motion do not bias the actual dynamics that one wants to simulate.

To clarify this procedure, it is particularly convenient to discuss the HMC algorithm for a scalar field ϕ (while the results for the case of lattice QCD will only be mentioned at the end of the discussion).

When looking at the problem of updating many configurations, it is convenient to consider the system as a microcanonical ensemble described by the classical Hamiltonian evolving the fields in Monte Carlo time τ

$$H[\pi, \phi] \equiv \frac{1}{2} \sum_n \pi_n^2 + S[\phi], \tag{4.10}$$

where in this case π are the conjugate momenta of the bosonic field variables ϕ. The evolution is governed by the equations of motion

$$\frac{\partial \pi}{\partial \tau} = -\frac{\partial H}{\partial \phi} = -\frac{\partial S}{\partial \phi}, \qquad \frac{\partial \phi}{\partial \tau} = \frac{\partial H}{\partial \pi} = \pi, \tag{4.11}$$

also known as molecular dynamic equations. The path of configurations with a certain (π, ϕ) lies on a hypersurface with constant energy, hence, all the configurations on that path will be automatically accepted. The conjugate variables evolve according to the Hamiltonian in small steps following the molecular dynamic evolution creating a *trajectory*. The first step in the implementation of the HMC algorithm, is the generation of momenta π from a Gaußian distribution for a given configuration.

In order to have an exact algorithm, i.e., one that is ergodic, stable and without bias in the implementation, the molecular dynamic trajectories need to fulfill the conditions of (i) Area preservation of integration measures $\mathcal{D}[\phi]\mathcal{D}[\pi]$ and (ii) Reversibility of trajectory *i.e.* $T_{md}(\pi', \phi' \leftarrow \pi, \phi) = T_{md}(-\pi, \phi \leftarrow -\pi', \phi')$. In order to check the reversibility condition, it is necessary to solve the equations discussed above, which are called "molecular dynamics" equations. The solution is obtained numerically, using some numerical integrator such as the leapfrog algorithm which evolve the conjugate variables alternatively. The numerical integration requires to divide the time interval $[0, \tau]$ into a finite number of steps of sufficiently small size ε. In the leapfrog solver, the two variables are evolved at different rates, with the conjugate momenta being evolved by a half-step $\varepsilon/2$, followed by the evolution along one full step of the variable ϕ, followed again by a final half-step for π. The procedure is repeated for all the interval

in which one divides the time evolution. It can be shown that solvers like the leapfrog preserve the integration measures [10]. For small values of τ, it is possible to formally prove that the HMC is ergodic [65]. The same cannot be obtained for generic lengths of the time interval, since the proof is based on an expansion in powers of τ. However, it is possible to rigorously ensure ergodicity by choosing a random $\tau \in [0, \tau_{\max}]$ from one updating step to another [65]. Regardless of the type of algorithm used to evolve the variables along the trajectory, any numerical solver will necessarily carry a non-zero rounding error $\mathcal{O}(\varepsilon^k)$, with k depending on the type of algorithm. It follows that one cannot guarantee reversibility and the algorithm, as described so far, would not be exact. This problem, however, has a simple solution, by means of the introduction of an accept/reject step, of the same type as the Metropolis-Hastings algorithm, which fixes any numerical error occurred during the molecular dynamics evolution. This makes the HMC algorithm exact and a viable numerical method for lattice QCD simulations. One can summarise the HMC strategy for a single trajectory as follows:

1. Given a configuration ϕ, generate a new set of conjugate momenta π from a Gaußian distribution.

2. Using the molecular dynamics equations, let (ϕ, π) evolve to (ϕ', π') along a trajectory with (approximately) constant H.

3. Compute acceptance probability $P_{acc} = \min[1, e^{-\Delta H}]$ with the conditions $P_{acc} \geq r$, r being a uniformly distributed pseudo-random number between 0 and 1.

The strategy is iterated for the given number of steps along the molecular dynamics trajectory. Typical lattice QCD simulations are performed with 50 to 100 steps for a complete trajectory, with an estimated computational cost proportional to $V^{\frac{5}{4}}$, where V is the lattice hypervolume [66, 67]

In lattice QCD simulations the variables that are updated are the pseudo-fermions and the link variables that are elements of the $SU(3)$ gauge group $U = \exp\left(i \sum_{i=1}^{8} \omega^{(i)} T_i\right)$, T_i being the algebra generators. The corresponding conjugate momenta are then $\pi_\mu = \sum_{i=1}^{8} \pi_\mu^{(i)} T_i$. The variables are evolved along the molecular dynamic trajectory by the force $F[U, \phi]$ defined as

$$F[U, \phi] = \sum_{i=1}^{8} T_i \nabla^{(i)} \left[S_G[U] + \phi^\dagger (DD^\dagger)^{-1} \phi \right] \in \mathfrak{su}(3), \tag{4.12}$$

where ϕ in this case is the pseudo-fermion field. Here one can notice that the contribution of the fermion action requires the evaluation of the term $\nabla^{(i)}(\phi^\dagger (DD^\dagger)^{-1}\phi)$ for each step along the trajectory.

4.3 Autocorrelation

In a Markov process, any variable will typically be affected by some form of correlation with the previously generated values in the chain, as it evolves in Monte Carlo time. This inevitably reduces the statistical independence of the variables in a Markov chain, and has an impact on the uncertainties of the observables that have to be estimated from the configurations generated in the Markov chain. Given a set of primary observables a^α enumerated by the α, for instance the plaquette operator in eq. 2.50, each observable can be obtained applying some valid update algorithm. The average of these observables will correspond to a stochastic estimator of the path integral expectation value $A^\alpha = \langle a_i^\alpha \rangle$. One can then repeat the simulation with the same number of updating steps, generating a statistically independent set of primary observables called *replica*. Finally, averaging over all of the replicas gives the true statistical mean of the primary observables $A^\alpha = \langle\langle a_i^\alpha \rangle\rangle$. One can then define the autocorrelation function between two subsequent variables in the Markov chain as [68]

$$\Gamma_\alpha(t) = \langle (a_\alpha^i - A_\alpha)(a_\alpha^{i+1} - A_\alpha) \rangle, \tag{4.13}$$

where t here is the Monte Carlo time and the average is over statistically independent replica ensembles. In the limit of large number N of updating steps, one can determine the error on the estimator A^α as

$$\sigma_\alpha^2 = \frac{1}{N} \sum_{t=-\infty}^{\infty} \Gamma_\alpha(t) \left[1 + \mathcal{O}\left(\frac{1}{N}\right) \right] \approx \frac{\Gamma_\alpha(0)}{N} 2\tau_{\text{int}}(A^\alpha), \tag{4.14}$$

where we introduced the integrated autocorrelation time τ_{int} defined in terms of the normalised autocorrelation function

$$\tau_{\text{int}}(A^\alpha) = \frac{1}{2} + \sum_{t=1}^{\infty} \rho(t), \qquad \rho(t) = \frac{\Gamma_\alpha(t)}{\Gamma_\alpha(0)}. \tag{4.15}$$

In practice, in simulations one can only compute a biased estimator of the autocorrelation function such that in eq. 4.13, the true mean A^α needs to be replaced by the one that can actually be measured $\overline{a}_\alpha$. Consequently, also $\rho(t)$ and τ_{int} are biased. Understanding the nature of the bias in autocorrelation functions is very important as it characterises the dynamics of the Monte Carlo process relevant for the observable A. Unfortunately, the integrated autocorrelation time is difficult to determine since the errors on $\Gamma_\alpha(t)$ remain roughly constant as a function of t [69]. Following the methods proposed by Madras and Sokal [70], later generalised by Wolff [68], we can estimate

τ_{int} introducing a window of updating steps W

$$\tau_{\text{int}}(A^{\alpha}) = \frac{1}{2} + \sum_{t=1}^{W} \rho(t). \tag{4.16}$$

The window is chosen to balance the systematic error due to the truncation of the infinite series. For typical simulations, the normalised autocorrelation function decays exponentially for large t

$$\rho(t) \sim \exp\Big(- \frac{t}{\tau_{n,\text{exp}}}\Big), \tag{4.17}$$

where $\tau_{n,\text{exp}}$ is the exponential autocorrelation time for the n mode contributing to the autocorrelation function. The slowest mode is the one with the largest autocorrelation time. This number provides information on the magnitude of the autocorrelation between two configurations separated by a single updating step. This suggest that the order of the systematic errors goes as $\mathcal{O}\left[\exp\left(\frac{t}{\tau_{\text{exp}}}\right)\right]$ [10, 68]. The exponential autocorrelation time can only be known at the end of the simulation, computing the expectation value of a primary quantity. Assuming the value of τ_{exp} is known, a conservative estimate of τ_{int} can be obtained using

$$\tau_{\text{int}} = \Big[\frac{1}{2} + \sum_{t=1}^{W} \rho(t)\Big] + \tau_{\text{exp}}\rho(W), \tag{4.18}$$

together with a judicious choice of W [1] [69].

4.3.1 Critical slowing down

Autocorrelation is related to a phenomenon known as critical slowing down, which becomes particularly problematic when approaching the critical point of a theory (e.g., approaching the continuum limit in a lattice QCD simulation, namely for $a \to 0$). It is therefore important to study the scaling of quantities like integrated and exponential autocorrelation time in the limit $a \to 0$. For the dynamical critical exponent z which depends on the updating algorithm, one has [69]

$$\tau_{a,\text{int}} \sim (\xi_a)^z, \qquad \tau_{\text{exp}} \sim \xi^z, \tag{4.19}$$

where ξ is the correlation length as defined in eq. 5.9 and discussed in section 2.2. For the HMC algorithm in full lattice QCD simulations the dynamical critical exponent is $z \approx 5$ [69, 71], with the computational effort expected to scale like a^{-10} [71].

[1] For example minimising the functional $E(W)$ as proposed in [69]

Yang-Mills theories (and QCD) are theories characterised by different topological sectors, hence, it is important that our updating algorithm correctly samples all of these sectors when performing lattice simulations. For coarse values of the lattice spacing, the HMC algorithm is indeed able to sample these sectors efficiently as it lets the system evolve along the molecular dynamics trajectory. However, as one approaches the continuum limit, changing topological sector becomes harder and harder; this results into an increase in the autocorrelation time and into an eventual breakdown of the ergodicity of the algorithm: this is due to the fact that, as one decreases the lattice spacing, it becomes increasingly more likely that the HMC trajectories get trapped within a topological sector. For values of the lattice spacing lower than 0.05 fm, this effect is particularly severe and the HMC trajectory gets completely trapped within a topological sector, realising what is known in the literature as *topological freezing* [72, 73, 69].

Considering that the lattice spacing is the UV cutoff of the lattice theory, critical slowing down and topological freezing put a limit on the type of particles which can be simulated on the lattice. In order to be able to get accurate results from numerical simulations and treat all particles in a fully relativistic way, the masses m_M of the physical states have to satisfy the following constraints:

$$L^{-1} \ll m_M \ll a^{-1}. \tag{4.20}$$

This means that even if one could perform simulations with a lattice spacing as small as 0.05 fm, which corresponds to $a^{-1} \approx 3.9$ GeV, this would not be sufficient to properly simulate B mesons, since their mass is $m_B \approx 5$ GeV.

This is a non-trivial problem that has to be taken into account when one wants to study heavy mesons on the lattice, for example in the case of inclusive semileptonic decays. As it will be discussed in more detail in chapter 8, we performed the simulations with a lattice spacing $a = 0.0815(30)$ and a bottom quark whose mass had an unphysical value, equal to twice the physical charm quark mass, giving a simulated B_s-meson with a mass $m_{B_s} \approx 3$ GeV. Obviously, this unphysically light value of the meson mass affects the available phase space of the inclusive semileptonic decay and consequently the results of our study.

Chapter 5

Monopoles in the Heisenberg model

In this chapter we shall present an original lattice study of the classical Heisenberg spin model, which was published in ref. [4]. In particular, we shall focus on the behaviour of monopole-like excitations that are created in the system by imposing appropriate boundary conditions. We shall show that the profiles of the magnetisation and of the energy density profiles are consistent with analytical calculations that were previously derived in quantum field theory in ref. [74].

5.1 Definition of the model

Consider a four-dimensional, isotropic, hyper-cubic lattice of lattice spacing a and spatial extent L. At each lattice site one can define the spin field variable $\boldsymbol{s}(x)$, a three-component real vector of unit length, with a certain orientation which defines its state.

Considering only nearest-neighbour interactions, the Hamiltonian of the Heisenberg model in D dimensions can be written as

$$\mathcal{H} = -J \sum_{\langle x,y \rangle} \boldsymbol{s}(x) \cdot \boldsymbol{s}(y), \tag{5.1}$$

where $\boldsymbol{s}(x)$ is the spin variable defined at the site x of a regular Euclidean lattice in D dimensions, the summation runs over all distinct nearest neighbours sites and J is the ferromagnetic coupling. It is trivial to note that the Heisenberg model enjoys a global $O(3)$ rotational symmetry: as the Hamiltonian depends only on the relative orientation between neighbouring spin variables, the latter can always be redefined by a global orthogonal transformation, i.e., by an element of the $O(3)$ group.

The partition function of this statistical system is written as

$$Z = \prod_x \sum_{\langle x,y \rangle} e^{-\mathcal{H}[\boldsymbol{s}]/T}, \tag{5.2}$$

where T denotes the temperature (natural units are assumed).

As usual in spin systems, one can define the magnetisation at a given site as

$$\langle \boldsymbol{s}(x) \rangle = \frac{1}{Z} \prod_y \sum_{\langle y,z \rangle} \boldsymbol{s}(x) e^{-\mathcal{H}[\boldsymbol{s}]/T}. \tag{5.3}$$

This is an important quantity, as it tells us in which phase the system is at a given value if the temperature. When the temperature is high, thermal fluctuations dominate, preventing distant spins to align and correlate. This is the disordered phase as the spins are randomly aligned and the magnetisation of the system is zero $\langle \boldsymbol{s}(x) \rangle = 0$. As the temperature is lowered the correlation among distant spins increases until one reaches a critical temperature T_c. At T_c the system undergoes a second-order phase transition where the magnetisation changes to $\langle \boldsymbol{s}(x) \rangle \neq 0$, meaning that the spins become aligned along the same direction. Therefore, for $T < T_c$ the system is in its ordered phase and the global $O(3)$ symmetry gets spontaneously broken.

In order to measure the correlation between spins at different locations, and capture the effect of thermal fluctuations, it is useful to define the correlation function

$$\langle \boldsymbol{s}(x)\boldsymbol{s}(y) \rangle = \frac{1}{Z} \prod_z \sum_{\langle z,w \rangle} \boldsymbol{s}(x)\boldsymbol{s}(y) e^{-\frac{\mathcal{H}[s]}{T}} \tag{5.4}$$

and the connected correlation function

$$\langle \boldsymbol{s}(x)\boldsymbol{s}(y) \rangle_{conn.} = \langle \boldsymbol{s}(x)\boldsymbol{s}(y) \rangle - \langle \boldsymbol{s}(x) \rangle^2. \tag{5.5}$$

While in the disordered phase the correlation function falls of exponentially with the distance, in the ordered phase the system is magnetised.

In ref. [4] we studied the classical Heisenberg model in $D = 4$ dimensions, where a long-range-order phase is known to exist at sufficiently low temperatures [75]. Moreover, being $D = 4$ the upper critical dimension, one can obtain analytic results for the critical exponents at the phase transition from calculation based on the mean-field technique (up to logarithmic corrections) [76, 77]. In the study, we used a Markov chain Monte Carlo simulation of vector-field configurations, generated by a combination of local heat-bath [78] and over-relaxation [79] updates.

In the ordered phase ($T < T_c$) of the spin system, the correlation function vanishes and the magnetisation becomes non-zero. In this phase it is interesting to study how the value of the magnetisation scales as we approach the critical point T_c, *i.e.* the point at which a second order phase transition occurs. By imposing a specific type of boundary conditions, it is possible to enforce the existence of topological excitations in this phase. Using an analytic field-theoretic approach, in ref. [74] it was shown that the magnetisation of the spin-system depends on the mass of the topological excitation enforced by the boundary conditions, which could then be interpreted as a "mono-pole" propagating in the Euclidean time direction. In our study we enforced the boundary conditions enforcing such "monopole-like" configurations on a four-dimensional lattice. This was done by constructing a map between the direction of $\boldsymbol{s}(x)$ at the spatial boundary with the direction of the spatial component x with respect to the centre of the system.

5.2 Results of the Monte Carlo simulations

The results for the i-th component of the magnetisation $\langle \boldsymbol{s}(x) \rangle$ for different values of the reduced temperature $t = (\frac{T-T_c}{T_c})$ are shown in figure 5.1. In the figure one can see the excellent agreement between the numerical results of the simulations and the analytic prediction derived in ref. [74],

$$\langle \boldsymbol{s}_i(x_i) \rangle = v \left[\left(1 - \frac{1}{2z^2} \right) \mathrm{erf}(z) + \frac{exp(-z^2)}{\sqrt{\pi} z} \right], \tag{5.6}$$

with $z = x_i \sqrt{2M/R}$, where, according to ref. [74], M would represent the mass associated to the topological excitation and v the asymptotic value of the magnetisation at large distances.

By fitting the numerical results to the analytic function in eq. 5.6, it is possible to extract the value of v and study its scaling as we approach the critical temperature. The scaling of these quantities near the critical temperature is particularly important because T_c is what is known as critical point. It turns out that a spin system in a given dimension d near the critical point exhibits the same behaviour as other theories which are described by the same critical point. This concept is known as *universality*. Two systems that share the same critical point are said to be in the same *universality class* [80]. This is also an important feature in lattice field theories. In particular, regardless of the method that is chosen to discretise the continuum action on the lattice, all these different approaches should belong to the same universality class, in

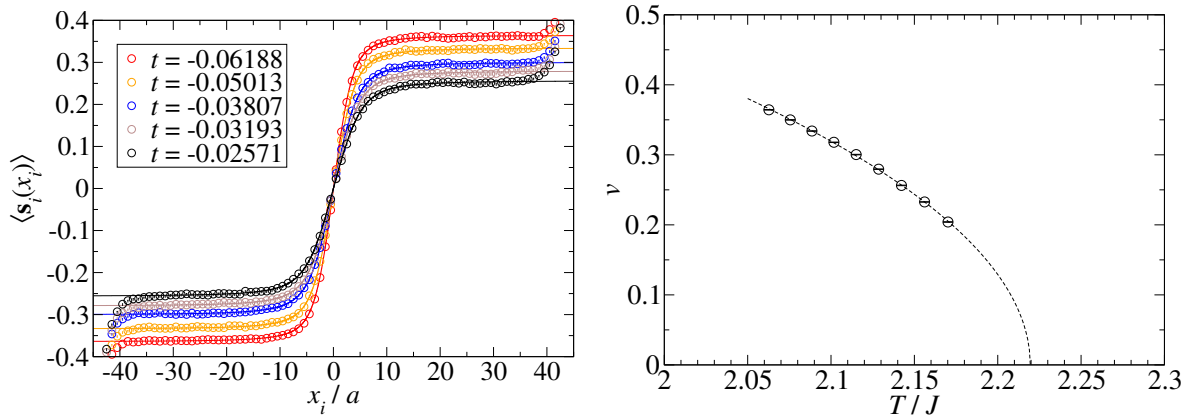

Figure 5.1: Left-hand side: Numerical results at $L/a = 90$ and $R/a = 20$ for the magnetisation profile as a function of the x_i coordinate. The plot shows the results obtained at different temperatures and the fit to eq: 5.6. Right-hand side: Magnetisation value at long distances v, obtained from fits to eq. 5.6, plotted against the temperature in units of the coupling, from different sets of simulations on lattices with $R = 20a$ and $L = 90a$, and their fit to eq. 5.7

order to recover the same theory when the dependence on the lattice spacing is removed at the critical point $a = 0$.

In the infinite volume limit, the modulus of the magnetisation is predicted to scale as $v \propto (-t)^{\beta}$, where β is the critical exponent expected to take the Gaußian value $\beta = \frac{1}{2}$. This scaling is confirmed by our results fitted by

$$v = A_v \sqrt{1 - \frac{T}{T_c}} \tag{5.7}$$

where $A_v = 1.376(5)$ and $T_c/J = 2.2195(7)$, as shown in figure 5.1.

In contrast with the conclusions drown in ref. [74], our results show that the parameter Ma depends on the time-extent R and therefore cannot be interpreted as a particle. In particular, figure 5.2 shows that the numerical results of $\langle \boldsymbol{s}_i(x_i) \rangle$ obtained with different values of R, all collapse on the same curve. From this one can conclude that M is proportional to R and one can infer that the topological excitation is characterised by an approximately constant $\mu = \frac{M}{R}$.

For this reason, in our study we proposed a different interpretation for the nature of the topological excitation as the *duration* of the excitation propagation. This statement is confirmed by looking at the scaling of aM which is predicted to be $aM = a\mu R = \mu(R/a)a^2 \propto t^{2\nu}$. This is indeed the scaling observed in figure 5.2 where the numerical

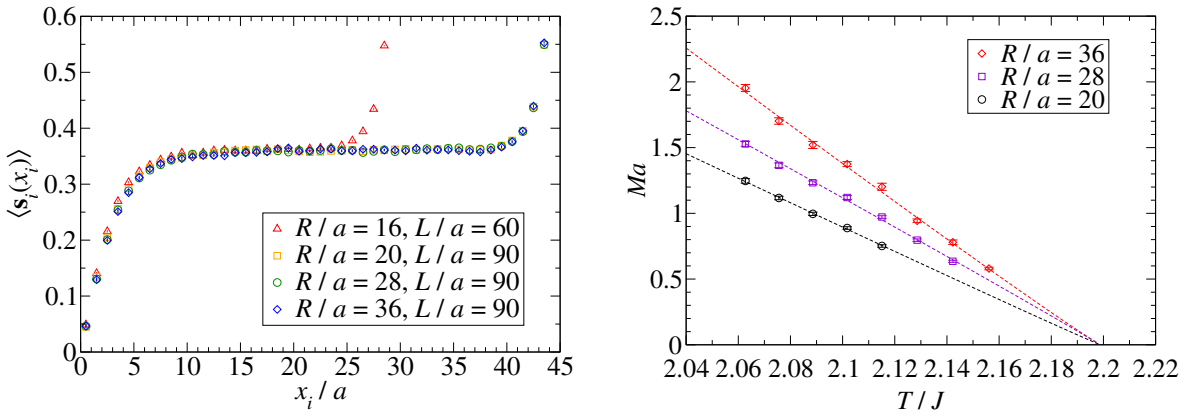

Figure 5.2: Left-hand-side panel: dependence of the spin profile $\langle \boldsymbol{s}_i(x_i) \rangle$ on the spatial coordinate x_i/a, as measured with respect to the center of the system, at a fixed temperature and for different values of the Euclidean-time extent of the lattice. All results shown in this plot were obtained from simulations with $T/J = 2.062725$. Right-hand-side panel: temperature dependence of the Ma parameter, extracted from the fits of our numerical data to eq. (5.6), for lattices with different values of R/a, and their fits to eq. (5.8).

results are fit to the function

$$aM = A_M \left(1 - \frac{T}{T + c} \right)^E . \tag{5.8}$$

The results in table 5.1 show that the critical exponent is indeed twice the value of ν obtained in the Gaußian approximation.

R/a	A_M	E	χ^2_{red}
20	21.3(1.5)	1.021(23)	0.50
28	23.4(1.8)	0.981(24)	2.34
36	34.6(2.3)	1.039(21)	1.76

Table 5.1: Results of the two-parameter fits of the data shown in the right-hand-side panel of figure 5.2 to eq. (5.8).

In the disordered phase ($T > T_c$), the thermal fluctuations dominate the tendency of the spins to correlate, which results in the correlation function to fall off exponentially with the distance between the spins

$$\langle \boldsymbol{s}(x) \boldsymbol{s}(y) \rangle \sim \exp\left(- \frac{|x - y|}{\xi(T)} \right), |x - y| \gg \xi, \tag{5.9}$$

where ξ is the correlation length. As the critical temperature is approached, the correlation length diverges and one observes the universal behaviour characterised by the

critical point.

The inverse of the correlation length $\frac{1}{\xi}$ is analogous to the energy gap, and hence to a particle mass in Euclidean quantum field theory. For this reason, one can rewrite the correlation function as

$$G(\tau, R) = \frac{a}{R}\langle \boldsymbol{S}(x_0)\boldsymbol{S}(x_0+\tau) = A\{e^{-m\tau} + e^{-m(R-\tau)}\}, \tag{5.10}$$

where τ is a generic point in the "temporal" direction, R is the temporal extent of the lattice, $\boldsymbol{S}(x_0)$ is the zero momentum spin operator $\boldsymbol{S}(x_0) = \frac{a^3}{L^3}\sum_{x_1,x_2,x_3} \boldsymbol{s}(x)$, m is the mass of the lightest particle state and $e^{-m(R-\tau)}$ is the term which arise from the fact that we are using periodic boundary conditions (PBC) and account for back-propagating particles.

In our work, we extracted the mass of the particle for different values of the reduced temperature t by fitting our numerical results to the function in eq. 5.10.

Now, as the temperature decreases and one approaches the critical temperature, the mass of the particle is expected to get smaller and eventually vanish at $T = T_c$. In order to quantitatively study the scaling of m, one needs to also to take into account the finite size corrections which follow a $\frac{1}{L}$-decay. This scaling behaviour is reproduced by our numerical results at $t \approx 0$, shown in table 5.2.

L/a	ma	L/a	ma
40	0.1043(11)	80	0.05105(35)
48	0.08373(60)	88	0.04694(34)
56	0.06749(41)	96	0.04005(12)
64	0.06099(45)	104	0.03302(19)
72	0.05829(32)		

Table 5.2: Results for the lightest mass contributing to the $G(\tau, R)$ correlator at $t \approx 0$, for different values of $L = R$.

Following this argument, we fit the data in table 5.2 to the function

$$am(L) = am + \frac{ak_1}{L}, \tag{5.11}$$

and find the result for am as $\frac{L}{a} \to \infty$ to be $am = -0.0058(37)$ which is compatible to 0 within less than two standard deviations.

Thus, assuming the finite volume effects are small, we expect the mass to scale with the reduced temperature as

$$am = \frac{mt^\nu}{\Lambda_+}, \tag{5.12}$$

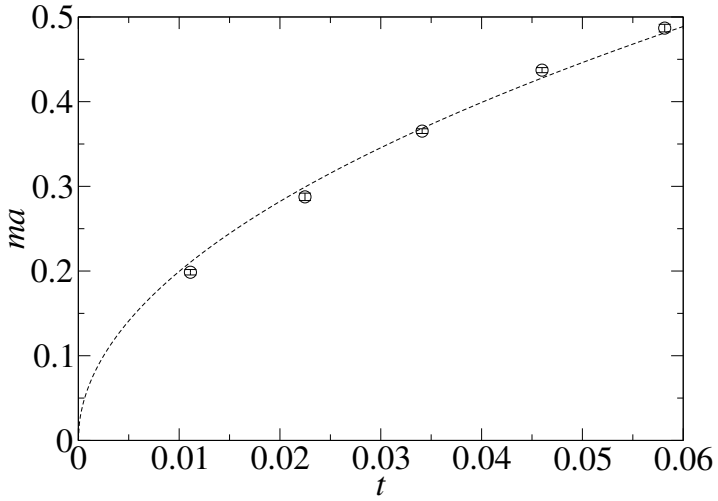

Figure 5.3: Mass values in units of the inverse lattice spacing at different reduced temperatures, extrapolated to the thermodynamic limit (circles), and their fit according to eq. (5.12) (dashed line).

where Λ_+ is a constant with dimension of an energy and according to a renormalisation-group analysis, the critical exponent near the Gaußian fixed point is expected to be $\nu = \frac{1}{2}$. This scaling is confirmed by our numerical results in figure 5.3, which clearly show the fact that the mass vanishes at $t = 0$. Fitting the numerical results to eq. 5.12 we obtain $m/\Lambda_+ = 1.995(24)$.

5.3 Discussion

Our study of the Heisenberg model on a four-dimensional Euclidean lattice allowed us to test the approximate analytical predictions that were derived by Delfino in ref. [74]. Even though $D = 4$ is the upper critical dimension, the model has interesting dynamical features: implementing boundary conditions that enforce topologically non-trivial field configurations (which, in a continuum version of the model, could be characterized by a non-trivial topological number under the second homotopy group $\pi_2(S^2)$), confirming the predictions for the energy-density and magnetisation profiles derived in ref. [74]. Our simulation results, however, also reveal that the scaling of the parameters (which, in this context, can be thought of as the "low-energy constants" appearing in the quantum-field-theoretical description of the spin model for $T \to T_c^-$) is not completely trivial, questioning a naïve interpretation of such topological configurations as *bona fide* particles. In particular, the parameter that was interpreted as the particle mass in ref. [74] is, instead, proportional to the duration of its propagation in Euclidean time.

Our findings have interesting implications. In particular, they can be contrasted

with those reported in an analogous numerical study in three dimensions [81], in which it was argued that Derrick's theorem [82] could be violated at the quantum level. While this possibility would be an intriguing one (especially in the view of recent arguments from axiomatic quantum field theory [83]), it should be noted that it would imply far-reaching consequences, including ones with dramatic phenomenological implications. For example, in relativistic astrophysics, a violation of Derrick's theorem would allow for the existence of bosonic stars consisting of particles that are the excitations of real scalar fields [84].

The study of topologically stable, monopole-like field configurations of finite energy in physical systems characterized by an intrinsic cutoff scale may also be of relevance in condensed-matter theory. Interpreting the statistical model that we simulated as the lattice regularisation of a quantum system in three spatial dimensions, the possible existence of artificial monopole-like excitations in this theory [85, 86, 87] may have important applications, including for quantum simulation [88] and for information communication [89]: recent work in this research area was reported, for instance, in the study of manganese germanide discussed in ref. [90].

Chapter 6

Confining strings in Yang-Mills theory at finite temperature

In this chapter we present an original lattice study of the effective string describing the low-energy regime of SU(2) Yang-Mills theory in three dimensions, that was published in ref. [3]. In particular, we discuss the behaviour of Polyakov-loop correlators at finite temperatures close to the deconfinement transition and analyse our numerical results in a comparison with analytical constraints from renormalisation-group arguments, from known results about the two-dimensional (Ising) universality class that describes the critical point of the theory, from conformal perturbation theory, and from Lorentz invariance, deriving quantitative bounds on the corrections to the effective string action beyond the Nambu-Gotō approximation.

In the "effective string theory" (EST) description, the flux tube joining together two colour sources in a confining gauge theory can be modeled as a thin vibrating string [91, 92, 93, 94, 95]. The EST enjoys a remarkable property: due to the peculiar features of the string action and to the symmetry constraints due to Poincaré invariance in the target space, the first few terms of the long-distance expansion of the EST action are universal [96, 97, 98, 99, 100, 101, 102].

The simplest Lorentz-invariant EST, which is the well-known Nambu-Gotō model [91, 92], is an exactly integrable, irrelevant, perturbation of the two-dimensional free Gaußian model [103], driven by the $T\overline{T}$ operator of the $D-2$ free bosons. Using an S-matrix bootstrap approach, it has been recently possible to constrain the EST action beyond the Nambu-Gotō approximation [104, 105]. Going beyond this approximation is an interesting open problem, since the terms beyond the Nambu-Gotō action encode important information about confinement.

An efficient way to study these corrections is through high-precision numerical

simulations of the interquark potential in lattice gauge theories at finite temperatures close to the thermal deconfinement transition, but still in the confining phase. With this motivation, ref. [3] addressed a study of the SU(2) Yang-Mills theory in $(2+1)$ dimensions, in the range of temperatures $0.8T_c \leq T \leq T_c$, where T_c denotes the deconfinement temperature. This is a particularly simple lattice gauge theory based on a non-Abelian Lie group, in which the non-perturbative features of Yang-Mills theories can be studied to much higher precision than in quantum chromodynamics. Moreover, the fact that the finite-temperature deconfinement transition for this model is a second-order one [106, 107], in the neighborhood of the deconfinement transition the model is expected to be in the universality class of the bidimensional Ising model [17] and the Polyakov loop correlator should correspond to the spin-spin correlator of the two-dimensional Ising model (which is known analytically).

6.1 Definitions and lattice setup

To simplify notations, in the following we will set the lattice spacing a to 1. We regularise the theory on a finite cubic lattice of spacing a and sizes N_t in the $\hat{0}$ ("Euclidean-time") direction and N_s in the two other ("spatial") directions, denoted as $\hat{1}$ and $\hat{2}$. We use the Wilson action and introduce the parameter β, defined as $\beta = 4/g^2$.

Following ref. [108], the scale-setting of the model can be defined in terms of the equation:

$$\sqrt{\sigma_0(\beta)} = \frac{1.324(12)}{\beta} + \frac{1.20(11)}{\beta^2} + \mathcal{O}(\beta^{-3}), \tag{6.1}$$

where σ_0 denotes the zero-temperature string tension.

The relation between the temperature T and the extent of the shortest compact size of the lattice is $N_t = 1/T$, hence T can be varied by changing N_t, or the lattice spacing (by tuning β). We studied the system in the temperature range $0.8 \leq T/T_c \leq 1$. Very accurate estimates of T_c for various values of N_t were reported in ref. [109].

The Polyakov loop through a point of spatial coordinates $\vec{x}$ is defined as:

$$P(\vec{x}) = \frac{1}{2}\mathrm{Tr}\prod_{t=0}^{N_t} U_0(t, \vec{x}) \tag{6.2}$$

and the correlator of two Polyakov loops is

$$G(R) = \left\langle \sum_{\vec{x}} P(\vec{x})\, P\left(\vec{x} + R\hat{k}\right) \right\rangle, \tag{6.3}$$

where $\hat{k}$ denotes one of the two spatial directions, the sum ranges over all spatial coordinates $\vec{x}$, and the $\langle \dots \rangle$ average is normalised in such a way that the expectation value of the identity operator is 1.

6.1.1 Interquark potential at finite temperature

In a finite-temperature setting, the potential energy V associated with two static fundamental color sources V can be obtained as:

$$G(R) \equiv \exp\left[-\frac{V(R,N_t)}{T}\right] = \exp\left[-N_t V(R,N_t)\right]. \tag{6.4}$$

For large spatial separation R between the color sources, in the confining phase one expects $V(R,N_t)$ to be linearly rising as a function of R:

$$G(R) \simeq \exp\left[-\sigma(T) N_t R\right], \tag{6.5}$$

where $\sigma(T)$ denotes a temperature-dependent string tension, which decreases with T and vanishes at $T = T_c$.

The periodic boundary conditions for the gauge fields along the compactified Euclidean-time direction leads to the interpretation of the thermal deconfinement transition as the breaking of a symmetry based on the center of the gauge group, $\mathbb{Z}_2$ in this case [110, 111, 112]. In particular, in the high-temperature phase ($T > T_c$), the center symmetry gets spontaneously broken and the Polyakov loop develops a non-zero expectation value; accordingly, the free energy associated with a static color source is finite, i.e. the theory is in its deconfined phase.

6.2 Svetitsky-Yaffe mapping

The behaviour of the theory in the vicinity of the deconfinement transition is expected to be described in terms of an effective action obtained by integrating out the spacelike link variables and projecting each Polyakov loop to the center of the gauge group. Thus, this maps a $(d+1)$-dimensional lattice gauge theory to a d-dimensional spin model, having the center of the original gauge group as a global symmetry, as can be deduced from renormalisation-group arguments [17]. For the continuous deconfinement transition of the SU(2) lattice gauge theory in three dimensions one thus expects to arrive at the universality class of the order-disorder phase transition of the two-dimensional Ising model, which can be solved exactly [113]. In particular, the ordered (low-temperature)

phase of the spin model corresponds to the deconfined (high-temperature) phase of the original gauge theory. These are the phases in which the order parameters of the two theories have non-zero expectation values.

One also notes that, while the Polyakov loop of the gauge theory can be mapped to the spin operator, the plaquette corresponds to the energy operator of the spin model. Thus, in particular, thermal perturbations from the critical point in the original gauge theory, which are driven by the plaquette operator, are mapped to perturbations of the effective spin model driven by the energy operator. Finally, close to the deconfinement temperature, the spin-spin correlator of the Ising model is expected to share the behaviour of the Polyakov loop correlator of the lattice theory, which can be used to derive information on the EST that describes this correlation function.

6.3 The spin-spin correlator of the two-dimensional Ising model

The expression of the spin-spin correlator of the two-dimensional Ising model is known, and has the form of the determinant of a matrix of finite size – the size being related to the distance between the spins [114]. In the scaling limit, these determinants can be reduced to a simpler form [115], which takes two different forms in the two phases of the model.

- In the $R \ll \xi$ regime, the two-point spin correlator reads

$$\langle \sigma(0)\sigma(R)\rangle = \frac{k_s}{R^{\frac{1}{4}}}\left[1 + \frac{t}{2}\ln\left(\frac{e_{\mathrm{E}}^{\gamma}t}{8}\right) + \frac{1}{16}t^2 + \frac{1}{32}t^3\ln\left(\frac{e_{\mathrm{E}}^{\gamma}t}{8}\right) + O(t^4\ln^2 t)\right], \quad (6.6)$$

  $\gamma_{\mathrm{E}} = 0.57721\ldots$ being the Euler-Mascheroni constant, and k_s a non-universal constant.

- In the $R \gg \xi$ regime, the two-point spin correlator reads

$$\langle \sigma(0)\sigma(R)\rangle = k_l K_0(t) \quad (6.7)$$

  where, again, k_l is a non-universal constant, while K_0 is the modified Bessel function of order zero, which, for large values of its argument, behaves as:

$$K_0(t) \simeq \sqrt{\frac{\pi}{2t}}e^{-t}\left[1 + O\left(\frac{1}{t}\right)\right]. \quad (6.8)$$

Note that the short-distance expansion of eq. (6.6) can also be obtained using conformal perturbation theory [116]. The importance of this approach is that it does not rely on the integrability of the spin model, and holds for any pair of lattice gauge theory and spin model with a second-order deconfinement/symmetry-breaking transition.

6.4 Effective string theory predictions

The literature on the EST description of confining flux tubes is large; see, for instance, the reviews [102, 117, 118]. The EST approach assumes that confining flux tubes can be described as thin, vibrating strings [91, 92, 93, 94, 95], whose energy is (approximately) proportional to their length. This implies a linearly confining potential between color sources.

At finite temperatures, the EST model predicts [96, 97]:

$$\left\langle P(0)P^{\dagger}(R)\right\rangle = \sum_{n} |v_n(N_t)|^2 2R\left(\frac{E_n}{2\pi R}\right)^{\frac{D-1}{2}} K_{(D-3)/2}(E_n R), \tag{6.9}$$

where D denotes the number of spacetime dimensions ($D = 3$ in our case), E_n denote the energy levels of the string and $v_n(N_t)$ their amplitudes.

Note that, for large R, the dominant contribution in eq. (6.9) is the lowest energy level E_0 and, for $D = 3$, one obtains the same expression that characterises the long-distance behaviour of the spin-spin correlator in the two-dimensional Ising model.

In the Nambu-Gotō string model [91, 92], each configuration of the string world-sheet has a weight proportional to the area of the world-sheet surface. this model is the simplest Poincaré invariant EST, and is a direct generalisation of the relativistic action for a pointlike particle to a bosonic string. The action of this EST is:

$$S_{\mathrm{NG}} = \sigma_0 \int_{\Sigma} d^2\xi \sqrt{g}, \tag{6.10}$$

where $g \equiv \det g_{\alpha\beta}$ and $g_{\alpha\beta} = \partial_\alpha X_\mu \, \partial_\beta X^\mu$ is the induced metric on the reference world-sheet surface Σ, where we denote the world-sheet coordinates as $\xi \equiv (\xi^0, \xi^1)$. Note that the only free parameter appearing in the action is the string tension σ_0 (with energy dimension two).

The Nambu-Gotō action admits a low-energy expansion in the number of derivatives of the transverse degrees of freedom of the string. The first few terms in this expansion

are

$$S = \sigma_0 R N_t + \frac{\sigma_0}{2} \int d^2\xi \left[\partial_\alpha X_i \cdot \partial^\alpha X^i + \frac{1}{8} (\partial_\alpha X_i \cdot \partial^\alpha X^i)^2 - \frac{1}{4} (\partial_\alpha X_i \cdot \partial_\beta X^i)^2 + \dots \right]. \tag{6.11}$$

Interestingly, one can show that all the additional terms in the expansion of eq. (6.11) beyond the Gaußian one yield an integrable, irrelevant perturbation of the Gaußian term [103]. This allows one to write the partition function of the model can be written explicitly; for the EST describing the two-point Polyakov-loop correlation function, the expression in D spacetime dimensions is

$$G(R) = \sum_{n=0}^{\infty} w_n \frac{2R\sigma_0 N_t}{E_n} \left(\frac{\pi}{\sigma_0} \right)^{\frac{D-2}{2}} \left(\frac{E_n}{2\pi R} \right)^{\frac{D-1}{2}} K_{(D-3)/2}(E_n R), \tag{6.12}$$

where the energy levels E_n are

$$E_n = \sigma_0 N_t \sqrt{1 + \frac{8\pi}{\sigma_0 N_t^2} \left(n - \frac{D-2}{24} \right)}. \tag{6.13}$$

and the weights w_n can be obtained from the expansion in powers of q of the Dedekind function that describes the large-R limit of eq. (6.12):

$$\left(\prod_{r=1}^{\infty} \frac{1}{1-q^r} \right)^{D-2} = \sum_{k=0}^{\infty} w_k q^k. \tag{6.14}$$

In $D = 3$ dimensions, w_k reduces to the number of partitions of the integer k.

For the effective Nambu-Gotō string we have an exact expression both for the $v(N_t)$ amplitudes and for the energy levels E_n. The lowest energy level reads

$$E_0 = \sigma_0 N_t \sqrt{1 - \frac{\pi}{3\sigma_0 N_t^2}} = \sigma(T) N_t, \tag{6.15}$$

where the "temperature-dependent string tension" is

$$\sigma(T) \equiv \sigma_0 \sqrt{1 - \frac{\pi}{3\sigma_0 N_t^2}}. \tag{6.16}$$

E_0 is the inverse of the correlation length, thus the Nambu-Gotō EST predicts the

critical temperature [119, 120]

$$\frac{T_{c,NG}}{\sqrt{\sigma_0}} = \sqrt{\frac{3}{\pi(D-2)}} \tag{6.17}$$

and the critical index $\nu = 1/2$. This prediction, however, is inconsistent with the Svetitsky-Yaffe correspondence, as the two-dimensional Ising-model value is $\nu = 1$. This suggests that the correct EST describing the gauge theory must include terms beyond the Nambu-Gotō approximation: these "bulk terms" and "boundary terms".

Bulk terms can be studied by assuming the most general form for the EST:

$$S = S_{\text{cl}} + \frac{\sigma_0}{2} \int d^2\xi \left[\partial_\alpha X_i \cdot \partial^\alpha X^i + c_2 (\partial_\alpha X_i \cdot \partial^\alpha X^i)^2 + c_3 (\partial_\alpha X_i \cdot \partial_\beta X^i)^2 + \dots \right]; \tag{6.18}$$

then the c_i coefficients can be fixed by imposing the Poincaré invariance of the gauge theory in the target space [96, 97, 98, 99, 100, 101]. In $D = 3$ dimensions, one then finds that the first few terms of the expansion coincide with those that are obtained from the expansion of the Nambu-Gotō action, while the first correction appears at order $1/N_t^7$ and can be written as [104, 105]

$$-\frac{32\pi^6}{225} \frac{\gamma_3}{\sigma^3 N_t^7} \tag{6.19}$$

where γ_3 is constrained to be larger than $-\frac{1}{768}$. This parameter encodes information on the EST.

Boundary corrections to the EST, on the other hand, describe possible interactions of the colour flux tube with the sources at its ends. At low temperatures the boundary correction behaves as $1/R^4$ and is the leading correction to the Nambu-Gotō EST. As for the bulk terms, Poincaré invariance also constrains the boundary terms: the leading correction compatible with the spacetime symmetries of the gauge theory can be shown to be [121]

$$b_2 \int d\xi_0 \left[\frac{\partial_0\partial_1 X \cdot \partial_0\partial_1 X}{1 + \partial_1 X \cdot \partial_1 X} - \frac{(\partial_0\partial_1 X \cdot \partial_1 X)^2}{(1 + \partial_1 X \cdot \partial_1 X)^2} \right], \tag{6.20}$$

with a non-universal coefficient b_2. The dominant term in the expansion of eq. (6.20) is

$$S_{b,2}^{(1)} = b_2 \int d\xi_0 (\partial_0\partial_1 X)^2 \tag{6.21}$$

and in in ref. [122] it was shown that:

$$\langle S^{(1)}_{b,2} \rangle = -b_2 \frac{\pi^3 N_t}{60 R^4} E_4(e^{-\frac{\pi N_t}{R}}) \tag{6.22}$$

where E_4 is the fourth-order Eisenstein series:

$$E_4(q) \equiv 1 + \frac{2}{\zeta(-3)} \sum_{n=1}^{\infty} \frac{n^3 q^n}{1-q^n} \tag{6.23}$$

while $\zeta(s)$ denotes the Riemann ζ function.

At low temperatures, eq. (6.22) induces a $1/R^4$ contribution to the interquark potential, while at high temperatures regime, the boundary correction leads to

$$\langle S^{(1)}_{b,2} \rangle = -b_2 \frac{4\pi^3}{15 N_t^3} E_4\left(e^{-\frac{4\pi R}{N_t}}\right), \tag{6.24}$$

which does not contribute to the temperature-dependent string tension.

6.5 Simulation setting and results

In this section we present the results of a our Monte Carlo simulations, obtained with the parallel C++ code developed in refs. [123, 124]. The gauge field configurations are updated using a local heat-bath [125, 126] and overrelaxation [79] algorithms.

We first tested the Svetitsky-Yaffe mapping, then we studied in detail the corrections to the Nambu-Gotō action.

6.5.1 Test of the Svetitsky-Yaffe conjecture

To test the Svetitsky-Yaffe mapping, we run simulations at $N_t = 6$, 7, 8, and 9 at various temperatures $T/T_c \leq 1$, see tab. 6.1.

$N_t \times N_s^2$	β	T/T_c	n_{conf}
9×96^2	11.3048	0.80	2.5×10^5
	11.72873	0.83	2.5×10^5
9×160^2	12.15266	0.86	2.5×10^5
7×96^2	9.228023	0.83	2.5×10^5
	9.561566	0.86	2.5×10^5

$N_t \times N_s^2$	β	T/T_c	n_{conf}
8×96^2	10.10736	0.80	2.5×10^5
	10.486386	0.83	2.5×10^5
	10.865412	0.86	2.5×10^5
6×96^2	8.258494	0.86	2.5×10^5
	8.546581	0.89	2.5×10^5

Table 6.1: Parameters of the first set of simulations.

In fig. 6.1 we show data at $T = 0.62 T_c$: the plot displays the Polyakov loop cor-

relator against the separation R between the colour sources (in units of the inverse temperature). The correlator is described well by a single exponential. Apart from the points at values of R of the order of a only few lattice spacings (which are expected to be affected by non-negligible discretisation effects), the bending of the data from short to intermediate distances, before the onset of the purely exponential decay, reveals the effective string corrections.

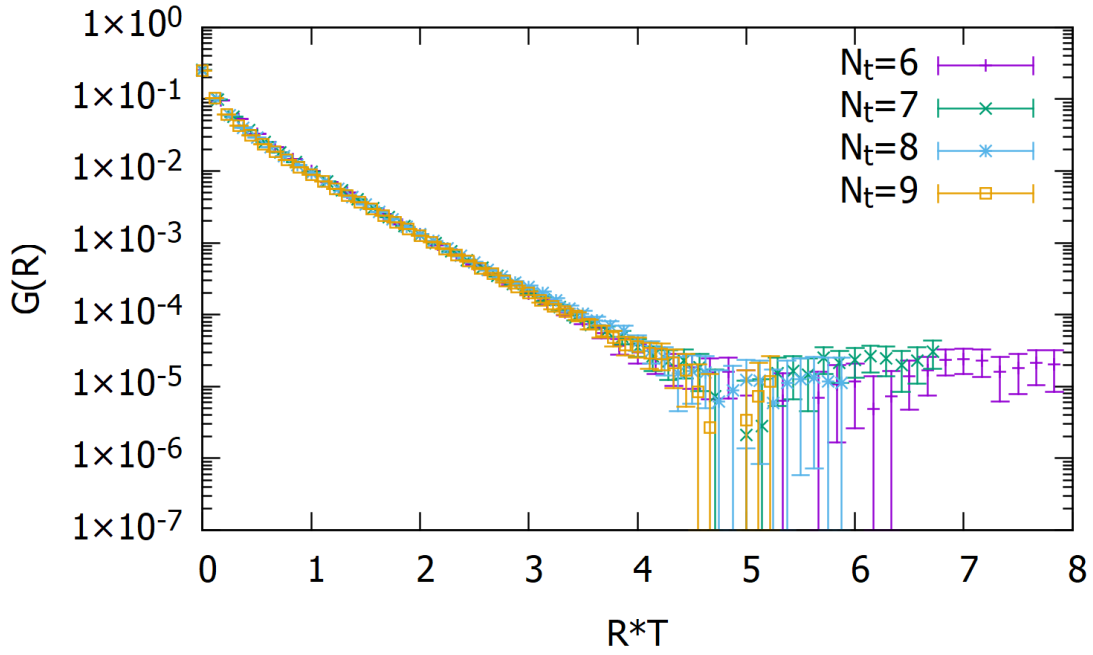

Figure 6.1: Polyakov-loop correlator $G(R)$ obtained for N_t values from 6 to 9 at the temperature $T = 0.62T_c$.

We tested the Svetitsky-Yaffe conjecture by fitting our data to the Ising-model predictions for the spin-spin correlator in eq. (6.6) and in eq. (6.7). The long-distance fits were performed with the following function

$$G(R) = k_l \left[K_0 \left(\frac{R}{\xi} \right) + K_0 \left(\frac{N_s - R}{\xi} \right) \right] \tag{6.25}$$

to account for the firs periodic copy of the lattice. Note that, like eq. (6.7), eq. (6.25) has only k_l and ξ as free parameters. The results of the fits are listed in tab. 6.2 and shown in fig. 6.2 and in fig. 6.3.

Table 6.2 shows that both at short and at long distances the fits yield good values of the reduced χ^2.

The results of the fits are shown in fig. 6.3.

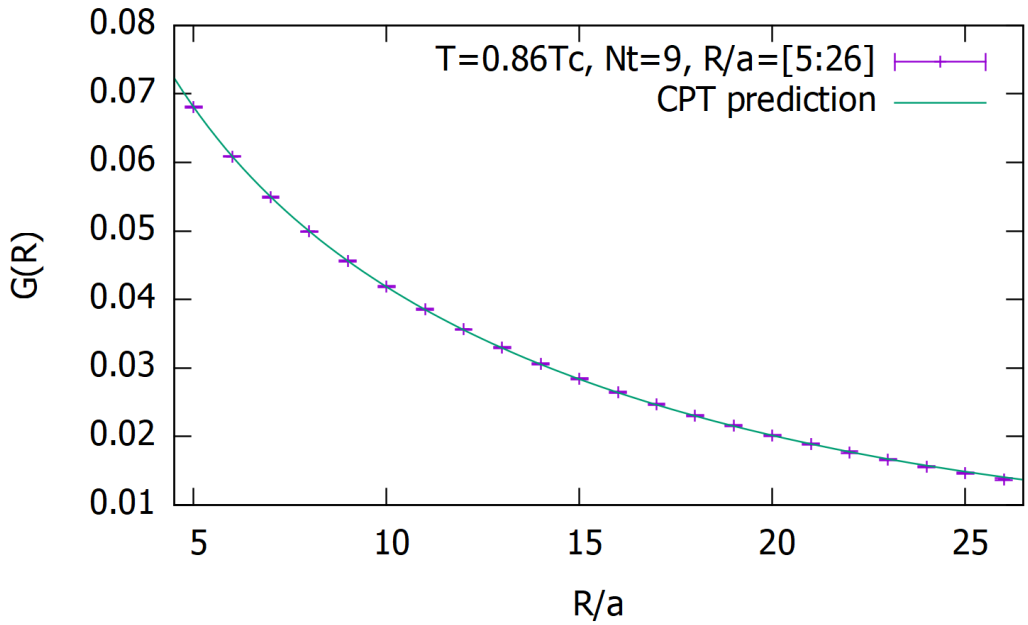

Figure 6.2: Fit of the simulation results at $N_t = 9$, $\beta = 12.15266$, $T/T_c = 0.86$ to the short-distance approximation of the spin-spin Ising correlator in eq. (6.6).

	$R_{\min}$	$R_{\max}$	amplitude	ξ	χ^2_{red}
eq. (6.6)	5	26	$k_s = 0.1534(2)$	22.05(6)	0.92
eq. (6.25)	6	47	$k_l = 0.0415(4)$	22.13(17)	0.33

Table 6.2: Results of the fits of the Polyakov loop correlator for $N_t = 9$, $\beta = 12.15266$ (corresponding to $T/T_c = 0.86$) to the short- and long-distance behaviours predicted according to the Svetitsky-Yaffe conjecture.

6.5.2 Effective string theory corrections to the Nambu-Gotō approximation

To study the EST corrections beyond the Nambu-Gotō approximation we analysed the behaviour of the ground-state energy E_0 as a function of the temperature, approaching the deconfinement transition temperature from below. This was done with the sets of simulations described in tab. 6.4, in tab. 6.5, and in tab. 6.6. For each of these ensembles, the value of E_0 was computed as the inverse of the correlation length ξ, obtaining the results summarised in tab. 6.7, in tab. 6.8, and in tab. 6.9.

The predicted critical index for the correlation length $\xi = 1/E_0$ is $\nu = 1/2$: this is incompatible with the one expected from the Svetitsky-Yaffe conjecture, which is $\nu = 1$, namely:

$$\xi \sim \left(1 - \frac{T}{T_c}\right)^{-1}, \tag{6.26}$$

N_t		T/T_c	R_{min}	R_{max}	amplitude	ξ	χ^2_{red}
6	eq. (6.6)	0.86	5	16	$k_s = 0.1630(4)$	14.13(5)	1.10
	eq. (6.25)	0.86	6	47	$k_l = 0.0491(5)$	14.25(15)	0.09
	eq. (6.6)	0.89	5	26	$k_s = 0.1660(4)$	18.65(7)	1.30
	eq. (6.25)	0.89	6	47	$k_l = 0.0473(6)$	18.40(24)	0.33
7	eq. (6.6)	0.83	5	15	$k_s = 0.1562(4)$	13.37(5)	1.15
	eq. (6.25)	0.83	6	47	$k_l = 0.04716(24)$	13.62(7)	0.33
	eq. (6.6)	0.86	5	22	$k_s = 0.1587(3)$	17.03(5)	0.83
	eq. (6.25)	0.86	6	47	$k_l = 0.0458(3)$	17.03(10)	0.19
8	eq. (6.6)	0.80	5	15	$k_s = 0.1497(4)$	12.75(5)	1.55
	eq. (6.25)	0.80	6	47	$k_l = 0.0454(7)$	13.07(17)	0.13
	eq. (6.6)	0.83	5	20	$k_s = 0.1526(4)$	15.65(6)	1.35
	eq. (6.25)	0.83	6	47	$k_l = 0.0445(4)$	15.86(13)	0.09
	eq. (6.6)	0.86	6	32	$k_s = 0.1543(3)$	20.36(7)	0.96
	eq. (6.25)	0.86	6	47	$k_l = 0.0429(4)$	20.05(20)	0.05
9	eq. (6.6)	0.80	5	17	$k_s = 0.1462(3)$	14.47(4)	0.75
	eq. (6.25)	0.80	6	47	$k_l = 0.0432(4)$	14.74(13)	0.16
	eq. (6.6)	0.83	5	25	$k_s = 0.1492(3)$	17.81(7)	1.01
	eq. (6.25)	0.83	6	47	$k_l = 0.0422(4)$	17.96(18)	0.23
	eq. (6.6)	0.86	5	26	$k_s = 0.1534(2)$	22.05(6)	0.92
	eq. (6.25)	0.86	6	47	$k_l = 0.0415(4)$	22.13(17)	0.33

Table 6.3: Fits of the Polyakov-loop correlator to the short- and long-distance behaviour expected from the Svetitsky-Yaffe mapping for different values of N_t and β.

or, alternatively:

$$\xi \sim \left(1 - \frac{N_{t,c}}{N_t}\right)^{-1}, \tag{6.27}$$

which corresponds to ground-state energy close to the deconfinement transition:

$$E_0 \sim 1 - \frac{N_{t,c}}{N_t}. \tag{6.28}$$

Thus, the dependence of E_0 on the temperature can be used to study the corrections to the Nambu-Gotō approximation of the EST. In addition, we note that the bootstrap calculations presented in refs. [104, 105] suggest

$$E_0(N_t) = N_t\sigma_0\sqrt{1 - \frac{\pi}{3N_t^2\sigma_0}} - \frac{32\pi^6\gamma_3}{225\sigma_0^3 N_t^7}. \tag{6.29}$$

We first tried to fit our lattice results data with a form based on the Nambu-Gotō model (with $\nu = 1/2$) and with one derived from the Ising model ($\nu = 1$). Neither fit describes the data well, as shown in fig. 6.4, in fig. 6.5, and in fig. 6.6: the Nambu-

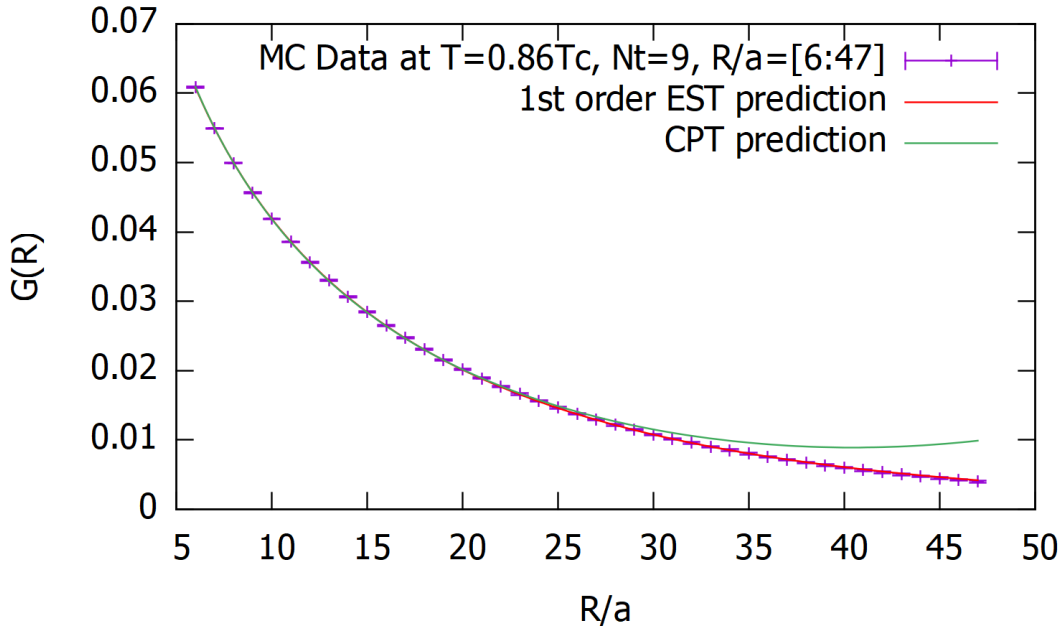

Figure 6.3: Fit of the results of our numerical simulations at $N_t = 9$, $\beta = 12.15266$, $T/T_c = 0.86$ using the short- and long-distance approximations of the spin-spin Ising correlator given in eq. (6.6) and in eq. (6.25).

β	N_t	N_s	T/T_c	n_{conf}
9	6	160	0.935	2.0×10^5
	7	96	0.801	2.0×10^5
	8	96	0.701	2.0×10^5
	9	96	0.623	2.0×10^5
	10	96	0.561	2.0×10^5
	11	96	0.510	2.0×10^5
	12	96	0.468	2.0×10^5

Table 6.4: Parameters of the simulations at $\beta = 9$.

Gotō curve fits the data well at low temperatures, but not close to the deconfinement transition. Conversely, the linear fit describes well the results close to the critical point, albeit only for the first few values of N_t. This is consistent with the expected low-energy universality, which suggests that the correct behaviour at short distances should include a $1/N_t^7$ correction to the Nambu-Gotō approximation. One can then assume the following form for the N_t dependence of the ground state energy:

$$E_0(N_t) = \text{Taylor}_4(E_0) + \frac{k_4}{(\sigma_0)^3 N_t^7}, \tag{6.30}$$

β	N_t	N_s	T/T_c	$n_{\rm conf}$
12.15266	8	240	0.960	2.0×10^5
	9	160	0.853	2.0×10^5
	10	96	0.768	2.0×10^5
	11	96	0.698	2.0×10^5
	12	96	0.640	2.0×10^5
	13	96	0.591	2.0×10^5
	14	96	0.549	2.0×10^5

Table 6.5: Parameters of the simulations at $\beta = 12.15266$.

β	N_t	N_s	T/T_c	$n_{\rm conf}$
13.42445	9	240	0.947	2.0×10^5
	10	160	0.852	2.0×10^5
	11	160	0.775	2.0×10^5
	12	96	0.710	2.0×10^5
	13	96	0.655	2.0×10^5
	14	96	0.609	2.0×10^5
	15	96	0.568	2.0×10^5

Table 6.6: Parameters of the simulations at $\beta = 13.42445$.

with

$$\mathrm{Taylor}_4(E_0) \equiv \sigma_0 N_t - \frac{\pi}{6N_t} - \frac{\pi^2}{72(\sigma_0)N_t^3} - \frac{\pi^3}{432(\sigma_0)^2 N_t^5} - \frac{5\pi^4}{10368(\sigma_0)^3 N_t^7}, \qquad (6.31)$$

where the Taylor expansion is known, and the only free parameters of the fit are σ_0 (the zero-temperature string tension) σ_0 and k_4.

The fits have good reduced χ^2 values, see tab. 6.10, and fig. 6.7, fig. 6.8 and fig. 6.9. We also note that the quality of the fits improves approaching the continuum limit, and the results for σ_0 are consistent with those from the literature [127, 108].

We also checked that our analysis yields values of k_4 that are consistent with each other (within their uncertainties), since the scale dependence of this coefficient is already accounted for by the $1/\sigma_0^3$ normalisation in eq. (6.30): see tab. 6.10 and tab. 6.11. Our final result for the k_4 coefficient is a weighted average of the three values from tab. 6.10: $k_4 = 0.050(8)$, from which one obtains

$$\gamma_3 = -\frac{225}{32\pi^6} k_4 = -0.00037(6). \qquad (6.32)$$

This value is consistent with the bound $\gamma_3 \geq -\frac{1}{768} \simeq -0.0013$ derived in refs. [104, 105].

Note that the term appearing with the γ_3 coefficient is only the first term of an

N_t	$R_{\min}$	$R_{\max}$	k_l	E_0	$\chi^2_{\rm red}$
6	7	47	0.0417(6)	0.0294(5)	0.07
7	7	47	0.0495(9)	0.0871(13)	0.58
8	8	47	0.0475(15)	0.1250(25)	0.56
9	8	47	0.0501(15)	0.1691(36)	0.30
10	9	47	0.0432(33)	0.1941(63)	2.00
11	9	47	0.0469(41)	0.2381(80)	0.72
12	9	47	0.0392(32)	0.2581(69)	0.09

Table 6.7: Numerical estimates for E_0 at different values of N_t and for $\beta = 9$.

N_t	$R_{\min}$	$R_{\max}$	k_l	E_0	$\chi^2_{\rm red}$
8	8	47	0.0338(10)	0.0135(5)	0.36
9	10	47	0.0416(4)	0.0452(3)	0.33
10	9	47	0.0416(13)	0.0695(17)	0.45
11	10	47	0.0423(16)	0.0922(22)	0.35
12	10	47	0.0414(20)	0.1132(32)	0.13
13	11	47	0.0408(26)	0.1334(42)	0.25
14	11	47	0.0355(16)	0.1440(30)	0.18

Table 6.8: Estimates for E_0 at different N_t values and for $\beta = 12.15266$.

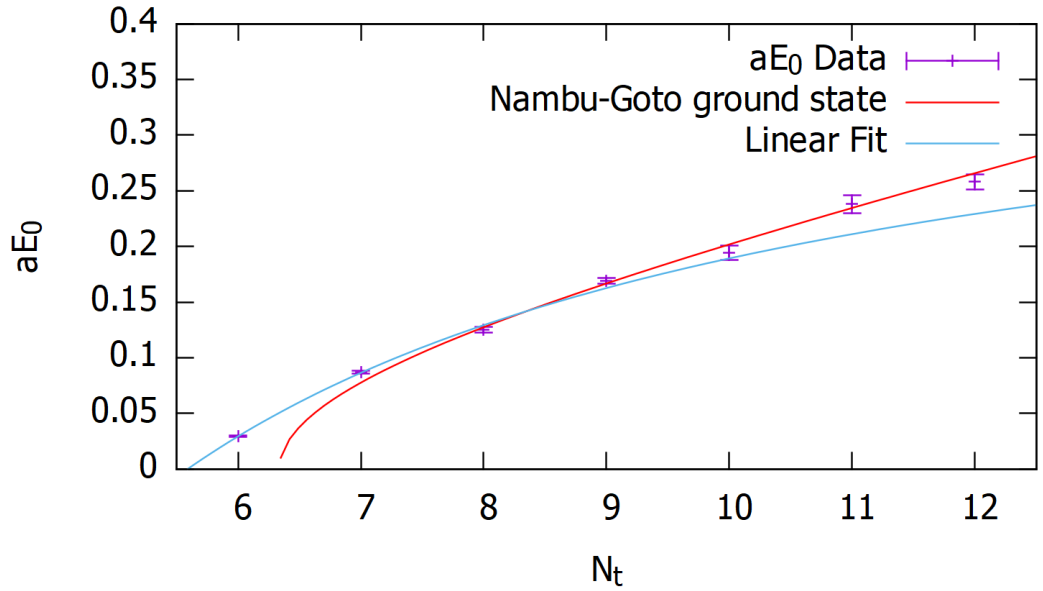

Figure 6.4: Fits of our lattice data for E_0 at $\beta = 9$ to the expectation for the string ground state (red line) and according to eq. (6.28) (blue curve).

infinite series of higher-order corrections to the Nambu-Gotō action. The statistical precision of our lattice results is not sufficient to obtain conclusive information about the subleading terms.

N_t	$R_{\rm min}$	$R_{\rm max}$	k_l	E_0	$\chi^2_{\rm red}$
9	9	47	0.0338(13)	0.0151(7)	0.32
10	11	47	0.0391(6)	0.0401(5)	0.06
11	12	47	0.0407(8)	0.0619(8)	0.05
12	11	47	0.0387(7)	0.0777(9)	0.52
13	12	47	0.0399(12)	0.0979(16)	0.06
14	12	47	0.0390(13)	0.1135(20)	0.19
15	12	47	0.0359(17)	0.1254(27)	0.25

Table 6.9: Estimates for E_0 at various values of N_t and for $\beta = 13.42445$.

β	$N_{t,\rm min}$	$N_{t,\rm max}$	k_4	σ_0	$\chi^2_{\rm red}$	literature
9	6	12	0.040(8)	0.02603(19)	1.60	0.02583(3)
12.15266	8	14	0.054(5)	0.01366(5)	0.89	0.01371(29)
13.42445	9	15	0.053(8)	0.01104(5)	1.33	0.01108(23)

Table 6.10: Fits of our numerical data to eq. (6.30). The last column shows the values of σ_0 reported in ref. [127] for $\beta = 9$, and in ref. [108] for $\beta = 12.15266$ and for $\beta = 13.42445$.

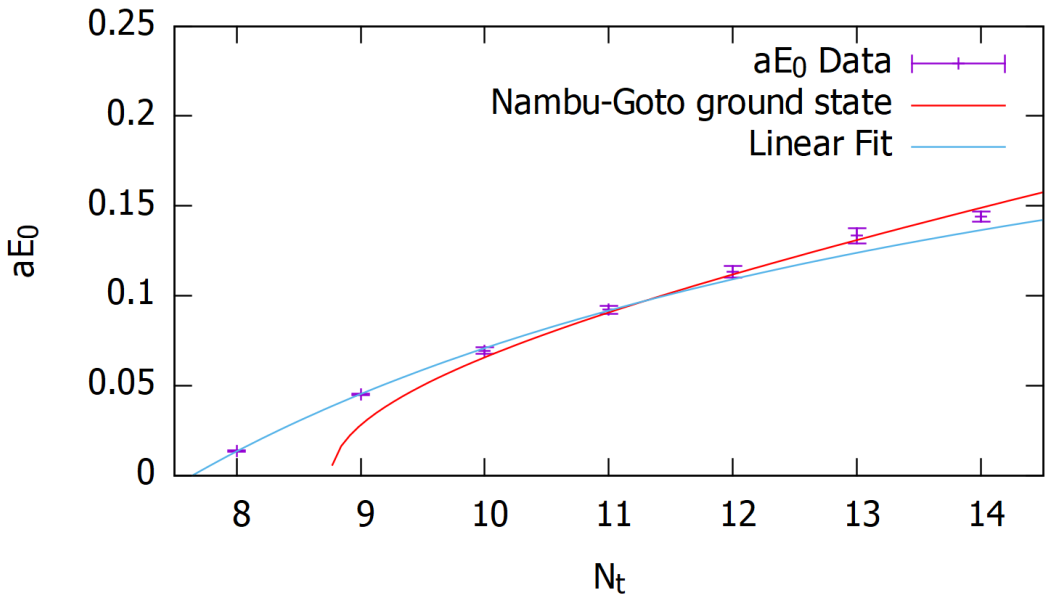

Figure 6.5: Same as in fig. 6.4, but for $\beta = 12.15266$.

Finally, it is interesting to compare our results with those that were reported in ref. [128] at $\beta = 16.0$: the values for E_0 reported in that work can be fitted to eq. (6.30) obtaining a k_4 value compatible with the one that we found at smaller values of β. Similarly, our results for γ_3 can be compared with those derived in refs. [129, 130, 131] for the SU(6) Yang-Mills theory in $D = 3$ from the lattice data of ref. [132], which was

β	$N_{t,\min}$	$N_{t,\max}$	k_4	$\chi^2_{\rm red}$
9	6	12	0.048(3)	1.62
12.15266	8	14	0.049(2)	0.89
13.42445	9	15	0.048(4)	1.24

Table 6.11: Fits of the lattice data to eq. (6.30) with the values for σ_0 from the literature.

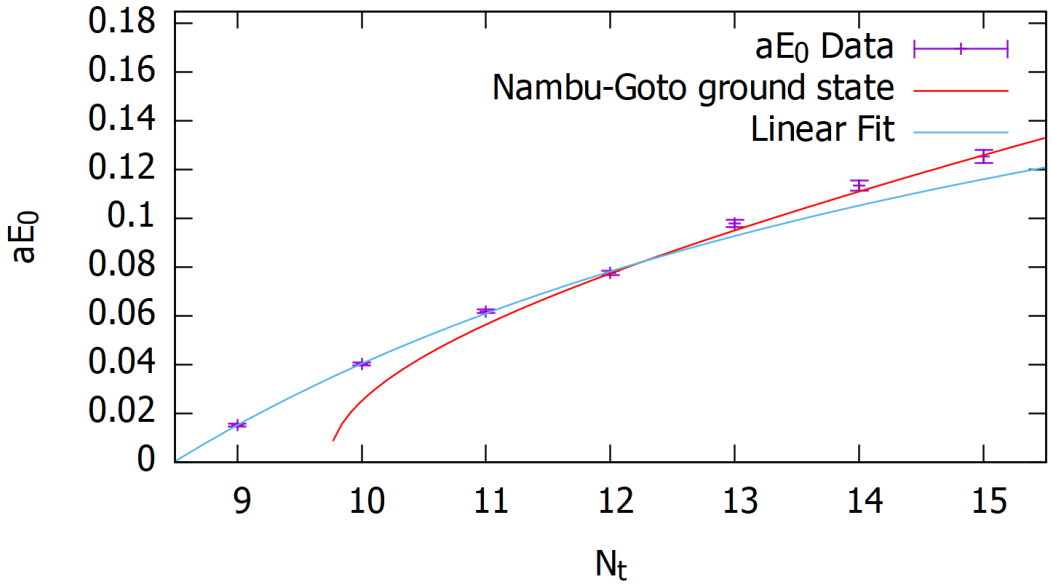

Figure 6.6: Same as in fig. 6.4, but for $\beta = 13.42445$.

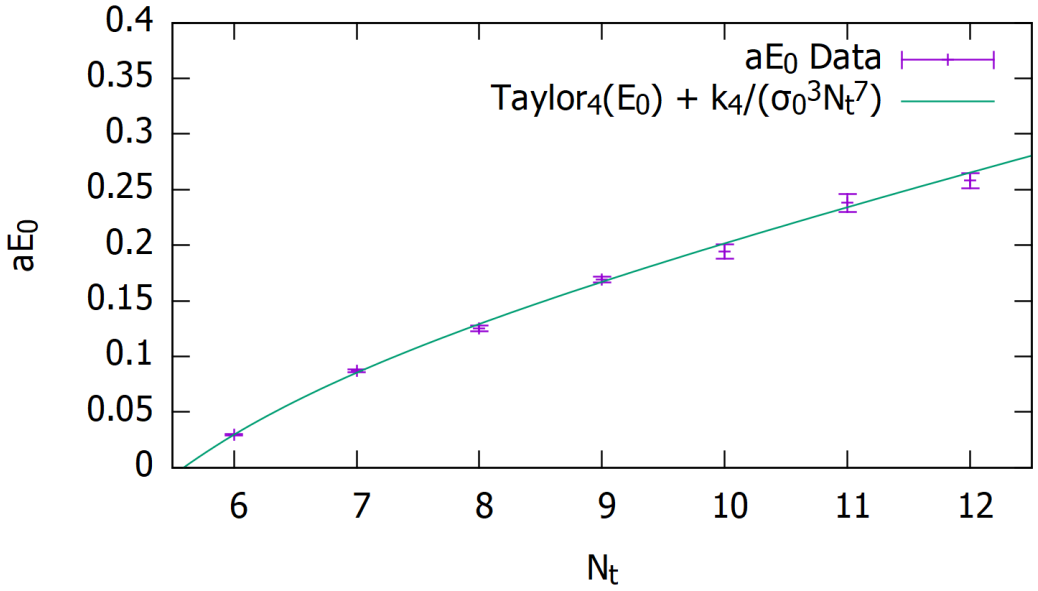

Figure 6.7: Fit of our lattice results for the ground-state energy at $\beta = 9$ to eq. (6.30).

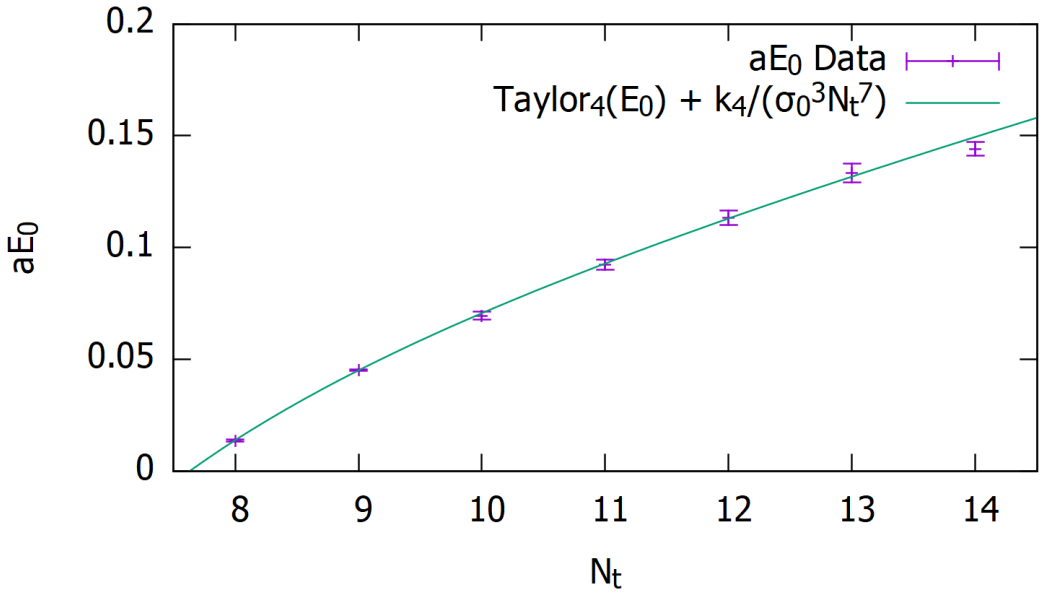

Figure 6.8: Same as in fig. 6.7, but for $\beta = 12.15266$.

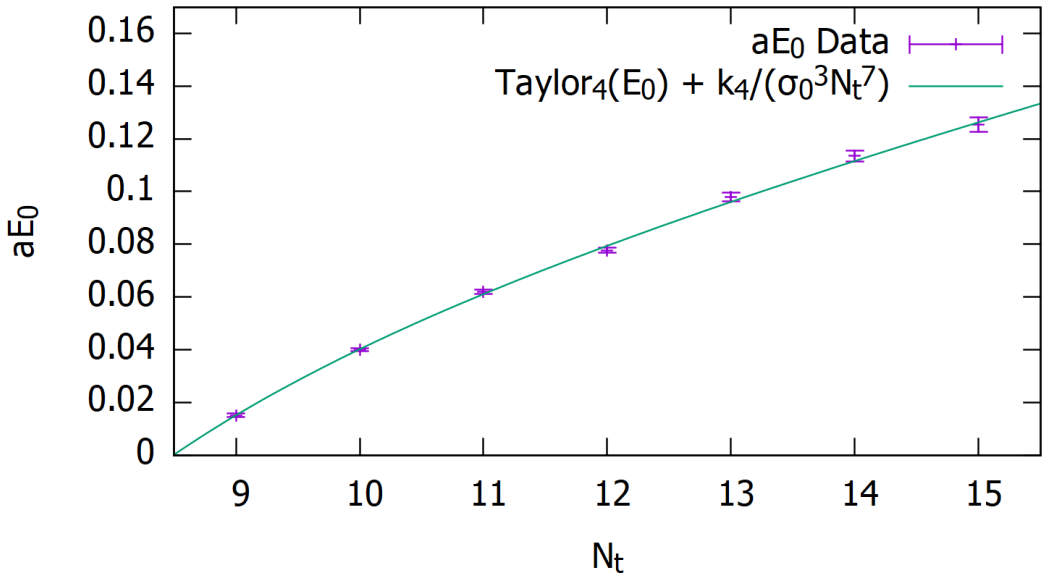

Figure 6.9: Same as in fig. 6.7, but for $\beta = 13.42445$.

of similar magnitude but had the opposite sign. This dependence of the coefficient on the gauge group suggests that, at this level of precision, the EST is not universal, and encodes, as expected, specific properties of the underlying Yang-Mills theory.

6.6 Conclusions

In this chapter we discussed a lattice study of the Polyakov-loop correlation function in the SU(2) lattice gauge theory in three dimensions, that was reported in ref. [3]. We compared our simulation results at finite temperatures, close to (and below) the deconfinement transition, with EST predictions and with expectations from the Svetitsky-Yaffe conjecture. We found good agreement between our lattice results and the form of correlator predicted in the Ising model close to the deconfinement temperature. We also obtained precise values for the ground-state energy E_0 of the effective string describing this gauge theory, from which we could study the deviations from the Nambu-Gotō approximation of the EST.

It would be interesting to explore the same type of contribution to the EST describing gauge theories in four dimensions, as analogous predictions can be formulated for the low-energy dynamics of quantum chromodynamics [133].

Chapter 7

Spectral functions and the inverse problem

Hadronic spectral functions are important quantities as they encode a lot of information about non-perturbative QCD. From their knowledge it is possible to extract all the information required to study phenomena like hadron scattering, hadron interaction and generally hadron's properties at zero and non-zero temperatures. Spectral functions appear naturally in the standard QFT description of correlation functions when using the Källén-Lehmann representation (eq. 2.30). For many years now, there has been a growing interest in trying to extract spectral functions from Euclidean lattice correlation functions, with the first attempt dating back to the mid eighties [134]. However, as will be discussed in this chapter, performing this task is highly non-trivial, leading to different approaches to the problem. We will start discussing spectral functions at finite temperature in order to introduce the relevant notation and draw explicitly the relations among spectral functions, Euclidean correlation functions and Minkowski retarded correlation functions. For the sake of notational clarity for the next two chapters we will replace $n_t, \boldsymbol{n}_i$ with $t, \boldsymbol{x}$ and we will leave the relations $t = an_t$, $\boldsymbol{x}_i = a\boldsymbol{n}_i$ implied. However, we will keep explicit the difference between Minkowski time t and Euclidean time τ.

7.1 Finite temperature spectral functions and correlation functions

An important feature of QFT is the possibility to organise field operators and their products according to their space-time position. In particular, for two generic field

operators ϕ^A, ϕ^B, we can define the time-ordering operation as

$$T\Big(\phi^A(t_1)\phi^B(t_2)\Big) = \theta(t_1 - t_2)\phi^A(t_1)\phi^B(t_2) \pm \theta(t_2 - t_1)\phi^B(t_2)\phi^A(t_1), \tag{7.1}$$

where θ denotes the Heaviside step-function. The sign in front of the second term in the right-hand-side of the equation 7.1 depends on whether the field operators represent bosons $(+)$ or fermions $(-)$.

The vacuum expectation value of time ordered operators can be used to construct the time-ordered correlator in Minkowski space-time by performing the integral transform

$$\mathcal{G}_T(\omega) = \int_{-\infty}^{\infty} dt\ e^{i\omega t}\langle 0|T\Big(\phi^A(t)\phi^B\Big)|0\rangle, \tag{7.2}$$

which is familiar from standard QFT time-dependent perturbation theory.

In the case in which we have bosonic field operators, the expectation value of the commutator coming from the time-ordering operation vanishes outside the Minkowski light-cone for causal quantum field theories. For this reason, it is convenient to define the causal or retarded correlation function in terms of the commutator of field operators

$$\mathcal{G}_R(\omega) = i\int_{0}^{\infty} dt\ e^{-\omega t}\langle 0|[\phi^A(t), \phi^B(0)]|0\rangle. \tag{7.3}$$

Looking at the form of the time-ordered correlator (eq. 7.2) and the retarded correlator (eq. 7.3), it is clear that they are related depending on whether the frequency ω is positive or negative

$$\mathcal{G}_R(\omega) = i\mathcal{G}_T(\omega) \text{ for } \operatorname{Re}\omega > 0, \qquad \mathcal{G}_R(\omega) = \Big(i\mathcal{G}_T^\dagger\Big)^* \text{ for } \operatorname{Re}\omega < 0. \tag{7.4}$$

From this considerations, we highlight that the integral transform in the definition of the retarded correlator (eq. 7.3) is performed over the positive half-axis and $\mathcal{G}_R$ is analytic in the half complex plane $\operatorname{Im}\omega > 0$.

Vacuum expectation values of Minkowski space-time Wightman functions at finite temperature are defined in terms of the trace over the equilibrium density matrix (eq. 2.10)

$$\mathcal{G}_M(t) = \langle 0|\phi^A(t)\phi^B(0)|0\rangle \equiv \operatorname{Tr}\{\hat{\rho}\phi^A(t)\phi^B(0)\}, \tag{7.5}$$

and like $\hat{\rho}$ enjoy time-translation invariance and reality condition

$$\mathcal{G}_M(t)\theta(t) = \mathcal{G}_M(-t)\theta(-t), \qquad \mathcal{G}_M^\dagger(t)\theta(t) = \mathcal{G}_M(-t^*)^*\theta(t), \tag{7.6}$$

where $\theta(t)$ enforces the correct time ordering. Furthermore, thermal Wightman func-

tions respect the Kubo-Martin-Schwinger (KMS) condition, which guarantees periodicity in Euclidean time

$$\mathcal{G}_M(t)\theta(t) = \mathcal{G}_M(-t - i\beta)\theta(t), \tag{7.7}$$

where $\beta = 1/T$.

Now, as already discussed in sections 3.3 and 2.2, the Osterwalder-Schrader theorem [13] guarantees the analytic continuation between the Euclidean correlation functions (eq. 7.9) and the Minkowski Wightman function (eq. 7.5)

$$G(\tau) = \mathcal{G}_M(-i\tau). \tag{7.8}$$

Then, it is possible to write the Euclidean correlation function in frequency space in terms of the Fourier series

$$G_E(\tau) = T \sum_{l \in \mathbb{Z}} G_E^{(l)}(\omega) e^{-i\omega_l \tau}, \tag{7.9}$$

where ω_l are the Matsubara frequencies, $\omega_l = 2\pi l T$ for boson fields and $\omega_l = (2l+1)\pi T$ and $G^{(l)}(\omega)$ are the Fourier coefficients defined as the integral transform

$$G_E^{(l)}(\omega) = \int_0^\beta dt\ e^{i\omega\tau} G_E^{(l)}(\tau). \tag{7.10}$$

Finally, one can define the thermal spectral function as the Fourier transform of the thermal Wightman function of the commutator $[\phi^A(t), \phi^B(0)]$

$$\rho(\omega) = \frac{1}{2\pi i} \int_{-\infty}^{\infty} dt\ e^{-i\omega t} \langle 0|[\phi^A(t), \phi^B(0)]|0\rangle. \tag{7.11}$$

Once again, we notice the similarity between the spectral function $\rho(\omega)$ (eq. 7.11) and the retarded correlation function (eq. 7.3). Using time-translation and the reality condition of equation 7.6, one can show that the thermal spectral function can be written as

$$\rho(\omega) = \frac{1}{2\pi i} \Big[\mathcal{G}_R(\omega) - \mathcal{G}^\dagger(\omega)^* \Big]. \tag{7.12}$$

In particular, if one chooses the field operators to be a creation and annihilation field operators, that is choosing $\phi^A(t) = \phi(t)$ and $\phi^B(0) = \phi^\dagger(0)$, then the spectral function is equal to the imaginary part of the retarded correlator (eq. 7.3)

$$\rho(\omega) = \frac{1}{\pi} \operatorname{Im} \mathcal{G}_R(\omega). \tag{7.13}$$

7.1.1 Spectral representation and correlators

All the functions defined above are useful in order to draw a connection between Euclidean correlation (eq. 7.9) functions which we can compute on the lattice and spectral functions (eq. 7.11). In this subsection, following ref. [135], we start by writing the Minkowski (eq. 7.5) and Euclidean correlation function (eq.7.9) in the spectral representation inserting a complete set of states between the two field operators

$$\mathcal{G}_M(t) = \frac{2i}{Z}\sum_{n,m}|\phi_{nm}|^2 e^{\beta\frac{(E_n+E_m)}{2}} e^{-iE_{nm}t}\sinh\Big(\frac{\beta E_{nm}}{2}\Big), \tag{7.14}$$

$$G_E(\tau) = \frac{1}{Z}\sum_{n,m}|\phi_{nm}|^2 e^{-\beta E_m} e^{-E_{nm}\tau}, \tag{7.15}$$

where we used the definition of correlators with the field operators being a pair of creation and annihilation operators and we introduced $\phi_{nm} = \langle n|\phi|m\rangle$, $E_{nm} = E_n - E_m$.

From equation 7.14, one can write also the spectral representation of the retarded correlator (eq. 7.3)

$$\mathcal{G}_R(\omega) = \frac{2}{Z}\sum_{n,m}\frac{-|\phi_{nm}|^2}{\omega - E_{nm}} e^{-\beta\frac{(E_n+E_m)}{2}}\sinh\Big(\frac{\beta E_{nm}}{2}\Big), \tag{7.16}$$

where we used

$$\int_0^\infty dt e^{i\omega t} e^{-iE_{nm}t} = \frac{i}{\omega - E_{nm}}. \tag{7.17}$$

The spectral function can then be obtained from the imaginary part of the retarded correlator, using equation 7.13. This is done by evaluating the pole in the upper half-plane, where the retarded correlator is analytic

$$\mathrm{Im}\,\mathcal{G}_R(\omega + i\varepsilon) \propto \mathrm{Im}\,\frac{-1}{(\omega + i\varepsilon) - E_{nm}} = \frac{-\varepsilon}{(\omega - E_{nm})^2 + \varepsilon^2} \tag{7.18}$$

In the upper-half plane, one can define the Poisson kernel as

$$\delta_\varepsilon(\omega) = \frac{1}{\pi}\frac{\varepsilon}{\omega^2 + \varepsilon^2}, \tag{7.19}$$

from which we have $\mathrm{Im}\,\mathcal{G}_R \propto \delta_\varepsilon(\omega - E_{nm})\pi$ and can write the thermal spectral function as

$$\rho^\varepsilon(\omega) = \frac{1}{Z}\sum_{n,m}|\phi_{nm}|^2 2\sinh\Big(\frac{\beta\omega}{2}\Big) e^{-\beta\frac{(E_n+E_m)}{2}}\delta_\varepsilon(\omega - E_{nm}). \tag{7.20}$$

From equation 7.19, one can see how the Poisson kernel is simply a *smeared* version

of a Dirac delta function. From this consideration follows that the spectral function defined in term of the Poisson kernel is understood as a smeared distribution of delta functions, with the weight given by the matrix element. Furthermore, it states that the smeared spectral function is the analytic continuation of the retarded correlator in Minkowski space-time [136]. These statements are particularly important once we will move our discussion to finite volume correlation functions.

The Fourier coefficients of equation 7.10 in the spectral representation can be written as

$$G_E^{(l)}(\omega) = \frac{2}{Z}\sum_{n,m}\frac{|\phi_{nm}|^2}{-i\omega + E_{nm}} e^{-\beta\frac{(E_n+E_m)}{2}} \sinh\Big(\frac{\beta E_{nm}}{2}\Big), \tag{7.21}$$

which show its relation with the retarded correlator $\mathcal{G}_R(i\omega) = G_E^{(l)}(\omega)$, for $l \neq 0$. From equation 7.21, one can infer that the retarded correlator is the analytic continuation of the Fourier coefficient. Now, since the retarded correlator is analytic only in the upper half plane, for $l = 0$ one can only study the value at the origin as $\lim_{\varepsilon\to 0^+}\mathcal{G}_R(i\omega)$.

Finally, exploiting the relation among the retarded correlator (eq. 7.16), the thermal spectral function (eq. 7.20) and the Euclidean correlator (eq. 7.15), one finds the Euclidean correlator expressed in terms of the spectral function

$$G_E(\tau) \pm G_E(\beta - \tau) = \int_0^\infty d\omega\ \rho^\varepsilon(\omega)\frac{e^{\omega\left(\frac{\beta}{2}-t\right)} \pm e^{-\omega\left(\frac{\beta}{2}-t\right)}}{2\sinh\left(\frac{\beta\omega}{2}\right)}, \tag{7.22}$$

where the sign depends on whether we use fermionic $(-)$ or bosonic $(+)$ operators. The type of the field operator used also determines whether the spectral function is even $(-)$ or odd $(+)$.

Equation 7.22 is the starting point for the lattice computation of the spectral function as the Euclidean correlator can be computed in lattice QCD simulation. However, the extraction of the spectral function from lattice correlator is an ill-posed inverse problem as it will be discussed in the next section. In the remaining sections, our focus will be towards problems in zero temperature QCD, hence we can obtain a zero temperature relation between Euclidean correlation functions and the spectral function sending $\beta \to \infty$

$$G_E(\tau) = \int_0^\infty d\omega\ \rho^\varepsilon(\omega)e^{-\omega\tau}, \tag{7.23}$$

with

$$\rho^\varepsilon(\omega) = \sum_n |\phi_{0n}|^2\delta_\varepsilon(\omega - E_n). \tag{7.24}$$

7.2 Correlation functions computed on the lattice and the inverse problem

The problem of extracting spectral densities from lattice correlation function belongs to the class of *inverse problems* and in principle can be solved mathematically by performing the Laplace transform of equation 7.23. However, because lattice correlators are obtained from Monte Carlo simulations, as discussed in chapter 4, the input data are necessarily affected by a certain statistical error. In ref. [137], the authors studied how the introduction of uncertainty in the input data affects the solution of the inverse problem, concluding that although a solution can be found, it will not be a stable solution and will possibly be obtained with an infinite uncertainty. This leads to the violation of one of the condition for a well-posed problem formulated by Hadamard [138], which make the extraction of spectral density from lattice correlators an ill-posed inverse problem. Furthermore, the problem gets even more complicated when we consider the fact that lattice simulations are necessarily performed in a finite volume, making the spectral density a badly-behaving distribution of Dirac delta functions due to the discretisation of the energy spectrum.

Over the years, many methods have been developed in order to tackle ill-posed inverse problems as they occur not only in physics but in many other areas of science [139, 140]. In the context of lattice QCD the most popular methods are the maximum entropy method (MEM) [141], methods based on Bayesian inference [142, 143] and the Backus-Gilbert method [144]. Recently a few more techniques have been developed, such as a reconstruction method based on the Chebyshev polynomials [145], a method based on conformal maps [136] and methods based on Machine Learning tools and Neural Networks [146, 147, 148]. Regardless of the different strategies, all these methods introduce some sort of regularisation which allows one to get a reasonable solution for the inverse problem.

In the following sections, we employed what is now known in the literature as HLT method, named after the initials of the authors of ref. [149]. This method is a modification of the strategy outlined in ref. [150] based on the Backus-Gilbert method. The starting point is the finite volume two-point, time-ordered Euclidean lattice correlation function

$$G(\tau) = \frac{1}{L^3} \sum_{\boldsymbol{x}} T\langle O(\boldsymbol{x}, \tau)\overline{O}(0)\rangle, \tag{7.25}$$

which, upon insertion of a complete set of state can be written as

$$G(\tau) = \frac{1}{L^3} \sum_n \frac{\langle 0|O(0)|n\rangle_L \langle n|\overline{O}(0)|0\rangle_L}{2\omega_n(L)} \Big(e^{-\tau\omega_n(L)} + e^{-(T+\tau)\omega_n(L)} \Big), \tag{7.26}$$

where T is the maximum time extent of the hyper-cubic lattice and the term $e^{-(T+\tau)\omega_n(L)}$ is there to include contributions coming from back-propagating states due to periodic boundary conditions. Now, using equation 7.23, we can express the correlator in terms of the finite volume spectral density

$$G(\tau) = \int_0^\infty d\tau \ \rho_L(\omega_n) \Big(e^{-\omega_n(L)\tau} + e^{-(T+\tau)\omega_n(L)} \Big), \tag{7.27}$$

with

$$\rho_L(\omega) = \sum_n \frac{\langle 0|O(0)|n\rangle_L \langle n|\overline{O}(0)|0\rangle_L}{2\omega_n(L)} \delta(\omega - \omega_n(L)). \tag{7.28}$$

The notation $\omega_n(L)$ highlights the fact that at finite volume the energy spectrum is a distribution of δ-functions which depends on the physical extent of the lattice volume. For this reason, even if we were able to solve the inverse problem we would still get a distribution which is not going to be the same as the infinite-volume spectral function.

For this reason, in ref. [150] the authors proposed as a possible solution to this problem, the introduction of a *smeared* integration kernel, which allows to study the spectral distribution extrapolating the results at infinite volume. We write the smeared spectral density as the result of the following convolution integral

$$\rho_L^\sigma(\omega) = \int_0^\infty \Delta_\sigma(\omega - \omega_n(L)) \rho_L(\omega), \tag{7.29}$$

where $\Delta_\sigma = \exp(-\omega^2/2\sigma^2)/\sqrt{2\pi}\sigma$ is a Gaußian function which tends to a δ-function in the limit $\sigma \to 0$.

Smeared spectral densities are smooth function of the energy and as such it is possible to study their infinite-volume limit. By choosing the same smearing function for different physical volumes, it is possible to obtain the physical spectral density, which is a continuous function, by performing the double limit

$$\rho(\omega) = \lim_{\sigma\to 0} \lim_{L\to\infty} \rho_L^\sigma(\omega). \tag{7.30}$$

Again, we stress that the order of the limit cannot be inverted because removing the smearing would give back a distribution of δ-functions, which is radically different from the continuous physical spectral density and for which the extrapolation to infinite-

volume would not converge to correct result.

7.2.1 The HLT method

In order to extract smeared spectral density from lattice correlation functions, one can use the HLT method [149], which is a model-independent algorithm based on the linear Backus-Gilbert regularisation [144]. The work in ref. [149] presents the first version of the HLT method, which was later improved and optimised in ref. [151, 152, 153]. In the following discussion we will mainly follow ref. [153], in which the updates are discussed thoroughly.

One can start by defining a generic lattice correlation function in terms of a basis function b_T

$$G(a\tau) = \int_{\omega_0}^{\infty} d\omega\ \rho_L(\omega) b_T(\tau, \omega), \tag{7.31}$$

where by comparison with equation 7.27, we identify $b_T(\tau, \omega) = \Big(e^{-a\tau\omega} + e^{(-T+\tau)a\omega}\Big)$, in which we wrote the lattice spacing explicitly. In QCD, the spectral density vanishes for $\omega < \omega_{\text{min}} = 2m_\pi$. Then, the value of ω_0 can freely be chosen from zero and ω_{min}.

The central idea of the algorithm is to introduce a smearing kernel as shown in equation 7.29. Since any choice of smearing kernel will always be a smooth function, standard theorems of numerical analysis guarantee that it can be approximated to arbitrary precision in terms of polynomials in the basis function

$$K(\omega; \boldsymbol{g}) = \sum_{\tau=1}^{\infty} g_\tau(\sigma) b_T(\tau, \omega), \tag{7.32}$$

and one can write the formula for the smeared spectral density as

$$\rho_L^\sigma(\omega) = a \sum_{\tau=1}^{\infty} g_\tau(\sigma) G(a\tau) = \int_0^{\infty} d\omega\ \rho_L(\omega) \Delta_\sigma(\omega - \omega_n(L)). \tag{7.33}$$

The problem of extracting the spectral density is then restricted to solving the linear problem of finding the polynomial coefficients $g_\tau(\sigma)$.

In practical lattice simulations, lattice correlators can only be known at a finite number of times, which means that we need to introduce a truncation of the infinite sums and define the reconstructed smearing kernel as

$$K(\omega; \boldsymbol{g}) = \sum_{\tau=1}^{\tau_{\text{max}}} g_\tau(\sigma) \Big(e^{-a\tau\omega} + e^{-(T+\tau)a\omega}\Big), \tag{7.34}$$

which inevitably introduces systematic errors in our determination of the spectral density.

One can then introduce the following functional to define the distance between the target and the reconstructed smearing kernel

$$A_n[\boldsymbol{g}] = \int_{\omega_0}^{\infty} d\omega \; w_n(\omega) \big| K(\omega; \boldsymbol{g}) - \Delta_\sigma(\omega - \omega_n(L)) \big|. \tag{7.35}$$

This corresponds to the L_2 norm in functional space and its minimisation gives us the coefficients $\boldsymbol{g}$ which best approximate the target smearing kernel.

The weight-functions $w_n(\omega)$ can be chosen from

$$w_\alpha(\omega) = e^{a\omega\alpha} \text{ with } \alpha = \big\{0, \frac{1}{2}, 2^-\big\}, \qquad w_c(\omega) = \frac{1}{\sqrt{e^{a(\omega-\omega_0)} - 1}}, \tag{7.36}$$

and can be distinguished from the tag $n = \{0, 1/2, 2^-, c\}$. The weigh functions w_α correspond to Jacobi polynomials (Legendre polynomials for $\alpha = 0$) as introduced already in ref. [149]. The parameter α effectively changes the rapidity of the convergence to the most stable result, reducing the systematic errors introduced by the imperfect reconstruction of $K(\omega; \boldsymbol{g})$, as it was demonstrated quantitatively in ref. [153]. Performing a change of variable in the expression for w_c, it can be shown after a few line of algebra that minimising $A_c[\boldsymbol{g}]$ corresponds in searching for the best approximation of the smearing kernel in terms of Chebyshev polynomials.

As already argued in ref. [149], minimising the functional $A_n[\boldsymbol{g}]$ without any sort of regularisation leads to gigantic polynomial coefficients $\boldsymbol{g}$ regardless of the weight function used. This happens as a consequence of the fact that we are trying to solve an ill-posed problem and, as already discussed in this section, this leads to very unstable solution with huge uncertainties.

For this reason, the HLT method uses the Backus-Gilbert regularisation which consists in minimising the functional

$$W_n[\boldsymbol{g}] = \frac{A_n[\boldsymbol{g}]}{A_n[\boldsymbol{0}]} + \lambda B[\boldsymbol{g}], \tag{7.37}$$

under the unit area constraint

$$\int_0^{\infty} d\omega K(\omega; \boldsymbol{g}) = 1. \tag{7.38}$$

The error functional $B[\boldsymbol{g}]$ is defined as

$$B[\boldsymbol{g}] = B_{\text{norm}} \sum_{\tau_1,\tau_2=1}^{\tau_{\max}} g_{\tau_1} g_{\tau_2} \,\text{Cov}(\tau_1,\tau_2), \tag{7.39}$$

where $\text{Cov}(\tau_1,\tau_2)$ is the covariance matrix of the lattice correlator $G(a\tau)$ and B_{norm} is often chosen to be $B_{\text{norm}} = \omega_n^2/G^2(a\tau_{\text{norm}})$, making the error functional dimensionless.

For fixed values of the algorithmic parameters $\boldsymbol{p} = (n, \lambda, \omega_0, \tau_{\max}, \tau_{\text{norm}})$, the minimisation of equation 7.37 consists in solving the linear problem

$$\left.\frac{\partial W_n[\boldsymbol{g}]}{\partial g_\tau}\right|_{\boldsymbol{g}=\boldsymbol{g}^{\boldsymbol{p}}} = 0, \tag{7.40}$$

which needs to be done for each energy and smearing radius considered in the determination of $\rho_L^\sigma(\omega)$. In the end, this will give the result of the smeared spectral density

$$\rho_L^\sigma(\omega;\boldsymbol{g}^{\boldsymbol{p}}) = \sum_{\tau=1}^{\tau_{\max}} g_\tau^{\boldsymbol{p}} G(a\tau). \tag{7.41}$$

The HLT procedure, as any method used for extracting the spectral density from lattice correlator, needs a reliable strategy to estimate both the statistical and systematic errors of the result. The statistical error can be estimated from the error functional $B[\boldsymbol{g}]$

$$\Delta_{\text{stat}}(\omega;\boldsymbol{g}^{\boldsymbol{p}}) = \sqrt{\frac{B[\boldsymbol{g}^{\boldsymbol{p}}]}{B_{\text{norm}}}}. \tag{7.42}$$

Its form suggests that in the ideal case of infinitely precise input data, the error functional vanishes and the regularisation is no longer needed as we are not in the case of an ill-posed problem anymore.

The systematic error can be obtained monitoring how the smeared spectral density changes alongside the quantity

$$d(\boldsymbol{g}^{\boldsymbol{p}}) = \sqrt{\frac{A_0[\boldsymbol{g}^{\boldsymbol{p}}]}{A_0[\boldsymbol{0}]}}. \tag{7.43}$$

In particular, following the procedure introduced in ref. [151] called *stability analysis*, one quotes as the best estimate for $\rho_L^\sigma(\omega)$, one of the results from the region in which $d(\boldsymbol{g}^{\boldsymbol{p}})$ is small and therefore the result is dominated by the statistical uncertainty. In this region, the result is stable within the statistical error to the variation of any algorithmic parameter contained in $\boldsymbol{p}$. The reason behind the stability analysis can be

understood by noticing that large values of $d(\boldsymbol{g^p})$ correspond to a large value of the norm functional $A_0[\boldsymbol{g^p}]$ and thus to a larger distance between the target and reconstructed kernel. In this region of large $d(\boldsymbol{g^p})$, results corresponding to different choice of weight function w_n and/or different λ are very different not only with respect to the target kernel but also with each other, making it almost impossible to select a single result. Instead, small values of $d(\boldsymbol{g^p})$, corresponding to a small distance between the reconstructed and target kernel, tend to be closer together and therefore agree within the statistical errors. Moreover, as a consequence of the Backus-Gilbert regularisation (eq. 7.37) and the minimisation (eq 7.40), small values of $d(\boldsymbol{g^p})$ are typically obtained for small values of λ meaning that the minimisation is focusing on the norm functional $A_0[\boldsymbol{g^p}]$ and not on the error functional. Thus, for small $d(\boldsymbol{g^p})$ the results tend to agree within the statistical errors because in this regime Δ_{stat} tend to grow because of the ill-posed nature of the problem.

An example of the stability analysis plot can be seen in figure 7.1, in which one can clearly see how the statistical error of $\rho^\sigma_L(\omega)$ grows as we reduce $d(\boldsymbol{g^p})$.

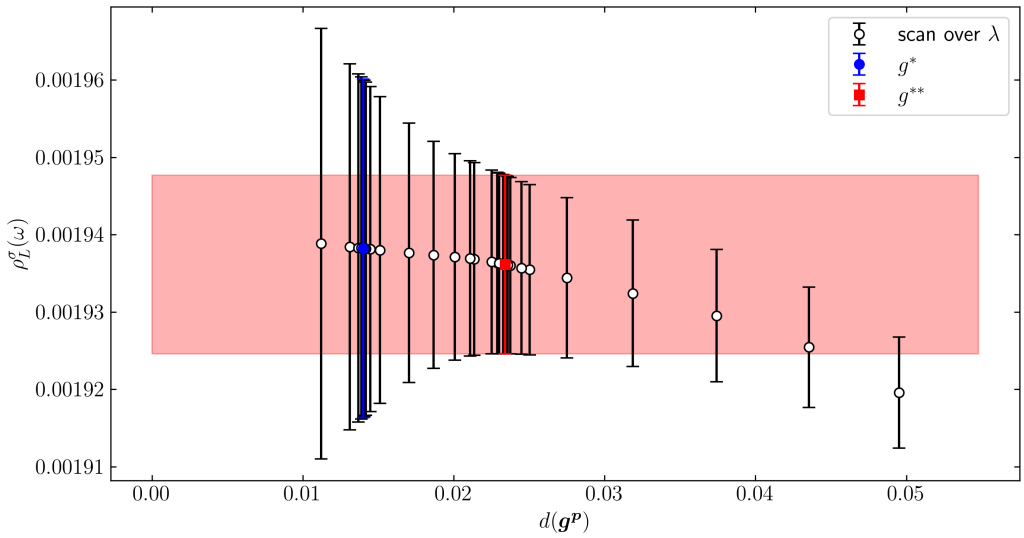

Figure 7.1: Stability analysis of the two-point correlation function with B_s meson interpolating operators, the same of figure 3.1. The data shows the results of the spectral density at $\sigma = 0.2/a$ and $\omega/E_0 = 0.9$, the full results are shown in figure 7.2. The plot shows the initial scan over λ and highlights two points satisfying the condition of equation 7.44. The red data point is the one selected as the final result with the red band showing that it is indeed compatible within the statistical error with all the other results. The red data point correspond to the optimal balance $A_{2^-}[\boldsymbol{g^*}*]/A_{2^-[\boldsymbol{g^{**}}]} = B[\boldsymbol{g^{**}}]$.

Following the procedures of ref. [149, 151], we estimate the central value of the

smeared spectral density and the residual systematic error from the results satisfying the conditions

$$\frac{A_{2^-}[\boldsymbol{g}^*]}{A_{2^-[\mathbf{0}]}} = 10B[\boldsymbol{g}^*], \qquad \frac{A_{2^-}[\boldsymbol{g}^{**}]}{A_{2^-[\mathbf{0}]}} = B[\boldsymbol{g}^{**}]. \tag{7.44}$$

Typically, both results for $\boldsymbol{g}^*$ and $\boldsymbol{g}^{**}$ will fall within the statistically dominated region for small $d(\boldsymbol{g}^{\boldsymbol{p}})$. In the few cases when this does not happen, it is still possible to estimate the systematic error associated to the smeared spectral density by taking the difference $\rho_L^\sigma(\omega, \boldsymbol{g}^*) - \rho_L^\sigma(\omega, \boldsymbol{g}^{**})$, even though it often gives a rather conservative estimate.

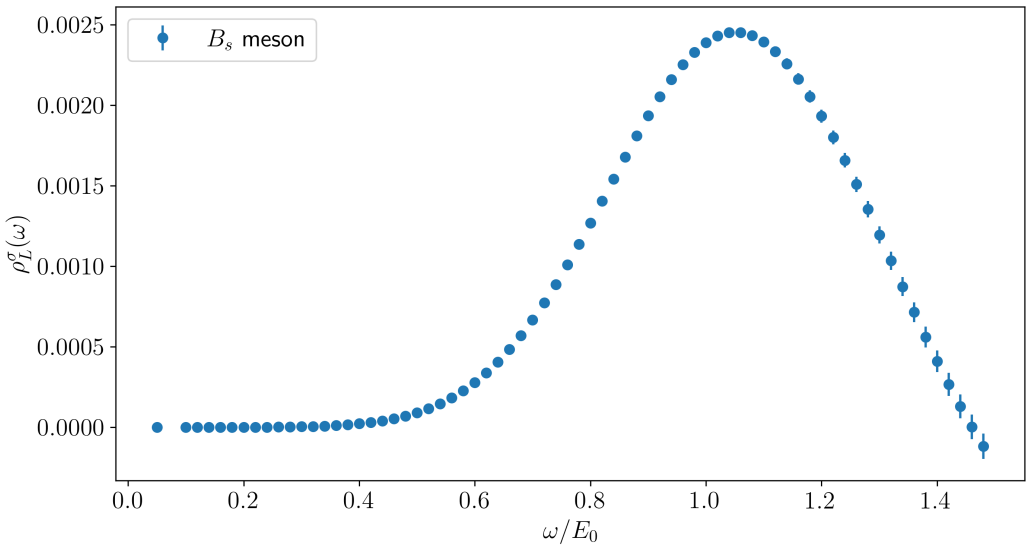

Figure 7.2: Smeared spectral density extracted using the HLT method from two-point correlation function using smeared meson interpolators of the B_s meson, the same of figure 3.1. The results show the peak corresponding the the ground state of the B_s meson previously found in equation 3.27, $E_0 = 1.2712$ in lattice units.

The final step to follow at the end of the HLT method would be to perform the ordered double limit of equation 7.30. However, as will be discussed in the next section and in chapter 8, all the numerical results discussed in this document were obtained with only a single physical lattice volume. Therefore, it would be impossible for the results discussed here to perform the infinite-volume extrapolation. Regardless of this limitation, in chapter 8, we will show how to perform the $\sigma \to 0$ extrapolation in the context of inclusive semileptonic decays as in that specific case we assume that our statistical errors are going to be larger than the finite volume effects. For an example of a correctly performed ordered double limit, one can see the discussion sections of references ref. [151, 153].

7.3 Glueball spectral function in $SU(3)$ Yang-Mills theory

Since the early days of QCD, obtaining precise predictions for the glueball spectrum has been a particularly challenging task, either using analytical or numerical methods. Moreover, clean experimental evidence of the very existence of glueballs is still missing, due to particularly difficult to understand mixing effects and to the fact that their masses are probably close to other hadronic bound states appearing in the decay channel of the J/ψ meson [154, 155, 156], making it a long standing unsolved problem.

The contamination of glueball states by additional hadronic bound states is a complication also in lattice QCD simulations, where despite the implementation of smeared operators, excited states often contribute to the correlation function, resulting in effective mass plots in which it is particularly difficult to identify the correct plateau. For this reason, as discussed in section 2.7, most lattice QCD studies of the glueball spectrum employ methods like the GEVP [22, 23]. The difficulty behind identifying and controlling excited states contaminations can be understood looking at the formula for the finite volume smeared spectral density, *i.e.*, the smeared version of equation 7.28

$$\rho_L^\sigma(\omega) = \sum_n \frac{\langle 0|O(0)|n\rangle_L \langle n|\overline{O}(0)|0\rangle_L}{2\omega_n(L)} \Delta_\sigma(\omega - \omega_n(L)), \tag{7.45}$$

where Δ_σ is the Gaußian kernel. The weight of the Gaußians Δ_σ located at a particular energy $\omega_n(L)$ is given by the magnitude of each matrix element $\langle n|\overline{O}(0)|0\rangle_L$. For this reason, in those cases in which the energies are too close together or the matrix elements are too large, resolving individual states might be a particularly laborious effort.

These considerations make the determination of glueball masses from effective mass plots and asymptotic exponential fits particularly prone to large systematic errors which could affect the calculation of the glueball spectrum. It is to address these difficulties that we decided to investigate an alternative method based on the extraction of smeared spectral functions [157]. The calculation of bound state masses from spectral functions was proposed for the first time in ref. [152] and in the context of glueball states in ref. [158].

In our study, we focused on the quenched QCD theory, that is $SU(3)$ Yang-Mills theory with no dynamical fermions, and we extracted the smeared spectral density from two-point correlation functions with glueball interpolating operators, defined in equation 2.73. Because of the broken Lorentz symmetry on the lattice, we built the correlation functions using the representations defined in section 2.7, and obtained

J^{PC}	β	$L^3 \times T$	N_{cnfg}
A_1^{++}	5.8941	$32^3 \times 32$	3420
A_1^{++}	6.0625	$32^3 \times 32$	15000
A_1^{++}	6.3380	$32^3 \times 32$	10000
E^{++}	5.8941	$32^3 \times 32$	3420

Table 7.1: Ensembles details for the glueball correlation functions.

results in the A_1^{++} and E^{++} channels, corresponding respectively to the 0^{++} and 2^{++} glueball states in the continuum limit. As already discussed in section 2.7, in the A_1^{++} we subtracted the vacuum expectation values from the two-point correlation functions. The details of the numerical results can be found in table 7.1.

Glueball correlators are notoriously noisy due to a particularly severe signal-to-noise ratio problem [159, 160]. One of the strategies which have been developed in order to overcome this issue is the variational method discussed in section 2.7. For each channel considered in this section, we built the GEVP correlator matrix including a large basis of glueball operators. Then after diagonalising the matrix and solving the eigenvalue equation 2.78 we were able identify the optimal operator defined in equation 2.77 with which construct the optimal correlation function.

One of the advantages of extracting spectral functions from glueball correlators is that we can explicitly verify that the correlator with the lowest eigenvalue coming from the solution of the GEVP equation is indeed the one that contribute the most to the optimal correlator. This is because the matrix elements $\langle n|\Phi(0)|0\rangle_L$ appearing in equation 7.45 in the case of the optimal correlator are in fact obtained from the linear combination of the matrix elements of the correlation functions used in the definition of equation 2.77, which correspond to the highest eigenvalues of the correlator matrix (eq. 2.76). The correlator corresponding to the highest eigenvalue is also the one with the highest overlap with the ground state energy. This can be seen clearly in the plot shown in figure 7.3.

The spectral functions shown in figure 7.3 were extracted from glueball correlation functions using the HLT method. As discussed in the section above, one of the important features of the method is the stability analysis shown in figure 7.1. Because glueball correlators are particularly noisy, much more than the meson lattice correlators shown in figure 3.1, we notice that the HLT algorithm tends to further minimise the error functional which results in a stability plot shown in figure 7.4. The difference between the plots in figure 7.4 and figure 7.1 highlight the fact that the study of the stability plots is a delicate stage of the HLT method, which sometimes could give as

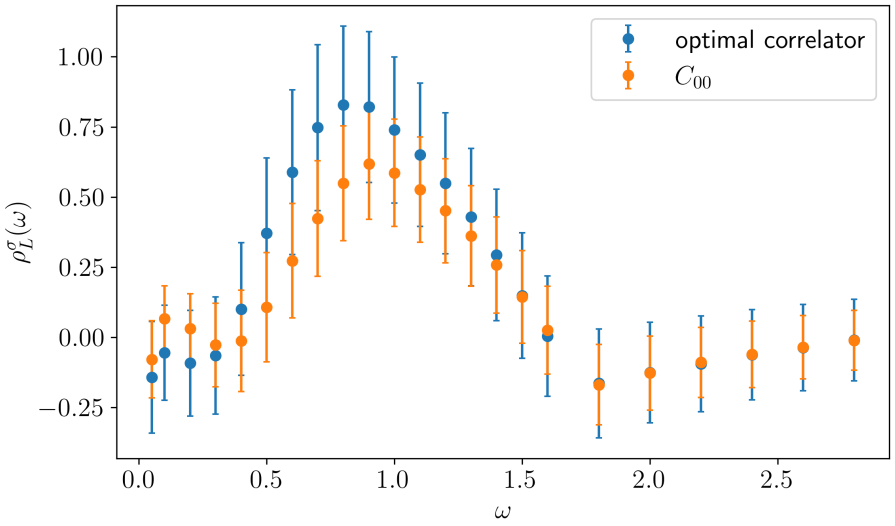

Figure 7.3: Smeared spectral density for the two-point glueball correlation function in the A_1^{++} channel obtain from simulations with $\beta = 5.8941$ and $L^3 \times T = 32^3 \times 32$. The Gaußian kernel used in the reconstruction had a smearing radius of $\sigma = 0.15/a$. The energies are all in lattice units. The points in blue show the smeared spectral density of the optimal correlator, while the points in orange show the smeared spectral density of the single correlator with the highest overlap with the ground-state energy.

the best result a conservative estimate of the systematic errors. Because of the noisy correlators, the HLT algorithm selects as the optimally balanced result ($k = 1$) a value with a large statistical uncertainty. However, studying carefully the stability plots for each energy value considered in the plot, one soon realises that there are points satisfying a different condition

$$\frac{A_\alpha[\boldsymbol{g}^*]}{A_\alpha[\mathbf{0}]} = kB[\boldsymbol{g}^*], \tag{7.46}$$

which are well within the stability plateau but with a smaller statistical uncertainty. For this reason, we decide to use the points satisfying the condition of equation 7.46 with $k = 2.5$ as the final values of our spectral reconstruction.

7.3.1 Fits of smeared spectral functions

In order to extract glueball masses from smeared spectral densities one can exploit the form of the smearing kernel used in the HLT method and define the model fit function as

$$f_k^\sigma(\omega) = \sum_k a_k \, e^{\frac{-(\omega-\omega_k)^2}{2\sigma^2}}, \tag{7.47}$$

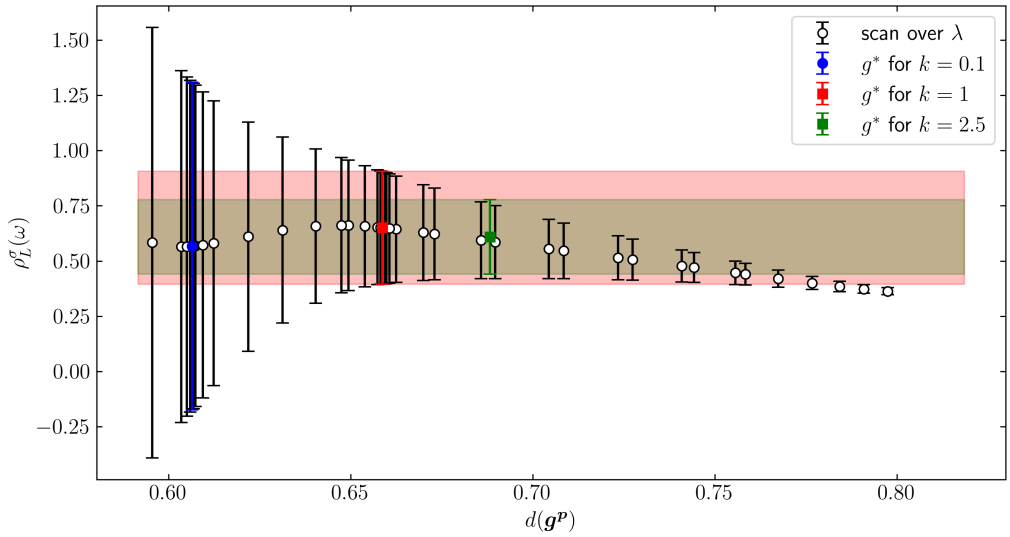

Figure 7.4: Stability plot for the smeared spectral function extracted from two-point glueball correlators obtained from simulations with $\beta = 5.8941$ and $L^3 \times T = 32^3 \times 32$. The data show the results of the HLT with $\sigma = 0.15/a$ and $\omega = 1.1$ in lattice units.

where k is an integer representing the number of states encoded in the model function and a_k, ω_k are the fit parameters related to the finite volume matrix elements and energies respectively. The fit parameters are determined by minimising the χ^2 functions containing the covariance matrix of the lattice correlators

$$\chi^2_{f_k^\sigma} = \sum_{\omega,\omega'} \big(f_k^\sigma - \rho_L^\sigma(\omega)\big)\, \mathrm{Cov}^{-1}_{\omega,\omega'}[\rho_L^\sigma]\big(f_k^\sigma(\omega') - \rho_L^\sigma(\omega')\big), \tag{7.48}$$

with

$$\mathrm{Cov}_{\omega,\omega'}[\rho_L^\sigma] = \frac{1}{N-1} \sum_{n=0}^{N-1} \big[\rho_{L,n}^\sigma(\omega) - \langle \rho_L^\sigma(\omega)\rangle\big]\big[\rho_{L,n}^\sigma(\omega') - \langle \rho_{L,n}^\sigma(\omega')\rangle\big]. \tag{7.49}$$

Now, in principle there is no limit in the number of energies that can be used to extract smeared spectral functions. However, it is a well known fact that lattice correlation function can contain only a limited number of time slices, due to the fact that we perform simulations in a finite volume. Moreover, the number of degrees of freedom is further constrained by the covariance matrix which takes into account the correlation between different time slices. These restriction in the number of degrees of freedom inevitably affects the number of degrees of freedom available in the fit of spectral densities. This happens because the spectral density evaluated at a single energy depends

on the temporal correlation functions at each lattice time. As a consequence, the problem of isolating the ground state energy from excited state contributions in temporal correlators is shifted to the problem of resolving to small values of σ the energy states in the spectral density.

Another important feature of fitting the spectral density comes from the fact that thanks to the Backus-Gilbert regularisation in the HLT method, the covariance matrix contained in the error functional $B[\boldsymbol{g}^{**}]$ is automatically regularised by the norm functional $A_\alpha[\boldsymbol{g}^{**}]$. What this means in practice is that the values of the covariance matrix will never get too small, due to the fact that whenever this may happen, the algorithm will try to minimise the norm functional instead of the error functional. In other words, this procedure guarantees that the covariance matrix will always be well-conditioned so that the inversion required in equation 7.48 will always be possible.

After reconstructing the smeared spectral density, we follow the procedure introduced in ref. [152] and perform a combined fit of spectral functions including the number of energy values which minimise the condition number of the covariance matrix $\mathrm{Cov}_{\omega,\omega'}[\rho_L^\sigma]$, and so maximise the information passed to the χ^2 function in equation 7.48. The condition number of the covariance matrix is also used in order to determine the smallest value of σ that can be used in order to get sensible results for our fit results. The non-linear fit was performed with the Levenberg-Marquardt algorithm implemented in the `python` function `scipy.optimize.curve_fit`, with prior guesses 1.0 for the matrix elements and 0.5, 0.5+0.2 for the two glueball states included in the fit. In figure 7.6, we show the results of the Gaußian fits using equation 7.47 including the first two states, *i.e.* $k = 2$. In the plot we also show the results for the first two states obtained with standard effective mass plots and temporal correlator fits by Athenodorou and Teper in ref. [161].

We obtained results from the fits of spectral densities for several values of the smearing radius $\sigma = \{0.15, 0.2, 0.24, 0.28, 0.3, 0.4\}$, however, in table 7.2 we only compare the results obtained with the smallest σ. The choice of the smearing radius is naturally dictated by the quality of the data, which for glueball lattice correlator is unfortunately very poor. Results with a different value of smearing radius can be seen in figure 7.7.

The results obtained from the fits of spectral densities for our smallest value of σ are close yet not perfectly compatible with the results obtained by in ref. [161] for both the ground state mass and the first excited state. Despite this not perfect agreement, we can consider our results to be acceptable considering that in a finite volume the separation between energy states should be around $2\pi/L \approx 0.2$ which is indeed confirmed by the values of the glueball masses extracted from the fits.

The fact that our results are very close to those obtained in ref. [161] is highly non-

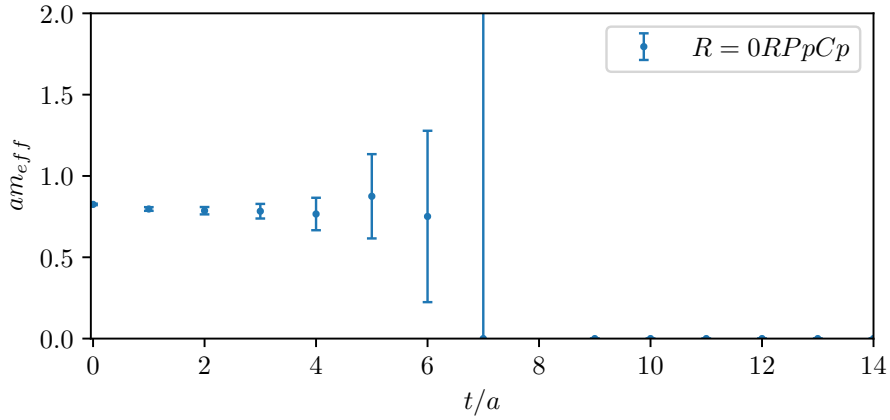

Figure 7.5: Effective mass plot for the ground state of A_1^{++} glueball correlation functions, obtained from simulations with $\beta = 5.8941$. The early onset of the plateau region is an effect of the use of the variational method to compute the optimal correlation function. The growth of the statistical error as we go to larger lattice times is due to the increase in noise that affects glueball correlation functions. The large statistical uncertainty affects the accuracy of the glueball mass calculation from fits of temporal correlators, as it may hint possible contributions from excited states.

trivial since the approach used to calculate the glueball masses is completely different and in principle there is no guarantee that they would yield the same results. The fact that we find reasonably close values for the glueball masses is an indication that we are indeed probing the same physics. However, the fact that both values obtained using the "standard" method in ref. [161] are larger than the values we obtain from our spectral density fits could suggest an overestimation of the glueball masses due to the contaminations of excited states in temporal correlation functions. As already mentioned, the "standard" method relies on fits of temporal correlation functions in the temporal region where one can safely identify a plateau in the corresponding effective mass plot, in the same way that was shown in figure 3.1. Glueball correlators are particularly noisy, which makes it particularly difficult to identify the plateaus used to extract glueball masses. The procedure for determining the glueball masses from effective mass plots is particularly challenging as one can often use only the first few lattice point in order to define the plateau region, which is often also affected by large uncertainties as one goes to larger times. This is clearly shown in figure 7.5 Consequently, it is hard to gauge whether the plateau is indeed purely a manifestation of the ground state, with the risk that contamination from other states could remain indistinguishable. Conversely, our alternative method based on the extraction of the glueball spectral functions allows to unequivocally identify the ground state mass and

the first excited state simply identifying the peaks in the spectral functions, appearing in correspondence of the matrix elements $\langle |n|\overline{\Phi}|0\rangle_L$.

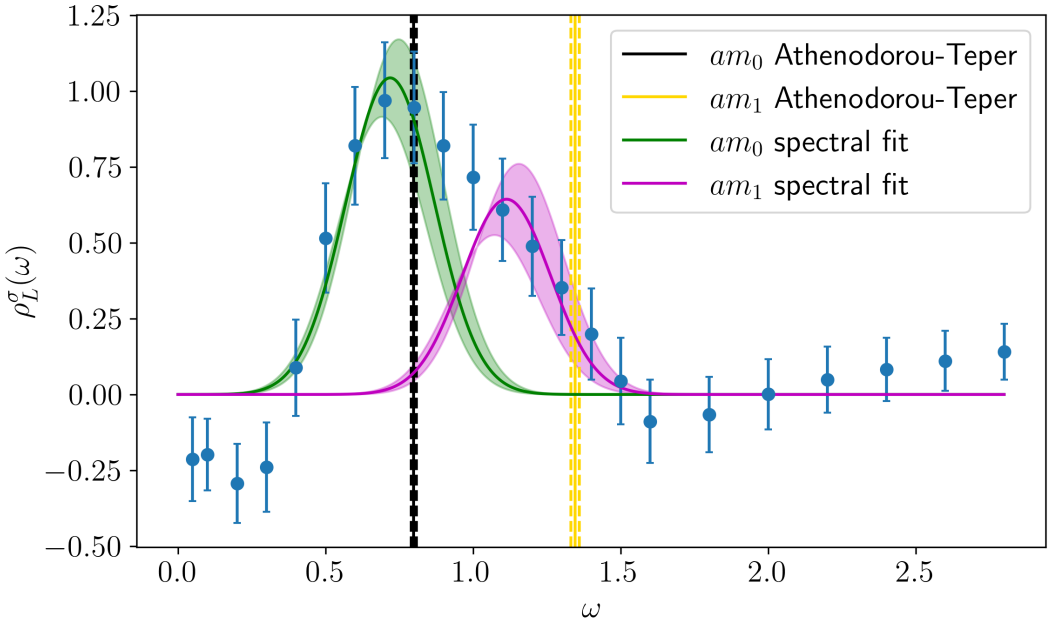

Figure 7.6: Smeared spectral density extracted from two-point glueball correlation functions obtained from simulations with $\beta = 5.8942$, $L^3 \times T = 32^3 \times 32$. The smearing radius is $\sigma = 0.15/a$, which is the smallest value of σ corresponding to the smallest condition number for the covariance matrix defined in equation 7.49. The vertical lines correspond to the fit results of temporal correlator in the plateau region of effective mass plots obtained in ref. [161] by Athenodorou and Teper. The green and purple Gaußian curves correspond respectively to the ground state mass and first excited state of the glueball. The reduced χ^2 of the two-Gaußian fit is $\chi^2_{\text{red}} = 2.67$

Another interesting feature of our method is that in principle it could allow us to identify states which would otherwise be impossible to determine. In figure 7.8 one can see a well recognisable peak exactly in between the two vertical lines corresponding to the glueball masses extracted with the "standard" method and a small peak roughly at $\omega = 0.4$ in lattice units. The small peak corresponds to an extremely light glueball mass which would be impossible to see using the "standard" method as it could only be detected for extremely long lattice times, which are exactly the times in which the glueball correlator is dominated by large statistical noise. While it could simply be a statistical fluctuation that could disappear as we increase the number of configurations of the ensemble, in the case in which the peak survived such a change, it would be a signal that our method indeed allows to identify states which could not be identified with any other method currently used within the lattice community. If this was indeed

J^{PC}	β	Athenodorou-Teper	spectral fits
A_1^{++}	5.8941	$am_0 = 0.799(10)$	$am_0^\sigma = 0.719(28)$
		$am_1 = 1.345(14)$	$am_1^\sigma = 1.113(41)$
	6.0625	$am_0 = 0.6365(43)$	$am_0^\sigma = 0.389(56)$
		$am_1 = 1.111(11)$	$am_1^\sigma = 0.766(35)$

Table 7.2: Comparison of the numerical results of the glueball masses obtained from Athenodorou and Teper in ref.[161] and those obtained fitting the smeared spectral density using equation 7.47 and the smeared spectral density extracted from two-point glueball correlation functions. The results from spectral fits are obtained using the smallest value of the smearing radius $\sigma = 0.15$

the case, it would certainly be an important aid in the quest for the calculation of the glueball spectrum, both in a quenched and in an unquenched setting.

All the results shown in this section are to be considered as produced at a very preliminary stage of our investigation. In fact, following the strategy of the HLT method, we should extract the values of the glueball masses for each value of sigma and for multiple values of the physical volume $L^3 \times T$. Only then, we would be able to perform the ordered double limit of equation 7.30 with the glueball masses in place of the spectral functions

$$\lim_{\sigma \to 0} \lim_{L \to \infty} am_L^\sigma. \tag{7.50}$$

Only at the end of this procedure we would be able to get an accurate comparison with the results obtained by Athenodorou and Teper in ref. [161] and any other lattice study of glueball masses. Moreover, exactly like for any other work involving lattice simulations, we will need to perform the extrapolations to the continuum limit using our results obtained with different values of β.

This is currently work in progress; the results of this study will be published in a new article [157] in the near future.

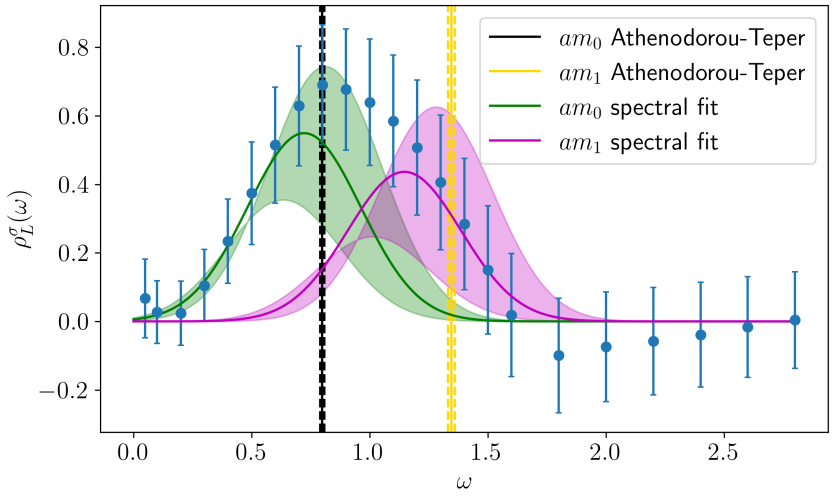

Figure 7.7: Smeared spectral density extracted from two-point glueball correlation functions obtained from simulations with $\beta = 5.8942$, $L^3 \times T = 32^3 \times 32$. The smearing radius is $\sigma = 0.24/a$. The vertical lines correspond to the fit results of temporal correlator in the plateau region of effective mass plots obtained in ref. [161] by Athenodorou and Teper. The green and purple Gaußian curves correspond respectively to the ground state mass and first excited state of the glueball. The reduced χ^2 of the two-Gaußian fit is $\chi^2_{\text{red}} = 1.209$

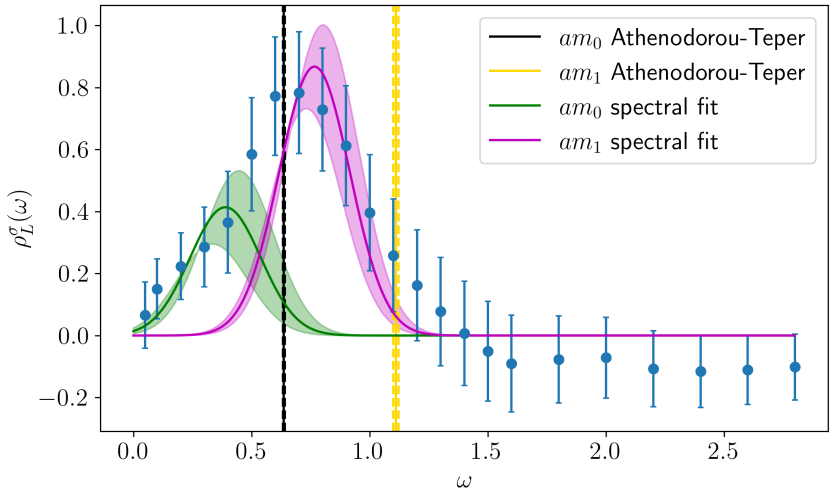

Figure 7.8: Smeared spectral density extracted from two-point glueball correlation functions obtained from simulations with $\beta = 6.0625$, $L^3 \times T = 32^3 \times 32$. The smearing radius is $\sigma = 0.15/a$. The vertical lines correspond to the fit results of temporal correlator in the plateau region of effective mass plots obtained in ref. [161] by Athenodorou and Teper. The green and purple Gaußian curves correspond respectively to the ground state mass and first excited state of the glueball. The reduced χ^2 of the two-Gaußian fit is $\chi^2_{\text{red}} = 1.33$

Chapter 8

Inclusive semileptonic heavy-meson decays

8.1 The Standard Model and flavour physics

With the discovery of the Higgs boson in 2012 at the Large Hadron Collider (LHC), the Standard Model (SM) of particle physics finally got the experimental confirmation for the process known as Higgs mechanism [162, 163], a fundamental piece in order to construct a perturbatively renormalisable theory.

The SM is currently our best attempt at understanding the physical processes involving fundamental forces and particles [164, 165, 166, 167]. It contains three generations of spin-1/2 fermions, which can interact through the strong, weak and electromagnetic forces by the exchange of spin-1 bosons. In each generation of fermions, there are two quarks with different electric charges and two leptons, one of which is the neutrally charged neutrino. Among each other, fermion generations differ only by the value of their rest masses which gets larger as we go from the first (u, d, e, μ_e) to the third (t, b, τ, μ_τ).

The fundamental interactions described in the SM are mediated by gauge bosons. We already defined the gluon as the mediator of the strong nuclear force. Then we have the photon γ as the mediator of the electromagnetic interaction and the Z and $W^{\pm}$ bosons as the mediators of the weak nuclear force. Unlike the photon and the gluons, the Z and $W^{\pm}$ are massive bosons which acquire mass due to the spontaneous breaking of the Electroweak symmetry [164].

The Standard Model Lagrangian density can be written as a linear combination of different sectors

$$\mathcal{L}_{SM} = \mathcal{L}_{gauge} + \mathcal{L}_{Dirac} + \mathcal{L}_{Y} + \mathcal{L}_{Higgs}, \tag{8.1}$$

where $\mathcal{L}_{gauge}$ and $\mathcal{L}_{Dirac}$ contains the gauge and fermionic degrees of freedom and coupling terms

$$\mathcal{L}_{gauge} = -\frac{1}{4}G^a_{\mu\nu}G^{a\mu\nu} - \frac{1}{4}W^i_{\mu\nu}W^{i\mu\nu} - \frac{1}{4}B_{\mu\nu}B^{\mu\nu} \tag{8.2}$$

$$\mathcal{L}_{Dirac} = \sum_{\psi} i\overline{\psi}_L \not{D}\psi_L + i\overline{\psi}_R \not{D}\psi_R. \tag{8.3}$$

$\mathcal{L}_Y$ the Higgs-Yukawa terms

$$\mathcal{L}_Y = -Y^d_{ij}\overline{Q}^I_{Li}\phi d^I_{R_j} - Y^u_{ij}\overline{Q}^I_{Li}\varepsilon\phi^* u^I_{Rj} + (\text{lepton terms}) + \text{h. c.}, \tag{8.4}$$

and $\mathcal{L}_{Higgs}$ the Higgs terms

$$\mathcal{L}_{Higgs} = D_\mu\phi^\dagger D^\mu\phi + \mu^2\phi^\dagger\phi - \lambda(\phi^\dagger\phi)^2. \tag{8.5}$$

The Standard Model Lagrangian is invariant under the local symmetry $SU(3)_C \times SU(2)_L \times U(1)_Y$, where $SU(3)_C$ is the QCD colour gauge group, $SU(2)_L$ represent the weak isospin while $U(1)_Y$ the weak hypercharge. The fermion content is organised in five fields for each fermion generation. Using the notation $(C, L)_Y$, one can write

$$Q^i_L(3,2)_{+1/6},\ \ U^i_R(3,1)_{+2/3},\ \ D^i_R(3,1)_{-1/3},\ \ L^i_L(1,2)_{-1/2},\ \ E^i_R(1,1)_{-1}, \tag{8.6}$$

where Q_L are left-handed quark doublets, U_R are right-handed, up-type quark singlets, D_R are right-handed, down-type quark singlets, L_L are left-handed charged lepton doublet and E_R are right-handed charged lepton singlet. This structure gives a global flavour symmetry to the SM Lagrangian density

$$U(3)^5 \times G_q \times G_l, \tag{8.7}$$

where G_q and G_l are the flavour symmetries of the quark and lepton fields

$$G_q = SU(3)_{Q_L} \times SU(3)_{U_R} \times SU(3)_{D_R}, \qquad G_l = SU(3)_{L_L} \otimes SU(3)_{E_R}. \tag{8.8}$$

Calculations based on the SM have been tested and often confirmed to a very high degree of precision by experimental measurements at very different energy scales. This has been achieved by constructing quantum field theories that work only in a limited energy or distance range called Effective Field Theories (EFT). For instance, one can exploit the wide separation between the Fermi scale and the mass of B- or D-mesons

in order to build an EFT and use it, together with renormalisation group arguments, to calculate the expected (inclusive) decay rates of these mesons with astonishing accuracy [168]. It is within this picture that many physicists advanced the idea that the SM itself can be an EFT such that all the processes currently left unexplained can eventually be described by a more fundamental theory accessible at an energy scale much larger than m_W.

In order to investigate this higher energy scale, one of the methods currently pursued is the indirect approach, which tries to detect deviations between the Standard Model and the experimental data coming from the particle colliders. If present, these deviations can only be explained by the effect of Beyond the Standard Model (BSM) physics occurring at loop-level and therefore highly suppressed at low energies.

One of the most promising sectors of the SM Lagrangian where we expect to find new physics is quark flavour physics and, in particular, in processes involving flavour changing neutral currents (FCNC). Flavour-changing interactions amongst quarks are mediated by the weak force. In a weak quark decay at tree-level, a quark of one flavour emits a $W^{\pm}$ boson and decays to a quark of a different flavour. The decay conserves electric charge so weak decays are from an up-type to a down-type quark or vice versa. FCNC on the other hand can only occur at loop-level in the SM through the so called box diagrams in which we have the exchange of two W bosons between the quarks. For instance, a promising physical process mediated by FCNC in which there might be a signal of new physics is the mixing of neutral B-mesons [169, 170, 171, 172] and K-mesons [173].

FCNC, together with the mixing of quark flavours and CP violation by the Jarlsog invariant define the flavour structure of the SM. All these features are encapsulated in the Cabibbo-Kobayashi-Maskawa (CKM) matrix [174, 175]. Determining the elements of this matrix is not only important to determine fundamental parameters of the standard model but also because, considering their role in flavour changing processes, their precise determination is fundamental in oder to check for possible deviations from the SM and look for possible new physics contributions.

8.2 The Cabibbo-Kobayashi-Maskawa matrix

The Higgs-Yukawa terms in the Standard Model Lagrangian density with only quark fields shown in equation 8.1 can be written as

$$\mathcal{L}_Y = -Y^d_{ij}\overline{Q}^I_{Li}\phi d^I_{R_j} - Y^u_{ij}\overline{Q}^I_{Li}\varepsilon\phi^* u^I_{Rj} + \text{h. c.}, \tag{8.9}$$

where $Y^{u,d}$ are the Yukawa coupling, which are 3×3 complex matrices, i, j are fermion generation labels, ε is the 2×2 antisymmetric tensor and ϕ is the Higgs field.

$$Q_L^I = \begin{pmatrix} U_L \\ D_L \end{pmatrix}$$

are left-handed quark doublets, and d_R^I and u_R^I are right-handed down- and up-type quark singlets, respectively, in the weak-eigenstate basis. The U_L and D_L quark fields represent the up- and down-type for each generation of quarks. The above equation is invariant under the $SU(2)_L \times U(1)_Y$ symmetry.

With the introduction of the Higgs field and its interaction with the Yukawa coupling in equation 8.9, we break explicitly the global flavour physics of the SM, which is reduced to the independent rotation of the fermion fields in equation 8.6 in flavour space. Three of the five $U(1)$ groups in equation 8.7 can be identified with the total baryon and lepton numbers, which are not broken by the Yukawa Lagrangian density. After the spontaneous symmetry breaking occurring through the Higgs mechanism, ϕ acquires a vacuum expectation value, $\langle\phi\rangle = (0, v/\sqrt{2})$, and the hypercharge group is spontaneously broken into the $U(1)_{em}$ group. The non-Abelian gauge groups in equation 8.7 are responsible for the flavour changing dynamics of the fermion fields and are explicitly broken by the Yukawa terms. Then equation 8.9 yields the mass terms for the quarks, where the physical states in the mass basis are obtained diagonalising $Y^{u,d}$ by four unitary matrices, $V_{L,R}^{u,d}$, as

$$M_{diag}^f = V_L^f Y^f V_R^f (v/\sqrt{2}), \qquad f = (u, d). \tag{8.10}$$

As a result, the charged-current $W^\pm$ interactions couple to the physical u_{Lj} and d_{Lk} quarks according to the Lagrangian density

$$\mathcal{L}_W = -\sqrt{\frac{1}{2}} g \overline{u_{Li}} \gamma^\mu V_{CKM} d_{Lj} W_\mu^+ + \text{h. c.} \tag{8.11}$$

with

$$V_{CKM} \equiv= V_L^u V_L^{d\dagger} = \begin{pmatrix} V_{ud} & V_{us} & V_{ub} \\ V_{cd} & V_{cs} & V_{cb} \\ V_{td} & V_{ts} & V_{tb} \end{pmatrix}. \tag{8.12}$$

V_{CKM} is the Cabibbo-Kobayashi-Maskawa matrix, which allows to relate the weak

eigenstates (d', s', b') with the mass eigenstates (d, s, b)

$$\begin{pmatrix} d' \\ s' \\ b' \end{pmatrix} = \begin{pmatrix} V_{ud} & V_{us} & V_{ub} \\ V_{cd} & V_{cs} & V_{cb} \\ V_{td} & V_{ts} & V_{tb} \end{pmatrix} \begin{pmatrix} d \\ s \\ b \end{pmatrix} . \tag{8.13}$$

The CKM matrix is a complex unitary matrix, $V^\dagger V = V^{-1} V = \mathbb{1}$. A generic 3×3 complex unitary matrix is dependent on $N(N-1)/2 = 3$ rotation angles, which in the case of the CKM matrix are known as Cabibbo mixing angles and $N(N+1)/2 = 6$ complex phases. Working in the mass basis, the Yukawa couplings are diagonal $Y^u = \text{diag}(y_u, y_c, y_t)$, $Y^d = \text{diag}(y_d, y_s, y_b)$, which leaves a residual invariance under the flavour group and allow the elimination of five of the six complex phases, corresponding to the relative phases of the quark fields. Therefore, the CKM matrix can be described using four physical parameters: three mixing angles and one CP-violating phase.

8.3 The $|V_{cb}|$ puzzle

In the previous section, we discussed the fundamental importance of the CKM matrix elements in the quest for signals of new physics beyond the SM. Considering the level of precision required to test the current tensions within the SM, a long standing effort has been done in trying to determine all the CKM matrix elements with precisions around the per-cent levels. This is not an easy task because the CKM matrix elements, being fundamental parameters of the SM, cannot be calculated directly from theoretical calculations. Hence, the only way to estimate these parameters is to study physical processes involving weak decays of quarks and combine theoretical calculations of certain quantities involved in the decay with experimental measurements of observables such as the decay rate.

Over the years, a puzzling discrepancy emerged from the determination of the $|V_{cb}|$ and $|V_{ub}|$ CKM elements. In particular, the values of $|V_{cb}|$ determined from inclusive and exclusive semileptonic B decays have differed at the level of about 3σ for quite some time. The latest results quoted by the flavour lattice averaging group (FLAG) world average [176] are reported in table 8.1, with figure 8.1 showing the current bounds obtained studying exclusive semileptonic and leptonic decays.

The discrepancy between the exclusive and inclusive determination, although being a persistent tension, is probably not going to be a signal of new physics, as it has been argued that models based on a new physics contribution struggle to explain this discrepancy in a consistent and significant way [177, 178]. Nevertheless, since the

	$\lvert V_{cb}\rvert$	$\lvert V_{ub}\rvert$
exclusive	$\lvert V_{cb}\rvert = (39.48 \pm 0.67) \cdot 10^{-3}$	$\lvert V_{ub}\rvert = (3.57 \pm 0.13) \cdot 10^{-3}$
inclusive	$\lvert V_{cb}\rvert = (42.00 \pm 0.64) \cdot 10^{-3}$	$\lvert V_{ub}\rvert = (4.32 \pm 0.29) \cdot 10^{-3}$

Table 8.1: Latest results for the magnitude of the CKM matrix elements $|V_{cb}|$ and $|V_{ub}|$ obtained studying exclusive and inclusive semileptonic decays, taken from ref. [176].

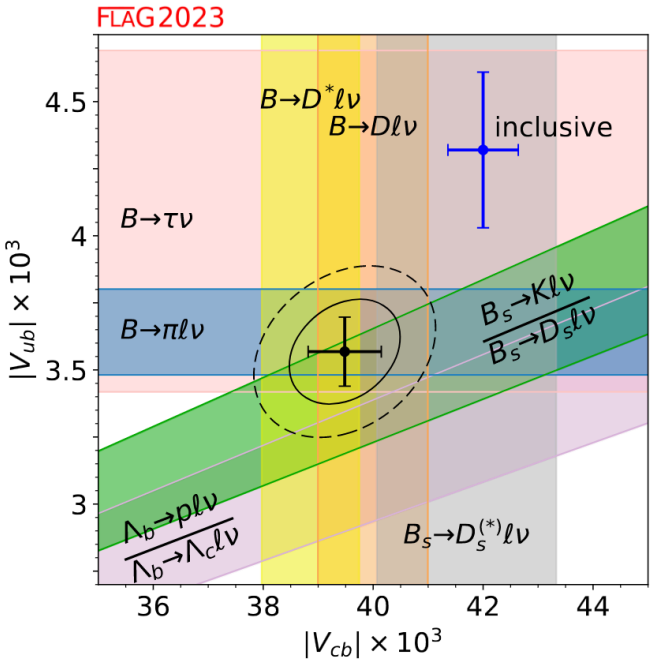

Figure 8.1: The plot show the summary of the determination of the CKM matrix elements $|V_{ub}|$ and $|V_{cb}|$. The black dot shows the global fit of exclusive theoretical and experimental contributions with dashed and solid circular lines representing the 68% and 98% confidence level contours respectively. The blue dot represent the latest results of the inclusive determinations. The plot is taken from ref. [176], in which all the works which contribute to the bounds are reported.

CKM matrix elements involved in the exclusive and inclusive processes parametrise the same quark mixing process, they should in principle be the same, regardless of the approach used in the analysis, which leads to the particle data group (PDG) average of the inclusive and exclusive determination of $|V_{cb}| = (40.8 \pm 1.4) \cdot 10^{-3}$. As one

can imagine, the average has a much larger uncertainty compared with the individual determinations, and this larger uncertainty can affect FCNC studies in an important way by limiting the precision of the calculations and therefore making it harder to find discrepancies with the experimental measurements [179, 180].

In the effort to better understand and possibly resolve this discrepancy, on the theoretical side a key role has been played by lattice QCD calculations of exclusive semileptonic decays. Lattice QCD allows to obtain accurate and systematically improvable predictions for a variety of quantities, including those relevant for decays of heavy mesons like decay constants and form factors. These quantities can then be combined with experimental measurements coming from B factories in order to get the estimate of the CKM matrix elements quoted in table 8.1. Modern lattice QCD estimation of the CKM matrix elements have reached an impressive level of precision which has helped to constrain the uncertainty related to the exclusive determination of $|V_{cb}|$ [176]. However, until recently, lattice QCD calculations were restricted to exclusive decays. This is due to the fact that dealing with multiple hadrons present in inclusive calculations with the current lattice methodology is exceedingly difficult if not impossible.

For this reason, in ref. [2] we performed one of the first lattice QCD study of inclusive decays based on the method proposed in ref. [181]. The study is based on a new strategy for the computation of inclusive decay rates through the reconstruction of spectral density contained in four-point correlation functions. This new technique in a certain sense circumvent the necessity for analytical continuation and could potentially enable the determination of arbitrary moments linked to general $B \to X\ell\nu$ decays. Naturally, an important test of this method is the comparison with the analytic results for the inclusive decay rates obtained employing the operator product expansion (OPE) [182, 183], where the observable is expanded in inverse powers of the heavy-quark mass [184, 185, 186].

8.4 Inclusive semileptonic decays

Inclusive decays of heavy mesons can be described using an effective Hamiltonian, built in order to separate the long-distance and the short distance energy scales

$$\mathcal{L}_{int} = -\mathcal{H}_{int} = -\frac{G_F}{\sqrt{2}}|V_{cb}|\left(\bar{c}\gamma_\mu(1-\gamma_5)b\right)\left(\bar{l}\gamma^\mu(1-\gamma_5)\nu_l\right) \tag{8.14}$$

$$\equiv -\frac{G_F}{\sqrt{2}}|V_{cb}|J_{q,\mu}J_l^\mu. \tag{8.15}$$

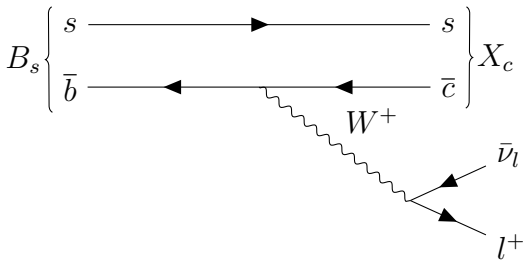

Figure 8.2: Feynman diagram of the $B \to X_c l\overline{\nu}$ inclusive semileptonic decay

where we used the well known relation between the Fermi coupling constant G_F and the Yukawa couplings g: $G_F/\sqrt{2} = g^2/8M_W^2$, while integrating out the W-boson.

We will work in the rest frame of the mother particle and consider massless leptons, such that we can write

$$p = (m_{B_s}, \mathbf{0}), \qquad q = p_l + p_{\overline{\nu}} = (q_0, \boldsymbol{q}), \qquad r = p - q = (\omega, -\boldsymbol{q}) \tag{8.16}$$

Then we write the general formula for the inclusive differential decay rate as

$$d\Gamma = \sum_{X_c} \sum_{s} \frac{1}{2m_B} \Big(\frac{2^3 p_l}{(2\pi)^3} \frac{1}{2E_l} \Big) \Big(\frac{d^3 p_{\overline{\nu}}}{(2\pi)^3} \frac{1}{2E_{\overline{\nu}}} \Big) |\mathcal{M}(\overline{B} \to X_c l\overline{\nu})|^2 \times (2\pi)^4 \delta^4(p - q - r), \tag{8.17}$$

where the matrix element is given by

$$\mathcal{M}(\overline{B} \to l\overline{\nu}) = \langle X_c l\overline{\nu} | H_{int} | \overline{B} \rangle \tag{8.18}$$

$$= \frac{G_F}{\sqrt{2}} |V_{cb}| \langle X_c l\nu | J_\mu(0) J^\mu(0) | \overline{B} \rangle. \tag{8.19}$$

Now, as the hadronic and leptonic part do not interfere, they can be separated into a hadronic and leptonic tensor

$$L^{\mu\nu}(p_l, p_{\overline{\nu}}) = p_\ell^\mu p_{\overline{\nu}}^\nu - p_\ell \cdot p_{\overline{\nu}} g^{\mu\nu} + p_\ell^\nu p_{\overline{\nu}}^\mu - i\epsilon^{\mu\alpha\nu\beta} p_{\ell,\alpha} p_{\overline{\nu},\beta} \ , \tag{8.20}$$

$$W^{\mu\nu}(p, q) = \sum_{X_c} (2\pi)^3 \delta^{(4)}(p - q - r) \frac{1}{2m_B(\boldsymbol{p})} \langle \bar{B}(\boldsymbol{p}) | J^{\mu\dagger}(0) | X_c(\boldsymbol{r}) \rangle \langle X_c(\boldsymbol{r}) | J^\nu(0) | \bar{B}(\boldsymbol{p}) \rangle, \tag{8.21}$$

where the sum over the charmed hadronic states X_c is defined as

$$\sum_{X_c} |X_c(\boldsymbol{r})\rangle\langle X_c(\boldsymbol{r})| \to \sum_{X_c} \int \frac{d^3\boldsymbol{r}}{(2\pi)^3} \frac{1}{2E_{X_c(\boldsymbol{r})}} |X_c(\boldsymbol{r})\rangle\langle X_c(\boldsymbol{r})|. \tag{8.22}$$

The hadronic tensor contains all the non-perturbative information on the hadron dynamics, hence, it is one of the most important object in non-perturbative studies of QCD. However, the hadronic tensor cannot be accessed analytically and for this reason one can use the Optical Theorem in order to relate the hadronic tensor to the imaginary part of the forward scattering amplitude, in a form which is equivalent to the calculation of spectral functions from the imaginary part of the retarded correlator 7.13

$$-\frac{1}{\pi}\,\mathrm{Im}\,T_{\mu\nu} = W_{\mu\nu} \tag{8.23}$$

with

$$T_{\mu\nu} = \frac{1}{2m_B}\int d^4x\; e^{iqx}\langle B|T\big(J^\mu(x)J^\mu(0)\big)|B\rangle. \tag{8.24}$$

A lattice calculation which exploited the Optical theorem was performed in [187], and represents an alternative attempt to the strategy we will discuss in this section.

We can write the differential decay rate in terms of only three kinematic variables q^2, q_0 and the lepton energy E_l

$$\frac{d\Gamma}{dq^2 dq^0 dE_\ell} = \frac{G_F^2|V_{cb}|^2}{8\pi^3} L_{\mu\nu}W^{\mu\nu}\ . \tag{8.25}$$

The hadronic tensor in equation 8.21 can be decomposed in five invariant structure functions

$$\begin{aligned} W^{\mu\nu}(p,q) = &- g^{\mu\nu}W_1(\omega,\boldsymbol{q}^2) + \frac{p^\mu p^\nu}{m_B^2}W_2(\omega,\boldsymbol{q}^2) + \frac{q^\mu q^\nu}{m_B^2}W_3(\omega,\boldsymbol{q}^2) \\ &+ \frac{p^\mu q^\nu + p^\nu q^\mu}{m_B^2}W_4(\omega,\boldsymbol{q}^2) - i\epsilon^{\mu\nu\alpha\beta}\frac{p_\alpha q_\beta}{m_B^2}W_5(\omega,\boldsymbol{q}^2)\ . \end{aligned} \tag{8.26}$$

In the following discussion it will be more convenient to work with the hadronic tensor written in its spectral representation

$$W_{\mu\nu}(\omega,\boldsymbol{q}) = \frac{(2\pi)^3}{2m_B}\langle\bar{B}(\mathbf{0})|J_\mu^\dagger(0)\delta(\hat{H}-\omega)\delta^3(\hat{\boldsymbol{P}}+\boldsymbol{q})J_\nu(0)|\bar{B}(\mathbf{0})\rangle\ , \tag{8.27}$$

where $\hat{H}$ and $\hat{\boldsymbol{P}}$ are respectively the QCD Hamiltonian and four-momentum operators and we changed the integration variable from (q^0,q^2) to $(\omega,\boldsymbol{q}^2)$.

Then, we can write the differential decay rate in terms of the contraction between

the hadronic and the leptonic tensor as it was derived in appendix C

$$\begin{aligned}\frac{d\Gamma}{d\boldsymbol{q}^2 d\omega dE_\ell}\frac{8\pi^3}{G_F^2|V_{cb}|^2} &= L_{\mu\nu}W^{\mu\nu} \\ &= -\{(m_B-\omega)^2-\boldsymbol{q}^2\}W_1+\frac{1}{2}\{\boldsymbol{q}^2-(m_B-\omega-2E_\ell)\}W_2 \\ &+2[(m_B-\omega)^2-\boldsymbol{q}^2][2E_\ell-(m_B-\omega)]W_5. \end{aligned} \tag{8.28}$$

We can perform the integral over the lepton energy E_l analytically within the kinematic range $[(q_0-\sqrt{\boldsymbol{q}^2})/2,(q_0+\sqrt{\boldsymbol{q}^2})/2]$, such that we are left with

$$\frac{d\Gamma}{d\boldsymbol{q}^2 d\omega}\frac{24\pi^3}{G_F^2|V_{cb}|^2} = -3(m_B-\omega)^2|\boldsymbol{q}^2|W_1+|\boldsymbol{q}|^2(3W_1+W_2) \tag{8.29}$$

The form factors can be re-written in an alternative basis in the three-dimensional space

$$\hat{\boldsymbol{n}}=\frac{\boldsymbol{q}}{\sqrt{\boldsymbol{q}^2}}\,, \qquad \boldsymbol{\epsilon}^{(a)}\cdot\hat{\boldsymbol{n}}=0\,, \qquad \boldsymbol{\epsilon}^{(a)}\cdot\boldsymbol{\epsilon}^{(b)}=\delta^{ab}\,, \qquad \{a,b\}=\{1,2\}\,. \tag{8.30}$$

As a consequence, we can write the following hadronic quantities in terms of the hadronic tensor's form factors

$$\begin{aligned} Y^{(1)} &= -\sum_{a=1}^{2}\sum_{i,j=1}^{3}\epsilon_i^{(a)}\epsilon_j^{(a)}W^{ij}\,, \qquad Y^{(2)}=W^{00}\,, \qquad Y^{(3)}=\sum_{i,j=1}^{3}\hat{n}^i\hat{n}^jW^{ij}\,, \\ Y^{(4)} &= \sum_{i=1}^{3}\hat{n}^i(W^{0i}+W^{i0})\,, \qquad Y^{(5)}=\frac{i}{2}\sum_{i,j,k=1}^{3}\varepsilon^{ijk}\hat{n}^kW^{ij}\,. \end{aligned} \tag{8.31}$$

Therefore, in the rest frame of the B-meson, all the information contained in the hadronic tensor can be interchangeably parametrised in terms of $Y^{(i)}\equiv Y^{(i)}(\omega,\boldsymbol{q}^2)$.

This will allow us to express the differential decay rate in terms of the $Y^{(i)}$ basis

$$\frac{d\Gamma}{d\boldsymbol{q}^2 d\omega}\frac{24\pi^3}{G_F^2|V_{cb}|^2} = |\boldsymbol{q}|^3(Y^{(1)}+Y^{(2)})-(m_B-\omega)|\boldsymbol{q}|^2Y^{(4)}+(m_B-\omega)^2(Y^{(3)}-Y^{(1)}). \tag{8.32}$$

Looking at both equation 8.29 and equation 8.32, we can see that there is no contribution to the total rate from the anti-symmetric part of the hadronic tensor decomposition. This will not be the case for the lepton energy moments and the other observables we will describe below. However, for now we will focus on completing the derivation of the inclusive calculation for the semileptonic decay rate.

In order to integrate the differential decay rate in equation 8.32, we need to define

its integration limits in terms of the final energy of the charmed hadron states ω and the transfer momentum $\boldsymbol{q}$

$$\omega \in \left[\sqrt{m_D^2 + \boldsymbol{q}^2}, m_B - \sqrt{\boldsymbol{q}^2}\right], \qquad \boldsymbol{q}^2 \in \left[0, \frac{(m_B^2 - m_D^2)^2}{4m_B^2}\right], \tag{8.33}$$

and we can re-write the expression of equation 8.32 in terms of $\omega_{\max}$

$$\frac{d\Gamma}{d\boldsymbol{q}^2 d\omega}\frac{24\pi^3}{G_F^2|V_{cb}|^2} = |\boldsymbol{q}|(\omega_{\max}-\omega)^2(Y^{(3)} - Y^{(1)}) + |\boldsymbol{q}|^2(\omega_{\max}-\omega)(2Y^{(3)} - 2Y^{(1)} - Y^{(4)}) + |\boldsymbol{q}|^3(Y^{(2)} + Y^{(3)} - Y^{(4)}). \tag{8.34}$$

For energies below $\omega_{\min} = \sqrt{m_D^2 + \boldsymbol{q}^2}$ arguments based on flavour and momentum conservation imply that the hadronic tensor vanishes, hence, we can write the correct integral over the phase space introducing the integration kernel

$$\Theta^{(l)}(x) = x^l \theta(x), \tag{8.35}$$

where $x = (\omega_{\max} - \omega)$ and $\theta(x)$ is the Heaviside function. Therefore, the total decay rate for inclusive semileptonic decays can be written as

$$\Gamma = \frac{G_F^2|V_{cb}|^2}{24\pi^3}\int_0^{\boldsymbol{q}_{\max}} d\boldsymbol{q} \sum_{l=1}^{2} |\boldsymbol{q}|^{3-l} \int_0^{\infty} d\omega\ \Theta^{(l)}(\omega_{\max}-\omega) Z^{(l)}(\omega, \boldsymbol{q}), \tag{8.36}$$

where we define $Z^{(l)}(\omega, \boldsymbol{q})$ as a linear combination of the $Y^{(i)}$

$$Z^{(0)} = Y^{(2)} + Y^{(3)} - Y^{(4)}\ , \qquad Z^{(1)} = 2Y^{(3)} - 2Y^{(1)} - Y^{(4)}\ , \qquad Z^{(2)} = Y^{(3)} - Y^{(1)}\ . \tag{8.37}$$

A more compact version of equation 8.36 can be written as

$$\Gamma = \frac{G_F^2|V_{cb}|^2}{24\pi^3}\int_0^{\boldsymbol{q}_{\max}} d\boldsymbol{q} \sum_{l=1}^{2} |\boldsymbol{q}|^{3-l} Z(\boldsymbol{q}^2), \tag{8.38}$$

with

$$Z(\boldsymbol{q}^2) = \int_0^{\infty} d\omega\ \Theta(\omega_{\max}-\omega) Z^{(l)}(\omega, \boldsymbol{q}). \tag{8.39}$$

Finally, it is possible to decompose the differential decay rate $d\Gamma/d\boldsymbol{q}^2$ in different contributions coming from parallel ($\|$) and perpendicular ($\perp$) components. The $\perp$ components are defined as those involving the polarization vector $\epsilon^{*(\alpha)}$, while the $\|$

ones are the rest. In addition, one can also decompose the differential decay rate in terms of the contributions coming from the insertion of vector (V) and axial-vector (A) current. As was already discussed, in the differential rate there is no contribution coming from the terms with AV and VA currents while for the lepton energy moments this is not the case.

8.4.1 Moments

Using the same formalism of the total decay rate, we can also define the moments of some interesting kinematic quantities. Among these, one can certainly count the hadronic mass moments $\langle (M_X^2)^n \rangle$ and the lepton energy moments $\langle E_\ell^{n_\ell} \rangle$, which have been measured experimentally. They are defined as

$$\langle (M_X^2)^n \rangle = \frac{\int d\boldsymbol{q}^2 dq_0 dE_\ell \, (\omega^2 - \boldsymbol{q}^2)^n \left[\frac{d\Gamma}{d\boldsymbol{q}^2 dq_0 dE_\ell} \right]}{\int d\boldsymbol{q}^2 dq_0 dE_\ell \left[\frac{d\Gamma}{d\boldsymbol{q}^2 dq_0 dE_\ell} \right]} , \tag{8.40}$$

$$\langle E_\ell^{n_\ell} \rangle = \frac{\int d\boldsymbol{q}^2 dq_0 dE_\ell \, E_\ell^{n_\ell} \left[\frac{d\Gamma}{d\boldsymbol{q}^2 dq_0 dE_\ell} \right]}{\int d\boldsymbol{q}^2 dq_0 dE_\ell \left[\frac{d\Gamma}{d\boldsymbol{q}^2 dq_0 dE_\ell} \right]} . \tag{8.41}$$

These quantities, like the case of the inclusive decay rate, require an integration over the whole interval of $\boldsymbol{q}^2$. For, this reason, it is convenient to define also differential moments obtained at fixed values of $\boldsymbol{q}^2$

$$H_n(\boldsymbol{q}^2) \equiv \langle (M_X^2)^n \rangle_{\boldsymbol{q}^2} = \frac{\int dq_0 dE_\ell \, (\omega^2 - \boldsymbol{q}^2)^n \left[\frac{d\Gamma}{d\boldsymbol{q}^2 dq_0 dE_\ell} \right]}{\int dq_0 dE_\ell \left[\frac{d\Gamma}{d\boldsymbol{q}^2 dq_0 dE_\ell} \right]} , \tag{8.42}$$

$$L_{n_\ell}(\boldsymbol{q}^2) \equiv \langle E_\ell^{n_\ell} \rangle_{\boldsymbol{q}^2} = \frac{\int dq_0 dE_\ell \, E_\ell^{n_\ell} \left[\frac{d\Gamma}{d\boldsymbol{q}^2 dq_0 dE_\ell} \right]}{\int dq_0 dE_\ell \left[\frac{d\Gamma}{d\boldsymbol{q}^2 dq_0 dE_\ell} \right]} , \tag{8.43}$$

and the second central moment or variance of the lepton energy distribution

$$L_{2c}(\boldsymbol{q}^2) = L_2(\boldsymbol{q}^2) - \Big(L_1(\boldsymbol{q}^2) \Big)^2 .$$

In the case of leptonic moments, the E_ℓ integral is modified with respect to equation 8.28, where an extra power of E_ℓ is added to the integral. Consequently, the

integration over the lepton energy gives

$$\frac{dL_1(\boldsymbol{q}^2)}{d\omega} = \boldsymbol{q}^4 Z^{(0)}_{n_\ell=1}(\omega,\boldsymbol{q}^2) + \boldsymbol{q}^3(\omega_{\max}-\omega)Z^{(1)}_{n_\ell=1}(\omega,\boldsymbol{q}^2) + \boldsymbol{q}^2(\omega_{\max}-\omega)^2 Z^{(2)}_{n_\ell=1}(\omega,\boldsymbol{q}^2) + \boldsymbol{q}(\omega_{\max}-\omega)^3 Z^{(3)}_{n)\ell=1}(\omega,\boldsymbol{q}^2), \tag{8.44}$$

where the $Z^{(l)}_{n_\ell=1}(\omega,\boldsymbol{q}^2)$ are given by

$$Z^{(0)}_{n_\ell=1} = \frac{Y^{(2)}+Y^{(3)}-Y^{(4)}}{2}\,, \qquad Z^{(1)}_{n_\ell=1} = \frac{-2Y^{(1)}+Y^{(2)}+3Y^{(3)}-2Y^{(4)}+2Y^{(5)}}{2}\,,$$
$$Z^{(2)}_{n_\ell=1} = \frac{-3Y^{(1)}+3Y^{(3)}-Y^{(4)}+Y^{(5)}}{2}\,, \qquad Z^{(3)}_{n_\ell=1} = \frac{-Y^{(1)}+Y^{(3)}}{2}\,. \tag{8.45}$$

One can then look at the differences with equation 8.32 and can notice how in equation 8.44 we have the contribution from $Y^{(5)}$ which contains the AV and VA components of the hadronic tensor.

Exactly like for the differential decay rate, we can calculate the first lepton energy moments introducing the integration kernel defined in equation 8.35

$$L_1(\boldsymbol{q}^2) = \sum_{l=0}^{3} \boldsymbol{q}^{4-l} Z^{(l)}_{n_\ell=1}(\boldsymbol{q}^2), \tag{8.46}$$

with

$$Z^{(l)}_{n_\ell=1}(\boldsymbol{q}^2) = \int_0^\infty d\omega\, \Theta^{(l)}(\omega_{\max}-\omega)\, Z^{(l)}_{n_\ell=1}(\omega,\boldsymbol{q}^2)\,. \tag{8.47}$$

Exactly the same procedure is followed for the second energy lepton moment

$$L_2(\boldsymbol{q}^2) = \sum_{l=0}^{4} \boldsymbol{q}^{5-l} Z^{(l)}_{n_\ell=2}(\boldsymbol{q}^2), \tag{8.48}$$

with

$$Z^{(l)}_{n_\ell=2}(\boldsymbol{q}^2) = \int_0^\infty d\omega\, \Theta^{(l)}(\omega_{\max}-\omega)\, Z^{(l)}_{n_\ell=2}(\omega,\boldsymbol{q}^2)\,, \tag{8.49}$$

where

$$
\begin{aligned}
Z^{(0)}_{n_\ell=2} &= 3\frac{Y^{(2)}+Y^{(3)}-Y^{(4)}}{10}\,,\\
Z^{(1)}_{n_\ell=2} &= \frac{7Y^{(1)}-5Y^{(2)}-11Y^{(3)}+8Y^{(4)}-10Y^{(10)}}{10}\,,\\
Z^{(2)}_{n_\ell=2} &= \frac{-27Y^{(1)}+5Y^{(2)}+31Y^{(3)}-15Y^{(4)}+30Y^{(5)}}{20}\,,\\
Z^{(3)}_{n_\ell=2} &= \frac{4Y^{(1)}-4Y^{(3)}+Y^{(4)}-2Y^{(5)}}{4}\,,\\
Z^{(4)}_{n_\ell=2} &= \frac{-Y^{(1)}+Y^{(3)}}{4}\,.
\end{aligned}
\tag{8.50}
$$

For the hadronic moment we have

$$
\bar{H}_{n=1}(\boldsymbol{q}^2)=\sum_{l=0}^{4} Z^{(l)}_{n=1}(\boldsymbol{q}^2)\,,\qquad Z^{(l)}_{n=1}(\boldsymbol{q}^2)=\int_0^\infty d\omega\,\Theta^{(l)}(\omega_{\max}-\omega)\,Z^{(l)}_{n=1}(\omega,\boldsymbol{q}^2)\,,
\tag{8.51}
$$

where the $Z^{(l)}_{n=1}(\omega,\boldsymbol{q}^2)$ are given by

$$
Z^{(0)}_{n=1}=m_B|\boldsymbol{q}|^3(m_B-2|\boldsymbol{q}|)\left(Y^{(2)}+Y^{(3)}-Y^{(4)}\right)\,,
$$

$$
\begin{aligned}
Z^{(1)}_{n=1} &= 2|\boldsymbol{q}|^4\left(Y^{(2)}+Y^{(3)}-Y^{(4)}\right)+m_B^2|\boldsymbol{q}|^2\left(-2Y^{(1)}+2Y^{(3)}-Y^{(4)}\right)\\
&\quad+m_B|\boldsymbol{q}|^3\left[-2\left(Y^{(2)}+Y^{(3)}-Y^{(4)}\right)+2\left(2Y^{(1)}-2Y^{(3)}+Y^{(4)}\right)\right]\,,
\end{aligned}
$$

$$
\begin{aligned}
Z^{(2)}_{n=1} &= m_B^2|\boldsymbol{q}|\left(-Y^{(1)}+Y^{(3)}\right)+|\boldsymbol{q}|^3\left[Y^{(2)}+Y^{(3)}-Y^{(4)}-2\left(2Y^{(1)}-2Y^{(3)}+Y^{(4)}\right)\right]\\
&\quad+m_B|\boldsymbol{q}|^2\left[-2\left(-Y^{(1)}+Y^{(3)}\right)+2\left(2Y^{(1)}-2Y^{(3)}+Y^{(4)}\right)\right]\,,
\end{aligned}
$$

$$
Z^{(3)}_{n=1}=-2m_B|\boldsymbol{q}|\left(-Y^{(1)}+Y^{(3)}\right)+|\boldsymbol{q}|^2\left[-2Y^{(1)}+2Y^{(3)}+2\left(-Y^{(1)}+Y^{(3)}\right)-Y^{(4)}\right]\,,
$$

$$
Z^{(4)}_{n=1}=|\boldsymbol{q}|\left(-Y^{(1)}+Y^{(3)}\right)\,.
\tag{8.52}
$$

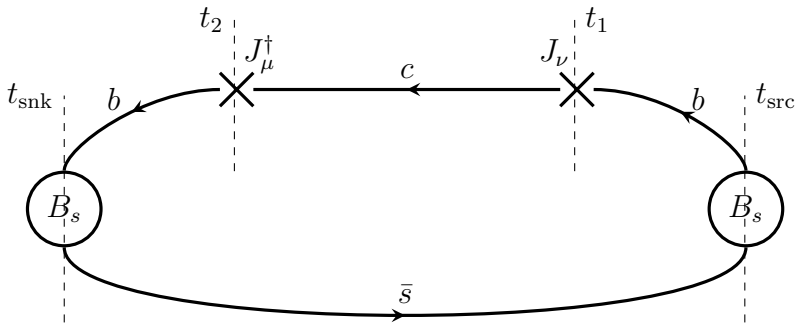

Figure 8.3: Schematic representation of the four-point Euclidean correlation function defined in eq. (8.53). The crosses represent the insertions of the weak currents at times t_1 and t_2, the meson states are created at time $t_{\rm src}$ and annihilated at time $t_{\rm snk}$. Between the currents we have the propagation of the charm quark, hence, the piece of the correlation functions defined between the currents contained all the possible charmed states X_c.

8.5 Inclusive decays from Euclidean correlation functions

The decay rate can be calculated on the lattice following the strategy introduced in ref. [187, 2], where the differential decay rate is given after the integration over ω and the integration kernel $\Theta^{(l)}(\omega_{\rm max} - \omega)$.

In order to perform such calculation, we need to compute four-point lattice correlation functions in which we have a double insertion of the weak current J^μ, as shown in figure 8.3. The four-point Euclidean correlator can then be defined as

$$C_{\mu\nu}(t_{\rm snk}, t_2, t_1, t_{\rm src}; \boldsymbol{q}) = \int d^3x\, e^{i\boldsymbol{q}\cdot\boldsymbol{x}}\, T\langle 0|\, \tilde{\phi}_B(\mathbf{0}; t_{\rm snk}) J_\mu^\dagger(\boldsymbol{x}; t_2) J_\nu(\mathbf{0}; t_1) \tilde{\phi}_B^\dagger(\mathbf{0}; t_{\rm src})\, |0\rangle \ , \tag{8.53}$$

where $\tilde{\phi}_B(\mathbf{0}; t)$ is a B-meson creation/annihilation operator projected onto zero spatial momentum by integrating over space at a time t.

A B-meson state with zero spatial momentum is then created at time $t_{\rm src}$ and annihilated at $t_{\rm snk}$. The two currents are inserted in between, at times t_2 and t_1. The charmed hadrons are created at time t_1 with a momentum insertion $-\boldsymbol{q}$ and propagate until they are transformed back to the B meson state at time t_2.

The four-point function $C_{\mu\nu}$ is saturated by the B-meson non-local matrix element

$$M_{\mu\nu}(t; \boldsymbol{q}) = e^{-m_B t} \int d^3x\, \frac{e^{i\boldsymbol{q}\cdot\boldsymbol{x}}}{2m_B} \langle \bar{B}(\mathbf{0}) | J_\mu^\dagger(\boldsymbol{x}, t) J_\nu(\mathbf{0}, 0) | \bar{B}(\mathbf{0}) \rangle \ , \tag{8.54}$$

when the double limit $t_{\mathrm{src}} \to -\infty$, $t_{\mathrm{snk}} \to \infty$ is taken. To include a proper normalization, one can analyse

$$M_{\mu\nu}(t_2 - t_1; \boldsymbol{q}) = Z_B \lim_{\substack{t_{\mathrm{snk}} \to +\infty \\ t_{\mathrm{src}} \to -\infty}} \frac{C_{\mu\nu}(t_{\mathrm{snk}}, t_2, t_1, t_{\mathrm{src}}; \boldsymbol{q})}{C(t_{\mathrm{snk}} - t_2) C(t_1 - t_{\mathrm{src}})} \,, \tag{8.55}$$

where $C(t)$ is the time-ordered B-meson two-point function

$$C(t) = T\langle 0|\, \tilde{\phi}_B(\mathbf{0}; t) \tilde{\phi}_B^\dagger(\mathbf{0}; 0)|0\rangle \tag{8.56}$$

and Z_B is its residue when a large time separation is taken, $C(t) \to Z_B e^{-m_B t}$.

It is possible to find a relation between the hadronic tensor in its spectral representation, defined in equation 8.27, and $M_{\mu\nu}(t; \boldsymbol{q})$

$$\begin{aligned} M_{\mu\nu}(t; \boldsymbol{q}) &= \int d^3x \, \frac{e^{i\boldsymbol{q}\cdot\boldsymbol{x}}}{2m_B} \langle \bar{B}(\mathbf{0})| J_\mu^\dagger(\mathbf{0},0) e^{-t\hat{H} + i\hat{\boldsymbol{P}}\cdot\boldsymbol{x}} J_\nu(\mathbf{0},0)|\bar{B}(\mathbf{0})\rangle \\ &= \frac{(2\pi)^3}{2m_B} \langle \bar{B}(\mathbf{0})| J_\mu^\dagger(\mathbf{0},0) e^{-t\hat{H}} \delta^3(\hat{\boldsymbol{P}} + \boldsymbol{q}) J_\nu(\mathbf{0},0)|\bar{B}(\mathbf{0})\rangle \\ &= \int_0^\infty d\omega \, W_{\mu\nu}(\omega, \boldsymbol{q}) \, e^{-\omega t} \,. \end{aligned} \tag{8.57}$$

Hence, one can obtain the hadronic tensor from lattice correlation function by solving the inverse problem defined in equation 8.57. In fact, the four-point correlation function following the normalisation by equation 8.56, is nothing else than a two-point correlation function defined between the two current insertion and hence dependent *only* on their time separation, in which all the possible charmed states X_c propagate. Therefore, extracting the hadronic tensor from equation 8.53 is *equivalent* of extracting the spectral density from a two-point correlation function which contains all the charmed states X_c.

It is clear then that the problem we face is in many ways similar to those faced in chapter 7, where we discussed how to extract spectral functions from two-point lattice correlators. Once again, we need to face an ill-posed inverse problem due to the fact that our lattice correlators have a non-zero statistical noise. The only difference compared to the problems of chapter 7 is that the kernel which defines the integration over the energy ω is not a delta-function but instead a Heaviside function, which is required in order to integrate correctly over the phase space of the inclusive decay.

As discussed in chapter 7, there are now many different methods that allow to overcome the ill-posed problem of an inverse Laplace transform, each with its own benefits and drawbacks. In this work we decided to use the one introduced in ref. [149]

known as HLT method. The HLT requires the introduction of smeared kernels in order to perform the reconstruction of the spectral density, or in this case of the components of the hadronic tensor. Hence, we defined a smeared version of the integration kernel $\Theta^{(l)}(\omega_{\max} - \omega)$

$$\Theta^{(l)}_{\sigma}(\omega_{\max} - \omega) = m_B^l \sum_{\tau=1}^{\infty} g^{(l)}_{\tau}(\omega_{\max}, \sigma)\, e^{-a\omega\tau} \,, \tag{8.58}$$

and

$$\int_0^{\infty} d\omega\, W_{\mu\nu}(\omega, \boldsymbol{q})\, \Theta^{(l)}(\omega_{\max} - \omega) = \lim_{\sigma\to 0} m_B^l \sum_{\tau=1}^{\infty} g^{(l)}_{\tau}(\omega_{\max}, \sigma)\, M_{\mu\nu}(a\tau; \boldsymbol{q}) \,, \tag{8.59}$$

As was already discussed in section 7.2.1, one of the fundamental step of the method is the ordered double limit defined in equation 7.30. In order to improve the quality of the extrapolation $\sigma \to 0$, it is convenient to define more than one smeared kernel as it was noticed in ref. [151]. Naturally, in the limit $\sigma \to 0$ all the kernels defined below will tend to the same, that is the unsmeared $\Theta^{(l)}(\omega_{\max} - \omega)$ kernel. The different kernels considered in this work are

$$\theta^{\mathtt{s}}_{\sigma}(x) = \frac{1}{1 + e^{-\frac{x}{\sigma}}} \,, \qquad \theta^{\mathtt{s1}}_{\sigma}(x) = \frac{1}{1 + e^{-\sinh\left(\frac{x}{r^{\mathtt{s1}}\sigma}\right)}} \,, \qquad \theta^{\mathtt{e}}_{\sigma}(x) = \frac{1 + \operatorname{erf}\left(\frac{x}{r^{\mathtt{e}}\sigma}\right)}{2} \,. \tag{8.60}$$

In the following we shall refer to $\theta^{\mathtt{s}}_{\sigma}(x)$ as the "sigmoid function", to $\theta^{\mathtt{s1}}_{\sigma}(x)$ as the "modified sigmoid function" and to $\theta^{\mathtt{e}}_{\sigma}(x)$ as the "error function". The parameters $r^{\mathtt{s1}}$ and $r^{\mathtt{e}}$ appearing in the previous formulae have been set to the values $r^{\mathtt{s1}} = 2.2$ and $r^{\mathtt{e}} = 2.0$ in order to produce similar (albeit not identical) shapes at finite values of σ for the different kernels. The numerical reconstruction of these three kernels is shown in figure 8.7

Another important issue to highlight is the fact that the smearing procedure is not only necessary in order to apply the HLT algorithm, but it is also necessary for theoretical reasons. Hadronic spectral densities, and therefore also $W_{\mu\nu}(\omega, \boldsymbol{q})$, are elements in the space of distributions and their product with another distribution, such as the θ-function, can only be defined through a regularisation procedure (when it exists). As we have discussed in chapter 7, finite volume spectral densities are composed by a distribution of δ-functions due to the quantisation of the energy spectrum. The connection between finite volume distributions and physical quantities can only be obtained following the ordered double limit defined in equation 7.30.

a (fm)	m_π (MeV)	$L^3 \times T$	$N_{\rm cnfg}$
0.0815(30)	375(13)	$32^3 \times 64$	150

Table 8.2: Details of the B55.32 ETMC gauge ensemble with $N_f = 2+1+1$ dynamical quarks and $m_\pi L \simeq 5.0$ generated in ref. [188, 189]. The number of analyzed gauge configurations, separated by 20 trajectories, is 150.

8.5.1 Lattice QCD calculation

The ETMC gauge ensemble used in this work is the one named B55.32, generated by ETMC together with other 14 ensembles with $N_f = 2 + 1 + 1$ dynamical quarks in refs. [188, 189] for determining the average up/down, strange and charm quark masses.

The actions used to simulate the gluons and the dynamical quarks in the configurations were the Iwasaki action [55] and the Wilson twisted-mass action [42, 47, 52], respectively. Using the mass renormalisation constants determined in ref. [190] the physical light, strange, and charm quark masses were found to be $m_{ud}^{\rm phys}(\overline{\rm MS}, 2\,{\rm GeV}) = 3.70(17)$ MeV, $m_s^{\rm phys}(\overline{\rm MS}, 2\,{\rm GeV}) = 99.6(4.3)$ MeV, and $m_c^{\rm phys}(\overline{\rm MS}, 2\,{\rm GeV}) = 1176(39)$ MeV, respectively.

As it was discussed extensively in section 3.3, in order to avoid the mixing of K- and D-meson states in the correlation functions, in the valence sector we used a non-unitary setup [48], such that the strange and charm valence quarks are simulated according to the Osterwalder-Seiler fermions [51], while the up and down valence quarks were regularised using the Twisted Mass action. The details about the gauge configurations are summarised in table 8.2,

The simulations of quark propagators were performed with valence quark masses $a\mu_s = 0.021$ and $a\mu_c = 0.25$ which correspond to renormalised strange and charm quark masses very close to their physical values. On the other hand, as it was already argued in section 4.3, the bottom quark could not be simulated at its physical value and for this reason we calculated two-point function using the interpolating operator $\overline{b}(x)\gamma_5 s(x)$ with a simulated b-quark mass equal to twice the physical charm mass, i.e. $m_b(\overline{\rm MS}, 2\,{\rm GeV}) \simeq 2.4$ GeV.

In order to improve the statistical precision of our correlation functions, we used the "one-end trick" stochastic method [34, 33] with 10 randomly chosen stochastic sources at a randomly chosen time-slice per gauge configuration. Then, in order to guarantee that cutoff effects on the pseudo-scalar mass are $O(a^2\mu_f)$, we set opposite Wilson parameters for the two valence quarks [52, 53, 191]. Moreover, in order to suppress contributions of the excited states in the B_s-meson correlation function, we

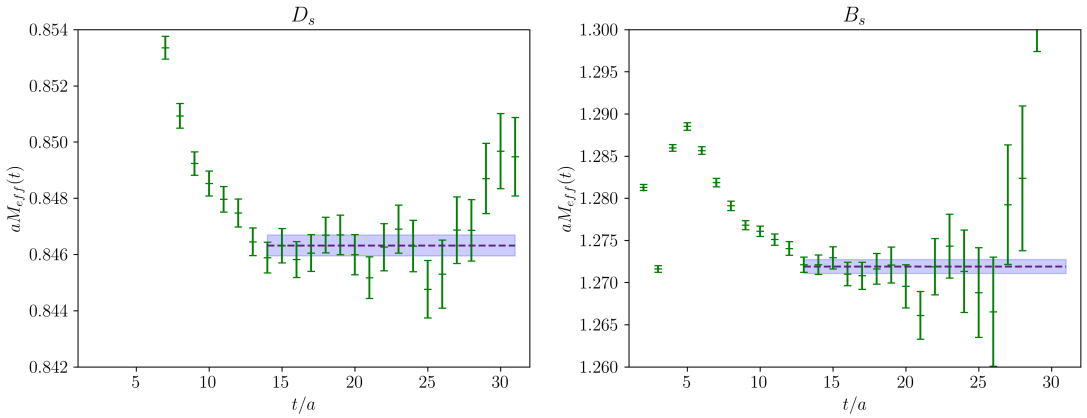

Figure 8.4: Effective mass $aM_{\text{eff}}(t) \equiv \log\left(C(t)/C(t+a)\right)$ in lattice units for the D_s-meson (left panel) and the B_s-meson (right panel) correlation function (8.56), evaluated using the ETMC gauge ensemble B55.32 for bare quark masses equal to $a\mu_b = 0.50$, $a\mu_c = 0.25$ and $a\mu_s = 0.021$, corresponding to renormalised quark masses $m_b(\overline{\text{MS}}, 2\,\text{GeV}) \simeq 2.4$ GeV, $m_c(\overline{\text{MS}}, 2\,\text{GeV}) \simeq 1.2$ GeV and $m_s(\overline{\text{MS}}, 2\,\text{GeV}) \simeq 100$ MeV. The values of the Wilson r-parameter of the two valence quarks are opposite, i.e. $r_c = -r_s$ in the D_s meson and $r_b = -r_s$ in the B_s meson.

have used Gaußian smeared interpolating quark fields [30] both at the source and at the sink, as it is shown in figure 3.1. The results for both the D_s and B_s two-point correlation functions are shown in figure 8.4 For the values of the smearing parameters we set $k_G = 4$ and $N_G = 30$. In addition, the APE smearing was applied to the gauge links [56] with $\alpha_{\text{APE}} = 0.5$ and $N_{\text{APE}} = 20$.

By averaging over the plateau regions shown in fig. 8.4, the fits of two-point correlators give the values for the ground-state masses to be respectively $m_{D_s} = 2.05(8)$ GeV and $m_{B_s} = 3.08(11)$ GeV.

The four-point lattice correlation functions defined in equation 8.53 are obtained by inserting the first weak current at time t_1, with fixed values for the pseudo-scalar interpolator to be $t_{\text{src}} = 0$ and $t_{\text{snk}} = T/2 = 32a$. The momentum is inserted together with the weak currents along only one spatial direction $\boldsymbol{q} = (0, 0, q)$, with eleven values ranging from $q = 0$ up to $q = q_{\text{max}} \simeq 0.9$ GeV. On the lattice, the momentum values are inserted using twisted boundary conditions (BC's) [36, 37, 38] in the spatial directions and anti-periodic BC's in time. For the sea quarks the BC are inverted with periodic BC's in the spatial directions while anti-periodic in time. The main advantage of using the twisted BC's for the valence quarks is that it lifts the limits of only simulating fermions with momentum values corresponding to integer multiples of $2\pi/L$. In refs. [192, 193] it was shown that for physical quantities which do not involve final-state interactions the use of different BC's for valence and sea quarks produces

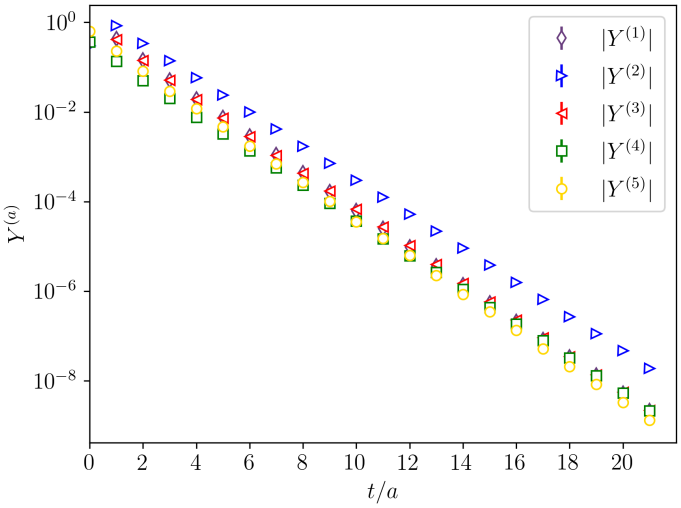

Figure 8.5: Time dependence of the correlators $Y^{(i)}(t;\boldsymbol{q})$ for $|\boldsymbol{q}| \simeq 0.5$ GeV calculated on the ETMC ensemble B55.32. The error bars are smaller than the point markers on this scale and a similar quality of the numerical signal is observed for the other momentum values considered in this work.

only finite-size effects that are exponentially small.

The weak currents are simulated using local vector and axial-vector quark currents, $\bar{b}(x)\gamma_\mu c(x)$ and $\bar{b}(x)\gamma_\mu\gamma_5 c(x)$. In the simulations performed in order to get the four-point correlators, the value of the Wilson r-parameter for the charm quark is chosen to be opposite to that of the b quark, i.e. $r_c = -r_b$, and therefore in our maximally twisted setup the vector and axial-vector currents renormalise respectively with the axial and vector renormalisation constants, Z_A and Z_V, determined in ref. [190].

We extract the matrix elements $M_{\mu\nu}(t_2 - t_1;\boldsymbol{q})$ using eq. (8.55). In order to calculate the differential decay rate we first need to decompose the hadronic tensor i the independent components $Y^{(i)}$ as it was discussed in the previous section, and then we can apply the smearing kernel $\Theta^{(l)}(\omega_{\max} - \omega)$ to the quantities $Z^{(l)}(\omega, \boldsymbol{q}^2)$, obtained from equation 8.37. Decomposing $M_{\mu\nu}(t_2 - t_2;\boldsymbol{q})$, we can define the following objects

$$
\begin{aligned}
Y^{(i)}(t;\boldsymbol{q}^2) &= \int_0^\infty d\omega\, Y^{(i)}(\omega,\boldsymbol{q}^2)\, e^{-\omega t}\,, \qquad a = 1,\cdots,5\,, \\
Z^{(l)}(t;\boldsymbol{q}^2) &= \int_0^\infty d\omega\, Z^{(l)}(\omega,\boldsymbol{q}^2)\, e^{-\omega t}\,, \qquad l = 0,1,2\,.
\end{aligned}
\tag{8.61}
$$

In order to show the numerical precision of the lattice correlation functions obtained for this work, we plot the correlators $Y^{(i)}(t;\boldsymbol{q})$ in the plot shown in figure 8.5, with injected momentum $|\boldsymbol{q}| \simeq 0.5$ GeV. Similar results are obtained for the other momenta

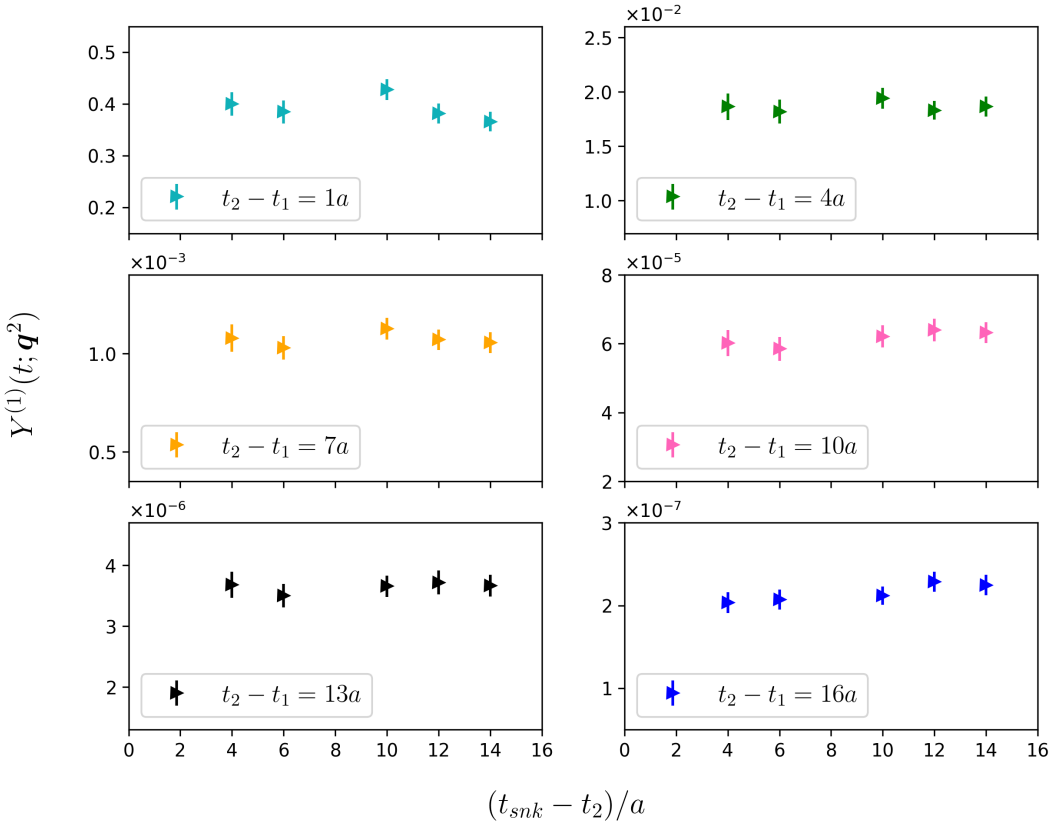

Figure 8.6: Correlator $Y^{(1)}(t, \boldsymbol{q}^2)$ at various time separations $t_2 - t_1$ for $|\boldsymbol{q}| \simeq 0.5$ GeV. The points in each sub-plot are obtained for different values of t_2, with the x-axis showing the distance between t_{snk} and the time t_2 at which the current is inserted.

considered in this work.

An important study to be performed when working with four-point correlation functions is to investigate possible contaminations coming from the excited states of the meson states defined at t_{snk} and t_{src}. In this section the main results we show are obtained setting $t_2 = 22a$ and $t = 18a$, which correspond to a time separation of $t_1 - t_{\text{src}} = 4a$. However, in order to check the correct limits $t_{\text{src}} \to -\infty$ and $t_{\text{snk}} \to \infty$, we repeated the analysis by setting $t_2 = \{18a, 20a, 22a, 26a, 28a\}$ and by varying the maximum value of t used to reconstruct the smearing kernels. This allowed us to variate the time separation between the current insertion times and the time at which the B meson states are defined. In order to check that there are no contributions affecting our $Y^{(i)}$ correlators, we show the plots in figure 8.6 where we compare the correlator $Y^{(1)}(t, \boldsymbol{q})$ at $|\boldsymbol{q}| \simeq 0.5$ GeV for different values of $t = t_2 - t_1$ and t_2. Similar results are obtained for the other correlators ($Y^{(2)}$, $Y^{(3)}$, $Y^{(4)}$ and $Y^{(5)}$), and, in all cases, we

observe that the onset of the $t_{\rm snk} \to \infty$ limit is reached within the uncertainties already for $t_{\rm snk} - t_2 = 4a$. Following this considerations, we chose the value $(t_{\rm snk} - t_2) = 10a$, corresponding to $t_2 = 22a$.

We now turn to the discussion of the systematics associated with the approximation of the kernels of eq. (8.60) by using the HLT method of ref. [149]. As it was thoroughly described in section 7.2.1, this is an important issue because, on the one hand, the reconstruction of a given kernel can never be exact with a finite number of time-slices and in the presence of errors. On the other hand, one can (and must) quantify the systematic error associated with an approximate reconstruction.

In order to study the systematic errors associated to the reconstruction of the spectral density, we considered the quantity $Z_\sigma^{(0)}(\boldsymbol{q}^2)$ (defined in equation (8.39)), for all the three smooth kernels given in equation 8.60. Following equation 8.59, we can get $Z_\sigma^{(0)}(\boldsymbol{q}^2)$ applying the coefficients g_τ^λ coming from the HLT algorithm (equation 7.40), which represents the approximated kernel at a fixed value of λ, to the correlator $Z^{(0)}(t; \boldsymbol{q}^2)$.

In figure 7.1, we showed how we can estimate the systematic errors coming from the reconstruction with the HLT algorithm. Because of the Backus-Gilbert regularisation on which the method is based, the results of the reconstruction will have a larger statistical error as we get closer to a better reconstruction. Vice versa, the central values of the reconstructions obtained with a large value of $d(\boldsymbol{g}^*)$ will have a smaller error but with the price of deviating a lot from the other values. In fig. 8.8 we replicate the stability analysis for the reconstructed value of $Z_\sigma^{(0)}(\boldsymbol{q}^2)$, which shows how the results obtained with different choice of smeared kernel all converge to the same region of normalised L_2-norm $A[g^\lambda]/A[0]$, within the statistical errors. There is no significant difference on the final results for $Z_\sigma^{(0)}(\boldsymbol{q})$ by decreasing λ with respect to $\lambda_\star$, which is the value that we pick as our final result for $Z_\sigma^{(0)}(\boldsymbol{q})$, and we repeat this procedure for all the other components $Z_\sigma^{(1)}(\boldsymbol{q}), Z_\sigma^{(2)}(\boldsymbol{q})$. By implementing this strategy, proposed in ref. [151], we have checked that the estimated errors on the different quantities that enter our determinations of the physical observables discussed below properly take into account the systematics associated with the kernel approximation.

In fig. 8.9 we show our results for the total decay rate, with the different points corresponding to different input parameters used in the analysis, as described in the figure's caption. The plot shows clearly that all results are compatible with each other. In order to take into account all the results showed in the figure, we use eq. (28) of ref. [190] to get an estimate of the central value and its standard deviation, corresponding to the filled red dots in the plot, and we quote that value as our final result for the total decay rate. This procedure is repeated for all other observables considered in this

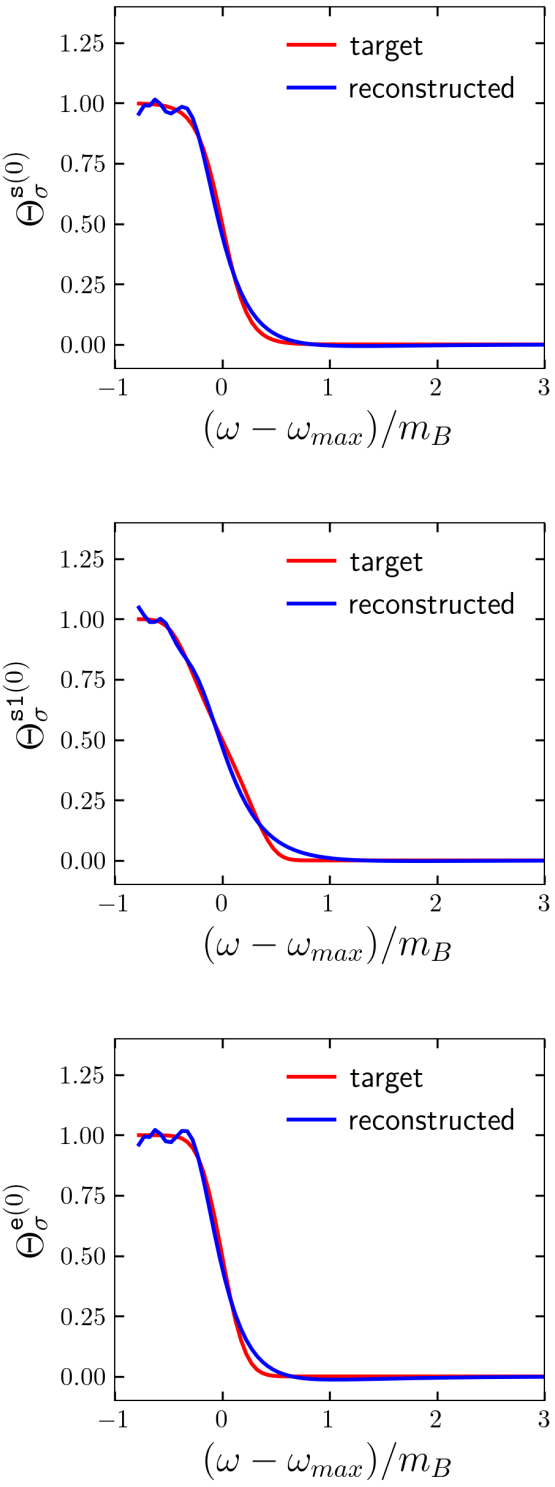

Figure 8.7: Reconstruction of the kernels $\Theta_\sigma^{(0)}(\omega_{\rm max}-\omega)$ defined with the three smearing types `s`, `s1` and `e`, see eq. (8.60), at $\lambda = \lambda_\star$. The data correspond to $|\boldsymbol{q}| \simeq 0.7$ GeV and $\sigma = 0.12 m_{B_s}$, the smallest value of the smearing parameter that we used.

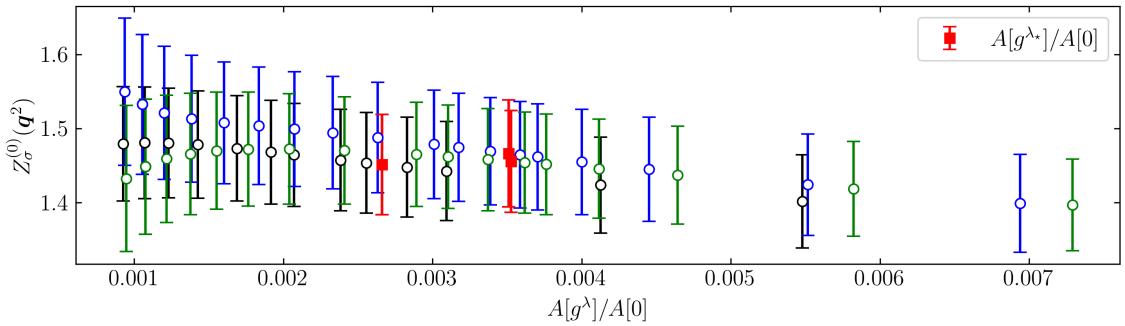

Figure 8.8: Integral $\bar{Z}_\sigma^{(0)}(\boldsymbol{q})$ of the hadronic correlator with three kernels, plotted as a function of $A[g^\lambda]/A[0]$. No significant difference is observed within the statistical errors for values $A[g^\lambda]/A[0]$ smaller than $A[g^{\lambda_\star}]/A[0]$.

work.

8.5.2 Extrapolation to $\sigma = 0$

All our results for the several observables considered in this section were obtained applying the HLT method with several values of the smearing parameter σ, for each of the smeared kernels $\Theta^{(l)}(x)$ with three different smeared versions of the θ-function in equation. 8.60. Following the HLT procedure, we use all these results in a combined $\sigma \to 0$ extrapolation for each contribution to the differential decay rate and to the leptonic and hadronic moments.

Now, as was already mentioned in this document, the limits of zero smearing radius and of infinite volume do *not* commute. Due to the quantisation of the energy spectrum in a finite volume, the $\sigma \to 0$ extrapolation must be performed only after the infinite-volume limit. However, considering the fact that all our results are obtained with a single physical volume, as shown in table 8.2, under the reasonable assumption that smeared QCD spectral densities are affected by exponentially suppressed finite-volume effects, we can safely assume that finite-volume effects are negligible with respect to our statistical uncertainties. Naturally, this assumption can only be verified performing the same simulation described in this section on larger volumes. This is something that the we are currently investigating and that unfortunately, due to the long time required by lattice QCD simulations could not have been finished before the compilation of this document. Examples of the correct ordered double limit can be found in refs. [153, 151].

In fig. 8.10 we show the $\sigma \to 0$ extrapolations of the three contributions $Z_\sigma^{(l)}(\boldsymbol{q}^2)$ to the differential decay rate for $|\boldsymbol{q}| \simeq 0.5$ GeV (plots on the left) and $|\boldsymbol{q}| \simeq 0.7$ GeV (plots on the right). The reconstruction of the kernels $\Theta_\sigma^{(0)}(\omega_{\max} - \omega)$ is more challenging from the numerical point of view with respect to the case of the kernels $\Theta_\sigma^{(l)}(\omega_{\max} - \omega)$ with

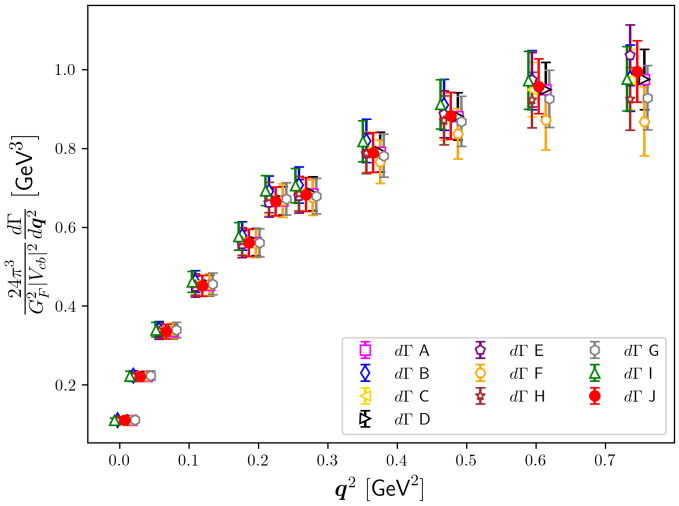

Figure 8.9: Results for $\frac{24\pi^3}{G_F^2|V_{cb}|^2}\frac{d\Gamma}{dq^2}$, obtained changing the parameters given as input to our analysis. The default values are: $A_{tr} = 1\times10^{-3}$, $\tau_{max} = 18$, extrapolations to $\sigma = 0$ using 5 values of σ. A_{tr} is defined in appendix B. The letters in the legend stand for: **A)** All parameter equal to default, the final result is given by extrapolating to $\sigma = 0$ the single components $X^{(i)}$ and then summing the extrapolations together. **B)** The same as case **(A)** but with extrapolations done employing all 10 values of σ, as quoted in the caption of fig. 8.10. **C)** A threshold changed to $A_{tr} = 1 \times 10^{-2}$. **D)** A threshold changed to $A_{tr} = 5 \times 10^{-3}$. **E)** All parameters equal to default, final result given by summing all the single contributions $X^{(i)}$ together and then extrapolation the sum to $\sigma = 0$. **F)** τ_{max} changed to $\tau_{max} = 15$. **G)** τ_{max} changed to $\tau_{max} = 16$. **H)** τ_{max} changed to $\tau_{max} = 17$. **I)** Same as default, analysis performed using the bootstrap method. **J)** Final results obtained considering all previous results listed here. Central value and standard deviation are calculated using the average procedure given by eq. (28) of ref. [190]. It is important to note that the analysis of all the cases listed above is performed taking the result corresponding to $\lambda = \lambda_\star$, the only exception being when we change the A_{tr} parameter. In these two cases we take the results corresponding to values of $A[g^\lambda]/A[0]$ smaller than A_{tr}.

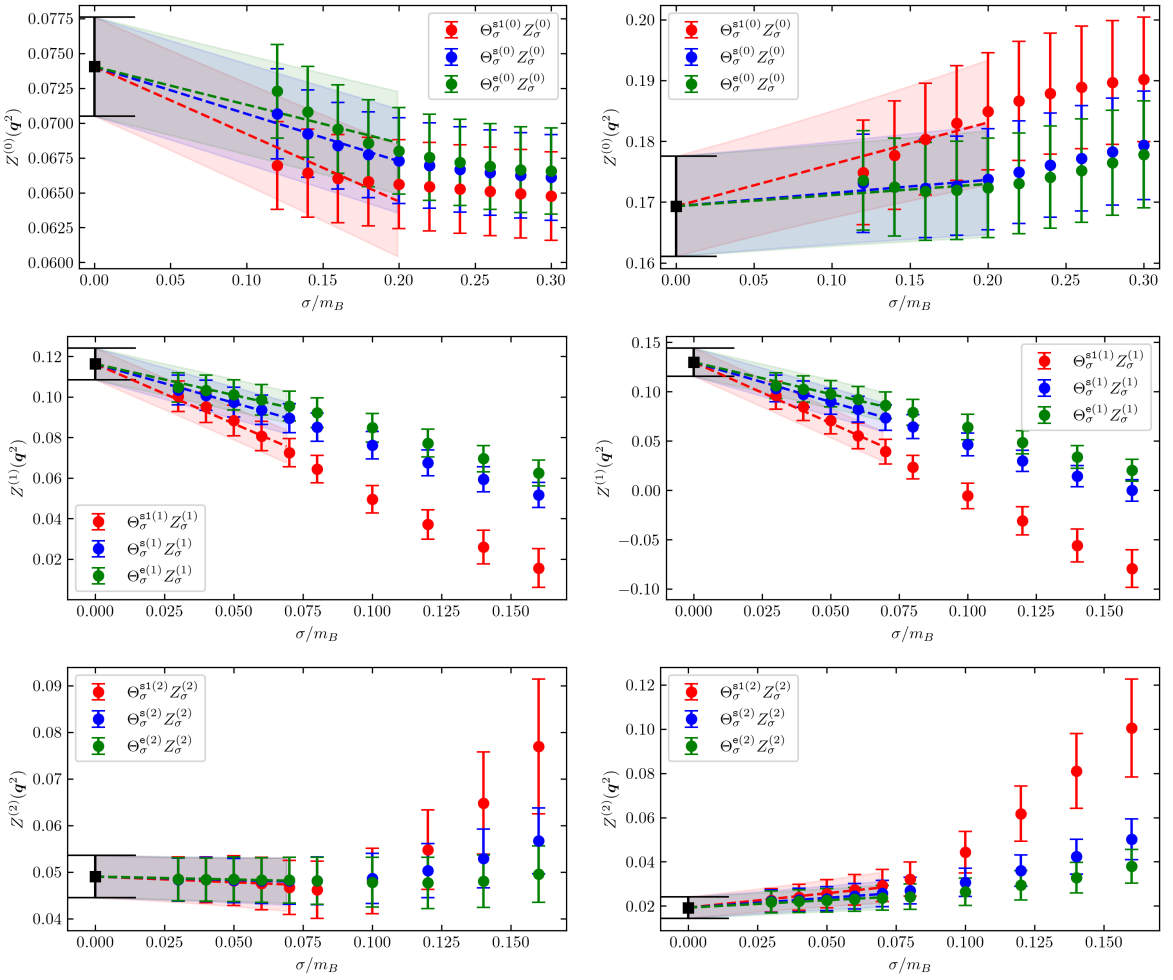

Figure 8.10: Combined $\sigma \to 0$ extrapolations of three contributions $Z^{(l)}(\boldsymbol{q}^2)$ to the differential decay rate, see eq. (8.39). The plots on the left correspond to $|\boldsymbol{q}| \simeq 0.5$ GeV while those on the right to $|\boldsymbol{q}| \simeq 0.7$ GeV. The reconstruction of the kernels $\Theta_\sigma^{(0)}(\omega_{\max} - \omega)$ is more difficult from the numerical point of view w.r.t. the case of the kernels $\Theta_\sigma^{(l)}(\omega_{\max} - \omega)$ with $l = 1, 2$. In all cases we have obtained results at 10 different values of σ that, in the case of $\Theta_\sigma^{(0)}(\omega_{\max} - \omega)$ span the region $\sigma \in [0.12 m_{B_s}, 0.3 m_{B_s}]$ while in the other case we have $\sigma \in [0.03 m_{B_s}, 0.16 m_{B_s}]$. In all cases we include the five smallest values of σ into a combined linear extrapolation to quote our results at $\sigma = 0$.

$l = 1, 2$. In all cases studied in this work we have obtained results at ten different values of σ that, for the kernel $\Theta_\sigma^{(0)}(\omega_{\max} - \omega)$ span the region $\sigma \in [0.12 m_{B_s}, 0.3 m_{B_s}]$ while for the other kernels we have $\sigma \in [0.03 m_{B_s}, 0.16 m_{B_s}]$. At all of the values of $\boldsymbol{q}^2$ we have included the five smallest σ values into a combined linear extrapolation to quote our results at $\sigma = 0$. As it is evident from the plots in fig. 8.10 there is a reassuring convergence of the results corresponding to the different kernels for small values of σ and the points included in the fit are always in the linear regime. This is the case also for the other values of momenta analyzed in this work. The χ^2/d.o.f. for all the $\sigma \to 0$ extrapolations performed in this work never exceed 1. In order to quantify the systematic error associated to the $\sigma \to 0$ extrapolation, we performed unconstrained linear extrapolations for the smallest five values of σ followed by an unconstrained quadratic extrapolation of all 10 points shown in the plots. This procedure is shown in figure 8.11, where one can see the unconstrained extrapolations for the results appearing also in the top-left panel of figure 8.10. In the plot of figure 8.11, we indicate the result of the combined linear extrapolation that we quote as our final value as the black point. From the plot one can can see how the results of the unconstrained linear extrapolations as well as the combined quadratic extrapolation are all compatible with each other within the uncertainties.

The final systematic error associated with the extrapolation $\sigma \to 0$ can be estimated following the method described in the caption of figure 8.9, where we combine in quadrature the statistical error of the combined linear extrapolation (black point) and the difference between the central values of the black and violet point representing the combined quadratic extrapolation. Looking at the plot in figure 8.11, one can see how this procedure largely takes into account the spread of the results coming from the different extrapolations, including the unconstrained ones. The same procedure has been repeated for all the sets of data analyzed in this work and similar plots can be shown in all cases.

In fig. 8.12 we show the $\sigma \to 0$ extrapolations of the four different terms that enter the calculation of the leptonic moment $L_1(\boldsymbol{q}^2)$.

8.6 Comparison between lattice QCD and OPE

In this section all the original work concerns the lattice calculations of the inclusive quantities defined in section 8.4 obtained from four-point correlation functions. Here we briefly summarise the OPE approach but we also highlight that all the OPE calculations were performed by Sandro Mächler and Paolo Gambino. The reason behind

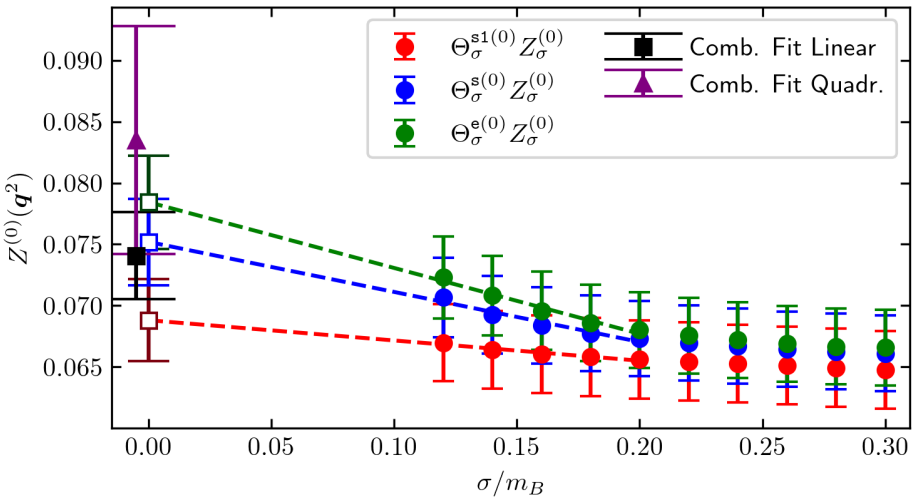

Figure 8.11: Systematics associated with the $\sigma \to 0$ extrapolation of $Z^{(0)}(\boldsymbol{q}^2)$ at $|\boldsymbol{q}| \simeq 0.5$ GeV, the same set of data shown in the top–left panel of fig. 8.10. The unconstrained linear extrapolations of the different sets of data, corresponding to the three different smearing kernels, are shown together with the results of the combined linear extrapolation of the five points at the smaller values of σ (black point) and of the combined quadratic extrapolation including all ten values of σ (violet point). The black and violet points have been slightly displaced on the horizontal axis to help the eye.

the inclusion of their results in this thesis is so that one can appreciate the comparison between the lattice QCD results and those obtained with the OPE.

The operator product expansion is a particularly useful method for computing observables which are sufficiently inclusive to admit a double expansion in α_s and in inverse powers of m_b [194, 184, 185, 186, 195], or more precisely of the energy release, which is of the order of $m_b - m_c$. For a generic observable M, one can get the expansion

$$\begin{aligned} M =& M^{(0)} + M^{(1)} a_s + M^{(2)} a_s^2 + \left(M_\pi^{(0)} + M_\pi^{(1)} a_s \right) \frac{\mu_\pi^2}{m_b^2} \\ &+ \left(M_G^{(0)} + M_G^{(1)} a_s \right) \frac{\mu_G^2}{m_b^2} + M_D^{(0)} \frac{\rho_D^3}{m_b^3} + M_{LS}^{(0)} \frac{\rho_{LS}^3}{m_b^3} + \dots \end{aligned} \tag{8.62}$$

where $a_s = \alpha_s(\mu)/\pi$ is the QCD coupling evaluated at a scale $\mu \sim m_b$ and the ellipsis represents higher-order terms in a_s and in $1/m_b$. The parameters μ_π^2, μ_G^2, ρ_D^3, ρ_{LS}^3 are expectation values of dimension-5 and dimension-6 local operators in the physical B meson. For instance,

$$\mu_\pi^2(\mu_k) = \frac{1}{2M_B} \langle B | \bar{b}_v \, \vec{\pi}^2 \, b_v | B \rangle_{\mu_k}, \qquad \mu_G^2(\mu_k) = \frac{1}{2M_B} \langle B | \bar{b}_v \frac{i}{2} \sigma_{\mu\nu} G^{\mu\nu} b_v | B \rangle_{\mu_k} \tag{8.63}$$

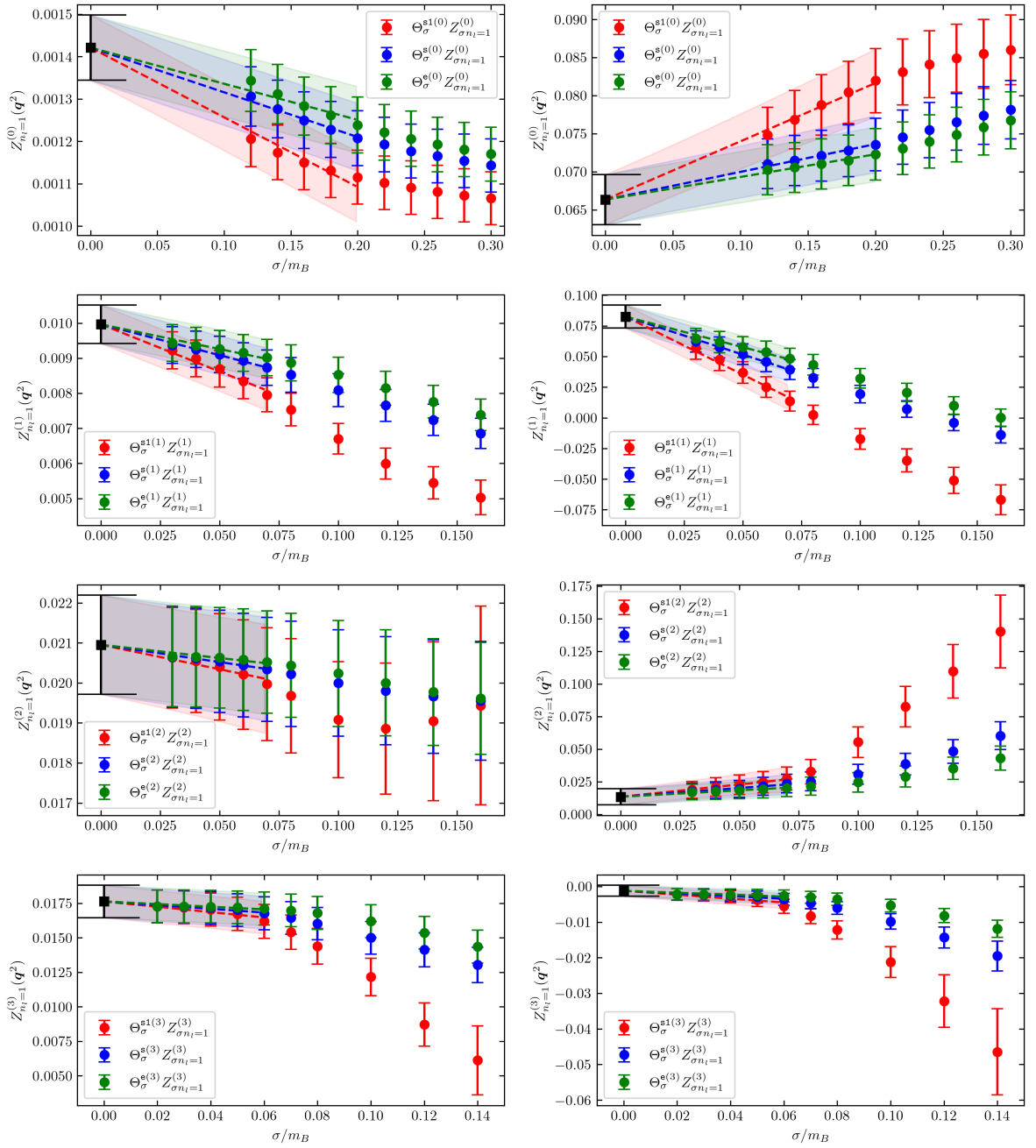

Figure 8.12: Combined $\sigma \to 0$ extrapolations of the four contributions $Z^{(l)}_{n_\ell=1}(\boldsymbol{q}^2)$ to the first leptonic moment, see eq. (8.47). The plots on the left correspond to $|\boldsymbol{q}| \simeq 0.26$ GeV while those on the right to $|\boldsymbol{q}| \simeq 0.78$ GeV.

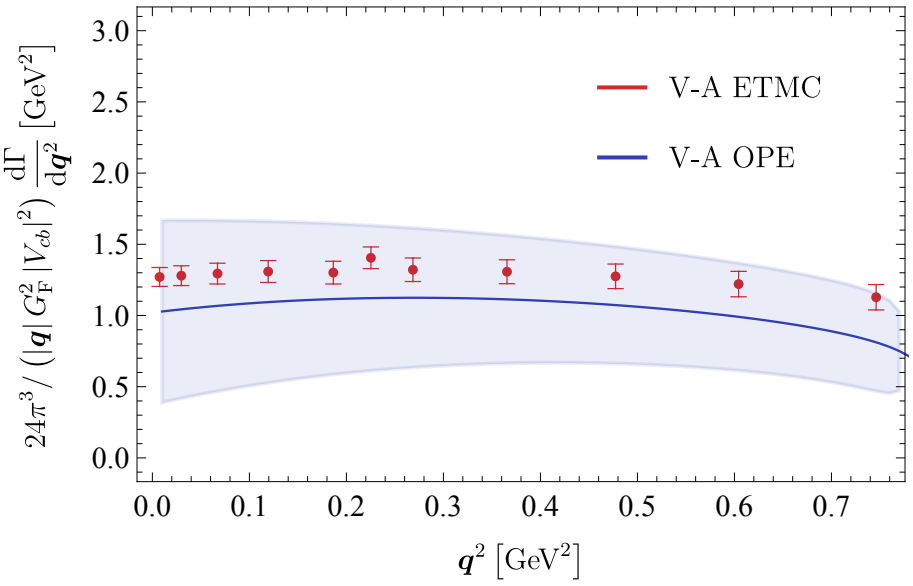

Figure 8.13: Differential $\boldsymbol{q}^2$ spectrum, divided by $|\boldsymbol{q}|$, in the SM. The plot shows the comparison of OPE (blue curve) with lattice data (red points).

where $\vec{\pi} = -i\vec{D}$, while D^μ is the covariant derivative, $b_v(x) = e^{-im_b v\cdot x} b(x)$ is the b field stripped of its high-frequency modes, and $G^{\mu\nu}$ is the gluon-field tensor.

In what is known as the kinetic scheme [196, 197, 198], one introduces the Wilsonian cutoff $\mu_k \sim 1$ GeV, in order to factorise long- and short-distance contributions. This allows to disentangle the physics coming from the *hard* scale $\sim m_b$ from that of the soft scale of order Λ_{QCD}. The physics associated to the hard scale is contained in the Wilson coefficients M_i which admit the α_s expansion. An important feature is that the power corrections only appear at order $O(\Lambda^2_{\mathrm{QCD}}/m_b^2)$, such that they can be considered to be comparatively suppressed.

The smearing provided by the phase-space integration, discussed in section 8.4, is also necessary for the convergence of the OPE for the quantities appearing in equation 8.36, as well as those defined in equations 8.40 and 8.43, which can all be expressed in the form of equation 8.62. The details of the OPE calculations are presented in ref. [2].

We start our comparison of lattice and OPE results with the $\boldsymbol{q}^2$ spectrum and the differential moments introduced in eq. (8.42) and in eq. (8.43). Figure 8.13 shows the $\boldsymbol{q}^2$ spectrum in the SM, that is, with the weak current containing both vector and axial-vector currents $V-A$. The agreement between the lattice results and the analytic curve obtained from the OPE is remarkably good, despite the latter has an uncertainty of about 50%. The large uncertainty of the OPE calculation is due to the large power correction arising from the fact that the value of the m_b considered is smaller than its

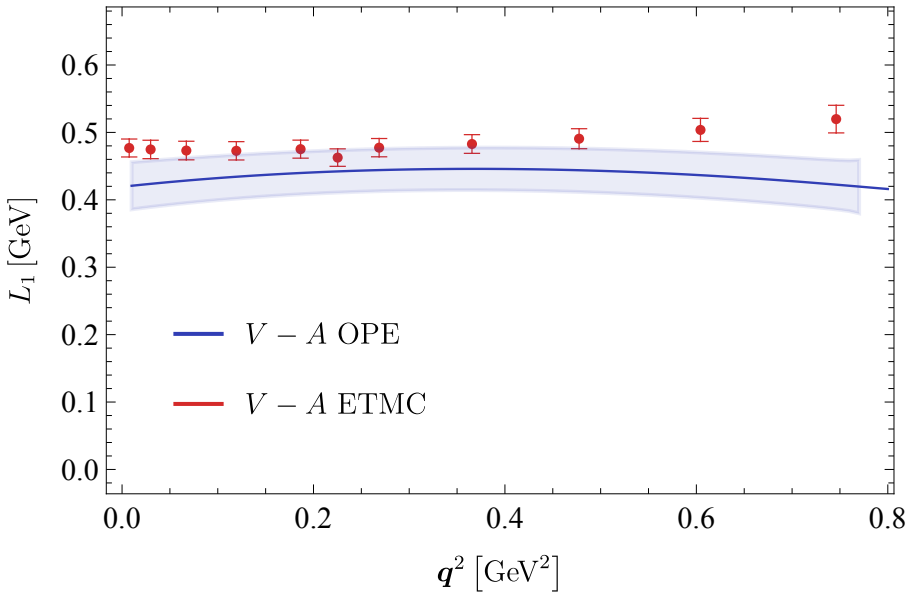

Figure 8.14: Differential lepton energy mean value, $L_1(\boldsymbol{q}^2)$, in the SM. The comparison of OPE with the lattice QCD results is shown.

physical value. This is done because the lattice calculation could not accommodate the simulation of physical b-quarks as already discussed in sections 8.5.1 and 4.3. It is important to notice that close to the partonic endpoint, corresponding to 0.82 GeV^2, we do not expect the OPE calculation to be reliable, as discussed extensively in ref. [2]. The corresponding hadronic endpoint is 0.75 GeV^2.

The uncertainties affecting both calculations can be greatly reduced by considering the differential moments. In particular, the OPE uncertainty becomes smaller because of the cancellations between power corrections to the numerator and to the denominator. This can be seen for instance in figure 8.14, where we show the first differential lepton energy moment, $L_1(\boldsymbol{q}^2)$, in the SM, where the agreement between the OPE curve and the lattice data is improved compared to figure 8.13 especially at low and moderate $\boldsymbol{q}^2$.

Considering that one can decompose the contributions to the total rate and to the moments according to the perpendicular and parallel components as well as individual currents, as discussed in section 8.4, in figure 8.15 we show the $\boldsymbol{q}^2$ spectrum in the individual channels. The first thing that one notice when comparing figure 8.15 with the plot in figure 8.13 is that in the individual channels the agreement between the OPE curves and the lattice data is poorer than in their sum, especially at large $\boldsymbol{q}$. This is something which can be expected as it could be a manifestation of quark-hadron duality violation. Of course, this needs to be checked comparing the results obtained at different volumes and, most importantly, extrapolated to the continuum

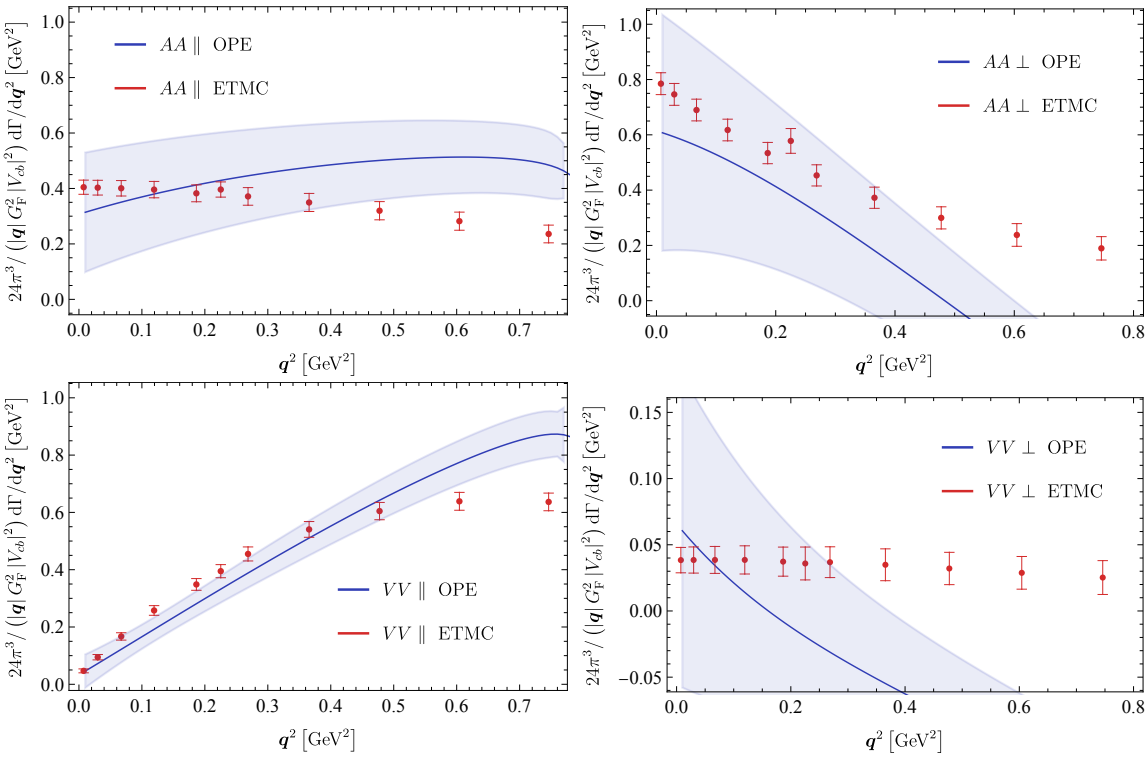

Figure 8.15: Differential $\boldsymbol{q}^2$ spectrum, divided by $|\boldsymbol{q}|$, in the various channels. The plots show the comparison between OPE and the lattice QCD results.

limit $a \to 0$. Furthermore, if one considers the figures for the $AA_\perp$ and $VV_\perp$ channels, it can be seen that the OPE central predictions turn negative at large and moderate $\boldsymbol{q}^2$, and that for $\boldsymbol{q}^2 > 0.6$ GeV^2 the spectrum is always negative within the errors. This unphysical behaviour would suggest that the error estimates are not reliable for large $\boldsymbol{q}^2$. Furthermore, the contribution coming from the $VV_\perp$ channel is particularly small which makes it very sensitive to large power corrections.

In figure 8.16, we also show plots for the differential lepton energy moment divided in the individual channels. Once again, compared to the differential decay rate we observe a better agreement between the OPE curves and the lattice data, especially at low $\boldsymbol{q}$. Once, again, the $VV_\perp$ channel seems to be the most problematic one which however is to be expected due to the fact that since its contribution is particularly close to zero, the expansion in powers of α_s and $1/m_b$ loses its justification. In these cases we also show the unexpanded version of the ratio, whose uncertainty is much larger, but we stress that away from the singularities the expanded form is preferable, and this appears to be confirmed by better agreement with the lattice data.

Figure 8.17 shows the second central moments computed at different values of $\boldsymbol{q}^2$ in the ETMC case. We do not display the $VV_\parallel$ channel, for which the OPE result would have a very large uncertainty. Unlike the first lepton energy moment, in the case of

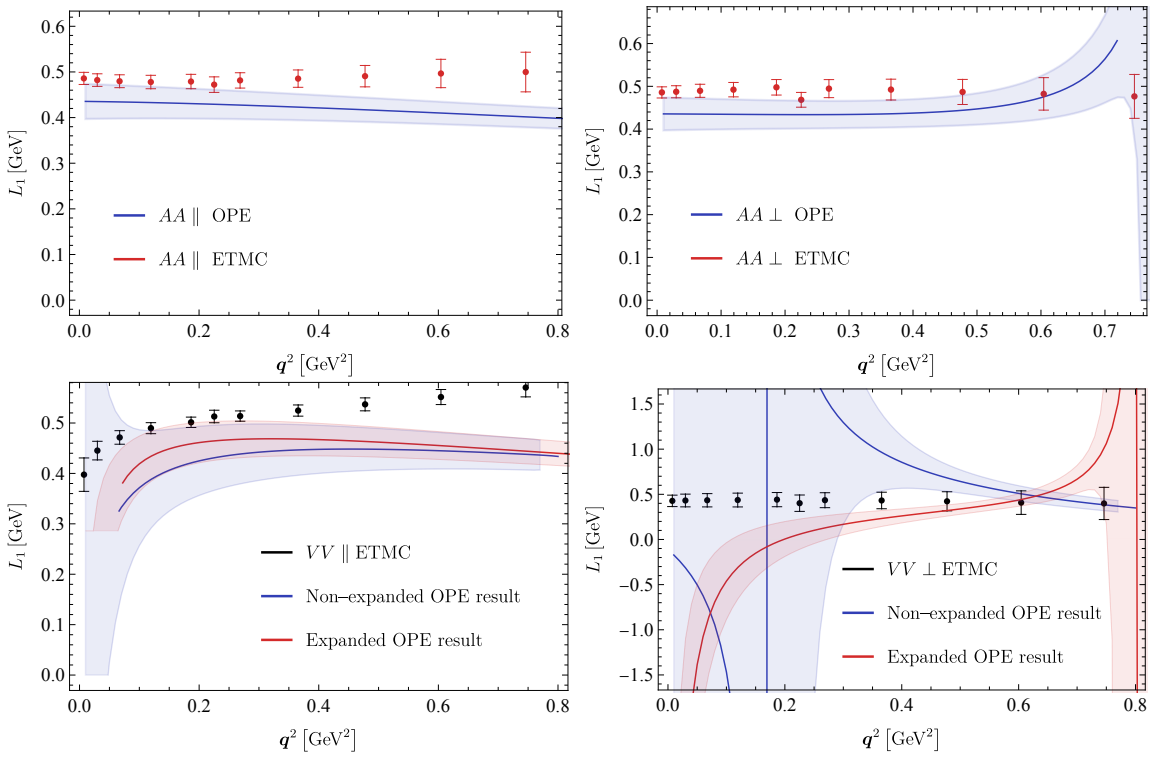

Figure 8.16: Differential moment $L_1(\boldsymbol{q}^2)$ in the various channels. The plots show the comparison between OPE and the lattice QCD results.

$L_{2c}(\boldsymbol{q}^2)$ the OPE fails to reproduce the lattice results within uncertainties, except for very small $\boldsymbol{q}^2$. This is something one should pay particular attention to in future works, because, even though it is true that the method for estimating the OPE uncertainty can fail due to multiple cancellations between large contributions to L_1 and L_2, it is also true that we were not able to estimate quantitatively the discretisation and finite-volume effects on the lattice results, which could affect the systematics entering this calculation in a non-trivial way.

8.6.1 Computations with a smooth kernel

In sections 8.4 and 7.2.1 we discussed how the central point for the extraction of inclusive quantities from lattice correlators is the numerical reconstruction of smeared kernels. While for the lattice calculations the integration kernels must be smooth functions, in the case the OPE one has the freedom to choose whether to use a sharp or smooth kernel knowing that for the latter the results would be unphysical. Hence, it is possible to perform the comparison between lattice QCD and OPE results for fixed values of the smearing radius σ. In this way it is possible to check that the level of agreement between the two calculations is not affected by the $\sigma \to 0$ limit, and to

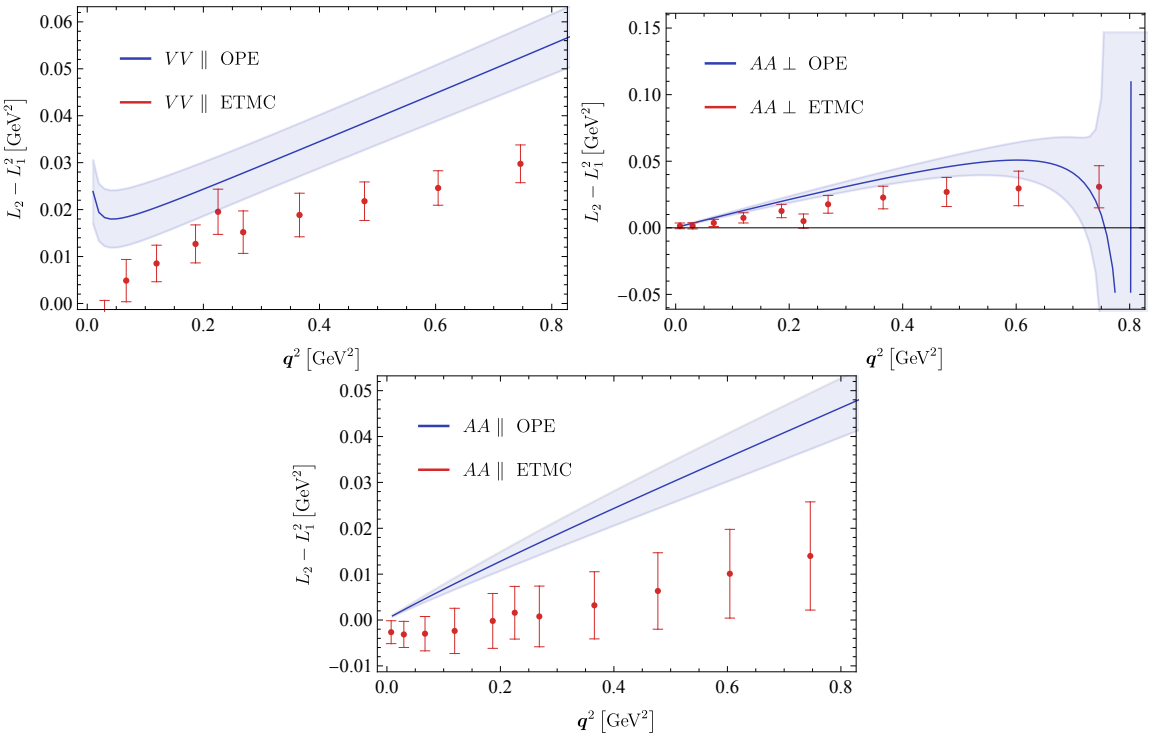

Figure 8.17: Differential moment $L_{2c} = L_2 - L_1^2$ in the various channels. The plots show the comparison between OPE and lattice QCD data.

extract information on the non-perturbative parameters of the OPE, as well as on the heavy quark masses, from slightly more precise lattice data.

In figure 8.18 we show the $\boldsymbol{q}^2$ spectrum in the different channels computed on the lattice using the sigmoid approximation $\theta^{\mathrm{s}}_\sigma$ of eq. (8.60) for $\theta(\omega_{\max} - \omega)$ with $\sigma = 0.12 m_B$. The comparison at fixed σ indicates a similar agreement between OPE and lattice QCD results, with a marginal improvements in the large $\boldsymbol{q}$ region. The comparison is shown also for the first differential lepton energy moment where figure 8.19 shows the results in the different channels with the exception of $VV_\perp$, due to the fact that the latter is dominated by large uncertainties in the OPE calculation.

Now, at fixed σ we notice a marked improvement of the agreement between the OPE and lattice QCD results at large $\boldsymbol{q}$ in the $AA_\parallel$ and $VV_\parallel$ channels, compared to the results shown in figure 8.16. On the other hand, the channel $AA_\perp$ seems to be slightly worse than in the $\sigma \to 0$ case.

8.6.2 Total width and moments

After we performing the integral over $\boldsymbol{q}^2$ defined in equations 8.36, 8.40 and 8.41, we can compare the numerical results obtained from the lattice QCD calculations with the

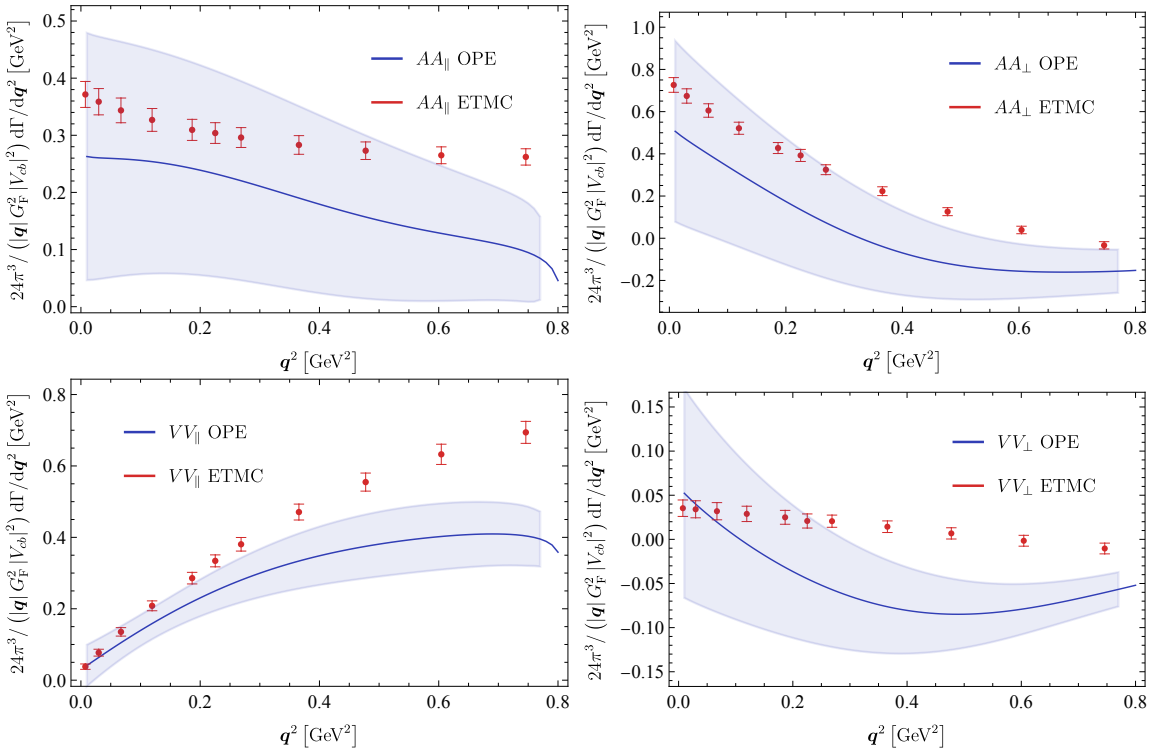

Figure 8.18: Differential $\boldsymbol{q}^2$ spectrum computed with a sigmoid approximation to the kernel with $\sigma = 0.12 m_B$. The plots show the comparison between OPE and lattice QCD results.

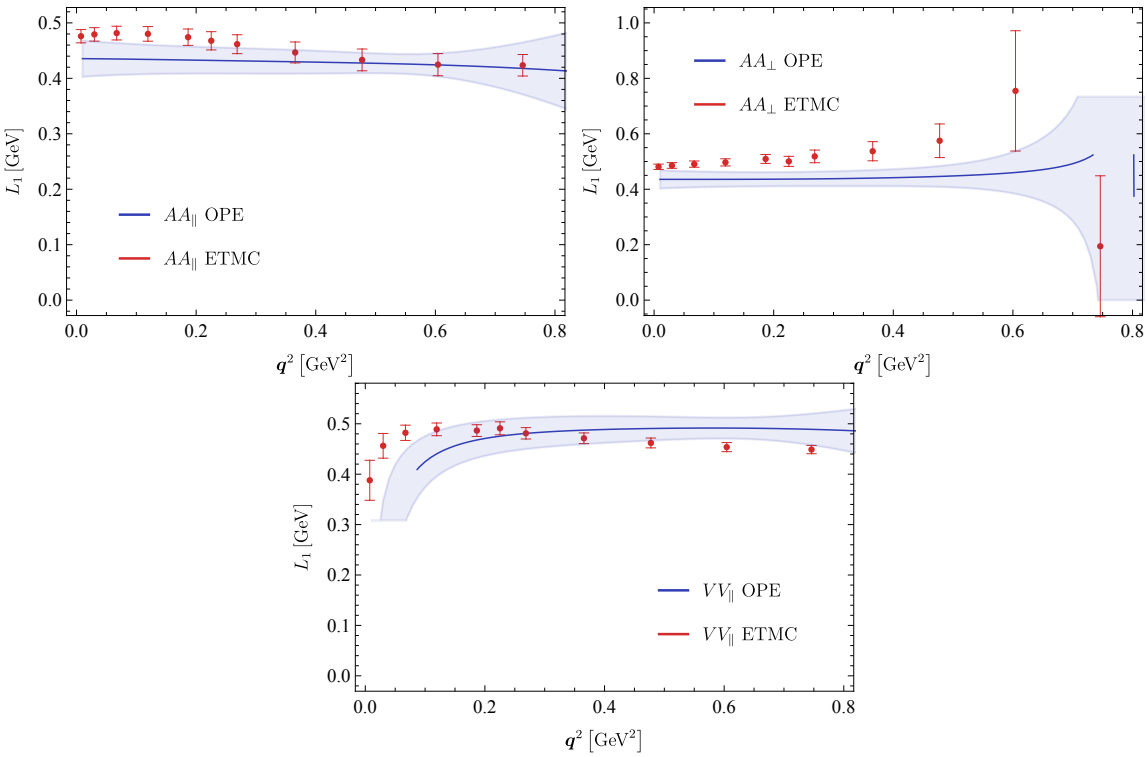

Figure 8.19: Differential first lepton moments computed with a sigmoid approximation to the kernel with $\sigma = 0.12 m_B$. The plots show the comparison between OPE and lattice QCD results.

	ETMC	OPE
$\Gamma/\lvert V_{cb}^2\rvert \times 10^{13}$ (GeV)	0.987(60)	1.20(46)
$\langle E_\ell \rangle$ (GeV)	0.491(15)	0.441(43)
$\langle E_\ell^2 \rangle$ (GeV^2)	0.263(16)	0.207(49)
$\langle E_\ell^2 \rangle - \langle E_\ell \rangle^2$(GeV^2)	0.022(16)	0.020(8)
$\langle M_X^2 \rangle$ (GeV^2)	3.62(14)	4.32(56)

Table 8.3: Total width and moments results from lattice QCD and OPE calculations.

analytic results coming from the OPE. In this case, as can be noticed from a first glance of the results presented in table 8.3, the OPE results will be slightly more precise as one can take advantage of two- and three-loop calculations presented in ref. [199]. For what concerns the lattice data, they can be interpolated by polynomials or piecewise polynomials such that one can perform the integration over $\boldsymbol{q}^2$ numerically. We can also test the relevance of the singularity at $\boldsymbol{q}^2_{\text{max}}$.

The OPE result for the total width receives large and concurring power and perturbative corrections, which leads to a $\sim$ 20–40% uncertainty. This is certainly an effect due to the fact that in our analysis we work with an unphysically light b quark, since for physical b-quark masses one gets an uncertainty close to 2% [200]. Indeed, the convergence of the OPE expansion deteriorates rapidly as m_b decreases approaching m_c, even from 2.7 to 2.4 GeV. This matter is further discussed in ref. [2].

An important point which is discussed in ref. [2] is that due to the B_s being unphysically light and the values for the c- and b-quark masses being closer than in the SM, the phase space available for the inclusive decay is limited compared to the physical case. As a consequence, the inclusive decay rate is nearly saturated by the ground state contribution of the charmed state D_s.

Despite this consideration, the comparison between the lattice QCD and OPE calculations is particularly interesting especially in the case of the variance of the lepton energy distribution which shows a clear and unexpected deviation. As already mentioned above, the reason behind this discrepancy could be due to underestimated uncertainties in our OPE calculation or to non-negligible lattice systematics.

Furthermore, by making a direct confrontation between the first principle lattice QCD calculation and results obtained using the OPE, we test for the first time the onset of quark-hadron duality, which is at the base of the OPE formulation.

The results presented in this chapter are unfortunately not yet ready to make strong phenomenological considerations. The limitations due to our simulations coming from a single ensemble forbids fundamental analysis like the infinite volume limit and

the continuum extrapolation which are now standard in the lattice QCD community. However, this study serves as a fundamental check on the feasibility of lattice QCD calculation of inclusive decays, where we discuss in great details some of the most delicate steps like the extraction of spectral densities and the extrapolation $\sigma \to 0$.

In order to go towards more phenomenologically relevant calculations, if one wants to study the inclusive semileptonic decay rate of B-meson it is necessary to find a way to circumvent the problem of the relativistic simulation of the b-quark mass. One of the possible methods which can be employed is the ETMC ratio method, proposed in ref. [201], where the observable of interest is computed for several values of heavy-quark mass and then extrapolated to the physical value. This method has already been applied to get lattice QCD calculations of quantities like the b-quark mass, the leptonic decay constant f_B, the bag parameters of $B_{(s)}$ mesons and the matrix elements of dimension-four and dimension-five operators appearing in the Heavy Quark Expansion of pseudo-scalar and vector meson masses [202, 203, 204, 205, 206].

Alternatively, a route which is currently being pursued is the inclusive calculation of $D_{(s)}$ meson decay rates. This research direction is particularly promising because of the readily available experimental results such as those for the branching ratio and for the electron energy spectrum [207, 208]. Furthermore, a first principle lattice QCD calculations of these quantities could help to understand the extent of the quark-hadron duality and thus to what extent the OPE can be applied to charmed inclusive decays,

One might raise the question of whether the foreseeable level of precision will be enough for accurately determining $|V_{cb}|$ and possibly resolve the $|V_{cb}|$ puzzle. At present, experimental uncertainties for $B \to X_c \ell \nu$ decays stand at 1.4% for the branching ratio and a few per mil for the first few moments of the lepton energy distribution. Achieving comparable precision through lattice calculations seems unlikely, at least in the beginning. Nevertheless, over a relatively short period, lattice calculations of inclusive semileptonic decays could potentially enhance the predictive capabilities of the Operator Product Expansion (OPE). This could be achieved by accessing other quantities that are either imprecise or beyond the reach of current experiments but have a strong dependence on non-perturbative parameters. Such calculations would enable the validation and improvement of the results obtained from the semileptonic fits, which form the basis of OPE predictions.

Chapter 9

Conclusions

In this doctoral thesis we discussed the non-perturbative regularisation of quantum field theory on a spacetime lattice, and used this theoretical framework to address numerically, through Monte Carlo simulations that were run on supercomputers, some non-trivial problems in strongly coupled physical systems.

The first problem that we addressed, whose results were reported in ref. [4], consisted in the study of topological excitations that can be induced in the classical Heisenberg spin model through suitable boundary conditions. As was argued in ref. [74], the energy density profile and the magnetisation that appear in the presence of such excitations can be studied using quantum field theory methods, by making an *Ansatz* for the form factor associated with these excitations. Our numerical results confirmed the overall picture predicted in ref. [74], albeit they also revealed that the scaling of the "low-energy constants" involved in the quantum-field-theoretical description of the spin model close to its critical point is not fully consistent with a straightforward interpretation of these topological configurations in terms of particle excitations.

In ref. [3], instead, we addressed a study of the properties of confining flux tube in a particularly simple gauge theory (gluodynamics with $N = 2$ colour charges in $D = 2+1$ spacetime dimensions) in a temperature regime close to the thermal deconfinement transition. We found that that the corrections beyond the universal terms in the effective string action turn out to be compatible with the predictions that were obtained in the literature using the bootstrap approach.

Finally, the problem that was the main focus of this doctoral thesis was the study of inclusive semileptonic decays of heavy-meson using lattice QCD. Following an approach that was recently put forward in ref. [181], we carried out such a study using a mathematically well-defined procedure to tackle the ill-posed inverse problem of extracting the hadronic tensor from lattice correlation functions, by means of the HLT

method [149] (which, as any linear method for the extraction of spectral densities, is general and can be applied to many problems, not only in lattice QCD but also in other problems in physics and even in other areas of science). The original results of our study, in which we combined the analysis of lattice configurations generated by the ETM collaboration with $N_f = 2 + 1 + 1$ dynamical quarks with those from configurations by the JLQCD collaboration, were reported in ref. [2]. In this work, only a single ensemble of ETM configurations has been used, hence, all the results presented in this thesis were obtained at a single lattice volume and a single value of the lattice spacing. Consequently, we could not perform any extrapolation to the infinite-volume limit nor to the continuum limit, which are left for future work. Nevertheless, the comparison that we carried out in ref. [2] between the lattice data and analytical results obtained from an operator-product-expansion approach already show a good agreement for the differential decay rate as well as other quantities like the hadron and lepton energy moments.

As we conclude this thesis, it is important to acknowledge the inherent challenges and limitations of lattice QCD. The numerical simulations demand significant computational resources, and systematic uncertainties related to discretisation and finite volume have to be properly taken into account.[1] Nonetheless, the insights gained through this research have reaffirmed the importance of lattice QCD as a fundamental approach for studying flavour physics, and other challenging physical problems in strongly coupled theories.

Looking to the future, the advancements made in this thesis provide a solid foundation for further investigations of inclusive semileptonic decays using lattice QCD, as well as for other non-trivial problems in QCD and in other strongly coupled theories. Indeed, we are currently trying to repeat the calculations that were carried out in this thesis for the inclusive decay rates of D-mesons, too. The hope is that the simulation of charm quarks at their physical mass will allow one to access the full phase space region and therefore to access all of the physical states relevant for these inclusive decays.

Considering the constant improvement of techniques and theoretical understanding of lattice QCD over the years, it can be speculated that the calculation of inclusive semileptonic decays will soon reach a high level of precision, which would have a big impact in the long standing effort of the determination of CKM matrix elements and

[1] The numerical calculations necessary to carry out a systematic study of the extrapolations to the infinite-volume limit, and then to the continuum limit, would require an amount of time and of computing resources that is far beyond those typical of a doctoral thesis project. Indeed, it is worth remarking that state-of-the-art, large-scale lattice QCD calculations like those involved in this study are nowadays among the scientific projects that take a significant fraction of tier-0 supercomputing facilities.

(possibly) the resolution of the $|V_{cb}|$ puzzle.

Appendix A

Euclidean gamma matrices

In Minkowski space-time gamma matrices obey the anti-commutation relation

$$\{\gamma_\mu^M, \gamma_\nu^M\} = 2g_{\mu\nu}\mathbb{1}, \tag{A.1}$$

with $\mu = 0, 1, 2, 3$ and $g_{\mu\nu} = \mathrm{diag}(1, -1, -1, -1)$.

Upon Wick rotation, the Euclidean gamma matrices γ_μ, $\mu = 1, 2, 3, 4$ can be obtained by the following relations

$$\gamma_1 = -i\gamma_1^M, \qquad \gamma_2 = -i\gamma_2^M, \qquad \gamma_3 = -i\gamma_3^M, \qquad \gamma_4 = \gamma_0^M, \tag{A.2}$$

and fulfill the anti-commutation relations

$$\{\gamma_\mu, \gamma_\nu\} = 2\delta_{\mu\nu}\mathbb{1}. \tag{A.3}$$

Then, one can define the matrix γ_5, which anti-commutes with all the other γ_μ matrices

$$\gamma_5 = \gamma_1\gamma_2\gamma_3\gamma_4, \tag{A.4}$$

with $\gamma_5^2 = \mathbb{1}$. Furthermore, it is easy to show that $\gamma_5 = \gamma_5^M$

$$\gamma_5^M = i(\gamma_0\gamma_1\gamma_2\gamma_3)_M = \frac{1}{i^2}(\gamma_4\gamma_1\gamma_2\gamma_3)_E = (\gamma_1\gamma_2\gamma_3\gamma_4)_E = \gamma_5. \tag{A.5}$$

Using the anti-commutation relation and the fact that in Euclidean space-time $(\gamma_\mu)^\dagger = \gamma_\mu = \gamma_\mu^{-1}$, one can show that $(\gamma_5)^\dagger = \gamma_5$. This is true in the so-called chiral representation where γ_5 is diagonal. Within this representation we can write the gamma matrices

explicitly

$$\gamma_{1,2,3} = \begin{bmatrix} 0 & -i\sigma_{1,2,3} \\ -i\sigma_{1,2,3} & 0 \end{bmatrix}, \quad \gamma_4 = \begin{bmatrix} 0 & \mathbb{1}_2 \\ \mathbb{1}_2 & 0 \end{bmatrix}, \quad \gamma_5 = \begin{bmatrix} \mathbb{1}_2 & 0 \\ 0 & \mathbb{1}_2 \end{bmatrix}, \tag{A.6}$$

where σ_i are the Pauli matrices:

$$\sigma_1 = \begin{bmatrix} 0 & 1 \\ 1 & 0 \end{bmatrix}, \quad \sigma_2 = \begin{bmatrix} 0 & -i \\ i & 0 \end{bmatrix}, \quad \sigma_3 = \begin{bmatrix} 1 & 0 \\ 0 & -1 \end{bmatrix}, \tag{A.7}$$

and $\mathbb{1}_2$ is the 2×2 unitary matrix.

To write everything explicitly, we have

$$\gamma_1 = \begin{bmatrix} 0 & 0 & 0 & -i \\ 0 & 0 & -i & 0 \\ 0 & i & 0 & 0 \\ i & 0 & 0 & 0 \end{bmatrix}, \quad \gamma_2 = \begin{bmatrix} 0 & 0 & 0 & -1 \\ 0 & 0 & 1 & 0 \\ 0 & 1 & 0 & 0 \\ -1 & 0 & 0 & 0 \end{bmatrix}, \quad \gamma_3 = \begin{bmatrix} 0 & 0 & -i & 0 \\ 0 & 0 & 0 & i \\ i & 0 & 0 & 0 \\ 0 & -i & 0 & 0 \end{bmatrix},$$

$$\gamma_4 = \begin{bmatrix} 0 & 0 & 1 & 0 \\ 0 & 0 & 0 & 1 \\ 1 & 0 & 0 & 0 \\ 0 & 1 & 0 & 0 \end{bmatrix}, \qquad \gamma_5 = \begin{bmatrix} 1 & 0 & 0 & 0 \\ 0 & 1 & 0 & 0 \\ 0 & 0 & -1 & 0 \\ 0 & 0 & 0 & -1 \end{bmatrix}. \tag{A.8}$$

Appendix B

Numerical details of the HLT method

In this appendix we report the explicit expressions for the numerical procedures employe in the HLT method discussed in section 7.2.1.

The Gaußian smeared kernels can be defined as

$$\Delta_\sigma(\omega, \omega_n) = \frac{1}{\sqrt{2\pi}\sigma Z} \exp\left(\frac{-(\omega - \omega_n)^2}{2\sigma^2}\right), \tag{B.1}$$

with

$$Z = \frac{1}{2}\left(1 + \mathrm{erf}\left(\frac{\omega_n}{\sqrt{2}\sigma}\right)\right). \tag{B.2}$$

The functional $A[g]$ is defined as

$$A[g] = \int_{\omega_{\min}}^{\infty} d\omega \; e^{\alpha\omega}\{K(\omega; g) - \Delta_\sigma(\omega, \omega_n(L))\}. \tag{B.3}$$

With this definition, the matrix A_{tr} is defined as

$$\begin{aligned} A_{tr} = &\frac{e^{-(r+t+2-\alpha)\omega_{\min}}}{r+t+2-\alpha} + \frac{e^{-(T-r+t-\alpha)\omega_{\min}}}{T-r+t-\alpha} \\ &+ \frac{e^{-(T-r-t-\alpha)\omega_{\min}}}{T-r-t-\alpha} + \frac{e^{2T-r-t-2-\alpha}\omega_{\min}}{2T-r-t-2-\alpha}. \end{aligned} \tag{B.4}$$

As discussed in section 7.2.1, the parameter α allow to change the Jacobi polynomial to be used in the reconstruction, and must satisfy the condition $\alpha < 2$.

The vector f_t is similarly defined as

$$f_t = (1 - \lambda) \int_{\omega_{\min}}^{\infty} d\omega e^{\alpha\omega} \Delta_\sigma(\omega, \omega_n) b_T(t + 1, \omega), \tag{B.5}$$

whose components can be calculated as

$$f_t = N(t+1)F(t+1) + N(T-t-1)F(T-t-1), \tag{B.6}$$

using

$$N(k) = \frac{1-\lambda}{2Z} \exp\left(\frac{(\alpha-k)((\alpha-k)\sigma^2 + 2\omega_n)}{2}\right), \tag{B.7}$$

$$F(k) = 1 + \mathrm{erf}\left(\frac{(\alpha-k)\sigma^2 + \omega_n - \omega_{\min}}{\sqrt{2}\sigma}\right. \tag{B.8}$$

In the limit $T \to \infty$, only the first term contribute to the vector f_t. Finally, the vector R_t is defined as

$$R_t = \int_0^\infty d\omega \; b_T(t+1,\omega) = \frac{1}{t+1} + \frac{1}{T-t-1}, \tag{B.9}$$

, where, once again we stress that only the first term survives for $T \to \infty$.

Appendix C

Decomposition of the inclusive decay rate

We begin by writing the hadronic tensor in its spectral representation

$$W^{\mu\nu}(p,q) = \frac{1}{2m_B}\langle B|J^{\mu}(0)(2\pi)^4\delta^4(\mathbb{P}-(p-q))[J^{\nu}]^{\dagger}|B\rangle. \tag{C.1}$$

Then it follows that the generic decomposition of the hadronic tensor in six independent form factors is

$$\begin{aligned} W^{\mu\nu}(p,q) = &- g^{\mu\nu}W_1(\omega,\boldsymbol{q}^2) + \frac{p^{\mu}p^{\nu}}{m_B^2}W_2(\omega,\boldsymbol{q}^2) + \frac{q^{\mu}q^{\nu}}{m_B^2}W_3(\omega,\boldsymbol{q}^2) \\ &+ \frac{p^{\mu}q^{\nu}+p^{\nu}q^{\mu}}{m_B^2}W_4(\omega,\boldsymbol{q}^2) - i\epsilon^{\mu\nu\alpha\beta}\frac{p_{\alpha}q_{\beta}}{m_B^2}W_5(\omega,\boldsymbol{q}^2)\ . \\ &- i\frac{p^{\mu}q^{\nu}-q^{\mu}p^{\nu}}{m_B^2}W_6(\omega,\boldsymbol{q}^2)\ . \end{aligned} \tag{C.2}$$

All the form factors appearing above are real due to the fact that the hadronic tensor satisfies the relation

$$[W^{\mu\nu}(\omega,\boldsymbol{p}^2)]^{\dagger} = W^{\mu\nu}(\omega,\boldsymbol{p}^2), \tag{C.3}$$

such that the symmetric part is real while the antisymmetric part is purely imaginary.

The form factor $W_6(\omega,\boldsymbol{q}^2)$ vanishes as a consequence of T-symmetry. This can be shown by first dividing the hadronic tensor in parity-even and parity-odd contributions

$$\begin{aligned} W_+^{\mu\nu}(p,q) &= W_{VV}^{\mu\nu}(p,q) + W_{AA}^{\mu\nu}(p,q), \\ W_-^{\mu\nu}(p,q) &= W_{VA}^{\mu\nu}(p,q) - W_{AV}^{\mu\nu}(p,q). \end{aligned} \tag{C.4}$$

The only parity-odd term in equation C.2 is the anti-symmetric term proportional to $W_5(\omega, \boldsymbol{q}^2)$ which is therefore purely imaginary

$$[W^{\mu\nu}_{VA}(p,q)]^\dagger = -W^{\mu\nu}_{AV}(p,q). \tag{C.5}$$

Under T-symmetry we have

$$\mathcal{T}V^\mu(0)\mathcal{T}^\dagger = -V_\mu(0), \qquad \mathcal{T}A^\mu(0)\mathcal{T}^\dagger = -A_\mu(0), \qquad \mathcal{T}\mathbb{P}\mathcal{T}^\dagger = \mathbb{P}_\mu, \tag{C.6}$$

where $\mathbb{P}^\mu$ is the QCD four-momentum operator.

Then for the B-meson state, we can define $\tilde{p} = (\omega, -\boldsymbol{q})$ and write

$$\mathcal{T}|B(p)\rangle = |B(\tilde{p})\rangle. \tag{C.7}$$

The vector component of the hadronic tensor can be written in the spectral representation as

$$\begin{aligned}
2m_B W^{\mu\nu}_{VV}(p,q) &= \langle B(p)|V^\mu(0)\,(2\pi)^4\delta^4(\mathbb{P}-(p-q))\;[V^\nu]^\dagger(0)|B(p)\rangle \\
&= \Big(\langle B(\tilde{p})|\mathcal{T}V^\mu(0)\,(2\pi)^4\delta^4(\mathbb{P}-(p-q))\;[V^\nu]^\dagger(0)\mathcal{T}^\dagger|B(\tilde{p})\rangle\Big)^\dagger \\
&= \Big(\langle B(\tilde{p})|V_\mu(0)\,(2\pi)^4\delta^4(\mathbb{P}-(\tilde{p}-\tilde{q}))\;[V_\nu]^\dagger(0)|B(\tilde{p})\rangle\Big)^\dagger \\
&= \langle B(\tilde{p})|V_\nu(0)\,(2\pi)^4\delta^4(\mathbb{P}-(\tilde{p}-\tilde{q}))\;[V_\mu]^\dagger(0)|B(\tilde{p})\rangle \\
&= 2m_B\,[W_{VV}]_{\nu\mu}(\tilde{p},\tilde{q})\;.
\end{aligned} \tag{C.8}$$

The same can be done for the axial contribution $W^{\mu\nu}_{AA}$.

Then, considering that the scalar product is parity invariant ($\tilde{p}\cdot\tilde{q} = p\cdot q$) and noticing that $\tilde{p}_\mu = p^\mu$, we can prove the following

$$[W^{\mu\nu}_{VV}(p,q)]^\dagger = W^{\nu\mu}_{VV}(p,q) = W^{\mu\nu}_{VV}(p,q), [W^{\mu\nu}_{AA}(p,q)]^\dagger = W^{\nu\mu}_{AA}(p,q) = W^{\mu\nu}_{AA}(p,q), \tag{C.9}$$

which shows that there cannot be any anti-symmetric part contributing to the parity-even hadronic tensor $W^{\mu\nu}_+$, and as a consequence that we must have $W_6(\omega, \boldsymbol{q}^2) = 0$.

Then we can contract the hadronic tensor as shown in equation 8.26 with the

leptonic tensor of equation 8.20 using the following formulae

$$L_{\mu\nu}(p_\ell, p_\nu) g^{\mu\nu} = -\left\{(m_B - \omega)^2 - \boldsymbol{q}^2\right\} \ ,$$

$$L_{\mu\nu}(p_\ell, p_\nu) \frac{p^\mu p^\nu}{m_B^2} = \frac{1}{2}\left\{\boldsymbol{q}^2 - (m_B - \omega - 2E_\ell)^2\right\} \ ,$$

$$L_{\mu\nu}(p_\ell, p_\nu) \frac{q^\mu q^\nu}{m_B^2} = 0 \ ,$$

$$L_{\mu\nu}(p_\ell, p_\nu) \frac{p^\mu q^\nu + q^\mu p^\nu}{m_B^2} = 0 \ ,$$

$$L_{\mu\nu}(p_\ell, p_\nu) \frac{\left\{-i\epsilon^{\mu\nu\alpha\beta} p_\alpha q_\beta\right\}}{m_B^2} = \left[(m_B - \omega)^2 - \boldsymbol{q}^2\right]\left[2E_\ell - (m_B - \omega)\right] \ . \tag{C.10}$$

Then the total contraction of the hadronic and leptonic tensor gives

$$\begin{aligned} L_{\mu\nu} W^{\mu\nu} = &-\{(m_B - \omega)^2 - \boldsymbol{q}^2\} W_1 + \frac{1}{2}\{\boldsymbol{q}^2 - (m_B - \omega - 2E_\ell)\} W_2 \\ &+ [(m_B - \omega)^2 - \boldsymbol{q}^2][2E_\ell - (m_B - \omega)] W_5. \end{aligned} \tag{C.11}$$

And the differential decay rate of equation 8.25 can thus be written as

$$\begin{aligned} \frac{d\Gamma}{d\boldsymbol{q}^2 d\omega dE_\ell} \frac{8\pi^3}{G_F^2 |V_{cb}|^2} &= L_{\mu\nu} W^{\mu\nu} \\ &= -\{(m_B - \omega)^2 - \boldsymbol{q}^2\} W_1 + \frac{1}{2}\{\boldsymbol{q}^2 - (m_B - \omega - 2E_\ell)\} W_2 \\ &\quad + 2[(m_B - \omega)^2 - \boldsymbol{q}^2][2E_\ell - (m_B - \omega)] W_5. \end{aligned} \tag{C.12}$$

List of Figures

List of Tables

Bibliography

[1] K. G. Wilson, "Confinement of quarks," *Phys. Rev. D* **10** (Oct, 1974) 2445–2459. https://link.aps.org/doi/10.1103/PhysRevD.10.2445.

[2] P. Gambino, S. Hashimoto, S. Mächler, M. Panero, F. Sanfilippo, S. Simula, A. Smecca, and N. Tantalo, "Lattice QCD study of inclusive semileptonic decays of heavy mesons," *JHEP* **07** (2022) 083, arXiv:2203.11762 [hep-lat].

[3] F. Caristo, M. Caselle, N. Magnoli, A. Nada, M. Panero, and A. Smecca, "Fine corrections in the effective string describing SU(2) Yang-Mills theory in three dimensions," *JHEP* **03** (2022) 115, arXiv:2109.06212 [hep-th].

[4] M. Panero and A. Smecca, "Topological excitations in statistical field theory at the upper critical dimension," *JHEP* **03** (2021) 231, arXiv:2012.12221 [cond-mat.stat-mech].

[5] A. Smecca, P. Gambino, S. Hashimoto, S. Mächler, M. Panero, F. Sanfilippo, S. Simula, and N. Tantalo, "Inclusive semileptonic B-decays from lattice QCD," *PoS* **LATTICE2022** (2023) 423, arXiv:2211.11833 [hep-lat].

[6] P. Gambino, S. Hashimoto, S. Mächler, M. Panero, F. Sanfilippo, S. Simula, A. Smecca, and N. Tantalo, "Towards the computation of inclusive decay rates using lattice QCD," in *51st International Symposium on Multiparticle Dynamics*. 9, 2022. arXiv:2209.15494 [hep-lat].

[7] F. Caristo, M. Caselle, A. Magnoli, A. Nada, M. Panero, and A. Smecca, "On the behaviour of the interquark potential in the vicinity of the deconfinement transition," *PoS* **LATTICE2021** (2022) 420, arXiv:2203.11504 [hep-lat].

[8] A. Smecca and M. Panero, "Monopole-like configurations in the O(3) spin model at the upper critical dimension," *PoS* **LATTICE2021** (2022) 121, arXiv:2109.10389 [hep-lat].

[9] R. P. Feynman, "Space-time approach to non-relativistic quantum mechanics," *Rev. Mod. Phys.* **20** (Apr, 1948) 367–387. https://link.aps.org/doi/10.1103/RevModPhys.20.367.

[10] C. Gattringer and C. B. Lang, *Quantum Chromodynamics on the Lattice*. Springer, Berlin, Heidelberg, 2010.

[11] J. B. Kogut, "An introduction to lattice gauge theory and spin systems," *Rev. Mod. Phys.* **51** (Oct, 1979) 659–713. https://link.aps.org/doi/10.1103/RevModPhys.51.659.

[12] D. Tong, "Lectures on gauge theory." https://www.damtp.cam.ac.uk/user/tong/gaugetheory.html.

[13] K. Osterwalder and R. Schrader, "Axioms for Euclidean Green's Functions," *Commun. Math. Phys.* **31** (1973) 83–112.

[14] M. Lüscher, "Construction of a Selfadjoint, Strictly Positive Transfer Matrix for Euclidean Lattice Gauge Theories," *Commun. Math. Phys.* **54** (1977) 283.

[15] A. Polyakov, "Thermal properties of gauge fields and quark liberation," *Physics Letters B* **72** no. 4, (1978) 477–480. https://www.sciencedirect.com/science/article/pii/0370269378907372.

[16] L. Susskind, "Lattice models of quark confinement at high temperature," *Phys. Rev. D* **20** (1979) 2610–2618. https://link.aps.org/doi/10.1103/PhysRevD.20.2610.

[17] B. Svetitsky and L. G. Yaffe, "Critical Behavior at Finite Temperature Confinement Transitions," *Nucl. Phys. B* **210** (1982) 423–447.

[18] L. G. Yaffe and B. Svetitsky, "First-order phase transition in the su(3) gauge theory at finite temperature," *Phys. Rev. D* **26** (Aug, 1982) 963–965. https://link.aps.org/doi/10.1103/PhysRevD.26.963.

[19] H. Fritzsch and M. Gell-Mann, "Current algebra: Quarks and what else?," *eConf* **C720906V2** (1972) 135–165, arXiv:hep-ph/0208010.

[20] B. Lucini, A. Rago, and E. Rinaldi, "Glueball masses in the large N limit," *JHEP* **08** (2010) 119, arXiv:1007.3879 [hep-lat].

[21] C. Michael and M. Teper, "The glueball spectrum in su(3)," *Nuclear Physics B* **314** no. 2, (1989) 347–362.

[22] C. Michael and I. Teasdale, "Extracting glueball masses from lattice qcd," *Nuclear Physics B* **215** no. 3, (1983) 433–446.

[23] B. Blossier, M. Della Morte, G. von Hippel, T. Mendes, and R. Sommer, "On the generalized eigenvalue method for energies and matrix elements in lattice field theory," *JHEP* **04** (2009) 094, arXiv:0902.1265 [hep-lat].

[24] H. B. Nielsen and M. Ninomiya, "Absence of Neutrinos on a Lattice. 2. Intuitive Topological Proof," *Nucl. Phys. B* **193** (1981) 173–194.

[25] P. T. Matthews and A. Salam, "The green's functions of quantised fields," *Il Nuovo Cimento (1943-1954)* **12** no. 4, (Oct, 1954) 563–565. https://doi.org/10.1007/BF02781302.

[26] P. T. Matthews and A. Salam, "Propagators of quantized field," *Il Nuovo Cimento (1955-1965)* **2** no. 1, (Jul, 1955) 120–134. https://doi.org/10.1007/BF02856011.

[27] H. Nielsen and M. Ninomiya, "A no-go theorem for regularizing chiral fermions," *Physics Letters B* **105** no. 2, (1981) 219–223. https://www.sciencedirect.com/science/article/pii/0370269381910261.

[28] P. H. Ginsparg and K. G. Wilson, "A remnant of chiral symmetry on the lattice," *Phys. Rev. D* **25** (May, 1982) 2649–2657. https://link.aps.org/doi/10.1103/PhysRevD.25.2649.

[29] H. Neuberger, "More about exactly massless quarks on the lattice," *Phys. Lett. B* **427** (1998) 353–355, arXiv:hep-lat/9801031.

[30] S. Gusken, "A Study of smearing techniques for hadron correlation functions," *Nucl. Phys. B Proc. Suppl.* **17** (1990) 361–364.

[31] B. Jegerlehner, "Krylov space solvers for shifted linear systems," arXiv:hep-lat/9612014.

[32] **XLF** Collaboration, K. Jansen, M. Papinutto, A. Shindler, C. Urbach, and I. Wetzorke, "Quenched scaling of Wilson twisted mass fermions," *JHEP* **09** (2005) 071, arXiv:hep-lat/0507010.

[33] **UKQCD** Collaboration, C. McNeile and C. Michael, "Decay width of light quark hybrid meson from the lattice," *Phys. Rev. D* **73** (2006) 074506, arXiv:hep-lat/0603007.

[34] **UKQCD** Collaboration, M. Foster and C. Michael, "Quark mass dependence of hadron masses from lattice QCD," *Phys. Rev. D* **59** (1999) 074503, arXiv:hep-lat/9810021.

[35] F. Joswig, S. Kuberski, J. T. Kuhlmann, and J. Neuendorf, "pyerrors: A python framework for error analysis of Monte Carlo data," *Computer Physics Communications* **288** (July, 2023) 108750.

[36] P. F. Bedaque, "Aharonov-Bohm effect and nucleon nucleon phase shifts on the lattice," *Phys. Lett. B* **593** (2004) 82–88, arXiv:nucl-th/0402051.

[37] G. M. de Divitiis, R. Petronzio, and N. Tantalo, "On the discretization of physical momenta in lattice QCD," *Phys. Lett. B* **595** (2004) 408–413, arXiv:hep-lat/0405002.

[38] D. Guadagnoli, F. Mescia, and S. Simula, "Lattice study of semileptonic form-factors with twisted boundary conditions," *Phys. Rev. D* **73** (2006) 114504, arXiv:hep-lat/0512020.

[39] A. Shindler, "Twisted mass lattice QCD," *Phys. Rept.* **461** (2008) 37–110, arXiv:0707.4093 [hep-lat].

[40] S. Aoki, "New phase structure for lattice qcd with wilson fermions," *Phys. Rev. D* **30** (Dec, 1984) 2653–2663. https://link.aps.org/doi/10.1103/PhysRevD.30.2653.

[41] R. Frezzotti, P. A. Grassi, S. Sint, and P. Weisz, "A Local formulation of lattice QCD without unphysical fermion zero modes," *Nucl. Phys. B Proc. Suppl.* **83** (2000) 941–946, arXiv:hep-lat/9909003.

[42] **Alpha** Collaboration, R. Frezzotti, P. A. Grassi, S. Sint, and P. Weisz, "Lattice QCD with a chirally twisted mass term," *JHEP* **08** (2001) 058, arXiv:hep-lat/0101001.

[43] **Alpha** Collaboration, R. Frezzotti, S. Sint, and P. Weisz, "O(a) improved twisted mass lattice QCD," *JHEP* **07** (2001) 048, arXiv:hep-lat/0104014.

[44] J. C. Ward, "An identity in quantum electrodynamics," *Phys. Rev.* **78** (Apr, 1950) 182–182. https://link.aps.org/doi/10.1103/PhysRev.78.182.

[45] Y. Takahashi, "On the generalized ward identity," *Il Nuovo Cimento (1955-1965)* **6** no. 2, (Aug, 1957) 371–375. https://doi.org/10.1007/BF02832514.

[46] G. Martinelli, C. Pittori, C. T. Sachrajda, M. Testa, and A. Vladikas, "A General method for nonperturbative renormalization of lattice operators," *Nucl. Phys. B* **445** (1995) 81–108, arXiv:hep-lat/9411010.

[47] R. Frezzotti and G. C. Rossi, "Twisted mass lattice QCD with mass nondegenerate quarks," *Nucl. Phys. B Proc. Suppl.* **128** (2004) 193–202, arXiv:hep-lat/0311008.

[48] R. Frezzotti and G. C. Rossi, "Chirally improving Wilson fermions. II. Four-quark operators," *JHEP* **10** (2004) 070, arXiv:hep-lat/0407002.

[49] A. Donini, V. Gimenez, G. Martinelli, M. Talevi, and A. Vladikas, "Nonperturbative renormalization of lattice four fermion operators without power subtractions," *Eur. Phys. J. C* **10** (1999) 121–142, arXiv:hep-lat/9902030.

[50] E. Gabrielli, G. Martinelli, C. Pittori, G. Heatlie, and C. Sachrajda, "Renormalization of lattice two-fermion operators with improved nearest-neighbour action," *Nuclear Physics B* **362** no. 1, (1991) 475–486. https://www.sciencedirect.com/science/article/pii/055032139190569J.

[51] K. Osterwalder and E. Seiler, "Gauge field theories on a lattice," *Annals of Physics* **110** no. 2, (1978) 440–471. https://www.sciencedirect.com/science/article/pii/0003491678900398.

[52] R. Frezzotti and G. C. Rossi, "Chirally improving Wilson fermions. 1. O(a) improvement," *JHEP* **08** (2004) 007, arXiv:hep-lat/0306014.

[53] R. Frezzotti, G. Martinelli, M. Papinutto, and G. C. Rossi, "Reducing cutoff effects in maximally twisted lattice QCD close to the chiral limit," *JHEP* **04** (2006) 038, arXiv:hep-lat/0503034.

[54] Y. Iwasaki, "Renormalization Group Analysis of Lattice Theories and Improved Lattice Action. II. Four-dimensional non-Abelian SU(N) gauge model," arXiv:1111.7054 [hep-lat].

[55] Y. Iwasaki, "Renormalization group analysis of lattice theories and improved lattice action: Two-dimensional non-linear o(n) sigma model," *Nuclear Physics B* **258** (1985) 141–156. https://www.sciencedirect.com/science/article/pii/0550321385906066.

[56] **APE** Collaboration, M. Albanese *et al.*, "Glueball Masses and String Tension in Lattice QCD," *Phys. Lett. B* **192** (1987) 163–169.

[57] W. H. Press, S. A. Teukolsky, W. T. Vetterling, and B. P. Flannery, *Numerical Recipes*. Cambridge University Press, Cambridge, United Kingdom, 2007.

[58] N. Metropolis, A. W. Rosenbluth, M. N. Rosenbluth, A. H. Teller, and E. Teller, "Equation of state calculations by fast computing machines," *The journal of chemical physics* **21** no. 6, (1953) 1087–1092.

[59] W. K. Hastings, "Monte Carlo sampling methods using Markov chains and their applications," *Biometrika* **57** no. 1, (04, 1970) 97–109. https://doi.org/10.1093/biomet/57.1.97.

[60] N. Cabibbo and E. Marinari, "A new method for updating su(n) matrices in computer simulations of gauge theories," *Physics Letters B* **119** no. 4, (1982) 387–390. https://www.sciencedirect.com/science/article/pii/0370269382906967.

[61] M. Creutz, "Monte carlo study of quantized su(2) gauge theory," *Phys. Rev. D* **21** (Apr, 1980) 2308–2315. https://link.aps.org/doi/10.1103/PhysRevD.21.2308.

[62] S. L. Adler, "Over-relaxation method for the monte carlo evaluation of the partition function for multiquadratic actions," *Phys. Rev. D* **23** (Jun, 1981) 2901–2904. https://link.aps.org/doi/10.1103/PhysRevD.23.2901.

[63] D. Weingarten and D. Petcher, "Monte carlo integration for lattice gauge theories with fermions," *Physics Letters B* **99** no. 4, (1981) 333–338. https://www.sciencedirect.com/science/article/pii/037026938190112X.

[64] S. Duane, A. Kennedy, B. J. Pendleton, and D. Roweth, "Hybrid monte carlo," *Physics Letters B* **195** no. 2, (1987) 216–222. https://www.sciencedirect.com/science/article/pii/037026938791197X.

[65] M. Luscher, "Computational Strategies in Lattice QCD," in *Les Houches Summer School: Session 93: Modern perspectives in lattice QCD: Quantum field theory and high performance computing*, pp. 331–399. 2, 2010. arXiv:1002.4232 [hep-lat].

[66] R. Gupta, G. W. Kilcup, and S. R. Sharpe, "Tuning the hybrid monte carlo algorithm," *Phys. Rev. D* **38** (Aug, 1988) 1278–1287. https://link.aps.org/doi/10.1103/PhysRevD.38.1278.

[67] M. Creutz, "Global monte carlo algorithms for many-fermion systems," *Phys. Rev. D* **38** (Aug, 1988) 1228–1238. https://link.aps.org/doi/10.1103/PhysRevD.38.1228.

[68] **Alpha** Collaboration, U. Wolff, "Monte Carlo errors with less errors," *Comput. Phys. Commun.* **156** (2004) 143–153, arXiv:hep-lat/0306017. [Erratum: Comput.Phys.Commun. 176, 383 (2007)].

[69] **Alpha** Collaboration, S. Schaefer, R. Sommer, and F. Virotta, "Critical slowing down and error analysis in lattice QCD simulations," *Nucl. Phys. B* **845** (2011) 93–119, arXiv:1009.5228 [hep-lat].

[70] N. Madras and A. D. Sokal, "The pivot algorithm: A highly efficient monte carlo method for the self-avoiding walk," *Journal of Statistical Physics* **50** no. 1, (Jan, 1988) 109–186. https://doi.org/10.1007/BF01022990.

[71] M. Luscher, "Topology, the Wilson flow and the HMC algorithm," *PoS* **LATTICE2010** (2010) 015, arXiv:1009.5877 [hep-lat].

[72] B. Allés, G. Boyd, M. D'Elia, A. Di Giacomo, and E. Vicari, "Hybrid Monte Carlo and topological modes of full QCD," *Phys. Lett. B* **389** (1996) 107–111, arXiv:hep-lat/9607049.

[73] L. Del Debbio, G. M. Manca, and E. Vicari, "Critical slowing down of topological modes," *Phys. Lett. B* **594** (2004) 315–323, arXiv:hep-lat/0403001.

[74] G. Delfino, "Order parameter profiles in presence of topological defect lines," *J. Phys. A* **47** (2014) 132001, arXiv:1401.2041 [cond-mat.stat-mech].

[75] J. Fröhlich, B. Simon, and T. Spencer, "Infrared bounds, phase transitions and continuous symmetry breaking," *Communications in Mathematical Physics* **50** no. 1, (Feb, 1976) 79–95. https://doi.org/10.1007/BF01608557.

[76] R. Kenna, "Finite size scaling for O(N) phi**4-theory at the upper critical dimension," *Nucl. Phys. B* **691** (2004) 292–304, arXiv:hep-lat/0405023.

[77] R. Bauerschmidt, D. C. Brydges, and G. Slade, "Scaling limits and critical behaviour of the 4-dimensional n-component $|\varphi|^4$ spin model," *Journal of Statistical Physics* **157** no. 4, (Dec, 2014) 692–742. https://doi.org/10.1007/s10955-014-1060-5.

[78] Y. Miyatake, M. Yamamoto, J. J. Kim, M. Toyonaga, and O. Nagai, "On the implementation of the 'heat bath' algorithms for Monte Carlo simulations of classical Heisenberg spin systems," *Journal of Physics C: Solid State Physics* **19** no. 14, (1986) 2539–2546. https://doi.org/10.1088%2F0022-3719%2F19%2F14%2F020.

[79] S. L. Adler, "An Overrelaxation Method for the Monte Carlo Evaluationvof the Partition Function for Multiquadratic Actions," *Phys. Rev.* **D23** (1981) 2901.

[80] D. Tong, "Lectures on statistical field theory." https://www.damtp.cam.ac.uk/user/tong/sft.html.

[81] G. Delfino, W. Selke, and A. Squarcini, "Vortex mass in the three-dimensional $O(2)$ scalar theory," *Phys. Rev. Lett.* **122** no. 5, (2019) 050602, arXiv:1808.09276 [cond-mat.stat-mech].

[82] G. Derrick, "Comments on nonlinear wave equations as models for elementary particles," *J. Math. Phys.* **5** (1964) 1252–1254.

[83] D. Davies, "Quantum Solitons in any Dimension: Derrick's Theorem v. AQFT," arXiv:1907.10616 [hep-th].

[84] F. E. Schunck and E. W. Mielke, "General relativistic boson stars," *Class. Quant. Grav.* **20** (2003) R301–R356, arXiv:0801.0307 [astro-ph].

[85] G. E. Volovik, "Linear momentum in ferromagnets," *Journal of Physics C: Solid State Physics* **20** no. 7, (1987) L83–L87. https://doi.org/10.1088%2F0022-3719%2F20%2F7%2F003.

[86] C. Castelnovo, R. Moessner, and S. L. Sondhi, "Magnetic monopoles in spin ice," *Nature* **451N7174** (2008) 42–45, arXiv:0710.5515 [cond-mat.str-el].

[87] P. Milde, D. Köhler, J. J. Seidel, L. M. Eng, A. Bauer, A. Chacon, J. Kindervater, S. Mühlbauer, C. Pfleiderer, S. Buhrandt, C. Schütte, and

A. Rosch, "Unwinding of a Skyrmion Lattice by Magnetic Monopoles," *Science* **31** (2013) 1076–1080.

[88] Y.-J. Lin, R. L. Compton, K. Jiménez-García, J. V. Porto, and I. B. Spielman, "Synthetic magnetic fields for ultracold neutral atoms," *Nature* **462** no. 7273, (2009) 628–632, arXiv:1007.0294 [cond-mat.quant-gas]. http://dx.doi.org/10.1038/nature08609.

[89] M. Hafezi, E. A. Demler, M. D. Lukin, and J. M. Taylor, "Robust optical delay lines with topological protection," *Nature Physics* **7** no. 11, (2011) 907–912, arXiv:1102.3256 [quant-ph]. http://dx.doi.org/10.1038/nphys2063.

[90] N. Kanazawa, A. Kitaori, J. S. White, V. Ukleev, H. M. Rønnow, A. Tsukazaki, M. Ichikawa, M. Kawasaki, and Y. Tokura, "Direct Observation of the Statics and Dynamics of Emergent Magnetic Monopoles in a Chiral Magnet," *Phys. Rev. Lett.* **125** (2020) 137202. https://link.aps.org/doi/10.1103/PhysRevLett.125.137202.

[91] Y. Nambu, "Strings, Monopoles and Gauge Fields," *Phys. Rev.* **D10** (1974) 4262.

[92] T. Gotō, "Relativistic quantum mechanics of one-dimensional mechanical continuum and subsidiary condition of dual resonance model," *Prog. Theor. Phys.* **46** (1971) 1560–1569.

[93] M. Lüscher, "Symmetry Breaking Aspects of the Roughening Transition in Gauge Theories," *Nucl. Phys.* **B180** (1981) 317.

[94] M. Lüscher, K. Symanzik, and P. Weisz, "Anomalies of the Free Loop Wave Equation in the WKB Approximation," *Nucl. Phys.* **B173** (1980) 365.

[95] J. Polchinski and A. Strominger, "Effective string theory," *Phys. Rev. Lett.* **67** (1991) 1681–1684.

[96] H. B. Meyer, "Poincaré invariance in effective string theories," *JHEP* **05** (2006) 066, arXiv:hep-th/0602281.

[97] M. Lüscher and P. Weisz, "String excitation energies in SU(N) gauge theories beyond the free-string approximation," *JHEP* **07** (2004) 014, arXiv:hep-th/0406205.

[98] O. Aharony and E. Karzbrun, "On the effective action of confining strings," *JHEP* **0906** (2009) 012, arXiv:0903.1927 [hep-th].

[99] O. Aharony and M. Dodelson, "Effective String Theory and Nonlinear Lorentz Invariance," *JHEP* **1202** (2012) 008, arXiv:1111.5758 [hep-th].

[100] F. Gliozzi, "Dirac-Born-Infeld action from spontaneous breakdown of Lorentz symmetry in brane-world scenarios," *Phys. Rev.* **D84** (2011) 027702, arXiv:1103.5377 [hep-th].

[101] F. Gliozzi and M. Meineri, "Lorentz completion of effective string (and p-brane) action," *JHEP* **1208** (2012) 056, arXiv:1207.2912 [hep-th].

[102] O. Aharony and Z. Komargodski, "The Effective Theory of Long Strings," *JHEP* **1305** (2013) 118, arXiv:1302.6257 [hep-th].

[103] S. Dubovsky, R. Flauger, and V. Gorbenko, "Effective String Theory Revisited," *JHEP* **09** (2012) 044, arXiv:1203.1054 [hep-th].

[104] J. Elias Miró, A. L. Guerrieri, A. Hebbar, J. Penedones, and P. Vieira, "Flux Tube S-matrix Bootstrap," *Phys. Rev. Lett.* **123** no. 22, (2019) 221602, arXiv:1906.08098 [hep-th].

[105] J. Elias Miró and A. Guerrieri, "Dual EFT bootstrap: QCD flux tubes," *JHEP* **10** (2021) 126, arXiv:2106.07957 [hep-th].

[106] J. Christensen and P. Damgaard, "Finite size scaling and conformal symmetry around the (2+1)-dimensional SU(2) deconfinement phase transition," *Nucl. Phys.* **B354** (1991) 339–368.

[107] M. Teper, "The Finite temperature phase transition of SU(2) gauge fields in (2+1)-dimensions," *Phys. Lett.* **B313** (1993) 417–424.

[108] M. J. Teper, "SU(N) gauge theories in (2+1)-dimensions," *Phys. Rev. D* **59** (1999) 014512, arXiv:hep-lat/9804008.

[109] S. Edwards and L. von Smekal, "SU(2) lattice gauge theory in 2+1 dimensions: Critical couplings from twisted boundary conditions and universality," *Phys. Lett. B* **681** (2009) 484–490, arXiv:0908.4030 [hep-lat].

[110] A. M. Polyakov, "Thermal Properties of Gauge Fields and Quark Liberation," *Phys. Lett.* **B72** (1978) 477–480.

[111] N. Weiss, "The Effective Potential for the Order Parameter of Gauge Theories at Finite Temperature," *Phys. Rev.* **D24** (1981) 475.

[112] L. D. McLerran and B. Svetitsky, "Quark Liberation at High Temperature: A Monte Carlo Study of SU(2) Gauge Theory," *Phys. Rev. D* **24** (1981) 450.

[113] L. Onsager, "Crystal statistics. 1. A Two-dimensional model with an order disorder transition," *Phys. Rev.* **65** (1944) 117–149.

[114] B. M. McCoy and T. T. Wu, *The two-dimensional Ising model*. Harvard University Press, Cambridge, 1973.

[115] T. T. Wu, B. M. McCoy, C. A. Tracy, and E. Barouch, "Spin spin correlation functions for the two-dimensional Ising model: Exact theory in the scaling region," *Phys. Rev. B* **13** (1976) 316–374.

[116] A. B. Zamolodchikov, "Renormalization Group and Perturbation Theory Near Fixed Points in Two-Dimensional Field Theory," *Sov. J. Nucl. Phys.* **46** (1987) 1090.

[117] B. B. Brandt and M. Meineri, "Effective string description of confining flux tubes," *Int. J. Mod. Phys.* **A31** (2016) 1643001, `arXiv:1603.06969 [hep-th]`.

[118] M. Caselle, "Effective String Description of the Confining Flux Tube at Finite Temperature," *Universe* **7** no. 6, (2021) 170, `arXiv:2104.10486 [hep-lat]`.

[119] P. Olesen, "Strings, Tachyons and Deconfinement," *Phys. Lett.* **160B** (1985) 408–410.

[120] R. D. Pisarski and O. Alvarez, "Strings at finite temperature and deconfinement," *Phys. Rev.* **D26** (1982) 3735.

[121] M. Billò, M. Caselle, F. Gliozzi, M. Meineri, and R. Pellegrini, "The Lorentz-invariant boundary action of the confining string and its universal contribution to the inter-quark potential," *JHEP* **1205** (2012) 130, `arXiv:1202.1984 [hep-th]`.

[122] O. Aharony and M. Field, "On the effective theory of long open strings," *JHEP* **1101** (2011) 065, `arXiv:1008.2636 [hep-th]`.

[123] M. Panero, "Thermodynamics of the QCD plasma and the large-N limit," *Phys. Rev. Lett.* **103** (2009) 232001, `arXiv:0907.3719 [hep-lat]`.

[124] A. Mykkänen, M. Panero, and K. Rummukainen, "Casimir scaling and renormalization of Polyakov loops in large-N gauge theories," *JHEP* **1205** (2012) 069, arXiv:1202.2762 [hep-lat].

[125] M. Creutz, "Monte Carlo Study of Quantized SU(2) Gauge Theory," *Phys. Rev.* **D21** (1980) 2308–2315.

[126] A. Kennedy and B. Pendleton, "Improved Heat Bath Method for Monte Carlo Calculations in Lattice Gauge Theories," *Phys. Lett.* **B156** (1985) 393–399.

[127] C. Bonati, M. Caselle, and S. Morlacchi, "The Unreasonable effectiveness of effective string theory: The case of the 3D SU(2) Higgs model," *Phys. Rev. D* **104** no. 5, (2021) 054501, arXiv:2106.08784 [hep-lat].

[128] A. Athenodorou and M. Teper, "Closed flux tubes in D = 2 + 1 SU(N) gauge theories: dynamics and effective string description," *JHEP* **10** (2016) 093, arXiv:1602.07634 [hep-lat].

[129] S. Dubovsky, R. Flauger, and V. Gorbenko, "Flux Tube Spectra from Approximate Integrability at Low Energies," *J. Exp. Theor. Phys.* **120** no. 3, (2015) 399–422, arXiv:1404.0037 [hep-th].

[130] P. Conkey and S. Dubovsky, "Four Loop Scattering in the Nambu-Goto Theory," *JHEP* **05** (2016) 071, arXiv:1603.00719 [hep-th].

[131] C. Chen, P. Conkey, S. Dubovsky, and G. Hernández-Chifflet, "Undressing Confining Flux Tubes with $T\bar{T}$," *Phys. Rev. D* **98** no. 11, (2018) 114024, arXiv:1808.01339 [hep-th].

[132] A. Athenodorou, B. Bringoltz, and M. Teper, "Closed flux tubes and their string description in D=2+1 SU(N) gauge theories," *JHEP* **1105** (2011) 042, arXiv:1103.5854 [hep-lat].

[133] S. Dubovsky and V. Gorbenko, "Towards a Theory of the QCD String," *JHEP* **02** (2016) 022, arXiv:1511.01908 [hep-th].

[134] F. Karsch and H. W. Wyld, "Thermal Green's functions and transport coefficients on the lattice," *Phys. Rev. D* **35** (Apr, 1987) 2518–2523. https://link.aps.org/doi/10.1103/PhysRevD.35.2518.

[135] H. B. Meyer, "Transport Properties of the Quark-Gluon Plasma: A Lattice QCD Perspective," *Eur. Phys. J. A* **47** (2011) 86, arXiv:1104.3708 [hep-lat].

[136] T. Bergamaschi, W. I. Jay, and P. R. Oare, "Hadronic Structure, Conformal Maps, and Analytic Continuation," arXiv:2305.16190 [hep-lat].

[137] M. Bertero, P. Boccacci, and P. E. Roy, "On the recovery and resolution of exponential relaxation rates from experimental data: A singular-value analysis of the Laplace transform inversion in the presence of noise," *Proc. R. Soc. Lond.* **A** (Sep, 1982) 15–29. https://doi.org/10.1098/rspa.1982.0117.

[138] J. Hadamard, "Sur les problèmes aux dérivées partielles et leur signification physique," *Princeton University Bulletin* (1902) 49–52.

[139] I. S. Krivenko and A. N. Rubtsov, "Analytic Continuation of Quantum Monte Carlo Data: Optimal Stochastic Regularization Approach," 2011.

[140] A. S. Mishchenko, N. V. Prokof'ev, A. Sakamoto, and B. V. Svistunov, "Diagrammatic quantum Monte Carlo study of the Fröhlich polaron," *Phys. Rev. B* **62** (Sep, 2000) 6317–6336. https://link.aps.org/doi/10.1103/PhysRevB.62.6317.

[141] J. E. Gubernatis, M. Jarrell, R. N. Silver, and D. S. Sivia, "Quantum Monte Carlo simulations and maximum entropy: Dynamics from imaginary-time data," *Phys. Rev. B* **44** (Sep, 1991) 6011–6029. https://link.aps.org/doi/10.1103/PhysRevB.44.6011.

[142] M. Jarrell and J. Gubernatis, "Bayesian inference and the analytic continuation of imaginary-time quantum Monte Carlo data," *Physics Reports* **269** no. 3, (1996) 133–195. https://www.sciencedirect.com/science/article/pii/0370157395000747.

[143] Y. Burnier and A. Rothkopf, "Bayesian Approach to Spectral Function Reconstruction for Euclidean Quantum Field Theories," *Phys. Rev. Lett.* **111** (2013) 182003, arXiv:1307.6106 [hep-lat].

[144] G. Backus and F. Gilbert, "The Resolving Power of Gross Earth Data," *Geophysical Journal International* **16** no. 2, (10, 1968) 169–205, https://academic.oup.com/gji/article-pdf/16/2/169/5891044/16-2-169.pdf. https://doi.org/10.1111/j.1365-246X.1968.tb00216.x.

[145] G. Bailas, S. Hashimoto, and T. Ishikawa, "Reconstruction of smeared spectral function from Euclidean correlation functions," *PTEP* **2020** no. 4, (2020) 043B07, arXiv:2001.11779 [hep-lat].

[146] L. Kades, J. M. Pawlowski, A. Rothkopf, M. Scherzer, J. M. Urban, S. J. Wetzel, N. Wink, and F. P. G. Ziegler, "Spectral Reconstruction with Deep Neural Networks," *Phys. Rev. D* **102** no. 9, (2020) 096001, arXiv:1905.04305 [physics.comp-ph].

[147] J. Karpie, K. Orginos, A. Rothkopf, and S. Zafeiropoulos, "Reconstructing parton distribution functions from Ioffe time data: from Bayesian methods to Neural Networks," *JHEP* **04** (2019) 057, arXiv:1901.05408 [hep-lat].

[148] M. Buzzicotti, A. De Santis, and N. Tantalo, "Teaching to extract spectral densities from lattice correlators to a broad audience of learning-machines," arXiv:2307.00808 [hep-lat].

[149] M. Hansen, A. Lupo, and N. Tantalo, "Extraction of spectral densities from lattice correlators," *Phys. Rev. D* **99** no. 9, (2019) 094508, arXiv:1903.06476 [hep-lat].

[150] M. T. Hansen, H. B. Meyer, and D. Robaina, "From deep inelastic scattering to heavy-flavor semileptonic decays: Total rates into multihadron final states from lattice QCD," *Phys. Rev. D* **96** no. 9, (2017) 094513, arXiv:1704.08993 [hep-lat].

[151] J. Bulava, M. T. Hansen, M. W. Hansen, A. Patella, and N. Tantalo, "Inclusive rates from smeared spectral densities in the two-dimensional O(3) non-linear σ-model," *JHEP* **07** (2022) 034, arXiv:2111.12774 [hep-lat].

[152] L. Del Debbio, A. Lupo, M. Panero, and N. Tantalo, "Multi-representation dynamics of SU(4) composite Higgs models: chiral limit and spectral reconstructions," *Eur. Phys. J. C* **83** no. 3, (2023) 220, arXiv:2211.09581 [hep-lat].

[153] **Extended Twisted Mass Collaboration (ETMC)** Collaboration, C. Alexandrou *et al.*, "Probing the Energy-Smeared R Ratio Using Lattice QCD," *Phys. Rev. Lett.* **130** no. 24, (2023) 241901, arXiv:2212.08467 [hep-lat].

[154] E. Klempt and A. Zaitsev, "Glueballs, Hybrids, Multiquarks. Experimental facts versus QCD inspired concepts," *Phys. Rept.* **454** (2007) 1–202, arXiv:0708.4016 [hep-ph].

[155] V. Crede and C. A. Meyer, "The Experimental Status of Glueballs," *Prog. Part. Nucl. Phys.* **63** (2009) 74–116, arXiv:0812.0600 [hep-ex].

[156] H.-X. Chen, W. Chen, X. Liu, Y.-R. Liu, and S.-L. Zhu, "An updated review of the new hadron states," *Rept. Prog. Phys.* **86** no. 2, (2023) 026201, arXiv:2204.02649 [hep-ph].

[157] M. Panero, A. Smecca, N. Tantalo, and D. Vadacchino, "The quenched glueball spectrum from smeared spectral densities," *in preparation* (2023) .

[158] J. M. Pawlowski, C. S. Schneider, J. Turnwald, J. M. Urban, and N. Wink, "Yang-Mills glueball masses from spectral reconstruction," arXiv:2212.01113 [hep-ph].

[159] G. Parisi, "The strategy for computing the hadronic mass spectrum," *Physics Reports* **103** no. 1, (1984) 203–211. https://www.sciencedirect.com/science/article/pii/0370157384900814.

[160] G. P. Lepage, "The Analysis of Algorithms for Lattice Field Theory," in *Theoretical Advanced Study Institute in Elementary Particle Physics*. 6, 1989.

[161] A. Athenodorou and M. Teper, "The glueball spectrum of SU(3) gauge theory in 3 + 1 dimensions," *JHEP* **11** (2020) 172, arXiv:2007.06422 [hep-lat].

[162] F. Englert and R. Brout, "Broken symmetry and the mass of gauge vector mesons," *Phys. Rev. Lett.* **13** (Aug, 1964) 321–323. https://link.aps.org/doi/10.1103/PhysRevLett.13.321.

[163] P. W. Higgs, "Broken symmetries and the masses of gauge bosons," *Phys. Rev. Lett.* **13** (Oct, 1964) 508–509. https://link.aps.org/doi/10.1103/PhysRevLett.13.508.

[164] A. Salam, "Weak and Electromagnetic Interactions," *Conf. Proc. C* **680519** (1968) 367–377.

[165] S. Weinberg, "A model of leptons," *Phys. Rev. Lett.* **19** (Nov, 1967) 1264–1266. https://link.aps.org/doi/10.1103/PhysRevLett.19.1264.

[166] M. Gell-Mann, "A Schematic Model of Baryons and Mesons," *Phys. Lett.* **8** (1964) 214–215.

[167] G. Zweig, *An SU(3) model for strong interaction symmetry and its breaking. Version 2*, pp. 22–101. 2, 1964.

[168] G. Isidori, F. Wilsch, and D. Wyler, "The Standard Model effective field theory at work," arXiv:2303.16922 [hep-ph].

[169] A. Lenz and U. Nierste, "Theoretical update of $B_s - \bar{B}_s$ mixing," *JHEP* **06** (2007) 072, arXiv:hep-ph/0612167.

[170] A. Lenz, U. Nierste, J. Charles, S. Descotes-Genon, A. Jantsch, C. Kaufhold, H. Lacker, S. Monteil, V. Niess, and S. T'Jampens, "Anatomy of New Physics in $B - \bar{B}$ mixing," *Phys. Rev. D* **83** (2011) 036004, arXiv:1008.1593 [hep-ph].

[171] A. Lenz, U. Nierste, J. Charles, S. Descotes-Genon, H. Lacker, S. Monteil, V. Niess, and S. T'Jampens, "Constraints on new physics in $B - \bar{B}$ mixing in the light of recent LHCb data," *Phys. Rev. D* **86** (2012) 033008, arXiv:1203.0238 [hep-ph].

[172] L. Di Luzio, M. Kirk, and A. Lenz, "Updated B_s-mixing constraints on new physics models for $b \to s\ell^+\ell^-$ anomalies," *Phys. Rev. D* **97** no. 9, (2018) 095035, arXiv:1712.06572 [hep-ph].

[173] M. Ciuchini, E. Franco, V. Lubicz, G. Martinelli, L. Silvestrini, and C. Tarantino, "Power corrections to the CP-violation parameter ε_K," *JHEP* **02** (2022) 181, arXiv:2111.05153 [hep-ph].

[174] N. Cabibbo, "Unitary Symmetry and Leptonic Decays," *Phys. Rev. Lett.* **10** (1963) 531–533.

[175] M. Kobayashi and T. Maskawa, "CP Violation in the Renormalizable Theory of Weak Interaction," *Prog. Theor. Phys.* **49** (1973) 652–657.

[176] **Flavour Lattice Averaging Group (FLAG)** Collaboration, Y. Aoki *et al.*, "FLAG Review 2021," *Eur. Phys. J. C* **82** no. 10, (2022) 869, arXiv:2111.09849 [hep-lat].

[177] M. Jung and D. M. Straub, "Constraining new physics in $b \to c\ell\nu$ transitions," *JHEP* **01** (2019) 009, arXiv:1801.01112 [hep-ph].

[178] A. Crivellin and S. Pokorski, "Can the differences in the determinations of V_{ub} and V_{cb} be explained by New Physics?," *Phys. Rev. Lett.* **114** no. 1, (2015) 011802, arXiv:1407.1320 [hep-ph].

[179] P. Gambino, M. Jung, and S. Schacht, "The V_{cb} puzzle: An update," *Phys. Lett. B* **795** (2019) 386–390, arXiv:1905.08209 [hep-ph].

[180] D. Bigi, P. Gambino, and S. Schacht, "A fresh look at the determination of $|V_{cb}|$ from $B \to D^* \ell \nu$," *Phys. Lett. B* **769** (2017) 441–445, arXiv:1703.06124 [hep-ph].

[181] P. Gambino and S. Hashimoto, "Inclusive Semileptonic Decays from Lattice QCD," *Phys. Rev. Lett.* **125** no. 3, (2020) 032001, arXiv:2005.13730 [hep-lat].

[182] K. G. Wilson, "Nonlagrangian models of current algebra," *Phys. Rev.* **179** (1969) 1499–1512.

[183] L. P. Kadanoff, "Operator Algebra and the Determination of Critical Indices," *Phys. Rev. Lett.* **23** (1969) 1430–1433.

[184] I. I. Y. Bigi, N. G. Uraltsev, and A. I. Vainshtein, "Nonperturbative corrections to inclusive beauty and charm decays: QCD versus phenomenological models," *Phys. Lett. B* **293** (1992) 430–436, arXiv:hep-ph/9207214. [Erratum: Phys.Lett.B 297, 477–477 (1992)].

[185] I. I. Y. Bigi, M. A. Shifman, N. G. Uraltsev, and A. I. Vainshtein, "QCD predictions for lepton spectra in inclusive heavy flavor decays," *Phys. Rev. Lett.* **71** (1993) 496–499, arXiv:hep-ph/9304225.

[186] B. Blok, L. Koyrakh, M. A. Shifman, and A. I. Vainshtein, "Differential distributions in semileptonic decays of the heavy flavors in QCD," *Phys. Rev. D* **49** (1994) 3356, arXiv:hep-ph/9307247. [Erratum: Phys.Rev.D 50, 3572 (1994)].

[187] S. Hashimoto, "Inclusive semi-leptonic B meson decay structure functions from lattice QCD," *PTEP* **2017** no. 5, (2017) 053B03, arXiv:1703.01881 [hep-lat].

[188] R. Baron *et al.*, "Light hadrons from lattice QCD with light (u,d), strange and charm dynamical quarks," *JHEP* **06** (2010) 111, arXiv:1004.5284 [hep-lat].

[189] **ETM** Collaboration, R. Baron *et al.*, "Light hadrons from $N_f = 2 + 1 + 1$ dynamical twisted mass fermions," *PoS* **LATTICE2010** (2010) 123, arXiv:1101.0518 [hep-lat].

[190] **ETM** Collaboration, N. Carrasco *et al.*, "Up, down, strange and charm quark masses with $N_f = 2 + 1 + 1$ twisted mass lattice QCD," *Nucl. Phys. B* **887** (2014) 19–68, arXiv:1403.4504 [hep-lat].

[191] P. Dimopoulos, R. Frezzotti, C. Michael, G. C. Rossi, and C. Urbach, "$O(a^2)$ cutoff effects in lattice Wilson fermion simulations," *Phys. Rev. D* **81** (2010) 034509, arXiv:0908.0451 [hep-lat].

[192] C. T. Sachrajda and G. Villadoro, "Twisted boundary conditions in lattice simulations," *Phys. Lett. B* **609** (2005) 73–85, arXiv:hep-lat/0411033.

[193] P. F. Bedaque and J.-W. Chen, "Twisted valence quarks and hadron interactions on the lattice," *Phys. Lett. B* **616** (2005) 208–214, arXiv:hep-lat/0412023.

[194] J. Chay, H. Georgi, and B. Grinstein, "Lepton energy distributions in heavy meson decays from QCD," *Phys. Lett. B* **247** (1990) 399–405.

[195] A. V. Manohar and M. B. Wise, "Inclusive semileptonic B and polarized Λ_b decays from QCD," *Phys. Rev. D* **49** (1994) 1310–1329, arXiv:hep-ph/9308246.

[196] I. I. Y. Bigi, M. A. Shifman, N. Uraltsev, and A. I. Vainshtein, "High power n of m(b) in beauty widths and n=5 —> infinity limit," *Phys. Rev. D* **56** (1997) 4017–4030, arXiv:hep-ph/9704245.

[197] A. Czarnecki, K. Melnikov, and N. Uraltsev, "Non-Abelian dipole radiation and the heavy quark expansion," *Phys. Rev. Lett.* **80** (1998) 3189–3192, arXiv:hep-ph/9708372.

[198] M. Fael, K. Schönwald, and M. Steinhauser, "Relation between the $\overline{\text{MS}}$ and the kinetic mass of heavy quarks," *Phys. Rev. D* **103** no. 1, (2021) 014005, arXiv:2011.11655 [hep-ph].

[199] M. Fael, K. Schönwald, and M. Steinhauser, "Third order corrections to the semileptonic $b \to c$ and the muon decays," *Phys. Rev. D* **104** no. 1, (2021) 016003, arXiv:2011.13654 [hep-ph].

[200] M. Bordone, B. Capdevila, and P. Gambino, "Three loop calculations and inclusive Vcb," *Phys. Lett. B* **822** (2021) 136679, arXiv:2107.00604 [hep-ph].

[201] **ETM** Collaboration, B. Blossier *et al.*, "A Proposal for B-physics on current lattices," *JHEP* **04** (2010) 049, arXiv:0909.3187 [hep-lat].

[202] **ETM** Collaboration, P. Dimopoulos *et al.*, "Lattice QCD determination of m_b, f_B and f_{Bs} with twisted mass Wilson fermions," *JHEP* **01** (2012) 046, arXiv:1107.1441 [hep-lat].

[203] **ETM** Collaboration, N. Carrasco *et al.*, "B-physics from $N_f = 2$ tmQCD: the Standard Model and beyond," *JHEP* **03** (2014) 016, arXiv:1308.1851 [hep-lat].

[204] **ETM** Collaboration, A. Bussone *et al.*, "Mass of the b quark and B -meson decay constants from N_f=2+1+1 twisted-mass lattice QCD," *Phys. Rev. D* **93** no. 11, (2016) 114505, arXiv:1603.04306 [hep-lat].

[205] P. Gambino, A. Melis, and S. Simula, "Extraction of heavy-quark-expansion parameters from unquenched lattice data on pseudoscalar and vector heavy-light meson masses," *Phys. Rev. D* **96** no. 1, (2017) 014511, arXiv:1704.06105 [hep-lat].

[206] P. Gambino, V. Lubicz, A. Melis, and S. Simula, "Masses, decay constants and HQE matrix elements of pseudoscalar and vector heavy-light mesons in LQCD," *J. Phys. Conf. Ser.* **1137** no. 1, (2019) 012005.

[207] **CLEO** Collaboration, D. M. Asner *et al.*, "Measurement of absolute branching fractions of inclusive semileptonic decays of charm and charmed-strange mesons," *Phys. Rev. D* **81** (2010) 052007, arXiv:0912.4232 [hep-ex].

[208] **BESIII** Collaboration, M. Ablikim *et al.*, "Measurement of the absolute branching fraction of inclusive semielectronic D_s^+ decays," *Phys. Rev. D* **104** no. 1, (2021) 012003, arXiv:2104.07311 [hep-ex].